Weathering and climate in the Himalaya since the Miocene - Insights from foreland basin sediments

Natalie Vögeli

▶ To cite this version:

Natalie Vögeli. Weathering and climate in the Himalaya since the Miocene - Insights from foreland basin sediments. Earth Sciences. Université Grenoble Alpes; University of lancaster, 2016. English. NNT : 2016GREAU033 . tel-01562043

HAL Id: tel-01562043
https://theses.hal.science/tel-01562043
Submitted on 13 Jul 2017

UNIVERSITÉ GRENOBLE ALPES

THÈSE

Pour obtenir le grade de

DOCTEUR DE L'UNIVERSITÉ GRENOBLE ALPES

Spécialité : **Sciences de la Terre, de l'Univers et de l'Environnement**

Arrêté ministériel : 7 Août 2006

Présentée par

Natalie Vögeli

Thèse dirigée par **Peter van der Beek**
et codirigée par **Pascale Huyghe and Yani Najman**

préparée au sein de **l'Institut des Sciences de la Terre**
et de l'école doctorale **Terre Univers Environnement**

Weathering and climate in the Himalaya since the Miocene - Insights from foreland basin sediments

Thèse soutenue publiquement le **30 septembre 2016**,
devant le jury composé de :

Stéphane Guillot
Directeur de Recherche CNRS, ISTerre, Université Grenoble Alpes, Grenoble, France, Président
Christian France-Lanord
Directeur de Recherche CNRS,CRPG, Nancy, France, Rapporteur
Peter Clift
Professor, Louisiana State University, United States, Rapporteur
Maarten Lupker
Oberassistent at ETH Zürich, Switzerland, Examinateur
Peter van der Beek
Professeur, ISTerre, Université Grenoble Alpes, Grenoble, France, Directeur de thèse
Pascale Huyghe
Maitre de Conf., ISTerre, Université Grenoble Alpes, Grenoble, France, Co-Directeur de thèse
Yani Najman
Reader, LEC, University of Lancaster, UK, Co-Directeur de thèse

Acknowledgements

First of all, I would like to thank my “rapporteurs“ (Christian France-Lanord and Peter Clift) and my “examinateurs” (Maarten Lupker and Stéphane Guillot) to have accepted to read and evaluate my thesis.

A big thank you goes to my supervisors Peter, Pascale and Yani! Thanks for introducing me to the Siwaliks and the Himalayas. Thanks for leading me through these three years and giving me the possibility to be part of the ITECC. Thank for all the scientific discussions and inputs, but still letting me creating my project and encouraging me do try new things. I really enjoy working with you!

I would like to thank Marie Curie action for the funding of the thesis, which allowed me to build up a network and working with a great group of people in Europe and being able to participate in our fieldtrip in Nepal and explore the Indian Siwalik. At this place I would also thank all my ITECC friends, we had a blast at all our workshops in the field. I will miss our gatherings. . .

A special thank goes to my field buddies Lorenzo and Gwladys, grazie and merci for all the days in the field, sometimes a bid hard, especially before breakfast :-), but also incredibly fun. Thanks for spending days in the DHL office with me, dressing up in traditional cloths, carrying rocks. . . I could go on forever. Merci Gwlagwla et Lolo!

Thanks to all the people in Potsdam, Cambridge and Lancaster, especially Dave and Montse, who helped me do my analyses during my secondments. Thanks Madeleine to show me how to do lithium columns and look hilarious dancing around in the lab in our suits. I also thank all the people, I spent time with, during my secondments, I had a lot of fun.

Merci à tous les gens de l’ISTerre, qui m’ont aidé à préparer mes échantillons et les analyser, notamment Francis, Sarah et Nathaniel. Merci à tous les autres pour des discussions scientifique ou pas scientifique et passer des moments sympas. Merci au gens de café du matin, ça faisait les matins toujours beaucoup plus agréable!

Merci à tous mes amis ici à ISTerre et Grenoble, pour les ”couch coffees”, les barathons, les bbq’s sur le fort, les bières, les rando à ski ou à pieds, les midis au lacs (merci Audrey) et et et. . . thanks a lot! Merci à toutes mes colocs, que j’ai eu pendant les trois années, c’était toujours un plaisir de rentrer à la maison après tous mes voyages. Thanks Ellie for all the bike rides to yoga, our endless discussion about recipes, when we were supposed to work ;-). Thanks Paul for helping making my thesis look nice :-) and Eric for being a great office mate, even if you left early ;-). Merci à tout le monde qui était là, qui m’a aidé avec le français, Latex, au labo...

Es riise grosses dankeschön au a alli Lüüt ide Schwiiz! Danke minere Familie fürd Understützig während mim ganze Geologie Studium, bis zum Dokter :-). Ich bin immer wider gern zrugg cho, wenn mängisch au nur für churz! Danke allne Fründe wo mich sind go bsueche uf Grenoble, für all die Wanderige, Brunchs und s‘ hänge a all denen Wuchenend. Ich hans immer sehr gnosse! Danke für die ville Skype dates, zum eifach nur pläuderele oder zum mich ufheitere, wenns mal nöd eifach gsi isch im Franzeland :-).

I spent three absolutely great years! Merci à tous! Danke allne! Thank to everyone!

Abstract

The Himalaya orogen has major impact on global and regional climate and acts as an orographic barrier for atmospheric circulations. The interplay of the Asian monsoon system and the tectonic evolution of the mountain belt make it an ideal laboratory to study interactions between tectonics, climate and erosion, and its implications on weathering and atmospheric CO_2 drawdown. Lateral variations in exhumation rates have been observed and studies on paleoclimate have been conducted in the central and western Himalaya, but the onset, the evolution and the characteristics of the monsoonal climate are still debated. Paleo weathering rates and intensities are challenging to reconstruct and remain poorly studied, especially in the eastern part of the orogen.

This thesis focuses on lateral variations in climate, weathering and vegetation along the Himalayan mountain range, on weathering regimes in the eastern Himalaya since Miocene times, and on the implications for the evolution of the Asian monsoon. The foreland basin sediments of the pre-Siwalik and Siwalik Groups contain a record of erosion, tectonics and paleoclimate. The approach focuses on a direct west-east comparison; I therefore sampled three previously dated sedimentary sections in the western Himalaya, namely the Joginder Nagar, Jawalamukhi and Haripur Kolar, which combine into a timespan of 20 Ma, and the Kameng river section in the east, which spans over the last 13 Ma.

Stable carbon isotopes on organic matter are used to reconstruct changes in vegetation. Stable carbon isotopes show important lateral variations, with a change toward more positive values in the west at ~7 Ma and in contrast no change in the east, indicating a change in vegetation from C3 to C4 plant in the west but not in the east. These variations implicate a change towards a dryer and more seasonal climate in the western Himalaya, whereas the climate in the eastern part remained too humid for C4 plants to spread, due to its proximity to moisture source (Bay of Bengal).

In order to reconstruct paleo weathering regimes by analyzing foreland basin sediments, it is important to take into account changes in provenance and possible influences of burial diagenesis. Results of heavy-mineral and petrographic analyses of the Kameng section provide better insight into diagenesis and provenance, showing that the older part of the Kameng section is influenced by diagenesis. Changes in provenance do not correlate with changes in clay mineralogy and major elements, which are therefore indicating an overall increase in weathering over time, with a remarkable change at ~8 Ma.

The compilation of the three sections in the west represent one of the longest sedimentary records in the Himalayas, spanning over 20 Ma. Clay minerals show similar trends in the west and the east, indicating the development of a more seasonal climate starting at ~8 Ma. Major elements show a trend toward stronger weathering over time in the west and the east, but the western Himalaya are generally more weathered than in the east, which is consistent with the interpretation of the stable carbon isotope data, suggesting the climate to be more humid in the east. More runoff and erosion inhibit extensive weathering of the sediments, whereas dry seasons with little runoff allow sediments to weather.

Lithium isotopic compositions were measured on bulk sediments as a new approach to reconstruct chemical weathering rates, applied for the first time on Siwalik sediments. Results show a change in weathering intensity in the west, where lithium isotopic values become more positive over time, whereas, they stay relatively constant in the east. More positive values in the west, suggest that the system becomes more weathering-limited and more incongruent.

Keywords: weathering, monsoon, Himalaya, lateral variations, stable carbon isotopes, clay mineralogy, Siwalik, pre-Siwalik, lithium isotopes. Miocene, foreland basin

Résumé

La chaîne himalayenne est influencée par le climat global et régional et joue un rôle de barrière orographique pour les circulations atmosphériques. Son évolution tectonique et la mousson asiatique qui l'affecte en font un laboratoire idéal pour les études du lien entre la tectonique, le climat et l'érosion et leurs implications pour l'altération. Des variations latérales de taux d'exhumation ont été documentées et des études paléoclimatiques ont été réalisées dans les parties centrale et occidentale de la chaîne, mais l'initiation, l'évolution et les caractéristiques de la mousson sont encore débattues. Les intensités et les taux d'altération engendrés ont été peu étudiés, surtout dans la partie orientale de l'Himalaya.

Cette thèse se focalise sur les variations latérales d'Ouest en Est de l'altération, de la végétation (évolution C3/C4) et du climat, le long de l'Himalaya depuis le Miocène à partir de l'enregistrement sédimentaire du bassin d'‘avant-pays. Les données apportent des nouvelles avancées pour la compréhension de l'évolution de la mousson asiatique. Pour ce travail, j'ai étudié trois coupes pré-Siwalik et Siwalik dans l'ouest de la chaîne (les coupes Joginder Nagar, Jawalamukhi et Haripur Kolar à Himachal Pradesh, Inde), qui documentent un enregistrement sédimentaire de 20 Ma, et une coupe dans l'est (la coupe de la Kameng à Arunachal Pradesh), qui quant à elle documente 13 Ma.

Les isotopes stable du carbone de la matière organique ont été utilisés pour reconstruire des changements de la végétation C3 à C4 et montrent des variations importantes entre l'ouest et l'est de la chaîne, avec une augmentation brutale des valeurs dans l'ouest à ~7 Ma, ce qui indique un changement de végétation des plantes C3 à C4. Au contraire, aucune variation n'est notée dans l'est, ce qui indique que la partie orientale caractérisée par une végétation C3 ne subit pas de changement majeur de végétation. Les variations indiquent un « assèchement » du climat et notamment une plus grande saisonnalité dans la partie occidentale de la paléoplaine. La partie orientale reste trop humide pour une évolution vers une végétation en C4, sans doute à cause de la proximité de source d'humidité du Golfe du Bengale.

Le long de la coupe orientale de la Kameng, il a été nécessaire d'étudier les changements de provenance et la diagenèse, pour les éliminer, avant de reconstruire les paléo-régimes d'altération. L'analyse des minéraux lourds a permis de repérer les changements de source et de montrer que seule la partie basse de la coupe a été influencée par la diagenèse. L'évolution de la minéralogie des argiles et des éléments majeurs montre que l'altération augmente avec le temps avec une période remarquable à ~8 Ma.

La compilation des trois coupes occidentales représente l'enregistrement le plus long du bassin d'avant-pays himalayen avec une durée de 20 Ma. L'évolution des argiles montre une tendance similaire entre les parties occidentale et l'orientale du bassin d'avant-pays, impliquant l'évolution vers un climat plus saisonnier à partir de ~8 Ma. Les éléments majeurs indiquent une augmentation du taux d'altération avec le temps, la partie occidentale étant généralement plus altérée que la partie orientale. Les résultats des éléments majeurs et des argiles sont cohérents avec les interprétations des isotopes stables du carbone, qui indiquent un climat plus saisonnier dans l'ouest.

Enfin, une nouvelle approche permettant de reconstruire les taux d'altération à partir de la composition isotopique du lithium a été testée pour la première fois dans les sédiments miocènes du bassin d’avant-pays. Les résultats montrent à nouveau un changement dans l’ouest de la chaîne, où les valeurs isotopiques deviennent plus positives avec le temps, alors que les valeurs dans l’est restent stables. Dans l’ouest, le facteur limitant du système limitant devient l’altération (altération “incongruente”), alors que dans l’est le facteur limitant est l’apport (altération “congruente”).

Mots clés: altération, mousson, Himalaya, variations latérales d’Est en Ouest, isotopes stables du carbone, isotopes de lithium, argiles, bassin d’avant-pays, Miocène, Siwalik

Table of Contents

Introduction

Tectonics and climate are interdependent, and have impact on erosion, topography and weathering. Topography resulting from mountain uplift and erosion influences rainfall patterns, hence regional climate (e.g. Bookhagen and Burbank, 2006, 2010; Strecker et al., 2007). The growth of orogens can also influence and change atmospheric circulations (Boos and Kuang, 2010; Molnar et al., 2010). Climate in turn can moderate tectonics through erosion (e.g. Willett, 1999; Whipple, 2009). Climate also has an impact on weathering regimes and erosion rates, which in turn are major controls on atmospheric CO_2. Together with carbon burial, the intensity of silicate weathering plays a central role in modulating atmospheric CO_2 drawdown on geological timescales (e.g. Berner et al., 1983; Kump et al., 2000). Atmospheric CO_2 has an influence on global temperature, which in turn influences climate and possibly weathering (Berner, 2004). Physical erosion and runoff, together with temperature, are limiting factors for chemical weathering (West et al., 2005), which make understanding interactions between erosion and climate crucial. It is critical to understand how changes in climate influence chemical weathering in order to determine the long-term behavior of the carbon cycle. By understanding past variations of the chemical weathering, past, present and future variations on the global carbon cycle can better be predicted.

Thus, tectonics, climate, weathering and erosion are coupled, but to which extent one influences the others is not yet fully understood. What impact does mountain uplift have on the global carbon cycle? How are physical erosion and chemical weathering linked? Can climate influence exhumation rates? Questions like these remain to be answered.

The Himalayan orogen is the largest mountain belt on Earth, and has major impacts on global and regional climate. It is therefore an excellent laboratory to study tectonics, climate and erosion couplings. It is important to investigate such couplings to understand the evolution of the mountain belt and the past climate. Resulting from the collision of the Indian and Eurasian continents, the Himalaya is home to the highest mountains on Earth. Spanning from Pakistan all the way to north-eastern India, the mountain belt acts as an orographic barrier for air masses (Boos and Kuang, 2010). Today's climate in the Himalayan region is influenced by two important atmospheric circulations: the Indian Summer Monsoon and the Westerlies (Kotlia et al., 2015) (Figure 1). The Indian Summer Monsoon (ISM) brings heavy precipitation to the Himalayan region during the northern-hemisphere summer months (Bookhagen and Burbank, 2010; Kotlia et al., 2015) . The Westerlies influence mostly the northwestern part of the Himalaya, bringing moisture from the Mediterranean, Black and Caspian Seas and are

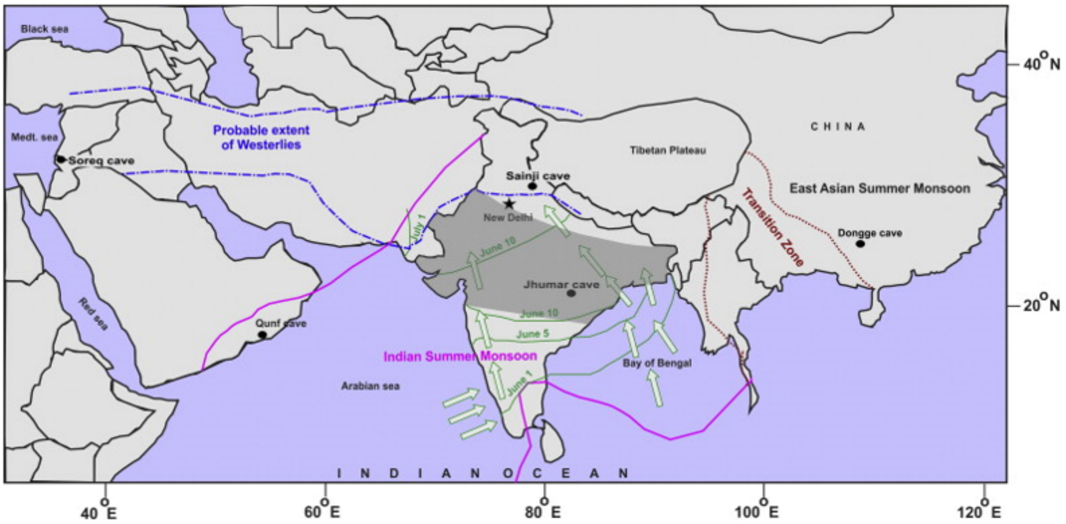

Figure 1: Modern monsoonal climate system and major atmospheric circulations influencing the Himalayan region (Kotlia et al., 2015).

mostly active during the winter months (Benn and Owen, 1998). These variations result in a specific precipitation pattern along the Himalayan mountain front, with a more arid and seasonal climate in the west and a more humid climate in the east, respectively (Figure 2; (Bookhagen and Burbank, 2006). Even though the major force driving the evolution of the Himalayan mountain belt is the India-Asia collision, the monsoonal climate has been argued to strongly influence topography and erosion rates on different timescales in the Himalaya (e.g. Bookhagen and Burbank, 2006; Bookhagen et al., 2005; Clift et al., 2008; Pratt-Sitaula et al., 2004), and even to have influenced the tectonic development of the range (Allen and Armstrong, 2012; Iaffaldano et al., 2011; Wobus et al., 2003).

The onset and the evolution of the Asian monsoon are still debated: while early studies estimated the onset to date from the Late Miocene (Kroon et al., 1991; Molnar et al., 1993), this timing has been pushed back in subsequent studies (e.g. Dettman et al., 2001; Guo et al., 2008). A recent study (Licht et al., 2014) dates the South and East Asian Monsoons back to the Late Eocene, based on seasonal carbon-isotope records from Myanmar and aeolian dust deposits in China. Several studies have focused on the reconstruction of monsoonal climate in the Himalayan region by looking stable-isotope, clay-mineral and major-element chemistry records in marine sediments of the Arabian Sea, the Bay of Bengal and the South China Sea (Kroon et al., 1991; France-Lanord et al., 1993; France-Lanord and Derry, 1994; Clift et al., 2008, 2014, amongst others). Others have focused on the more proximal foreland basin sediments of the so-called Siwalik Group, in order to reconstruct paleo-vegetation by using stable carbon and oxygen isotopes (Quade et al., 1989, 1995; Quade and Cerling, 1995; Sanyal et al., 2010, amongst others).

Interpretations on strengthening or weakening of the monsoon vary widely (Figure 3), depending on the proxies used and the interpretation of the term "monsoon". In order to discuss monsoon strength, a precise definition of the term monsoonal climate is required. The physical definition of

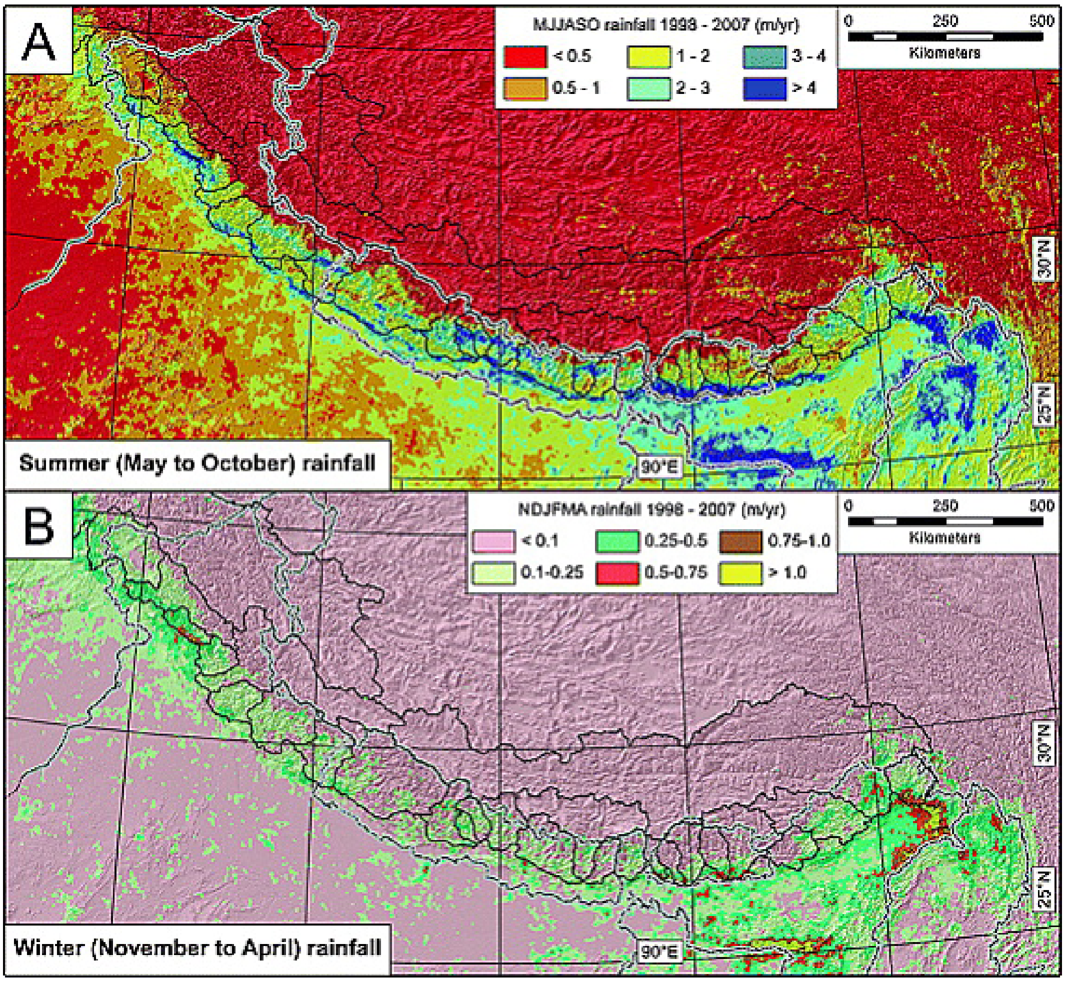

Figure 2: Modern day precipitation pattern in the Himalayan region (Bookhagen and Burbank, 2010). Summer precipitation in A and winter precipitation in B. Note the remarkable difference between the amount of summer and winter precipitation, and the changing precipitation pattern from west to east.

the Asian monsoon pertains to the wind patterns existing over Asia. Its impact on humidity, rainfall patterns, seasonality etc., and how these are recorded by different sedimentary proxies, remains to be discussed. To avoid confusion, paleoclimatic studies should use terms such as seasonality, aridity and their implications for the Asian monsoon, rather than interpreting proxies directly in terms of “strengthening” or “weakening” of the monsoon.

Notwithstanding these difficulties, understanding the spatial and temporal evolution of climate is crucial to constrain the links between climate and evolution of the Himalayan mountain belt. Most of the previous studies of proximal foreland-basin sediments have focused on the western and central part of the Himalaya (see Sanyal and Sinha (2010) for a synthesis); the eastern part of the orogen remains poorly studied with regard to climate. Reconstructing past weathering rates is possibly even more challenging, but crucial to understand the couplings between climate, tectonics and erosion.

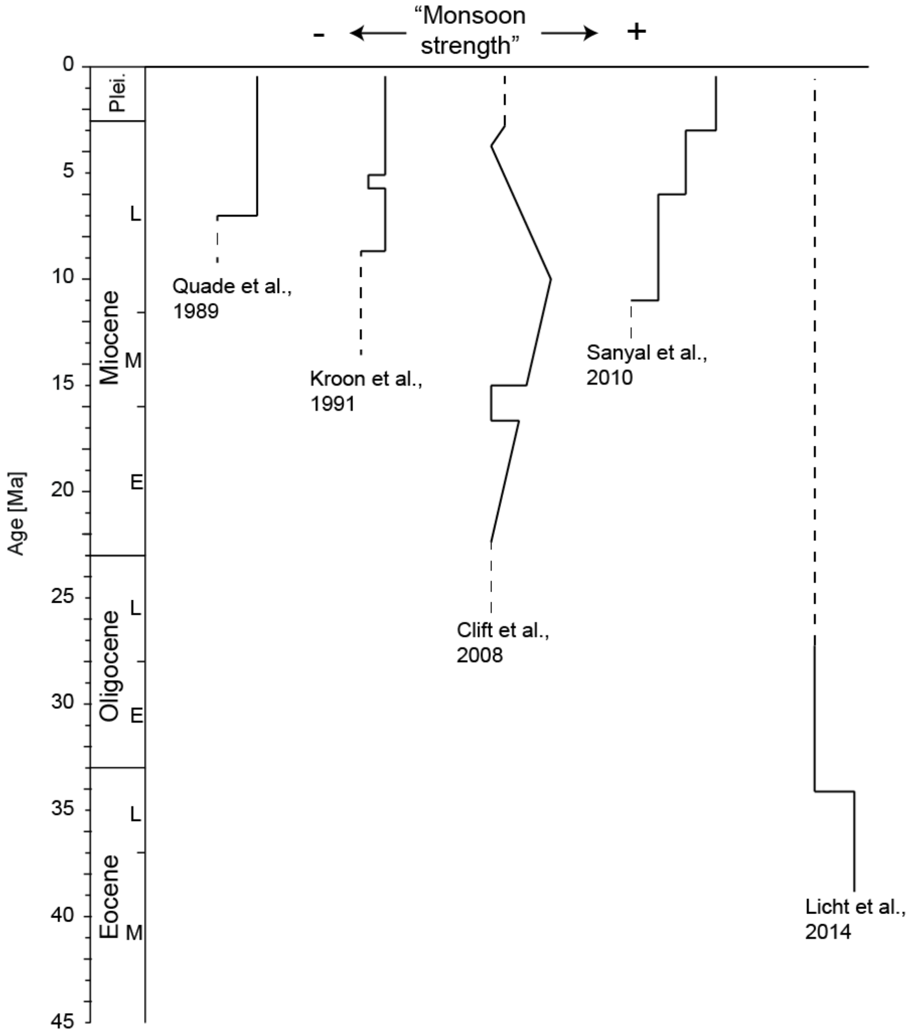

Figure 3: Discrepancy in periods of monsoon intensification/ strengthening/ onset, depending on proxies and interpretations.

With this study, I aim to provide further insight into the lateral and temporal evolution of climate in the Himalayan region, by looking at the proximal record of pre-Siwalik and Siwalik sediments in the Himalayan foreland basin. The sedimentary records studied in this thesis span over 20 Myr (compilation of the Joginder Nagar, Jawalamukhi and Haripur Kolar section) in the western Himalaya and 13 Myr (Kameng river section) in the eastern part of the orogen, respectively.

This thesis is divided into six chapters. The first chapter introduces the Himalayan geology and the context of the studied sedimentary sections. The second chapter is dedicated to large-scale differences in the evolution of vegetation, as recorded by stable carbon isotopes in organic matter and soil carbonate nodules, and its implications for variable climate evolution along strike in the Himalaya. In chapter three, I zoom in to the poorly studied eastern part of the Himalaya, where I constrain the weathering regime over the last 13 Ma from the Kameng Siwaliks. I use heavy minerals and petrography, together with previously published geochemical, geochronological and themrochronological proxies, to unravel changes in provenance and diagenesis that could possibly influence the weathering signal. Having constrained these, I use sediment geochemistry and clay mineralogy to gain further insight into the evolution of weathering in the eastern Himalaya. In the fourth chapter, I focus on lateral variations in the weathering regimes. Therefore, I sampled three previously dated pre-Siwalik and Siwalik sections in north-western India, providing a compiled but continuous age record over the last 20 Ma. I aim to understand changes in weathering and their implications for seasonality and climate. Chapter five presents preliminary results of a lithium-isotope study on Siwalik sediments, using a newly developed method by Bohlin et al. (prep). I discuss the implications of lithium isotopes for silicate and chemical weathering rates and their controls on the atmospheric CO_2 drawdown.

In the sixth and last chapter, I conclude my findings in a general context of the Himalayan orogen. The thesis terminates with some perspectives for further research and questions that have arisen during the three years of my PhD work. Chapters two and three have been submitted to the journals *Geology* and *Basin Research*, respectively. Chapter four is likewise written in paper style and will shortly be submitted.

Chapter 1

Geological setting

1.1 Evolution of the Himalayan orogen - India-Asia collision

The formation of the Himalayan mountain belt and the Tibetan Plateau results from the collision between the Indian and the Eurasian plates, which began in early Eocene (Garzanti et al., 1987; Najman et al., 2010; Hu et al., 2016) and caused major crustal shortening and thickening (Hodges, 2000; Yin and Harrison, 2000). The India-Asia collision is an ongoing process. The onset of the collision is debated, with ages ranging from ~70 Ma to 38 Ma (Aitchison et al., 2007; Hu et al., 2016); most of the studies suggest a collision age from 55 to 50 Ma (Garzanti et al., 1987; Najman et al., 2010). The northwards drift of the Indian plate resulted in the closure and subduction of the Tethys ocean, which initiated the formation of Early to Late Cretaceous fore-arc basins (An et al., 2014; Hu et al., 2016) and resulted in the formation of the Trans-Himalayan granitoid batholith belt (Searle et al., 1987). Continent collision subsequently caused crustal-scale thrusting in the Himalayan orogen (Figure 1.1). The Cenozoic thrust system separates major lithotectonic units in the Himalaya (Yin and Harrison, 2000). The Himalayas are bound by the Tibetan plateau in the north and the Indus-, Ganga- and Brahmaputra floodplains in the south. Two syntaxes terminate the Himalayan arc in the west (Nanga Parbat) and in the east (Namche Barwa), respectively.

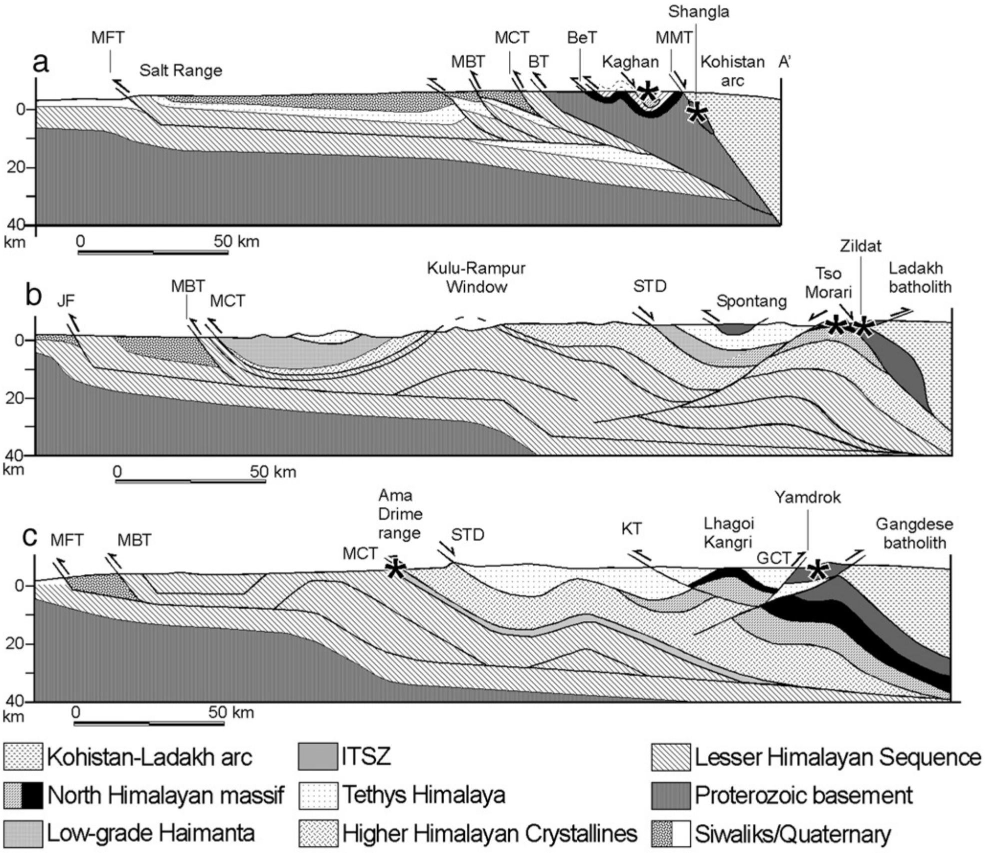

Figure 1.1: Cross-sections from through the Himalayas from Guillot et al. (2008); a) Pakistan Himalaya, b) Indian Himalaya, c) southern Tibet.

1.2 Major tectonic units

The Himalaya south of the Indus-Tsangpo suture zone is classically divided into four major lithotectonic units, the Tethyan Sedimentary Series (TSS), the High Himalayan Crystalline Series (HHCS), the Lesser Himalayan Series (LHS) and the Sub-Himalayas (SH). These lithotectonic units are bound by a late-Cenozoic north dipping fault system, which constists from north to south, the South Tibetan Detachment (STD), the Main Central Thrust (MCT), the Main Boundary Thrust (MBT) and the Main Frontal Thrust (MFT) (DeCelles et al., 2001; Le Fort, 1986; Yin and Harrison, 2000). The Himalayan units are bound by the Indus-Tsangpo suture zone (ITSZ) north of the South Tibetan Detachment system and the Himalayan foreland basin (Indus, Ganges, Brahmaputra) in the south (Figure 1.2)

The Indus-Tsangpo suture zone (ITSZ), which separates the Indian and Asian crusts, consists of sedimentary rocks, melange, ophiolites of the Neotethys ocean and the Cretaceous-Tertiary Gangdese Batholith. Two Cenozoic thrusts form the boundaries of the suture zone (Yin and Harrison, 2000).

The Tethyan Sedimentary Series (TSS) is a Paleozoic-Eocene sedimentary succession deposited on the northern passive margin of India (e.g. Gaetani and Garzanti, 1991). The TSS consists of sedimentary and low grade metasedimentary rocks: mainly phyllites, limestones and quartzose sandstones (DeCelles et al., 2001). They are interbedded with Paleozoic and Mesozoic volcanic rocks (Yin, 2006). The TSS are located between the ITSZ and the STD.

The Higher Himalayan Crystalline Series (HHCS) are bound by the STD in the north and the MCT in the south. They consist of high grade metamorphic rocks including paragneiss, schist, migmatite, marble and orthogneiss (DeCelles et al., 2001). Miocene leucogranites are widespread in the HHCS (e.g. Gansser, 1964).

The MCT and the MBT are the boundaries of the Lesser Himalayan unit in the north and the south, respectively, with an internal duplex structure (DeCelles et al., 1998a). Rocks of the LHS mainly consist of Proterozoic-Cambrian clastic sediments, metasedimentary and metavolcanic rocks and some augengneiss (Yin, 2006)). The LHS has been sub-divided into the Inner (iLH) and Outer (oLH) Lesser Himalaya, based on depositional age and different ϵNd isotopic signatures. The Lower-Proterozoic iLH has a more negative ϵNd, whereas the Middle-Upper Proterozoic oLH has ϵNd similar to the HHCS (Ahmad et al., 2000). Locally the LHS is crosscut by mafic and felsic intrusions (Guillot et al., 2008).

The rocks of the southernmost Sub-Himalayan unit are non-metamorphosed syntectonic clastic sediments of the pre-Siwalik and Siwalik Groups, which formed in the Himalayan foreland basin and are thrusted over the Indus-, Ganges- and Brahmaputra- alluvial plains along the MFT. They crop out in the foothills of the Himalaya and span the entire mountain front.

1.3 Foreland basin sediments - Pre-Siwaliks/ Siwaliks

The oldest pre-Siwalik sedimentary rocks in the Himalayan foreland basin are the late Oligocene/ early Miocene Dharamsala Group in north western India and the Dumri formation in Nepal (DeCelles et al., 1998a) They consist of continental fluvial, lacustrine or deltaic sediments (White et al., 2001). Their

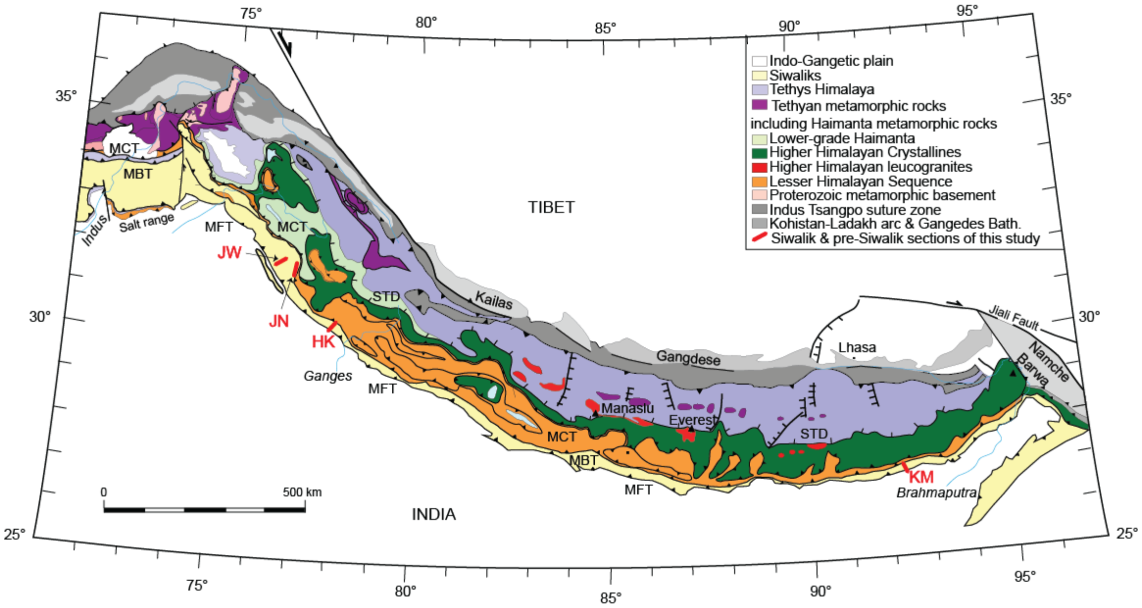

Figure 1.2: Geological map of the Himalaya modified after Guillot et al. (2008). Sampled Siwalik sections are indicated in red. JN: Joginder Nagar; JW: Jawalamukhi; HK: Haripur Kolar; KM: Kameng.

deposition is followed by the deposition of the Siwaliks, which form the foothills of the Himalaya and reach along the entire mountain front from Pakistan to the northeastern states of India. They represent the Miocene to Pliocene fill of the Himalayan foreland basin, with some longitudinal age variation along strike (Chirouze et al., 2012). An overall thickening of beds and coarsening upward is observed over the entire Siwalik Group and is interpreted to reflect a gradual transition from distal to proximal facies, as the Himalayan deformation propagated. They are divided into the Lower, Middle and Upper Siwaliks, with gradual boundaries. These informal subgroups locally correspond to formations with varying names. The Lower Siwaliks (LS) consist of an alteration between mudstone with some paleosols and fine- to medium-grained sandstone. The layers are a few meters thick. The LS is associated with a depositional environment of high-sinuosity streams and overbank deposits. The Middle Siwaliks (MS) are a stack of tens of meters thick medium- to coarse-grained sandstone beds often rich in mica deposited by a large braided river system. The Upper Siwaliks (US) contain beds of tens of meter thick conglomerates with interlayers of sand- and less frequently mudstone. They were deposited closer to the mountain front by a gravelly braided river system (Chirouze et al., 2013; Nakayama and Ulak, 1999). Paleosols within the pre-Siwalik and Siwalik sediments are associated with soil carbonate nodule. The abundance of soil carbonate nodules varies laterally, and such nodules have never been reported further east than Nepal. For this study three pre-Siwalik and Siwalik were sampled in north western India and one Siwalik section in north eastern India (Figure 1.2) and are described in following sub-chapters.

1.3.1 Joginder Nagar, Jawalamukhi and Haripur Kolar sections, Himachal Pradesh, NW India

The three sedimentary sections of Joginder Nagar (JN) (pre-Siwalik), Jawalamukhi (JW) and Haripur Kolar (HK) (both Siwalik) indicated on Figure 1.2 have been dated by magnetostratigraphy and span from 20-1 Ma (Meigs et al., 1995; Sangode et al., 1996; White et al., 2001). The Joginder Nagar section (Figure 1.3) is mostly pre-Siwalik and contains rocks of the Lower and Upper Dharamsala Formations. The uppermost unit is composed of Lower Siwalik rocks/sediments. Boundaries for the Lower/Upper Dharamsala are set at 16.5 Ma and at 12.5 Ma for the Upper Dharamsala/LS (White et al., 2001). The Dharamsala Formation consist of fine- to medium- grained sandstone, siltstones and mudstones, associated with development of paleosols, with abundant soil carbonate nodules (White et al., 2001).

In the Jawalamukhi section, LS, MS and US rocks are present (Figure 1.4), whereas the Haripur Kolar section contains only MS and US sediments (Thomas et al., 2002). The boundary between the LS and MS in the JW section is set at 10.9 Ma and between MS and US at 6.8 Ma, respectively (Meigs et al., 1995). The Jawalamukhi section contains a coarsening upward sequence with beds of mudstone, siltstone and sandstone at the base of the section and conglomerate becoming more abundant towards the top (Meigs et al., 1995; Najman et al., 2009). In the Jawalamukhi section the MS are characterized by the abundance of conglomerate, which is not abundant in other Siwalik sections. Paleosols are developed and carbonate nodules are present.

In the HK section (Figure 1.5) the boundary between the MS and US is set at 5.23 Ma (Sangode et al., 1996). Sediments of the HK section are characterized by alternating mudstone and sandstone. Mudstones are associated with well-developed paleosols with presence, of carbonate nodules Thomas et al. (2002). Figure 1.6 shows characteristic sedimentary features of the sections.

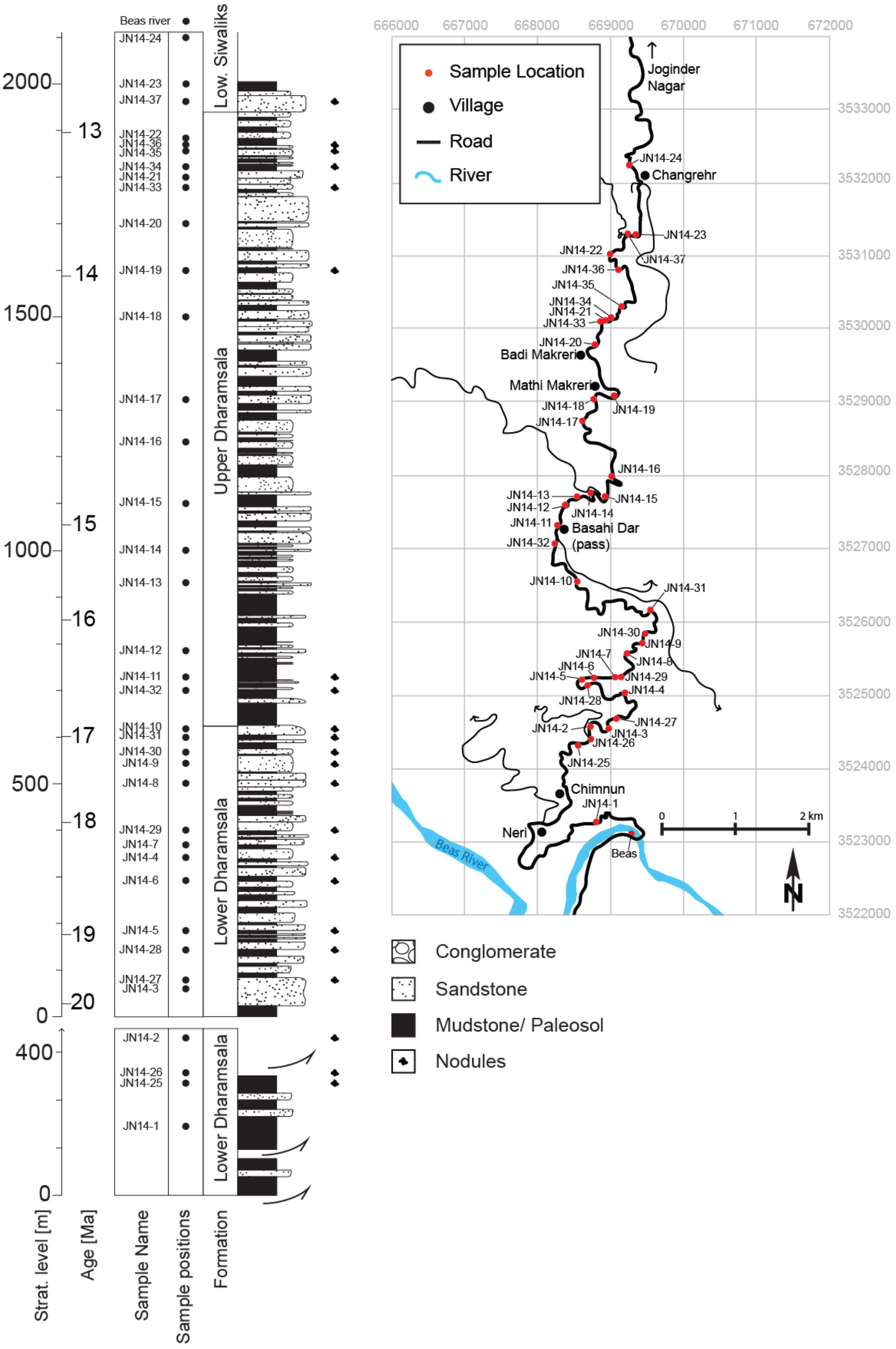

Figure 1.3: Stratigraphy and location map (UTM Zone 43N) of the Joginder Nagar section; stratigraphy from White et al. (2001)

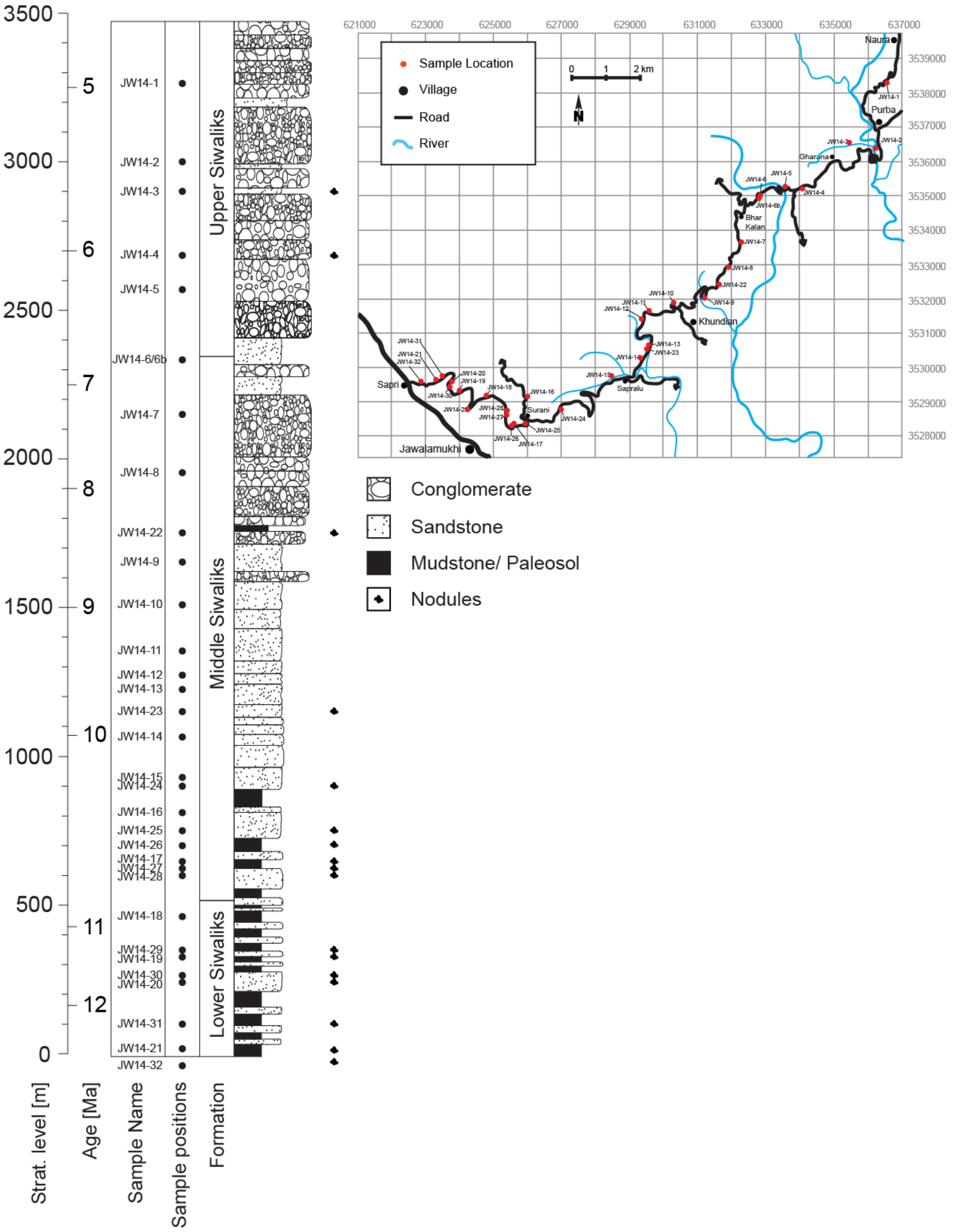

Figure 1.4: Jawalamukhi section location map (UTM Zone 43N) and stratigraphy ; stratigraphy after Meigs et al. (1995).

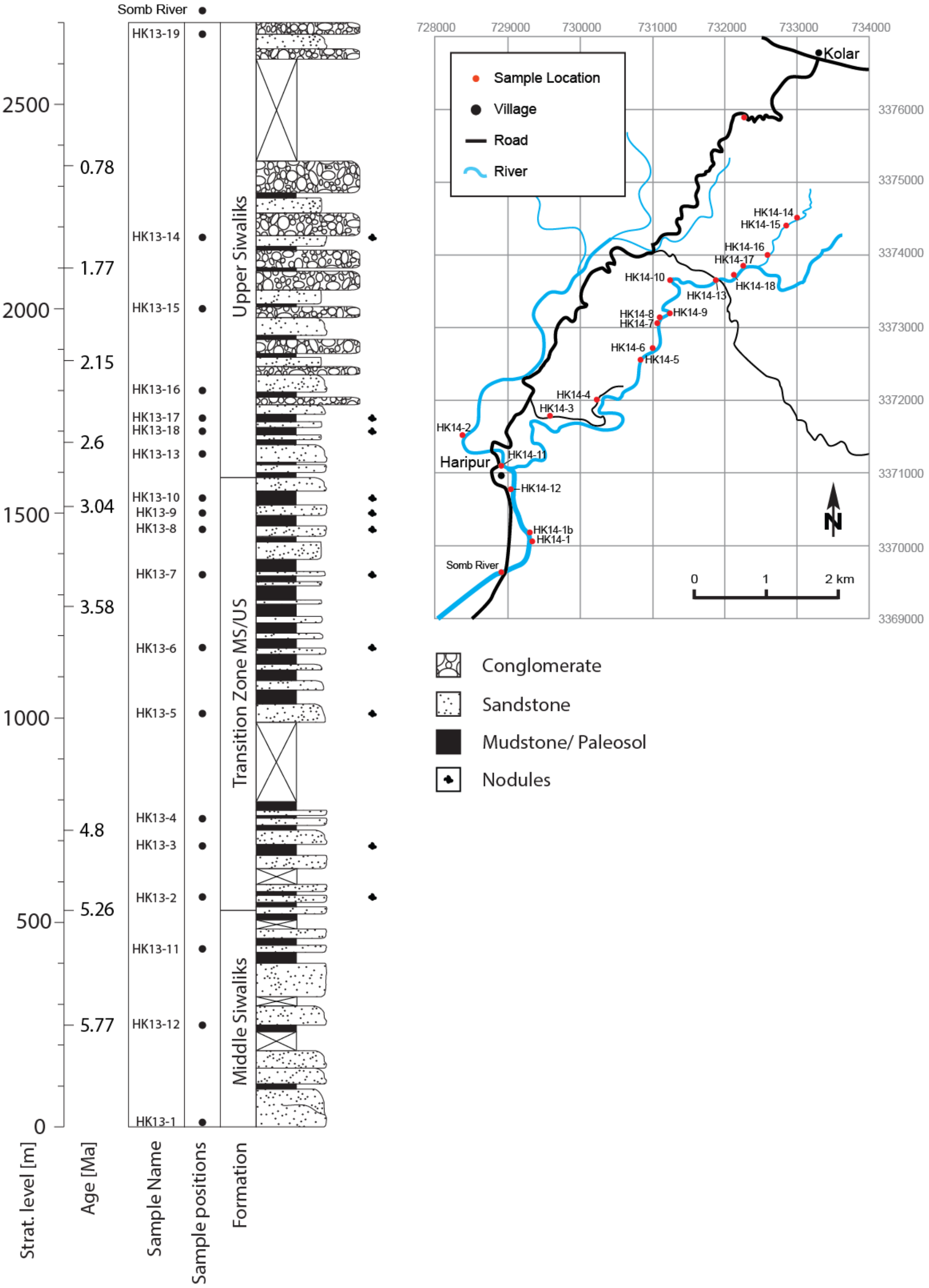

Figure 1.5: Haripur Kolar section location map (UTM Zone 43N); magnetostratigraphy after Sangode et al. (1996); the stratigraphy was described by Thomas et al. (2002).

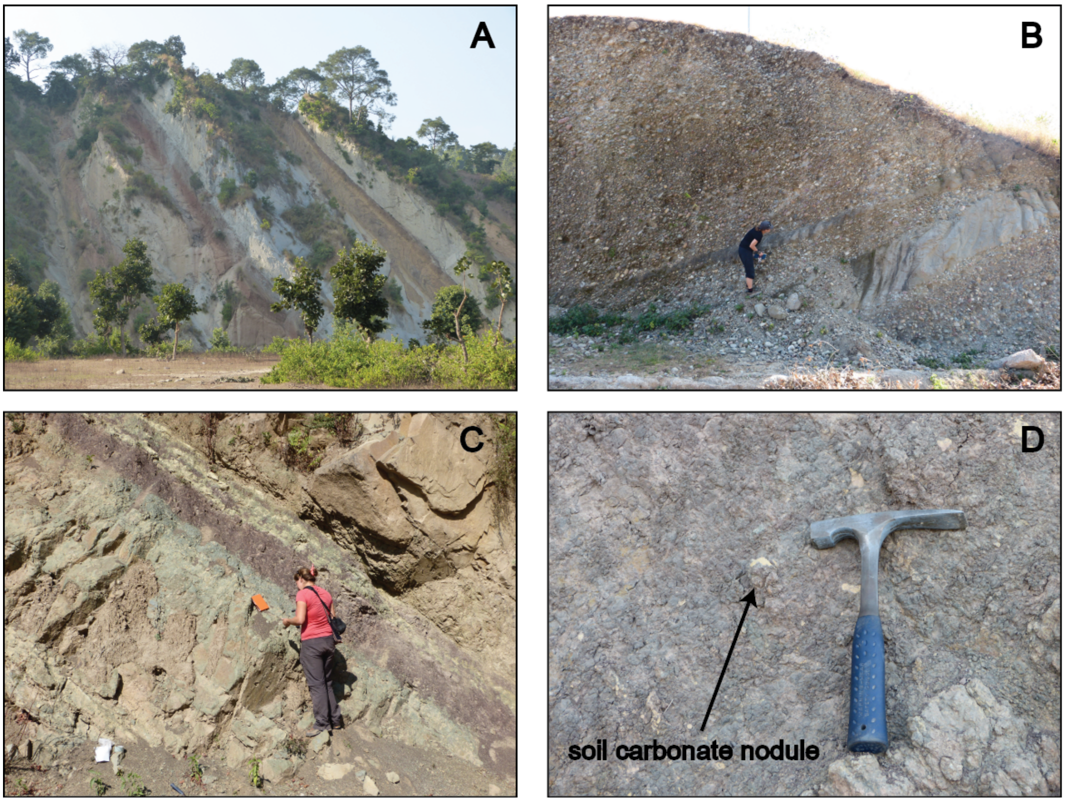

Figure 1.6: Paleosols of the Haripur Kolar section near HK14-2; B: Upper Siwalik conglomerates of the Jawalamukhi section near JW14-7; C: Paleosol of the Joginder Nagar section near JN14-28; D: Soil carbonate nodule in a paleosol of the Joginder Nagar section near JN14-10.

1.3.2 Kameng section, Arunachal Pradesh, NE India

The Kameng River Section is located near the town of Bhalukpong, Arunachal Pradesh in North Eastern India (Fig 5.1). The modern Kameng River drains the HHCS and the LHS before it flows through the Siwaliks and finally enters the floodplain where it flows into the Brahmaputra River. In Arunachal, the Siwaliks are divided into the Dafla, Subansiri and Kimin Formations (Karunakaran and Rao, 1976; Kumar, 1997) which have been correlated with the LS, MS and US, respectively (Yin, 2006). The Kameng River Section has been magnetostratigraphically dated by Chirouze et al, (2012) and spans from 13 to 1 Ma. The exposed LS range from ca. 13 Ma to 10.5 Ma. The MS/US boundary was set at 2.6 Ma (Chirouze et al., 2012). The Kameng River Section is approximately 6 km thick and bound by the MBT in the north, and the MFT in the south, placing Siwalik rocks onto Quaternary sediments of the Brahmaputra plain (Burgess et al., 2012). Within the Kameng section the Tippi Thrust places the LS over the US, therefore the younger part with MS and US is found in the footwall of the Tippi thrust to the south, whereas the older part of the section is in the hanging wall to the north (Chirouze et al., 2013) (Figure 1.7). The LS contain layers of mudstones alternating with sandstones. The MS are characterized by tens of meters thick layers of medium- to coarse-grained “salt and pepper” sandstones. The US consist of sandstone with more frequent layers of conglomerate. Mudstones become less abundant. Generally, paleosols are poorly developed and soil carbonate nodules are lacking in the Kameng section. Figure 1.8 shows characteristic sedimentary features of the Kameng section.

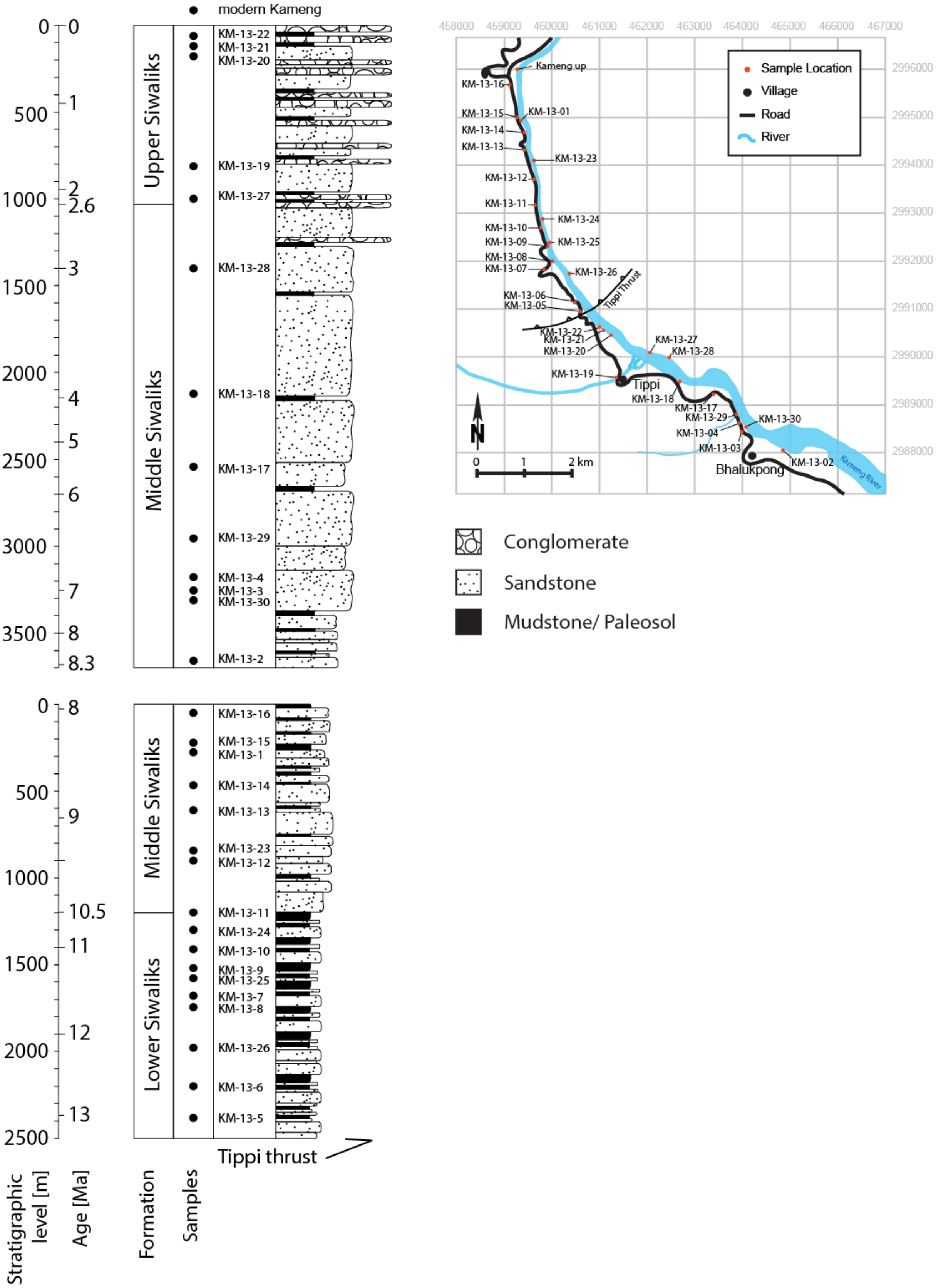

Figure 1.7: Kameng river section: Stratigraphy after Chirouze et al. (2012), map (UTM Zone 46N) with sample locations in red.

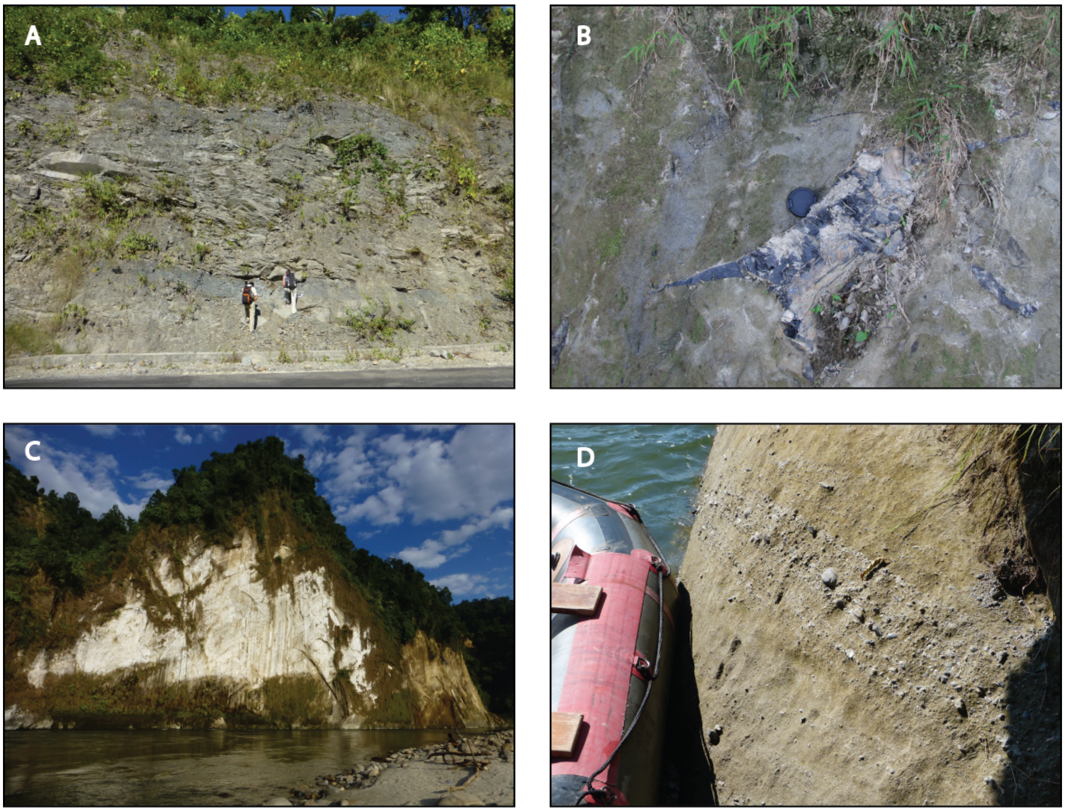

Figure 1.8: Kameng river section. A: Mudstone of the Lower Siwalik near KM13-7; B: Fossil tree trunk in the Middle Siwalik sandstone near KM13-2; C: Thick sandstone layer of the Middle Siwalik near KM13-18; D: Conglomerate layer in the Upper Siwalik near KM13-27.

Chapter 2

Lateral climatic variation in the Himalaya since the Miocene: a West – East comparison

N. Vögeli, Y. Najman, P.van der Beek, P. Huyghe, P. Wynn, G. Govin

Submitted to EPSL, November 2016

Abstract

The Himalaya has a major influence on global and regional climate (Boos and Kuang, 2010; Molnar et al., 2010), it has been suggested that the monsoonal climate in turn plays a major role in the erosion and relief pattern of the belt (Bookhagen and Burbank, 2006; Wobus et al., 2003). The foreland basin of the Himalaya contains a record of tectonics and paleoclimate since Miocene times, within the detrital pre-Siwalik and Siwalik Groups. Previous work has mainly focused on the central and eastern Himalaya, where a shift in climate has been observed at ~7 Ma (e.g. Quade et al., 1989). The eastern part of the orogen is poorly studied. In order to track vegetation as a marker of monsoon intensity and seasonality, we analyzed δ^{13}C on soil carbonate and associated δ^{13}C on bulk organic carbon from previously dated pre-Siwalik and Siwalik Group sedimentary sections in the West (Joginder Nagar, Jawalamukhi, Haripur Kolar) and, for the first time, in the East (Kameng) of the Himalayan foreland basin. Sedimentary records span from 20-1 Ma in the West and 13-1 Ma in the East, respectively. The presence of soil carbonate in the West, but its absence in the East is a first indication of lateral climatic variation. δ^{13}C in soil carbonate shows a shift from around -10 ‰ to -2 ‰ at ~7 Ma in the West. This is confirmed by δ^{13}C analyses on bulk organic carbon, which show a shift from around -23 ‰ to -19 ‰ at the same time. Such a shift in isotopic value is likely to be associated with a change in vegetation type from C3 to C4. By contrast δ^{13}C in bulk organic carbon remains at around -23 ‰ in the East. We suggest that the lateral variations on stable carbon isotopes are linked to differences in climate along strike of the orogen since ~7 Ma.

2.1 Introduction

The Himalaya has a major influence on global and regional climate (Boos and Kuang, 2010; Molnar et al., 2010). Whilst the major force driving the evolution of the mountain belt is the India-Asia convergence, it has been suggested that the Asian monsoon climate in turn plays a major role in its erosion and relief pattern (Bookhagen and Burbank, 2006; Clift et al., 2008).

The modern climate shows significant east-west variation in the Himalaya, with mean-annual precipitation on the plains and foothills being higher and the intra-annual variability or "seasonality" lower in the east (Wobus et al., 2003; Bookhagen and Burbank, 2010). The Indian Summer Monsoon and the Westerlies are two important atmospheric circulations influencing the Himalayan region (Kotlia et al., 2015). The Indian Summer Monsoon takes up moisture in the Bay of Bengal and transports it towards the Himalaya during the northern hemisphere summer months, whereas the Westerlies bring moisture from the Mediterranean, Black and Caspian Sea and are most efficient in winter (Benn and Owen, 1998). Understanding the onset as well as the spatial and temporal variability of the monsoon climate is crucial to constrain the links between climate and the evolution of the Himalayan mountain belt.

The record of spatial and temporal variations in vegetation holds information on climate evolution, in particular the origin and transport of humidity and atmospheric circulations. The foreland basin of the Himalaya contains a sedimentary record of tectonics and paleoclimate since Miocene times, within the molassic pre-Siwalik and Siwalik Groups. Carbon and oxygen isotopic compositions of soil carbonates and soil organic matter from Siwalik sediments in Nepal, Northwest India, and Pakistan have been used to reconstruct changes in vegetation and climate during the Neogene (Quade et al., 1989, 1995; Quade and Cerling, 1995; Sanyal et al., 2010, amongst others). These records consistently show a shift in δ^{13}C values at ~7 Ma, which has been interpreted as recording a change in vegetation, from C3 to C4 plants characterized by distinct isotopic signals: pure C3 vegetation has $\delta^{13}C_{org}$ values between -22 ‰ and -30 ‰, whereas C4 plants range between -14 ‰ and -10 ‰ (Cerling et al., 1997). In modern soils, carbonate precipitates in equilibrium with soil CO_2 (Cerling et al., 1989); the fractionation between organic matter and soil carbonate is 14-17 ‰, depending on temperature (Cerling, 1984). As C3 plants are favored in a cool and humid climate, whilst C4 plants prefer intense light, warm and water-stressed conditions (Ehleringer, 1988), this vegetation shift also indicates a climate change. A similar shift has been recorded in the distal sediments of the Bay of Bengal (France-Lanord and Derry, 1994), and it has been argued that the expansion of C4 plants is a global phenomenon due to a decrease in atmospheric pCO_2 (Cerling et al., 1997), others argue that the pCO_2 was already at a level, favorable for C4 plants, during Oligocene (Pagani et al., 2005; Beerling and Royer, 2011).

However, the focus of previous studies on climate and vegetation records has been entirely on the western and central Himalaya; no such data are available from east of Nepal. In order to obtain better insight into the evolution of the monsoon climate, precipitation patterns and the expansion of C4 plants along strike in the Himalaya, we present and compare new δ^{13}C and δ^{18}O data of pedogenic carbonate and organic matter from the northwestern and the poorly studied eastern Himalayan foreland basin.

2.2 Geological Setting and methods

Neogene Himalayan foreland basin sediments are composed of the fluvial Dharamsala Group (pre-Siwalik) in the Late Oligocene and early Miocene (White et al., 2001) and the Siwalik Group since the early Miocene. The sediments of the Siwalik Group are exposed near-continuously along the front of the Himalayan range, with only minor age variation along strike (Chirouze et al., 2012). They were deposited in the foreland before being incorporated in the foothills due to southward propagation of the deformation and onset of motion on the Main Frontal Thrust. The Siwalik Group generally shows overall coarsening and thickening upward, interpreted as recording increasingly proximal deposition (DeCelles et al., 1998b), and is divided into the Lower, Middle and Upper Siwaliks (LS, MS, US). Paleosols are developed throughout most of the Siwalik sections, with lateral and temporal variations in abundance (being more abundant in the LS and in the west). These are characterized in western and central Himalayan sections by the presence of soil-carbonate nodules, which show a carbon and oxygen isotopic shift at ~7 Ma (Quade et al., 1989, 1995; Sanyal et al., 2010).

We sampled three pre-Siwalik and Siwalik sedimentary sections in the western Himalaya (Joginder Nagar, Jawalamukhi and Haripur Kolar sections in Himachal Pradesh) and one Siwalik section in the eastern Himalaya (Kameng River section in Arunachal Pradesh) (Figure 2.1). All sections have previously been dated by magnetostratigraphy (Meigs et al., 1995; Sangode et al., 1996; White et al.,

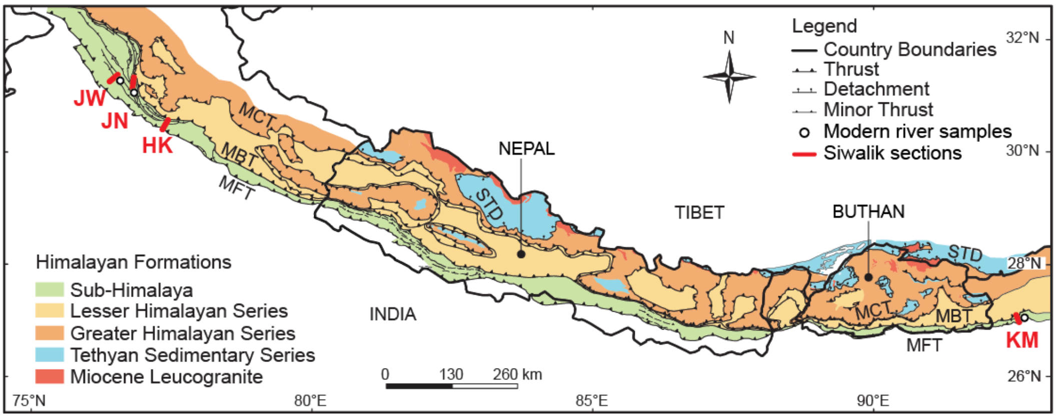

Figure 2.1: Geological map of the Himalaya (after Hirschmiller et al. (2014), with major faults: MFT: Main Frontal Thrust, MBT: Main Boundary Thrust, MCT: Main Central Thrust, STD: South Tibetan Detachment. Sampled sedimentary sections are indicated in red: JW: Jawalamukhi; JN: Joginder Nagar; HK: Haripur Kolar; and KM: Kameng.

2001; Chirouze et al., 2012). They span a time range of 20-1 Ma in the west and 13-1 Ma in the east. In the western sections, we collected paleosols and associated carbonate nodules, as well as fine-grained mudstone in zones without well-developed paleosols. Carbonate nodules are lacking in the Kameng section; therefore only mudstones, where possible from paleosols, were sampled. Additionally, modern river mud was sampled in both the west and the east in proximity of the sections. Modern river samples in the west (Beas River and Jner Khad River) were taken at an elevation of $\sim$640 m, whereas the modern Kameng River sample in the east was collected at 100 m elevation.

^{13}C/^{12}C and ^{18}O/^{16}O ratios of soil carbonate nodules were determined using a multiflow analyser linked to an Isoprime 100 continuous flow mass spectrometer at the University of Lancaster, UK. Approximately 600-700 μg of sample powder was drilled from each carbonate nodule and digested online at 90°C with dehydrated phosphoric acid in a He-flushed exetainer. Product CO_2 was analyzed for $\delta^{13}C_{CO_2}$ and $\delta^{18}O_{CO_2}$ and corrected against VPDB and VSMOW respectively using within run analyses of international standard NBS18, LSVEC and CO-1. Within-run standard replication (1S.D) was <0.1 ‰ for both C and O isotope ratios. Sample replication based on separate drill aliquots of powder from the same carbonate nodule was <0.1‰ for δ^{13}C and <0.2 ‰ for δ^{18}O (1SD).

^{13}C/^{12}C ratios of bulk organic matter were determined using an Elementar Vario Micro elemental analyser linked to a VisION continuous flow mass spectrometer at the University of Lancaster. The carbonate content of each sample was removed by acid digestion using 1M ultrapure HCl and the resultant sample washed repeatedly using de-ionised water and centrifugation. Approximately 10 mg of each prepared sediment sample was combusted within tin capsules at 960 °C to yield CO2 for determination of $\delta^{13}C_{org}$. δ^{13}C values were corrected against VPDB using internal reference materials calibrated to international standards. Within-run δ^{13}C replication (1S.D) was <0.2 ‰ for standards and <0.25 ‰ for samples.

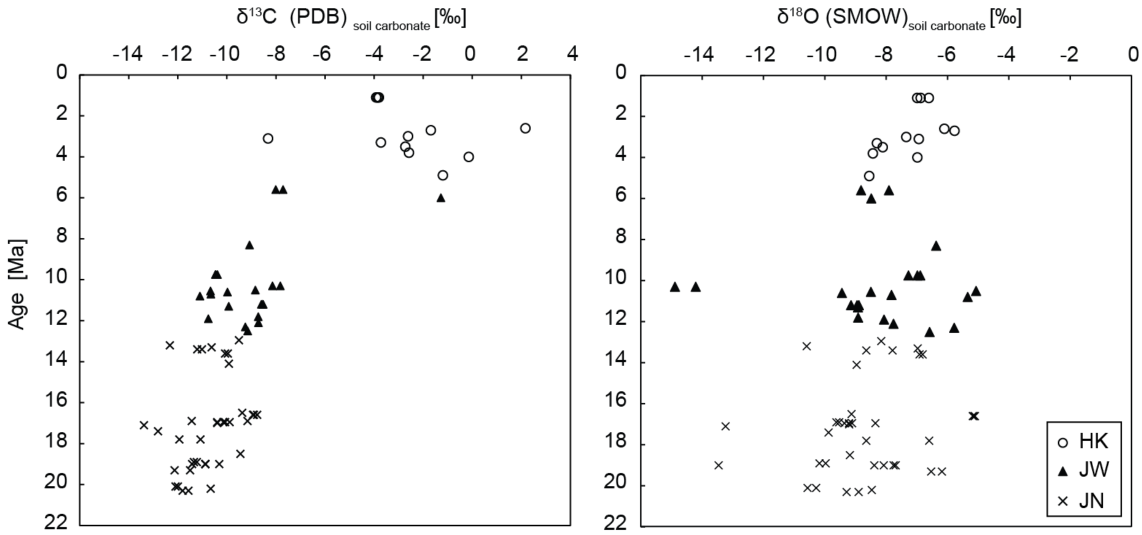

Figure 2.2: $\delta^{13}C_{soilcarb.}$ and $\delta^{18}O$ values of soil carbonate in the western Himalaya. Different colors indicate the different sections (HK: Haripur Kolar; JW: Jawalamukhi; JN: Joginder Nagar).

2.3 Results

The three sections in Himachal Pradesh (Western Himalaya) provide a continuous record over the past 20 Ma (Figure 2.2). Prior to ~7 Ma, $\delta^{13}C$ values of soil carbonate ($\delta^{13}C_{soilcarb.}$) range between -8 ‰ and -13 ‰, whereas at ~7 Ma a shift towards more positive $\delta^{13}C$ values ranging from +2 ‰ to -8 ‰, is observed (Figure 2.2). $\delta^{18}O$ values range mostly from -11 ‰ to -4 ‰, except in the older part of the sections, where some values are as low as -14 ‰. Only a slight trend towards more positive $\delta^{18}O$ values over time is observed.

We also measured a continuous record of $\delta^{13}C$ of organic carbon ($\delta^{13}C_{org}$) in both the western and eastern sections (Figure 2.3). In the west, a clear shift towards more positive $\delta^{13}C_{org}$ values is observed at ~7 Ma, synchronous with the $\delta^{13}C_{soilcarb.}$ Before 7 Ma, $\delta^{13}C_{org}$ values range between -23 ‰ and -27 ‰, while values are more positive, from -18 ‰ to -23 ‰, after 7 Ma. In the east, in contrast, $\delta^{13}C_{org}$ values remain constant between -29 ‰ and -23 ‰ since the middle Miocene and no shift towards more positive values is observed. Organic matter from modern river sediments show $\delta^{13}C$ values of approximately -26 ‰ and -23.5 ‰ in the west and in the east, respectively (Figure 2.3).

2.4 Discussion and conclusions

C4 plants dominate in the modern Ganga floodplain, whereas C3 plants are dominant in the Brahmaputra floodplain (Galy et al., 2008b). Measured $\delta^{13}C_{org}$ values of modern river muds in both the west (Beas and Jner Khad River) and the east (Kameng River) are in the range of C3 plants, although we would expect the vegetation in the west to be dominated by C4 plants. However, these modern river sediments

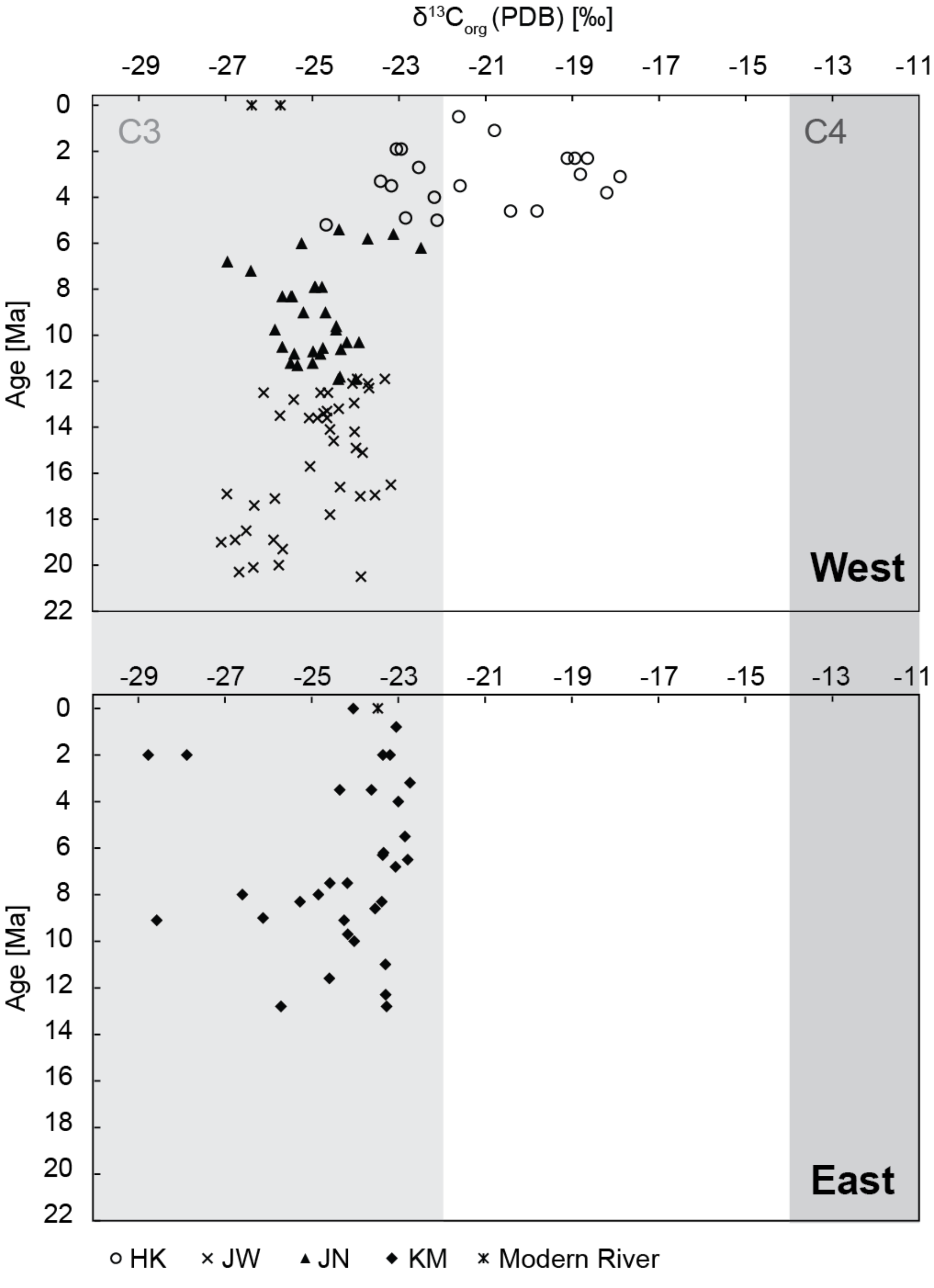

Figure 2.3: $\delta^{13}C_{org}$ of bulk organic carbon in the western (HK: Haripur Kolar; JW: Jawalamukhi; JN Joginder Nagar) and the eastern (KM: Kameng) Himalayan sections. Light and dark grey bars indicate $\delta^{13}C_{org}$ values characteristic of C3 and C4 plants, respectively (Cerling et al., 1997).

in the west were not collected in the floodplain but at the mountain front, where they contain detrital organic carbon of C3 plants transported from higher elevations (Dobremez, 1978) and/or fossil organic carbon from Himalayan formations (Galy et al., 2008b). Pre-Siwalik and Siwalik sediments were deposited further into the floodplain, and hence should carry a signal of floodplain vegetation.

Earlier studies (Quade and Cerling, 1995; Quade et al., 1995; Singh et al., 2007; Sanyal et al., 2010) have measured δ^{13}C on soil carbonate nodules, which can only be found in the western and central Himalayan Siwalik sections, and have consistently found a change towards more positive values at ~7 Ma. This change was interpreted in terms of a shift in vegetation initially dominated by C3 plants, to a vegetation containing C4 species. In order to compare the western and the eastern Himalaya, we rely on $\delta^{13}C_{org}$ of bulk organic matter, as soil carbonate nodules are absent in the east. In both the western and the eastern sections, $\delta^{13}C_{org}$ values range between -23 ‰ and -29 ‰ before 7 Ma, indicating a vegetation dominated by C3 plants. After 7 Ma, $\delta^{13}C_{org}$ in the western sections demonstrates an isotopic shift to values enriched in ^{13}C, suggesting a component of the organic matter comprises C4 species. Carbonate nodules from western Himalayan sections analyzed as a part of this study show a similar trend, demonstrating a shift from C3 dominated vegetation composition, to an increasing proportion of C4 species in the younger sections. The $\delta^{13}C_{org}$ of bulk organic matter does not show a pure C4 signal (-14 ‰ to -10 ‰) after 7 Ma in the west, but rather a mixture of C3 and C4 vegetation with values around -19 ‰. In the east, $\delta^{13}C_{org}$ values stay in the range of C3 plants throughout the sedimentary succession (Figure 2.3).

Although $\delta^{13}C_{org}$ should represent the values of the vegetation in the floodplain at the time of sediment deposition, it is likely to be biased by several influences/factors: organic carbon brought in from high elevations (Dobremez, 1978), mixed C3/C4 vegetation in the floodplain and/or influence of more negative fossil organic carbon. The amount of fossil organic carbon present in floodplain sediments can be estimated by the amount of total organic carbon content (TOC) in the sediments (Galy et al., 2008b,a). There is a linear correlation between TOC and modern OC in the Himalayan river systems. Galy et al. (2008a) estimated fossil organic carbon transported in the Ganga and Brahmaputra between 0.02 and 0.03 %, at a TOC value of 0.1 %, the amount of fossil carbon would be 20-30 % of the organic matter. Sediments of the sampled sections mostly have TOC values above 0.1 % (Appendix 2.4), and therefore contain mostly floodplain organic carbon. Incorporation of fossil organic carbon of Himalayan source rocks, with an average $\delta^{13}C_{org}$ fossil of -25.5 ‰ (Galy et al., 2008b), would render the $\delta^{13}C_{org}$ signal more negative, and diminish the shift towards more positive values. However, the influence of fossil carbon is too small to completely obscure the signal from floodplain vegetation, therefore we can assume that even with input of more negative fossil organic carbon, any change in the east towards a more positive signal would still be visible. Influences of fossil carbon can be considered as equal in the west and the east, but lateral variation still exist. Additionally, the efficiency of oxidation and renewal of organic carbon can influence the $\delta^{13}C_{org}$ signal (Galy et al., 2008b, 2011). Organic carbon renewal varies between the Ganges and Brahmaputra foreland basin, being more efficient in the Ganges floodplain, due to different floodplain settings (Galy et al., 2008b). Carbon renewal takes place during the transit in the floodplain (Galy et al., 2008b), by looking at paleosols and floodplain sediments, organic matter reflects that of the vegetation of the floodplain, Differences in floodplain dynamics durnig the transport are therefore unlikely to cancel out the C4 signal in the eastern Himalaya.

$\delta^{18}O_{soilcarb.}$ values of the three western sections show a slight change towards more positive values, comparable to $\delta^{18}O$ values of the Surai Khola section in Nepal (Quade et al., 1995). Only $\delta^{18}O_{soilcarb.}$ values of soil carbonates in Pakistan show a clear shift towards more positive values at ~8-6 Ma (Quade et al., 1995). A change in $\delta^{18}O_{soilcarb.}$, which forms in situ from soil water, can be associated with a change in soil temperature or precipitation. The difference in longitude and therefore a slight difference in paleo-temperature and/or paleo-precipitation pattern, within the three western sections, could have a slight influence on the $\delta^{18}O$ and therefore bias the change in $\delta^{18}O$ over time. As all sediments were deposited in the foreland, the influences of altitudinal effects (Dansgaard, 1961) can be excluded. More positive values over time therefore likely indicate a trend towards a warmer, more arid climate conducive to the growth of C4 vegetation, consistent with the work of Dettman et al. (2001).

C3 and C4 plants grow in different environments and can therefore be used as an indirect climate indicators. Our data, show that a change in vegetation occurred at ~7 Ma in the western Himalaya, but not in the east, where C3 plants have been dominant since the middle Miocene. Differences in floodplain setting, while influencing the signal, cannot explain the observed lateral difference (Galy et al., 2008b, 2011) and neither can input of fossil organic carbon. There must, therefore, be remarkable lateral variations in the evolution of the climate in the Himalayan region. The change at 7 Ma in the west and central Himalayas has been interpreted as resulting from a “stronger monsoon”, reflected by greater seasonality (Quade et al., 1989, 1995; Quade and Cerling, 1995). However, increased seasonality does not necessarily reflect more monsoon precipitation; it could also indicate less winter precipitation and thus a more arid (annual-average) climate (Molnar, 2005). C3 plants in the east indicate lower seasonality and higher annually averaged precipitation, consistent with modern precipitation patterns (Bookhagen and Burbank, 2010). The expansion of C4 plants in the west could therefore be a consequence of decreased winter precipitation, hence more seasonality associated with less (annually averaged) humidity, leading to a more arid climate. Overall, this difference in the $\delta^{13}C$ composition post 7 Ma is proposed to reflect water availability, with a lower water availability in the west initiating a decline in C3 plants and a rise in C4 vegetation (cf. Freeman and Colarusso, 2001). Dettman et al. (2001) likewise suggest a change in Indian summer monsoon characteristics at 7.5 Ma and drying of the climate.

This scenario is supported by a change in $\delta^{18}O_{soilcarb.}$ towards more positive values. Higher humidity in the east could be explained simply by the proximity to the Bay of Bengal, which is the major moisture source (Bookhagen et al., 2005). The western Himalayas are influenced by the Westerlies (Kotlia et al., 2015), which bring winter precipitation. A decrease in the intensity of the Westerlies at 7 Ma would lead to more seasonality in the western floodplain, with drier periods in winter. Another explanation for a generally more arid climate in the western Himalayas would be a decrease of moisture transport from the Bay of Bengal and the Arabian Sea, possibly linked to a decrease in the intensity of the Indian Summer Monsoon . The spatially variable record of $\delta^{13}C_{org}$ values that we record strongly suggests that the change in vegetation at 7 Ma did not occur everywhere along the Himalayan foreland

and supports the findings of Pagani et al. (2005) and Beerling and Royer (2011), who suggest a pCO_2 level favoring C4 plants was already reached during the Oligocene. Other, regionally dependent factors, such as differences in seasonality or humidity, have clearly played a role in determining Himalayan vegetation patterns through time.

Appendices

Appendix 1

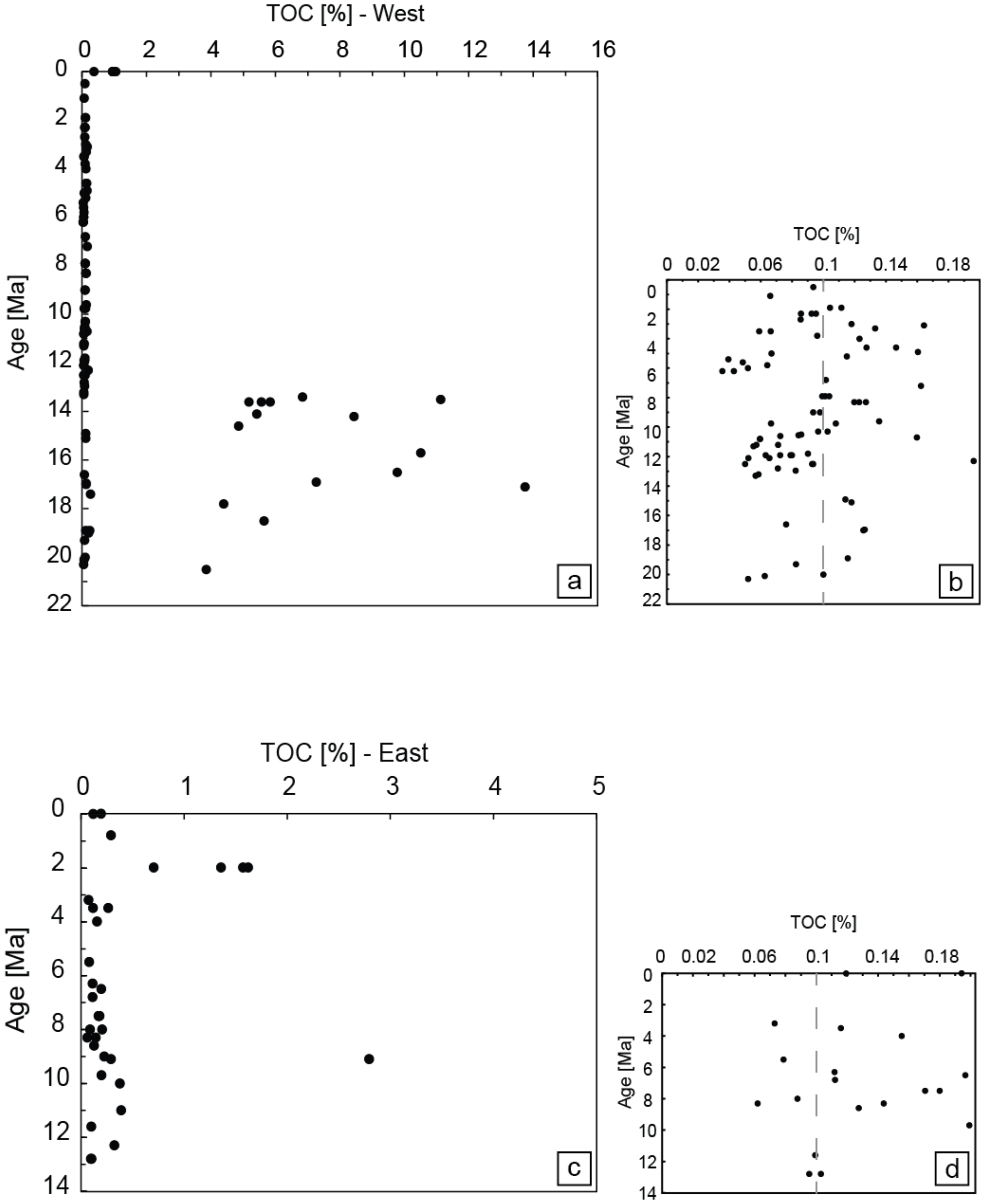

Figure 2.4: Total organic carbon content (TOC) vs age [Ma], a and c show the whole range of TOC, whereas b and c zoom in to see values below 0.2 %. TOC values above 0.07% indicate more biogenicC$_{org}$, from soil organic matter and floodplain vegetation, rather than detrital and fossil C$_{org}$ (Galy et al., 2008b).

Appendix 2

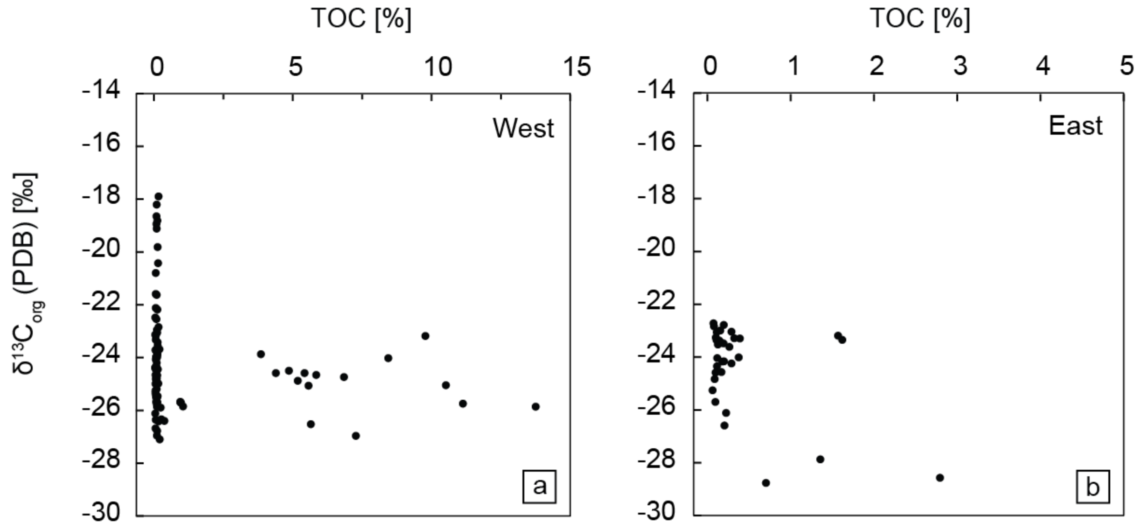

Figure 2.5: Total organic carbon (TOC) vs. $\delta^{13}C_{org}$ in the western (a) and eastern (b) sections, respectively. No clear correlation is observed.

Appendix 3

Table 2.1: Results carbon and oxygen stable isotopes

Sample	Section	Latitude	Longitude	Age [Ma]	Stratigraphic unit	$\delta^{13}C_{org}$ (VPDB) [‰]	TOC [%]	$\delta^{13}C_{carb.}$ (VPDB) [‰]	$\delta^{18}O_{carb.}$ [‰]
KM-13-1	KM	27.07635	92.59032	8.6	MS	-23.53	0.128		
KM-13-4	KM	27.01831	92.63689	6.8	MS	-23.06	0.112		
KM-13-6-f	KM	27.04193	92.6016	12.8	LS	-23.27	0.103		
KM-13-7-f	KM	27.04796	92.595	11.6	LS	-24.59	0.0993		
KM-13-10-f	KM	27.05601	92.59451	11	LS	-23.3	0.39		
KM-13-12-f	KM	27.06508	92.59296	10	MS	-24.02	0.377		
KM-13-13-f	KM	27.07064	92.59106	9	MS	-26.12	0.225		
KM-13-15-f	KM	27.07664	92.58941	8.3	MS	-23.39	0.144		
KM-13-16-f	KM	27.08288	92.58792	8	MS	-26.6	0.205		
KM-13-17	KM	27.02503	92.631	5.5	MS	-22.85	0.0788		
KM-13-18	KM	27.02714	92.62373	4	MS	-23	0.155		
KM-13-19-f	KM	27.02773	92.61025	2	MS	-27.88	1.36		
KM-13-20-c	KM	27.03583	92.60939	0.8	US	-23.05	0.29		
KM-13-23-f	KM	27.06862	92.59293	9.7	MS	-24.17	0.199		
KM-13-26-f	KM	27.0473	92.60042	12.3	LS	-23.29	0.323		
KM-13-28-f	KM	27.03198	92.62179	3.2	MS	-22.73	0.073		
KM-13-29	KM	27.02077	92.6359	6.3	MS	-23.36	0.112		
KM-13-30-f	KM	27.01873	92.63692	7.5	MS	-24.18	0.18		
AR 121	KM	27.0278	92.6102	2	US	-23.36	1.62		
AR 122	KM	27.0278	92.6102	2	US	-28.77	0.706		
AR 123	KM	27.0278	92.6102	2	US	-23.2	1.57		
AR 124	KM	27.02768	92.62208	3.5	MS	-24.35	0.116		
AR 125	KM	27.02167	92.63362	3.5	MS	-23.62	0.265		
AR 19	KM	27.0229	92.63482	6.2	MS	-23.34	0.0998		
AR 127	KM	27.01947	92.633	6.5	MS	-22.79	0.197		
AR 128	KM	27.01192	92.64003	7.5	MS	-24.58	0.171		
AR 129	KM	27.01222	92.64325	8	MS	-24.84	0.0878		
AR 20	KM	27.00472	92.64173	8	MS	-24.42	0.0951		
AR 115	KM	27.07633	92.58787	8.3	MS	-25.27	0.062		
AR 114	KM	27.07633	92.58787	8.3	MS	-23.94	0.155		
AR 117	KM	27.07192	92.5887	9.1	MS	-28.58	2.79		
AR 118	KM	27.07192	92.5887	9.1	MS	-24.25	0.291		
AR 119	KM	27.04138	92.60068	12.8	LS	-25.71	0.0954		
Holo Terrace	KM	26.93378	92.83468	0.01		-24.04	0.119		
Kameng down f		26.93378	92.83468	0	modern	-23.49	0.194		
Jner Khad f		31.95524	76.44086	0	modern	-26.4	0.372		
Beas f		31.83091	76.78938	0	modern	-25.74	0.978		

Table 2.1: Results carbon and oxygen stable isotopes (cont.)

Sample	Section	Latitude	Longitude	Age [Ma]	Stratigraphic unit	$\delta^{13}C_{org}$ (VPDB) [‰]	TOC [%]	$\delta^{13}C_{carb.}$ (VPDB) [‰]	$\delta^{18}O_{carb.}$ [‰]
HK14-1-f2	HK	30.4422	77.38809	5.8	MS	-23.72	0.0642		
HK14-2-f	HK	30.45423	77.37869	5.2	US	-24.68	0.115		
HK14-3-f	HK	30.45651	77.39129	4.9	US	-22.85	0.16		
HK14-3-nod	HK	30.45651	77.39129	4.9	US			-1.2	-8.55
HK14-4-f	HK	30.45829	77.39821	4.6	US	-20.12	0.137		
HK14-5-f	HK	30.46323	77.40434	4	US	-22.19	0.123		
HK14-5-nod	HK	30.46323	77.40434	4	US			-0.15	-6.98
HK14-6-f	HK	30.46468	77.40628	3.8	US	-18.21	0.0961		
HK14-6-nod	HK	30.46468	77.40628	3.8	US			-2.58	-8.43
HK14-7-nod	HK	30.46751	77.40686	3.5	US			-2.73	-8.11
HK14-7-f	HK	30.46751	77.40686	3.5	US	-22.38	0.0627		
HK14-8-nod	HK	30.46838	77.40708	3.3	US	0		-3.72	-8.3
HK14-8-f	HK	30.46838	77.40708	3.3	US	-23.43	0.133		
HK14-9-f	HK	30.46897	77.40817	3.1	US	-17.9	0.164		
HK14-9-nod	HK	30.46897	77.40817	3.1	US			-8.33	-6.93
HK14-10-f	HK	30.47293	77.40885	3	US	-18.82	0.118		
HK14-10-nod	HK	30.47293	77.40885	3	US			-2.62	-7.34
HK14-14-f	HK	30.48028	77.42713	1.1	US	-20.8	0.0661		
HK14-14-nod	HK	30.48028	77.42713	1.1	US			-3.86	-6.82
HK14-15-f	HK	30.47946	77.42542	1.9	US	-23	0.104		
HK14-16-f	HK	30.47599	77.42282	2.3	US	-18.9	0.0911		
HK14-17-nod	HK	30.47433	77.41952	2.6	US			2.17	-6.1
HK14-18-nod	HK	30.47352	77.41778	2.7	US			-1.69	-5.77
HK14-18-f	HK	30.47352	77.41778	2.7	US	-22.55	0.0854		
HK14-19-f	HK	30.49312	77.41986	0.5	US	-21.63	0.0935		

Table 2.1: Results carbon and oxygen stable isotopes (cont.)

Sample	Section	Latitude	Longitude	Age [Ma]	Stratigraphic unit	$\delta^{13}C_{org}$ (VPDB) [‰]	TOC [%]	$\delta^{13}C_{carb.}$ (VPDB) [‰]	$\delta^{18}O_{carb.}$ [‰]
JW14-1-f	JW	31.97275	76.44439	5	US	-22.12	0.0669		
JW14-2-f	JW	31.95524	76.44086	5.4	US	-24.38	0.0393		
JW14-3-f	JW	31.95628	76.43329	5.6	US	-23.13	0.0485		
JW14-3-nod	JW	31.95628	76.43329	5.6	US			-7.86	-8.36
JW14-4-f	JW	31.94535	76.4182	6	US	-25.25	0.0518		
JW14-4-nod	JW	31.94535	76.4182	6	US			-1.28	-8.48
JW14-5-f	JW	31.94485	76.41322	6.2	US	-22.49	0.0391		
JW14-6b-f	JW	31.94353	76.40516	6.8	MS	-26.96	0.102		
JW14-7-f	JW	31.93085	76.39915	7.2	MS	-26.42	0.162		
JW14-8-f	JW	31.92472	76.3947	7.9	MS	-24.88	0.101		
JW14-10-f	JW	31.91442	76.37782	9	MS	-24.95	0.0957		
JW14-12-f	JW	31.91054	76.36847	9.6	MS	-24.45	0.136		
JW14-17-f2	JW	31.88286	76.32742	10.6	MS	-24.34	0.0725		
JW14-17-nod	JW	31.88286	76.32742	10.6	MS			-9.98	-9.44
JW14-19-f	JW	31.8923	76.31125	11.3	LS	-25.34	0.0553		
JW14-19-nod	JW	31.8923	76.31125	11.3	LS			-9.93	-8.92
JW14-20-f	JW	31.89519	76.30822	11.9	LS	-23.92	0.0736		
JW14-20-nod	JW	31.89519	76.30822	11.9	LS			-10.76	-8.07
JW14-21-f	JW	31.89552	76.30435	12.3	LS	-23.69	0.196		
JW14-21-nod	JW	31.89552	76.30435	12.3	LS			-9.25	-5.78
JW14-22-f	JW	31.91991	76.39185	8.3	MS	-25.55	0.123		
JW14-22-nod	JW	31.91991	76.39185	8.3	MS			-9.09	-6.37
JW14-23-nod	JW	31.90277	76.37	9.75	MS			-10.44	-7.04
JW14-23-f	JW	31.90277	76.37	9.75	MS	-24.06	0.0873		
JW14-24-nod	JW	31.8879	76.3422	10.3	MS			-7.98	-14.54
JW14-24-f	JW	31.8879	76.3422	10.3	MS	-24.2	0.0997		
JW14-25-nod	JW	31.88367	76.33209	10.5	MS			-8.85	-5.06
JW14-25-f	JW	31.88367	76.33209	10.5	MS	-25.69	0.0858		
JW14-26-nod	JW	31.88303	76.32775	10.55	MS			-10.67	-8.5
JW14-26-f	JW	31.88303	76.32775	10.55	MS	-24.75	0.0842		
JW14-27-nod	JW	31.8862	76.32556	10.7	LS			-10.65	-7.82
JW14-27-f	JW	31.8862	76.32556	10.7	LS	-24.98	0.16		
JW14-28-nod	JW	31.88687	76.32561	10.8	LS			-11.1	-5.34
JW14-28-f	JW	31.88687	76.32561	10.8	LS	-25.11	0.0595		
JW14-29-nod	JW	31.88747	76.31362	11.2	LS			-8.55	-8.99
JW14-29-f	JW	31.88747	76.31362	11.2	LS	-25.25	0.0641		
JW14-30-nod	JW	31.89371	76.30812	11.8	LS	0		-8.72	-8.91
JW14-30-f	JW	31.89371	76.30812	11.8	LS	-24.36	0.0901		
JW14-31-nod	JW	31.89627	76.30575	12.1	LS			-8.72	-7.76
JW14-31-f	JW	31.89627	76.30575	12.1	LS	-23.89	0.0588		
JW14-32-nod	JW	31.89509	76.29923	12.5	LS			-9.16	-6.58
JW14-32-f	JW	31.89509	76.29923	12.5	LS	-24.72	0.0931		

Table 2.1: Results carbon and oxygen stable isotopes (cont.)

Sample	Section	Latitude	Longitude	Age [Ma]	Stratigraphic unit	$\delta^{13}C_{org}$ (VPDB) [‰]	TOC [%]	$\delta^{13}C_{carb.}$ (VPDB) [‰]	$\delta^{18}O_{carb.}$ [‰]
JN14-1-f	JN	31.83252	76.7839	20.5	LD	-23.88	3.86		
JN14-2-f2	JN	31.84433	76.78319	20.1	LD	-26.36	0.0625		
JN14-2-nod	JN	31.84433	76.78319	20.1	LD			-12.07	-10.49
JN14-5-f	JN	31.85027	76.78211	19	LD	-27.1	0.207		
JN14-5-nod	JN	31.85027	76.78211	19	LD			-10.87	-9.07
JN14-6-f	JN	31.85049	76.78384	18.5	LD	-26.52	5.65		
JN14-6-nod	JN	31.85049	76.78384	18.5	LD			-9.46	-9.18
JN14-8-f	JN	31.85334	76.78873	17.4	LD	-26.34	0.264		
JN14-8-nod	JN	31.85334	76.78873	17.4	LD			-12.81	-9.87
JN14-9-f	JN	31.85452	76.79082	17.1	LD	-25.86	13.7		
JN14-9-nod	JN	31.85452	76.79082	17.1	LD			-13.38	-13.23
JN14-10-f	JN	31.86204	76.78157	16.9	LD	-26.97	7.27		
JN14-10-nod	JN	31.86204	76.78157	16.9	LD			-10.3	-9.57
JN14-11-f	JN	31.86903	76.77904	16.5	UD	-23.19	9.78		
JN14-11-nod	JN	31.86903	76.77904	16.5	UD			-9.38	-9.13
JN14-13-f	JN	31.87261	76.78188	15.7	UD	-25.05	10.5		
JN14-14-f	JN	31.87288	76.78415	15.1	UD	-23.84	0.118		
JN14-15-f	JN	31.87232	76.78606	14.9	UD	-23.99	0.114		
JN14-17-f	JN	31.88188	76.78286	14.6	UD	-24.5	4.86		
JN14-18-f	JN	31.88432	76.78474	14.2	UD	-24.02	8.44		
JN14-19-f	JN	31.88481	76.78768	14.1	UD	-24.59	5.42		
JN14-19-nod	JN	31.88481	76.78768	14.1	UD			-9.92	-8.96
JN14-21-f	JN	31.89415	76.78654	13.5	UD	-25.74	11.1		
JN14-24-f	JN	31.9135	76.79047	12.8	LS	-25.43	0.071		
JN14-25-nod	JN	31.84216	76.78153	20.2	LD			-10.67	-8.47
JN14-26-nod	JN	31.84261	76.78306	20.3	LD			-11.69	-9.09
JN14-26-f	JN	31.84261	76.78306	20.3	LD	-26.69	0.0519		
JN14-27-nod	JN	31.84561	76.78667	19.3	LD			-11.82	-6.35
JN14-27-f	JN	31.84561	76.78667	19.3	LD	-25.68	0.0825		
JN14-28-nod	JN	31.84966	76.78281	18.9	LD			-11.29	-10.07
JN14-28-f	JN	31.84966	76.78281	18.9	LD	-26.34	0.177		
JN14-29-nod	JN	31.85065	76.78768	17.8	LD			-11.51	-7.62
JN14-29-f	JN	31.85065	76.78768	17.8	LD	-24.59	4.4		
JN14-30-nod	JN	31.85563	76.79126	17	LD			-10.4	-9.2
JN14-30-f	JN	31.85563	76.79126	17	LD	-23.89	0.126		
JN14-31-nod	JN	31.85842	76.79214	16.95	LD			-10.13	-9
JN14-31-f	JN	31.85842	76.79214	16.95	LD	-23.55	0.126		
JN14-32-nod	JN	31.86697	76.77873	16.6	UD			-8.87	-5.14
JN14-32-f	JN	31.86697	76.77873	16.6	UD	-24.36	0.0762		
JN14-33-nod	JN	31.8943	76.78596	13.6	UD			-10.02	-6.86
JN14-33-f	JN	31.8943	76.78596	13.6	UD	-24.87	5.53		
JN14-34-nod	JN	31.8945	76.78743	13.4	UD			-11.12	-8.22
JN14-34-f	JN	31.8945	76.78743	13.4	UD	-24.74	6.85		
JN14-35-nod	JN	31.89595	76.78894	13.3	UD			-10.63	-6.97
JN14-35-f	JN	31.89595	76.78894	13.3	UD	-24.66	0.0567		
JN14-36-nod	JN	31.90057	76.78863	13.2	UD			-12.32	-10.59
JN14-36-f	JN	31.90057	76.78863	13.2	UD	-24.39	0.0585		
JN14-37-nod	JN	31.9049	76.79	12.95	LS			-9.51	-8.15
JN14-37-f	JN	31.9049	76.79	12.95	LS	-24.03	0.0823		
JN97-022B	JN	31.9125	76.79167	12.5	LS	-26.12	0.05		
JN97-004B	JN	31.84417	76.78306	20	LD	-25.77	0.1		

Chapter 3

Weathering regime in the Eastern Himalaya since the mid-Miocene: Implication from detrital geochemistry and clay mineralogy of the Kameng River Section, Arunachal Pradesh, India

N. Vögeli, P. Huyghe, P, van der Beek, Y. Najman, E. Garzanti, C. Chauvel

Submitted to Basin Research, July 2016

Abstract

It is crucial to understand lateral differences in paleo-climate and weathering in order to fully understand the evolution of the climate in the Himalayan region. Many studies have been made on the western and central Himalaya, but the eastern Himalaya remains poorly studied with regard to paleoclimate and past weathering history. Here we present a multi-proxy study on the foreland basin Mio-Pliocene sedimentary section along the Kameng River in Arunachal Pradesh, India, in order to obtain a better insight on the weathering history in the eastern Himalaya. We analyzed a continuous sedimentary record over the last 13 Ma. Results of heavy minerals and petrography give a better insight into diagenesis and provenance, showing that the older part of the section is influenced by diagenesis, and that sediments were not only deposited by a large Trans-Himalayan river and the palaeo-Kameng river, but also by small local tributaries. By taking into account changes in diagenesis and provenance, results of clay mineralogy and major element analysis show an overall increase in weathering over time, with a remarkable change at ~8 Ma.

3.1 Introduction

The Himalayan orogen has played an important role in the evolution of past climate (e.g. Raymo and Ruddiman, 1992; Molnar et al., 1993). The monsoonal climate, in turn has a major influence on Himalayan erosion and relief patterns (Thiede et al., 2004; Bookhagen and Burbank, 2006; Clift et al., 2008). The Himalaya is therefore an excellent laboratory to investigate the links between climate, erosion and tectonics. Even though the evolution of the mountain belt is primarily driven by the India-Asia continent-continent collision, unravelling the past variations of monsoonal strength and weathering regimes is crucial to understanding the role of climate in the evolution of the mountain belt.

Chemical weathering and weathering fluxes to the ocean are a response to climate, tectonics and erosion (Galy and France-Lanord, 1999). Weathering fluxes and erosion rates in the Himalaya appear to have been relatively constant over the past 12 Ma, as recorded by sediments in the Bay of Bengal (Derry and France-Lanord, 1996; Galy et al., 2010). Lupker et al. (2012) showed that sediments are significantly weathered in the floodplain. However, past weathering regimes of the eastern Himalayan foreland basin sediments have never been properly constrained. Possible controls on these rates by monsoonal strength or tectonic parameters are not yet fully understood, although this has been the subject of speculation (e.g. Clift et al., 2008).

Several sedimentary sections within the foreland basin of the Himalayan range, especially in the western and central Himalaya, have previously been dated and studied with the aim of determining hinterland exhumation rates, provenance and paleoclimate (Quade and Cerling, 1995; Ghosh et al., 2004; Sanyal et al., 2004; van der Beek et al., 2006, amongst others). However, the paleo-climate in the eastern Himalaya remains poorly studied.

We here present new data on the weathering history in the Eastern Himalaya by using whole-rock geochemistry and clay mineralogy from the 13 Ma to 1 Ma Siwalik sedimentary record. Samples were collected from Miocene-Quaternary foreland basin sediments along the Kameng section in Arunachal Pradesh, north-eastern India (Figure 3.1), which has been dated by magnetostratigraphy (Chirouze et al., 2012). To extract the weathering signal, it is crucial to also understand the provenance and diagenetic history of the sediments, in order to be able to deconvolve the signal. New heavy mineral and petrography data are used as additional indicators for provenance and diagenesis and combined with existing data of Cina et al. (2009) and Chirouze et al. (2012, 2013). Nd and Hf bulk rock isotopic data (Chirouze et al., 2013) and U-Pb ages of detrital zircons (Cina et al., 2009) suggest a change in provenance between 7 and 3 Ma, with paleo-Brahmaputra sediments being deposited in the Kameng river section during this period. Apatite fission track (AFT) ages (Chirouze et al., 2013) show the maximum paleo-temperature in the sediments, which can be used as a first indicator for diagenesis.

3.2 Geological Setting

3.2.1 Himalayan Geology

The formation of the Himalayan mountain belt resulted from the collision between the Indian and the Eurasian continental margins, which began ca 60 to 50 Ma (Garzanti et al., 1987; Najman et al., 2010; Hu et al., 2016) and subsequently caused major crustal shortening and thickening (Hodges, 2000; Yin and Harrison, 2000). The Himalaya, south of the suture zone, can be divided into four major lithotectonic units (Figure 3.1), which are the Tethyan Sedimentary Series (TSS), the Higher Himalayan Crystalline Series (HHCS), the Lesser Himalayan Series (LHS) and the Sub-Himalayas (SH). These lithotectonic units are bound by a north dipping fault system, which are from north to south, the South Tibetan Detachment System (STDS), the Main Central Thrust (MCT), the Main Boundary Thrust (MBT) and the Main Frontal Thrust (MFT) (DeCelles et al., 2001; Le Fort, 1986; Yin and Harrison, 2000). The HHCS consist mainly of high-grade metasedimentary rocks and granites, whereas the LHS are largely Proterozoic low-grade metasedimentary rocks. The rocks of the southernmost SH unit are the non-metamorphosed clastic sediments of the Siwalik group, which were deposited in the Himalayan foreland basin and are thrusted over the Indus-, Ganges- and Brahmaputra- alluvial plains along the MFT. North of the suture zone, the southern margin of the Asian plate is comprised of the Trans-Himalaya, which predominantly consists of Cretaceous-Paleogene Andean-type Gangdese batholiths (Wen et al., 2008). The suture zone itself, along which the Brahmaputra river flows, is marked by, amongst other lithologies, ophiolitic fragments (Hébert et al., 2012).

3.2.2 Foreland basin sediments – The Siwalik Group

The synorogenic sediments of the Siwalik Group form the foothills of the Himalaya along the entire mountain front from Pakistan to northeastern India. They represent the Neogene infill of the Himalayan foreland basin (DeCelles et al., 1998b; Ojha et al., 2009; Chirouze et al., 2012). An overall coarsening and thickening upward trend is commonly observed throughout the Siwalik Group, which is divided into the Lower, Middle and Upper Siwaliks (LS, MS, US) sub-groups. The LS consist of alternating

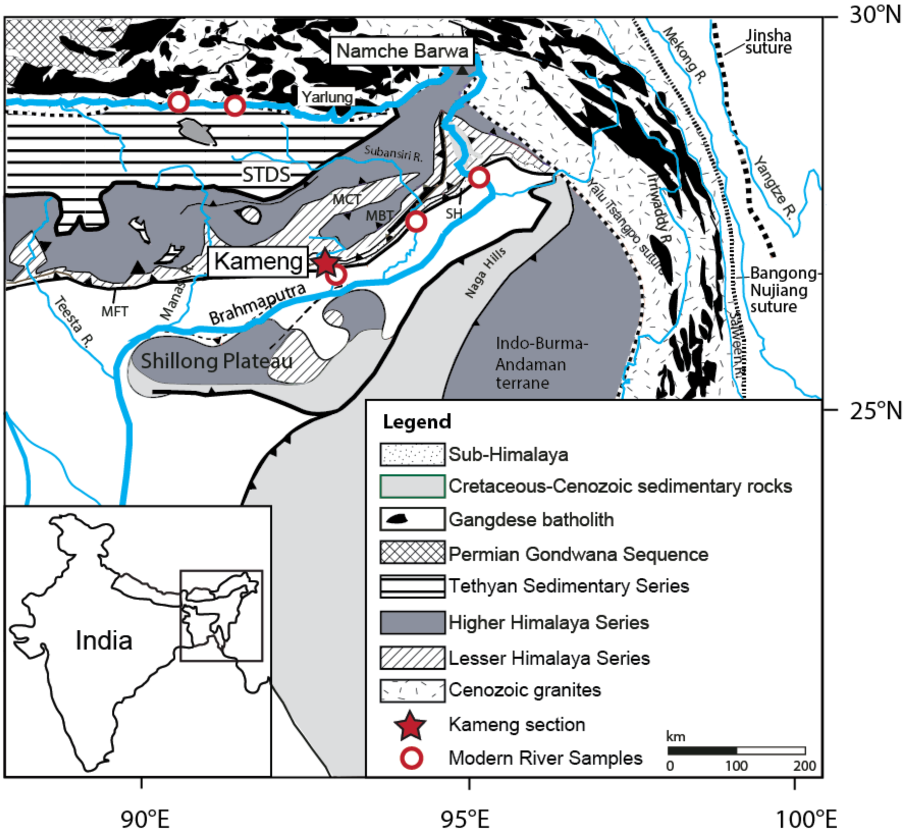

Figure 3.1: Geological map of the Eastern Himalaya modified from Chirouze et al. (2013). Red star indicates the Siwalik Section along the Kameng River. Red circles indicate sampling locations of modern river sand and mud.

mudstone with some paleosols and fine- to medium-grained sandstone. The beds are a few meters thick. The LS is associated with a depositional environment of high-sinuosity streams. The MS consists of a stack of tens of meter thick medium- to coarse-grained mica-rich sandstone beds deposited by a large braided river system. The US contains tens of meter thick conglomerates with interlayers of sandstone and less commonly mudstone, and can be attributed to a gravelly braided river system (Nakayama and Ulak, 1999; Chirouze et al., 2013).

The Kameng River Section is located near the town of Bhalukpong, Arunachal Pradesh in north-eastern India (Figure 3.1). The modern Kameng River drains the HHCS and the LHS before it flows through the Siwaliks and finally enters the floodplain where it merges with the Brahmaputra River. The Kameng River Section has been magnetostratigraphically dated by Chirouze et al. (2012) and spans from 13 to 1 Ma. The exposed LS range from ca. 13 Ma to 10.5 Ma. The MS/US boundary was dated at 2.6 Ma (Chirouze et al., 2012). The Kameng River Section is approximately 6 km thick and is bound by the MFT, placing Siwalik rocks onto Quaternary sediments of the Brahmaputra plain (Burgess et al., 2012). The MBT separates the Siwaliks from the Lesser Himalayan Series in the North. Within the Kameng section, the Tippi Thrust places the LS over the US, therefore the younger part of the sequence, with MS and US exposure, is found in the footwall of the Tippi thrust to the south, whereas the older part crops out in the structural upper part of the section to the north (Figure 3.2). Detrital zircons U-Pb and Nd and Hf bulk rock isotope data show that the Kameng Siwalik Group was sourced from the HHCS and LHS by a paleo-Kameng River and between 7 and 3 Ma by the paleo-Brahmaputra draining also the suture zone and Asian plate (Cina et al., 2009; Chirouze et al., 2013). Reset AFT ages can be used to constrain timing and burial depth (Chirouze et al., 2013). Sediments of the Kameng River section older than 8 Ma underwent burial diagenesis at temperatures above 110°C (Chirouze et al., 2013), the AFT annealing temperature (Donelick et al., 2005). The source area exhumation rate in the Kameng river section has remained fairly constant over the past 13 Ma as determined from detrital zircon fission track data (Chirouze et al., 2013).

3.3 Sampling and Methods

3.3.1 Sampling strategy

We sampled the Kameng River Section according to the paleomagnetostratigraphy sampling points of Chirouze et al. (2012). Samples were collected in pairs of adjacent fine- (mud/siltstones) and coarse-grained (sandstones) sediment beds of the same age. To have a continuous age record, 2-3 samples per Ma were collected. Additionally, modern river sand and mud were sampled from the Kameng and Subansiri Rivers, which drain the Higher and Lesser Himalaya, and the Siang River, which additionally drains the suture zone and Asian plate. Previously sampled Yarlung river sediments, were also analysed (cf. Figure 3.1).

3.3.2 Methods

3.3.2.1 Heavy Minerals and petrography

Heavy-mineral and sandstone petrography analyses were performed at the Department of Earth and Environmental Sciences at Università di Milano-Bicocca, using standard techniques as described in Garzanti and Andó (2007) (see supplementary information for more details).

Sand/Sandstone petrography: A split aliquot of 16 Neogene sandstones and one modern sand sample were cut into standard thin sections, if necessary after impregnation with araldite, stained with alizarine red to distinguish dolomite and calcite, and analysed by counting 400 points under the petrographic microscope (Gazzi-Dickinson method; Ingersoll et al. (1984)). Sand and sandstones are classified according to their main components (Q = quartz; F = feldspars; L = lithic fragments), considered only where QFL exceeds 10%. They are listed in order of abundance (e.g., in a feldspatho-quartzose sand Q > F > 10% QFL > L); an adjective reflecting the most common rock-fragment type may be added (e.g., metamorphiclastic).

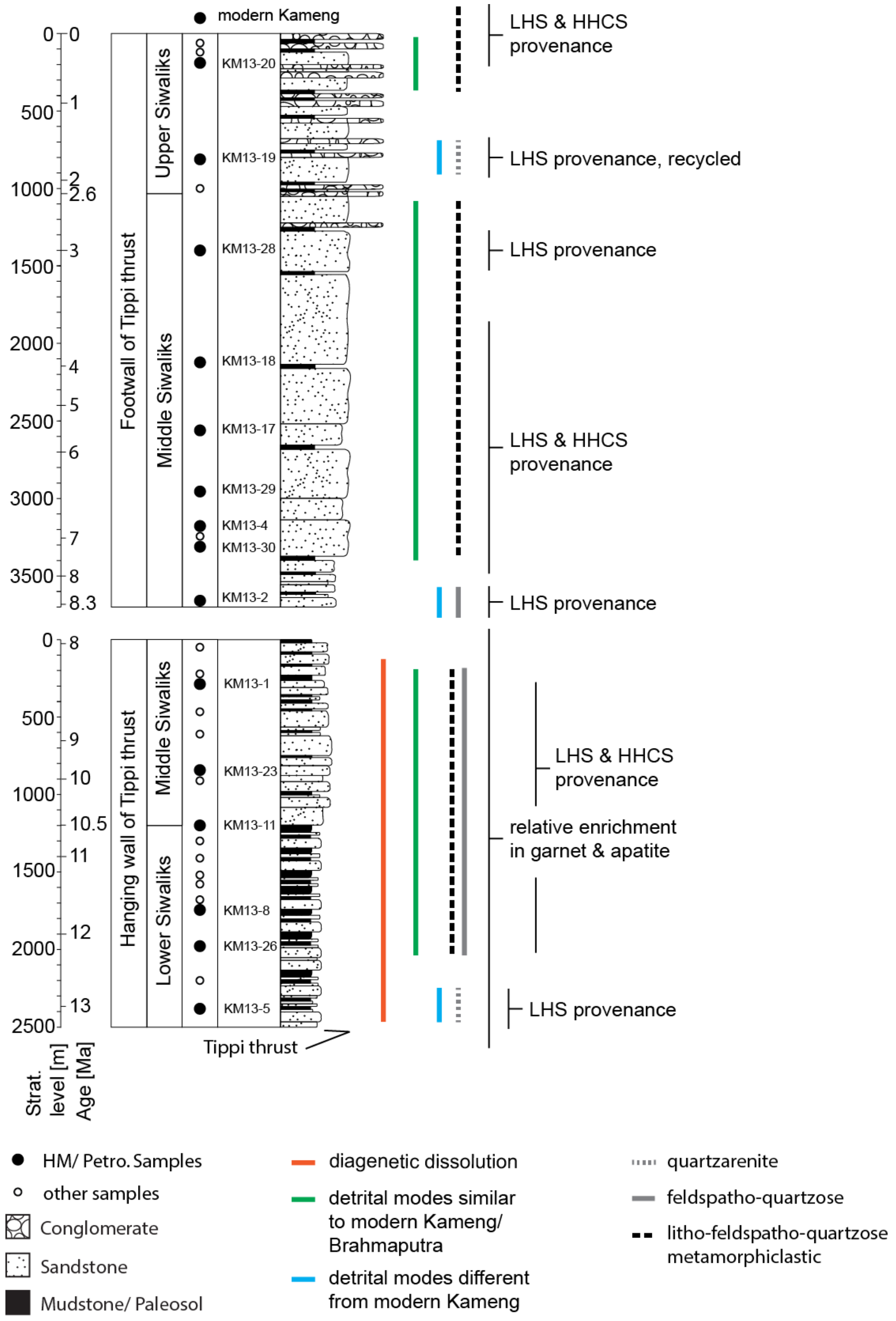

Figure 3.2: Summary of heavy mineral and Petrography data of the Kameng river section.

Heavy minerals: Although bulk-sample analyses represent the only correct option for accurately estimating percentages of detrital minerals, the presence of detrital grains with great size differences in relatively poorly sorted alluvial sediments makes mounting and identification difficult (Mange and Maurer, 1992). Practical reasons thus may exist to set lower and upper size limits to the analysed size-window, which in any case should be large enough to include most of the detrital population and thus to obtain a faithful characterization of the heavy-mineral suite (Garzanti et al., 2009). In this study we selected a very wide ($\geq 5\ \phi$) size window for analysis (> 15 μm or 15-500 μm), and thus considered 85% of the bulk sediment, cutting only the extreme fine (12±7%) and coarse (3±3%) tails of the size distribution. From a split aliquot of the chosen size-window separated by dry sieving, the dense fraction was separated by centrifuging in sodium polytungstate (density ~2900 kg/m^3) and recovered by partial freezing with liquid nitrogen. From each sample, 200 to 280 transparent detrital minerals were analysed in grain mounts by point counting under the petrographic microscope, a technique that allows the true volume percentages of each mineralogical species to be obtained (Galehouse, 1971).

Heavy-mineral concentration was calculated as the volume percentage of total (HMC) and transparent (tHMC) heavy minerals (Garzanti and Andó, 2007). The complete results of petrographic and heavy-mineral analyses are provided in Appendix 3.1.

3.3.2.2 Clay minerals

Clay minerals were extracted from 21 selected, mostly fine-grained, samples. Samples were crushed to smaller pieces and diluted with MilliQ water. Carbonate and organic matter were removed by adding buffer 1M acetic acid and H_2O_2, respectively, and heating the samples overnight. Samples were cleaned with MilliQ water after each removal. In order to separate the <2μm fraction, samples were diluted in MilliQ water and centrifuged for 8 min at 700 rpm, thereafter only the top 7 cm of the liquid, where the suspended load is situated, was pumped off. This procedure was repeated until a volume of 2l was achieved (Moore and Reynolds, 1997). The fraction <2 μm was stored in MilliQ water. Oriented aggregates were made on glass slides. X-ray diffractograms were carried out on air-dried and glycosylated samples on a Bruker D8 Advance X-Ray Diffractometer at the ISTerre, University of Grenoble-Alpes.

A semi-quantitative peak analysis on the XRD patterns was undertaken in order to obtain the clay-mineral distribution. This method is based on the peak height of the XRD of the different clay minerals by adding them up to 100% (Capet et al., 1990), allowing a percentage of different clay minerals with a relative error of approximately 5% to be obtained (Holtzappel, 1985). Illite crystallinity, also known as Kübler Index (KI), is the full width at half maximum (FWHM) of the 10 Å peak on the glycolated X-ray diffractogram (Kübler and Goy-Eggenberger, 2001). The KI measurement is a statistical means to determine low grade metamorphism and diagenetic fields in sedimentary rocks. With increasing burial and very low-grade metamorphism, smectites and illite–smectite mixed-layers re-crystallize and progressively transform into illites and finally into muscovite. These transformations, very complex in detail, lead to a progressive decrease in the width of the 10 Å peak as measured on an X-ray diffractogram. Therefore, low KI values correspond to well-crystallized minerals, whereas high KI values indicate poorly crystallized minerals. The KI measurements allow us to establish three subdivisions within the very low-grade metamorphism field: diagenesis, anchizone and epizone. In this paper, authigenic clays, such as smectites, which are produced under enhanced weathering conditions (Hillier, 1995) are used to distinguish different periods of weathering.

3.3.2.3 Major elements

Pairs of fine- and coarse-grained samples were ground to a powder with an agate mortar. Loss of ignition (LOI) was determined by weight loss after an hour at 1000°C. Major element concentrations were determined after dissolution of 50-70 mg of powder in a mixture of HF and HNO_3 heated for about 72h at 90°C. The solution was then treated with boric acid to neutralize the HF and with H_2O_2 to dissolve organic matter, and further diluted with MilliQ water. Analyses were performed using a Varian 720-ES inductively coupled plasma atomic emission spectrometer (ICP-AES) in ISTerre at the University of Grenoble-Alpes following the method of Chauvel et al. (2011). The accuracy of the measurements is evaluated at 3% by comparing the concentrations measured on international reference material, run as unknown, with the reference values (Appendix 3.2).

Hydration (H_2O^+) of selected samples was measured at the SARM, CNRS, CRPG in Nancy, France with the Karl Fischer titration method (Fischer, 1935).

The degree of chemical weathering of the sedimentary rocks is illustrated by using ratios of mobile to immobile elements, such as K/Si, H_2O^+/Si and K/Al (Lupker et al., 2013). Sediment hydration, H_2O^+, is a proxy for chemical weathering that traces mineral hydrolysis and secondary neo-formations(Lupker et al., 2012). K/Si and H_2O^+/ Si are dominantly controlled by the grain size of sediments in modern rivers, and secondarily by weathering. To better constrain the trends over time, the ratio of K/Al is used to quantitatively track weathering trends. As K/Si and H_2O^+/Si are affected by grain-size effects (Lupker et al., 2012), ratios were normalized to a common average Al/Si composition of 0.22, with a regression line through a coarse-grained end member and the sample (Appendix 3.2; Lupker et al. (2013)). Normalized ratios are shown as K/Si* and H_2O^+/Si*.

3.4 Results

3.4.1 Heavy minerals and petrography

Compositions of Siwalik sandstones are shown in figure 3.3. The oldest sample (KM13-5, 13 Ma), which was collected in proximity of the Tippi thrust, is a virtually pure quartzarenite with very low-rank metasedimentary rock fragments and an extremely poor, zircon-dominated heavy-mineral assemblage. Detrital modes contrast with those of modern Kameng sand.

The overlying sandstone samples (13 to 8 Ma) in the hanging wall of the Tippi Thrust, range from feldspatho-quartzose to litho-feldspatho-quartzose metamorphiclastic with approximately equal amounts of plagioclase and K-feldspar, more abundant biotite than muscovite, and mainly schist, gneiss, metasandstone, slate/phyllite and granitoid rock fragments. A few dolostone rock fragments appear upward. Heavy-mineral assemblages are very poor and garnet-dominated with tourmaline, zircon, apatite and rutile.

The ZTR index (sum of zircon, tourmaline and rutile over total transparent heavy minerals), which constitutes an indicator of mineralogical stability (Hubert, 1962) lies between ~20 and 50, with one outlier at 13 Ma, through the 13-8 Ma Lower to Middle Siwalik succession exposed in the hanging wall of the Tippi Thrust (Figure 3.4). Transparent heavy-mineral percentages are invariably very poor with dominant garnet, epidote only sporadically recorded, and amphibole, staurolite, kyanite and sillimanite never recorded.

By contrast, in the Middle Siwalik section exposed in the footwall of the Tippi Thrust (samples aged < 8 Ma) - excepting samples KM13-2 (8.3 Ma) and KM13-19c (2 Ma), which have different provenance - ZTR is mostly less than one. Heavy-mineral assemblages are mostly moderately poor to rich, and amphibole and epidote are invariably abundant. Sandstone samples in the central part of the Middle Siwaliks (8-3 Ma) are litho-feldspatho-quartzose metamorphiclastic rocks with approximately equal amounts of plagioclase and K-feldspar, more abundant biotite than muscovite, and mainly schist, gneiss, metasandstone, slate/phyllite, granitoid, volcanic, metavolcanic and siltstone/sandstone rock fragments. Heavy-mineral assemblages range from moderately poor to rich and mainly include amphibole, garnet and epidote, with minor kyanite, chloritoid and staurolite. Fibrolitic sillimanite becomes common at 3-4 Ma. Composition of this 8-3 Ma interval is comparable to that of the modern day Kameng and Brahmaputra rivers (Figure 3.3).

Intercalated in both the lowermost (KM13-2, 8.3 Ma) MS and lowermost (KM13-19, 2 Ma) US are feldspatho-quartzose to quartzose sandstones with more abundant K-feldspar than plagioclase, minor metamorphic rock fragments and very poor heavy-mineral assemblages including abundant (or even dominated by) zircon and tourmaline.

The youngest sandstone sample (KM13-20, ~0.8Ma) is a litho-feldspatho-quartzose with more abundant K-feldspar than plagioclase, more abundant biotite than muscovite and mainly low-rank metamorphic rock fragments. The moderately poor heavy mineral assemblage includes garnet, amphibole, epidote, tourmaline, kyanite and mainly fibrous sillimanite. Composition is broadly similar to modern Kameng sand.

Modern Kameng sand is litho-feldspatho-quartzose metamorphiclastic, with approximately equal amounts of plagioclase and K-feldspar, more abundant biotite than muscovite, and mainly gneiss, schist, granitoid, shale and metasandstone rock fragments. Moderately rich heavy-mineral assemblages include abundant hornblende, garnet, subordinate epidote, minor tourmaline and fibrous and prismatic sillimanite.

3.4.2 Clay minerals

Clay minerals in the <2μm fraction of clayey beds in the Siwalik Group consist mainly of illite, chlorite, smectite and kaolinite (Figure 3.5). The clay-mineral assemblage varies with time and depth within the Kameng section. The oldest part of the section, from 13 to 8 Ma, is dominated by illite- and chlorite-

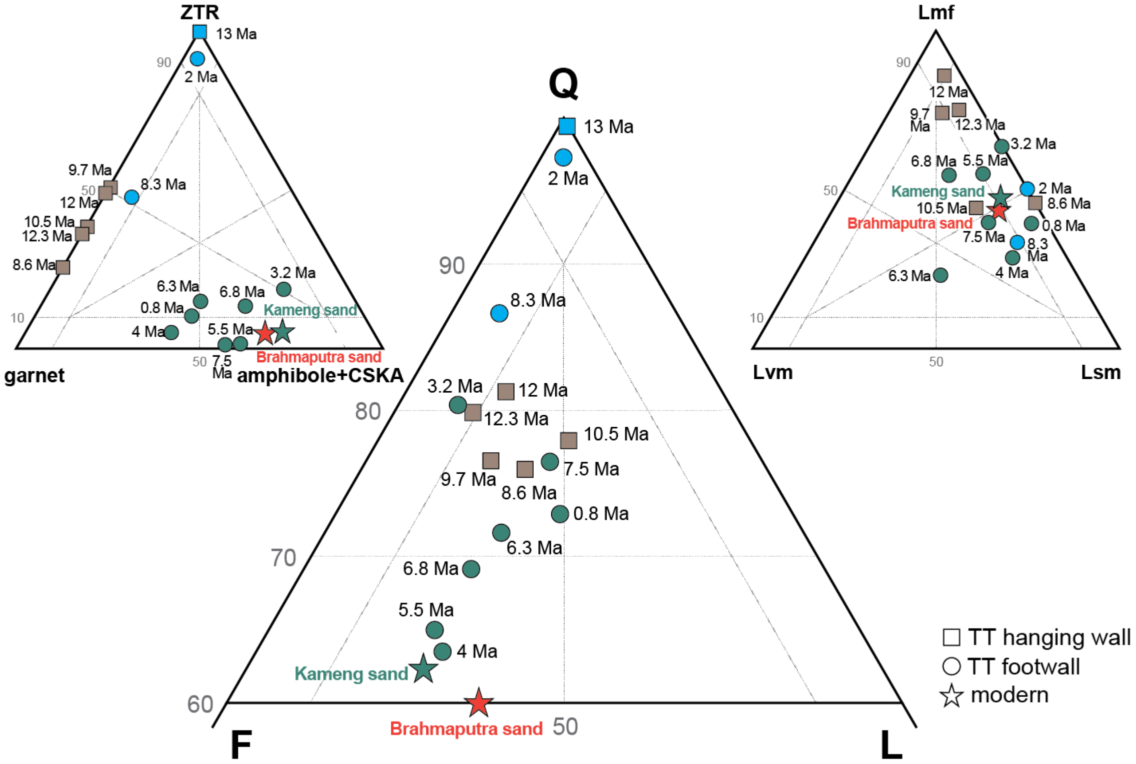

Figure 3.3: Changes in the composition of Siwalik sandstones in the last 13 Ma are controlled by both provenance and diagenesis. Strongly diagenized sandstones in the hanging wall of the Tippi thrust (TT) are richer in quartz and yield heavy-mineral assemblages dominated by relatively stable garnet, zircon and tourmaline (in brown). Litho-feldspatho-quartzose sandstones younger than 8 Ma (in green) in the footwall of the Tippi thrust are less diagenized and display compositions compatible with both modern Kameng and Brahmaputra sand collected at Tezpur (data after (Garzanti et al., 2004). Only sample KM13-19 (2 Ma) is quartzose with only a few stable heavy minerals, suggesting deposition by a tributary largely recycling LHS quartzites. Blue = detrital modes very different from modern Kameng; Q = quartz; F = feldspars; L = lithic grains (Lvm = volcanic, low-rank metavolcanic and high-rank metabasites; Lsm = sedimentary and metasedimentary; Lmf = medium-rank and high-rank felsic metamorphic; ZTR = zircon + tourmaline + rutile; CSKA = chloritoid + staurolite + kyanite + andalusite + sillimanite).

rich assemblages (illite+chlorite/∑clays > 0.6). The part of the section dated between 8 and 3 Ma is dominated by a higher smectite content of around 50%. From 3 to 1 Ma, around the boundary of the Middle and Upper Siwaliks, kaolinite is the most abundant clay mineral, whereas smectite is virtually absent. Strata younger than 1 Ma, are again characterized by higher smectite contents. The oldest sample (13 Ma) differs from the rest and has an unusually high smectite content for its depth. Another outlier is the sample at 4 Ma, a sandstone with extremely low clay content. XRD peaks are small for this sample, making precise semi-quantitative analysis difficult and therefore has to be interpreted with caution.

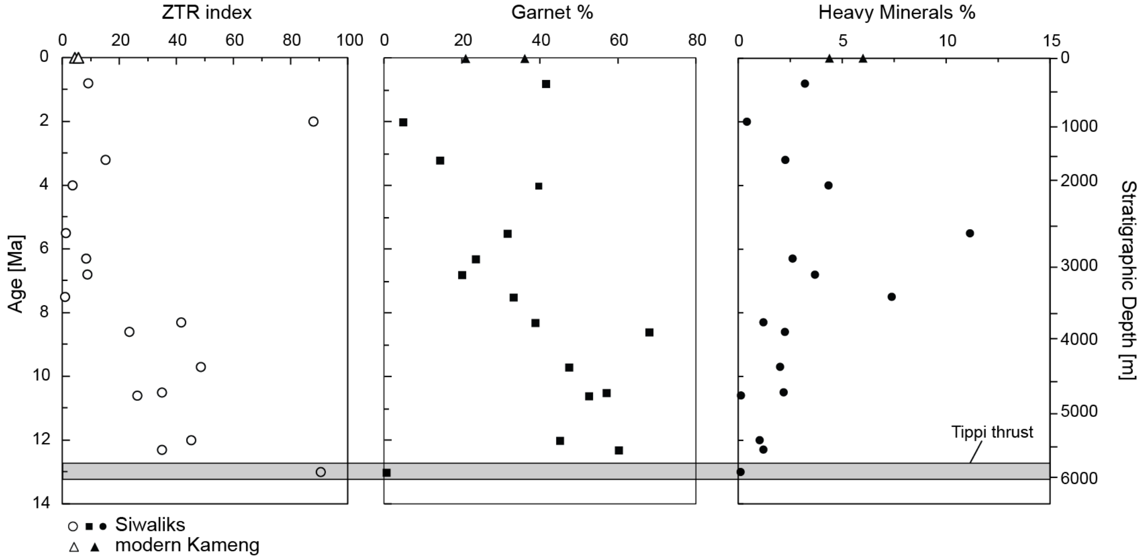

Figure 3.4: ZTR index (sum of zircon, tourmaline and rutile over total transparent heavy minerals, Hubert (1962)) abundance of garnet [%] and total Heavy Minerals [%] vs age [Ma] and stratigraphic depth [m]. ZTR index generally increases with age indicating more dissolution with increasing stratigraphic depth. Garnet shows relative enrichment with increasing depth. Heavy mineral abundance decreases with depth. The sample at 13 Ma (grey band) is anomalous and appears to be influenced by the Tippi thrust.

The illite crystallinity (KI) varies from 0.11 to 0.53 Δ°2Θ, from well-crystallized minerals with crystallinity similar to muscovites from the HHCS (Huyghe et al., 2011) to less or even poorly crystallized minerals. There is no clear trend throughout the section, with most of the KI values between 0.1 to 0.3 Δ°2Θ (Epi- and Anchizone); only two value are above 0.4 Δ°2Θ.

Clay mineral assemblages from modern eastern Himalayan rivers (Yarlung, Siang, Subansiri and Kameng) are shown in (Figure 3.6). They are dominated by illite and chlorite (illite+chlorite/ $\sum$clays > 0.7; Figure 3.5), except the uppermost sample of the Yarlung River, which has almost 50% smectite. Mud from riverbanks of the Yarlung/Siang River system suggests that the proportion of illite and chlorite increases downstream. Muds of the Yarlung upstream of the Eastern Syntaxis have a higher smectite content, compared to downstream. Himalayan tributaries to the Brahmaputra such as the Subansiri and the Kameng have an illite content up to ~90% (illite+chlorite/$\sum$clays >0.8).

3.4.3 Major elements and H_2O^+

Major-element concentrations (Appendix 3.2) were measured on pairs of coarse- and fine-grained samples of similar age, where possible. The difference between coarse- and fine-grained samples is well reflected in the major element composition, as shown in Figure 3.7: sandstones generally have higher SiO_2, whereas finer sediments such as mudstones have a higher K_2O, Al_2O_3 and H_2O^+. The ratio of the immobile elements Al_2O_3/SiO_2 is thus a direct reflection of grain size (Lupker et al., 2012). The

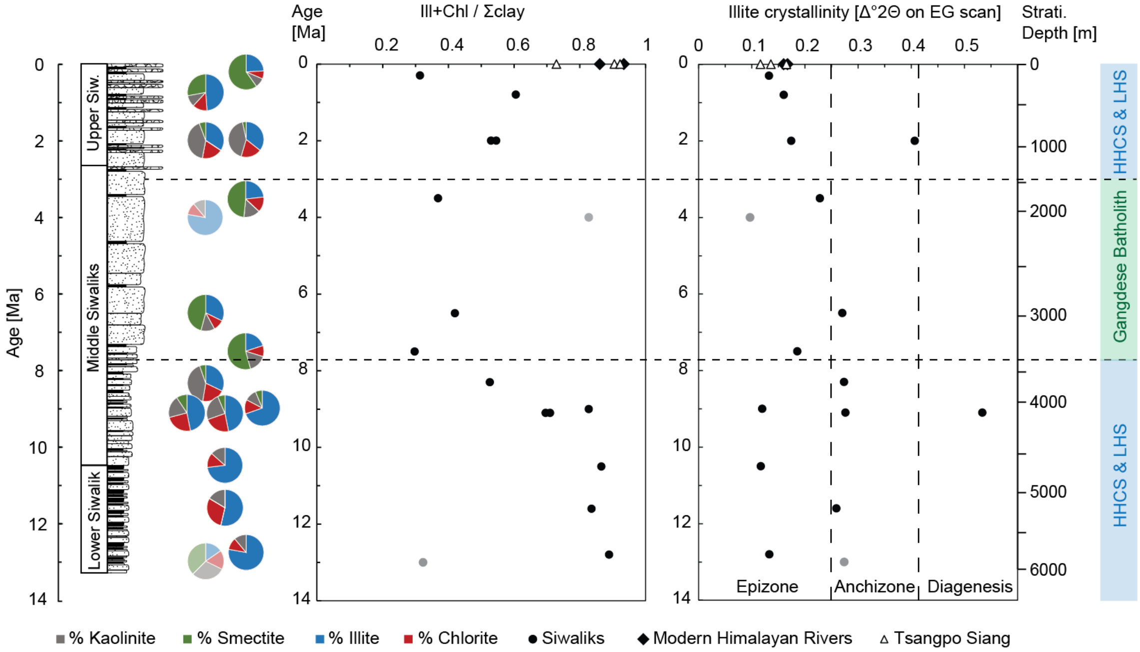

Figure 3.5: Illite+Chlorite/Sum of clays and illite crystallinity (Δ°2Θ on EG scan) vs age [Ma] and depth [m]. Triangles indicate modern river samples, grey circles show samples with anomalous clay assemblages. Provenance, as determined from Nd and Hf isotopes, (Chirouze et al., 2013) and from U-Pb on zircon (Cina et al., 2009), is indicated on the right.

modern Kameng muds have a relatively high SiO_2 concentration of approximately 79 wt%.

Differences in grain size are also obvious when Al/Si is plotted against K/Si (Figure 3.8), with much lower Al/Si and K/Si ratios for coarse-grained sediments due to higher proportions of quartz grains in the coarse fraction. Lupker et al. (2013) also used this diagram to highlight the degree of chemical weathering (Figure 3.8): unaltered protolith produces sediment with high K/Si at a given Al/Si while weathering removes mobile elements such as K and lowers the K/Si ratio. We calculated the 95% confidence interval of the regression for each of the three groups within the Siwaliks (Lower, Middle and Upper) and found that regression lines had different slopes. Sediments of the LS define a steep slope and fall next to the data reported by Lupker et al. (2013) for the Himalayan tributaries; by contrast, the MS and US samples define flatter slopes in figure 3.8 and plot close to the Brahmaputra samples of Lupker et al. (2013). The relatively limited number of analysed samples coming from both the MS and the US make the difference between the two harder to discern.

Normalized ratios K/Si* and H_2O^+/Si* versus age are shown in figure 3.9. Normalized ratios allow for the comparison of chemical compositions of samples with different grain sizes (e.g. sandstone and mudstone). K/Si* and K/Al show similar trends with rather constant and high ratios between 13 and 10 Ma, followed by a period of lower values, which indicates more weathered rock. The lack of fine-grained sediments between 8 and 3 Ma renders the interpretation of the trend in this part of the section difficult. In the period from 4-1 Ma ratios are widely spread, with a significant difference between coarse- and

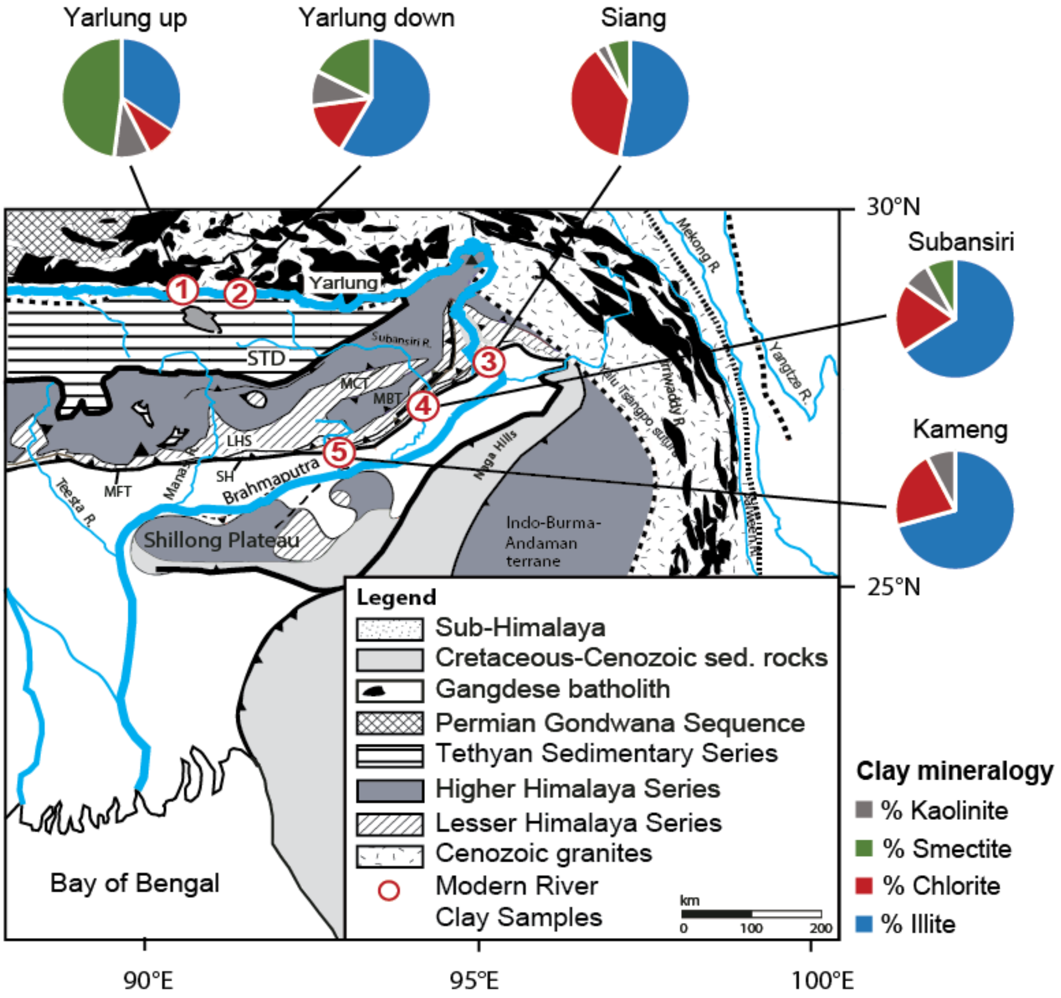

Figure 3.6: Clay mineral assemblages of modern rivers (1,2: Yarlung, 3: Siang, 4: Subansiri, 5: Kameng) in the Eastern Himalaya. Geological map modified after Chirouze et al. (2013).

fine-grained rocks. Modern river K/Si* and K/Al values are again higher.

3.5 Discussion

As noted above, when using a sedimentary record to determine a weathering history, it is necessary to also understand the provenance and degree of diagenesis that the sediments have been subjected to, in order to be able to deconvolve the signal.

3.5.1 Provenance evolution of the Kameng sediments

Previous studies have shown changes in provenance in the Kameng section through time (Cina et al., 2009; Chirouze et al., 2013).ϵNd variations indicate paleo-Brahmaputra provenance between 7 and 3

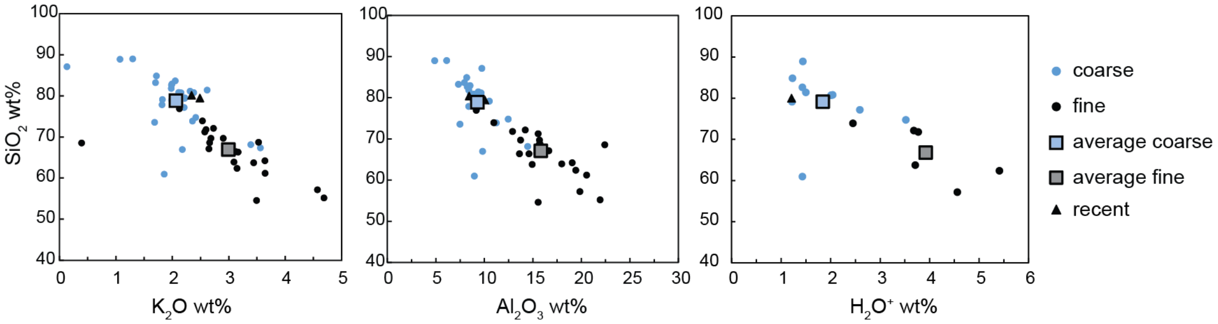

Figure 3.7: Correlation between SiO_2 and K_2O, Al_2O_3 and H_2O^+, fine-grained sediments (in black) show depletion in SiO_2. Mineralogy and major element concentrations vary from fine- to coarse-grained sediments.

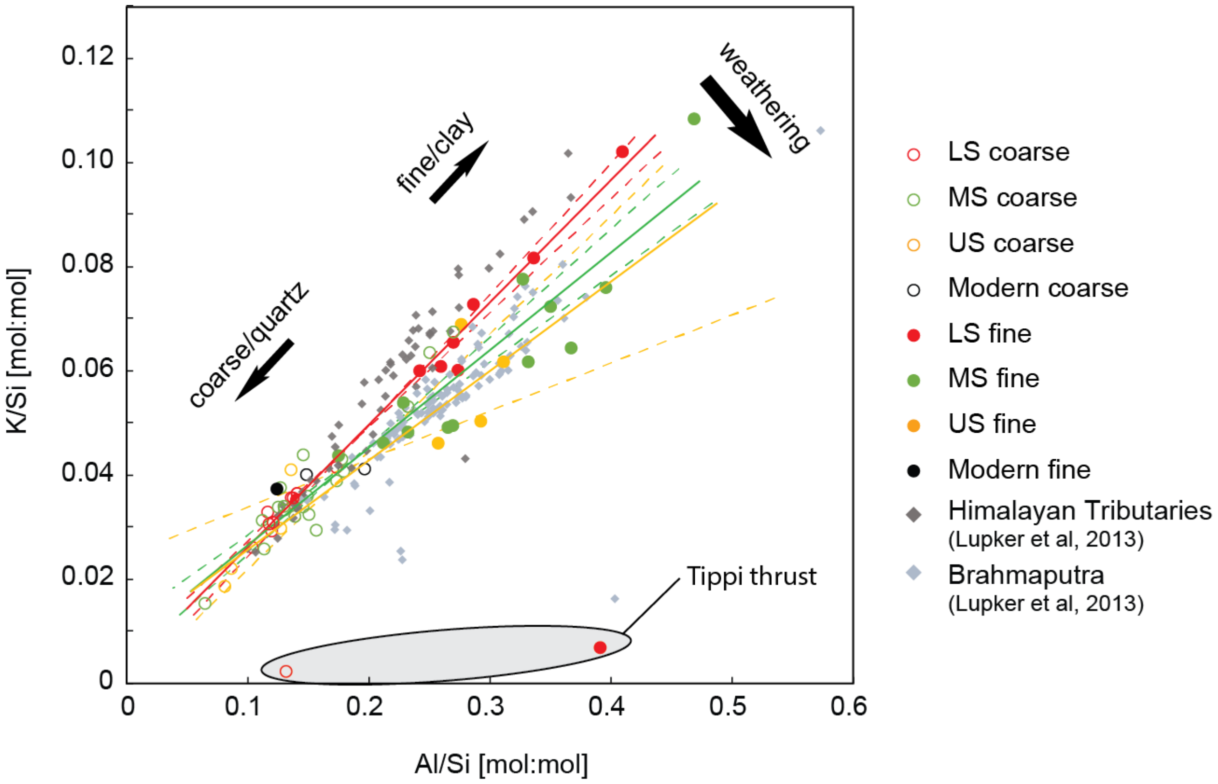

Figure 3.8: Evolution of the K/Si of fine- and coarse-grained sediments of the Kameng Siwaliks. Outliers are rock sampled in proximity to the Tippi thrust and the signal is overprinted by dissolution due to fluid circulation. Different colors indicate different time periods; red for the Lower Siwalik, green for the Middle Siwalik and yellow for the Upper Siwalik. Dotted lines represent the 0.95 confidence level of the linear regression (method after Lupker et al. (2013)).

Ma (Chirouze et al., 2013), with less negative values of around ϵNd -13, characteristic for the modern Brahmaputra (Singh and France-Lanord, 2002), during this time interval compared to values between

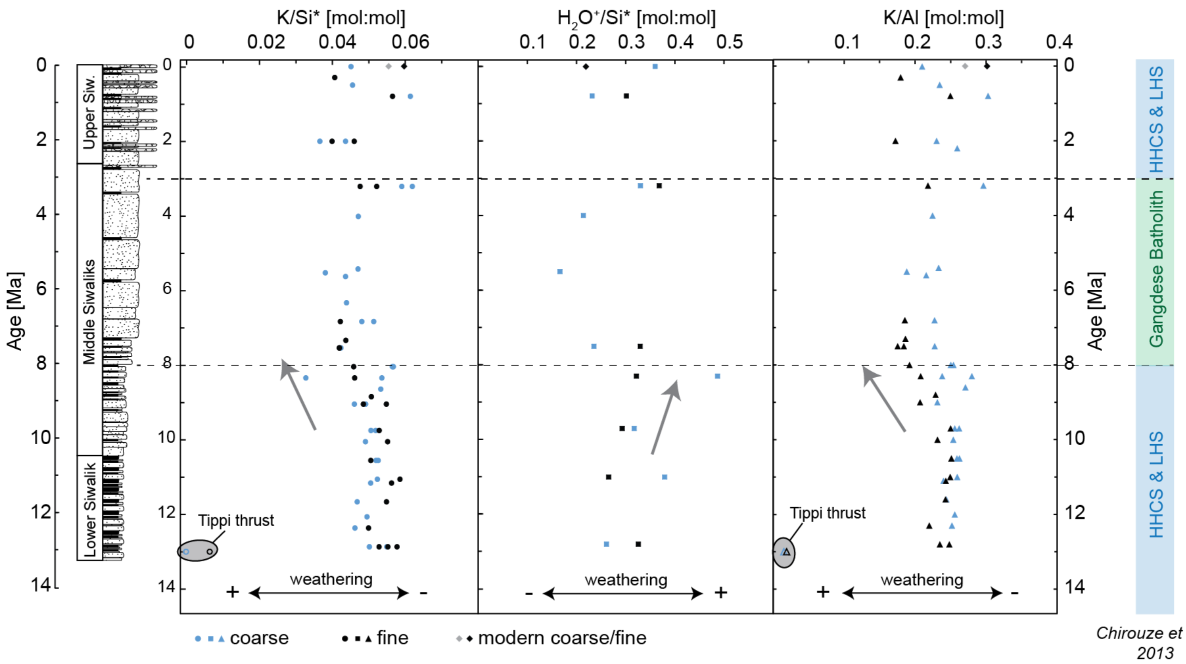

Chirouze et al., 2013

Figure 3.9: Evolution of K/Si*, H_2O^+/Si* and K/Al over time in the Kameng River section. Arrows indicate a change in weathering regime. H_2O^+/Si* is anti-correlated to K/Si* and K/Al. Modern River values are indicated in grey/black diamonds. Outliers are encircled and show sediments influenced by the formation of the Tippi thrust. Provenance change from Sm and Nd isotopes are indicated in blue and green (Chirouze et al., 2013)

-15 and -18, close to modern Kameng sand, in samples above and below this interval. This change in provenance is supported by U-Pb zircon ages (Cina et al., 2009), with ages <200 Ma, with a major cluster between 40-60 Ma, being present in the Middle Siwalik, but not in the Lower Siwalik. Such grains are typical of derivation from the Cretaceous-Paleogene Trans-Himalayan Gangdese batholith (Cina et al., 2009), which forms a major part of the Brahmaputra drainage (Figure 3.1).

Modern Kameng sand indicates provenance largely from the HHCS, with significant contribution from the LHS, revealed by relatively low metamorphic indices, and probably some recycling of Siwalik molasse units accreted at the front of the orogen (Garzanti et al., 2004). Siwalik sandstones in the Kameng section display several significant mineralogical changes, traced by variations of petrographic and mineralogical indices (Figure 3.3). Sudden changes, often represented by a single sample (e.g. KM13-2 and KM13-19c), are ascribed to sediments deposited by tributaries of limited length, draining the Himalayan foothills (Garzanti and Andó, 2007), intercalated with trunk-river deposits as a consequence of lateral channel shifts. Deposits of small tributaries can be associated with recycling of Siwalik molasse or erosion of quartzites, abundant in the LHS of Arunachal Pradesh (Yin, 2006). All other sandstone samples, i.e. KM13-26c to KM13-1 (13-8 Ma), KM13-30c to KM13-28c (7-3 Ma) and KM13-20c ($\sim$0.8Ma) represent deposition by a major trunk river (Figure 3.3).

A more varied lithic population characterizes sandstones between 7 and 3 Ma, where volcanic, metavolcanic and metabasite rock fragments are more frequently recorded, associated with sedimentary to low-rank meta-sedimentary lithic fragments. These rock fragments could be derived from north of the Higher Himalaya, which would be consistent with a contribution from Suture Zone and Transhimalayan units and possible deposition by a paleo-Brahmaputra longitudinal trunk river (Chirouze et al., 2013), as evidenced from Sm-Nd bulk geochemistry and U-Pb detrital zircon ages, as detailed above. Staurolite, kyanite and sillimanite appear and tend to become more abundant upward, documenting provenance from amphibolite-facies HHCS granitoid gneisses and schists since ~8 Ma. Nevertheless, biotite is the predominant detrital mica since 12 Ma, suggesting provenance from amphibolite-facies rocks of the HHCS.

Clay mineral assemblages represent a mixture of detrital and authigenic clay minerals (Hillier, 1995; Huyghe et al., 2005). Diagenetic transformations occurring during burial further complicate the provenance signal. Modern rivers in the eastern Himalaya (Kameng, Subansiri, Siang) have relatively poor smectite content, in contrast to the uppermost Yarlung River sample. The higher smectite content in this Yarlung sample could be related to contributions from mafic and ultramafic rocks found in the suture zone. The Yarlung smectite component is reduced in the Siang River downstream, due to input from Himalayan rivers draining catchments with lower smectite content and/or rapid erosion of the Namche Barwa syntaxis, assuming that rapid erosion was active at the given time. We therefore would expect paleo-Brahmaputra deposits to have lower smectite content compared to the Yarlung, and with similar smectite content to rivers such as the Kameng, draining the southern Himalayan slopes only. This is not the case between 7 and 3 Ma in the Kameng section, where in spite of the interpreted palaeo-Brahmaputra input during this period, an increase in smectite is observed. Variations in clay mineralogy do not correlate to provenance variations in the Kameng section. Dominance of smectite in the clay mineral assemblage could therefore be related to a change in diagenesis or weathering regime.

3.5.2 Diagenesis

Partially reset AFT ages below ~4000 m of estimated burial depth in the Kameng section (Chirouze et al., 2013) are a clear indicator that sediments were heated to 60-120°C, the temperature above which AFT annealing starts (Tagami and O'Sullivan, 2005). This trend is confirmed by the ZTR index showing diagenetic dissolution of less stable heavy minerals, which is detected from a depth of about 3500 m, corresponding to a depositional age of ~8 Ma, (Figures 3.2 and 3.4). Less stable detrital minerals may undergo extensive and even complete intrastratal dissolution during burial diagenesis, leaving behind a residual assemblage that may differ substantially from the original depositional suite. Mineralogical trends observed up-section, therefore, are typically the result of selective diagenetic control superposed on provenance and paleo-drainage changes, which can render the interpretation equivocal. Grains in the footwall of the Tippi Thrust, younger than 8 Ma, show little evidence of corrosion and have significantly lower ZTR indices (Figure 3.3). Influence of diagenesis is therefore negligible in this age bracket.

The sample collected from the Tippi Thrust (KM13-5, 13 Ma), is strongly influenced by fluids circulating probably during the formation of the Tippi thrust, leaving behind pure quartzite and leaching mobile major elements, as well as forming secondary smectite.

Illite crystallinity or Kübler Index (KI) (Kübler and Jaboyedoff, 2000; Kübler and Goy-Eggenberger, 2001) allows the detection of illitisation of smectites that starts at temperatures of about 70-95°C (Dunoyer De Segonzac, 1970). AFT data from the central part of the Siwalik foreland basin suggest that these temperatures were reached at depths of approximately 1800-2000 m (van der Beek et al., 2006). However, besides the increase of temperature with depth, many other factors (geochemical peculiarities of different sequences, kinetics, fluids etc.) may influence the progress of this reaction, complicating attempts to use it as a geothermometer (Hillier, 1995). Deterioration of illite crystallinity is not observed within the Kameng section, whereas it was shown to take place below 2100 m depth in the Karnali section (Huyghe et al., 2005). This result suggests that 1) the clay fraction of the Kameng samples mainly contains inherited illites that were affected by metamorphism in their source area and 2) not all of the smectites in this part of the Siwalik foreland basin have been illitised. Nonetheless, two samples of the Kameng section at 2 and 9 Ma display illites with poor crystallinity. At 2 Ma and a depth of ~1000 m smectite is unlikely to be illitised, this sample also shows an anomalous provenance from LHS, whereas at 9 Ma at a depth of ~4000 m partial illitisation is possible.

Diagenetic reactions and post-depositional weathering would lead to a loss of mobile elements (increasing weathering indices) down-section (Lupker et al., 2013). As mobile major elements do not show a decrease with depth and time, we can assume that major-element concentrations are not strongly affected by diagenesis (Figure 3.9). Only KM13-5 at 13 Ma, which is located in proximity to the Tippi thrust, shows major depletion in mobile elements, as well as an abnormal clay and heavy mineral composition, likely due to fluid circulation during the formation of the Tippi thrust.

3.5.3 Weathering in the Eastern Himalaya since 13 Ma

Ratios of mobile to immobile major elements can be used to track weathering of sediments (Lupker et al., 2012, 2013). The ratio of K/Al is used to show trends in weathering of sediments (Figure 3.9). If we consider that weathered rocks experience fluid-rock interactions, then a loss of potassium reflects more weathering. In order to rule out the influence of grain size, normalized ratios K/Si* and H_2O^+/Si* are used to compare sediments with different grain sizes (Bouchez et al., 2012; Lupker et al., 2012, 2013). Especially the K/Si* and the K/Al ratios show an increase in weathering at starting around 10 Ma and reaching a maximum at 8 Ma, which corresponds well with the smectite-rich period, also starting at ~8 Ma (Figure 3.5). Thus two independent proxies show a change towards increased weathering at ~8 Ma. The fact that smectite is absent in the modern Trans-Himalayan rivers suggests that smectite in the Kameng section was formed secondarily by weathering, rather than being brought in with the paleo Brahmaputra at that time. Smectite-kaolinite rich assemblages persist in the Upper Siwaliks. The same change in clay mineralogy has been observed in other Siwalik sections, such as the Karnali and Surai Khola in western Nepal (Huyghe et al., 2005) as well as in the distal Bay of Bengal (France-Lanord et al., 1993; Galy et al., 1996) and was ascribed to environmental change. However, new results from Leg 354 in the Bengal Fan do not observe a change in clay mineralogy with time (France-Lanord et al., 2015).

Rocks younger than 3.5 Ma, mostly US sediments, show greater variations of their K/Si*,H_2O^+/Si*and Al/Si ratios from strongly weathered to less weathered signal. A strong weathering signal could potentially be biased by recycled Siwalik molasse. Upper Siwalik sediments might have partly experienced weathering twice, once before and once after they have been recycled. Modern river sediments are less weathered than the Siwaliks.

A trend towards stronger weathering can be observed from the Lower to the Upper Siwaliks (Figure 3.8). Confidence levels of the regression lines show a clear separation of the LS, which are less weathered, whereas MS and US overlap, but are clearly more weathered than the LS. Rocks in proximity to the Tippi Thrust differ strongly from all other data points (and are not taken into account for the regression lines) with a strong depletion of potassium. Overall a strengthening in the degree of weathering is observed upsection, but it remains hard to quantify the amount of change.

Location within the basin should be taken into account when interpreting trends in weathering proxy data, since much weathering occurs in the floodplain and therefore detritus in mountain front rivers are typically less weathered compared to detritus in rivers of the floodplain (Lupker et al., 2012). LS were deposited in the floodplain, whereas MS and US were deposited more proximal to the mountain front. We would therefore expect LS to be more weathered than younger sediments, if the signal was dominantly the result of position with respect to the floodplain. This is not the case; both the trend to increased weathering through time, and the significant shift at 10-8 Ma are not consistent with a hypothesis whereby the trend is due to position within the floodplain.

Quade and Cerling (1995) have suggested an intensification of the Indian Summer Monsoon at 7 Ma, from stable carbon-isotope records in paleosols from Pakistan and Nepal. Sanyal et al. (2010) defined several periods of strong monsoon intensity at 11, 6 and 3 Ma, by looking at isotope ratios of pedogenic clay and carbonates and clays of the Siwaliks in northwestern India. Clift et al. (2008) suggest a strong monsoon from 16 to 10 Ma with a gradual weakening afterwards between 10 and 3 Ma. Sediment accumulation rates and grain size in the distal Bengal fan decrease between 7 and 1 Ma (France-Lanord et al., 1993). Our data shows decreasing K/Al, also seen in the Bengal Fan by Clift et al. (2008). Together with enhanced smectite abundance, it suggests a stronger weathering regime starting at ~8 Ma, which could be linked to a more seasonal climate. An overall increase in weathering is observed in the Kameng section. Sediments younger than 3.5 Ma might partly be recycled Siwalik sediments, where the weathering signal is biased, but nevertheless they seem more weathered than the Lower Siwalik. However, that rather subtle change in weathering is probably linked to changes in the seasonality as well as to local change in climate and precipitation patterns.

Formation of the main Himalayan thrusts (MFT, MBT, MCT) could enhance erosion rates and have therefore an influence on weathering, but they remain hard to date and they are poorly studied in the eastern Himalaya. Robinson et al. (2003) suggest the onset of the MCT in early Miocene, older than the Kameng sediments. The onset of movement along the MBT in the eastern Himalaya is not well constrained, but as the MBT thrusts the LHS over the MS of 8 Ma, the onset of MBT motion must be after 8 Ma. The onset of movement along the local Tippi thrust and the MFT are at around 1 Ma (Chirouze et al., 2013), and do not show a major influence on weathering. There is no obvious correlation of the thrust with change in weathering, it is therefore most likely not influenced by tectonic changes. The source area exhumation rates in the Kameng are relatively constant (Chirouze et al., 2013), therefore the change in weathering in the east is likely climatically controlled and directly influenced by the moisture transport from the Bay of Bengal, although not sufficient trigger a change in vegetation in the eastern Himalaya as depicted by stable carbon isotope data (Vögeli et al., 2015).

3.6 Conclusion

The Himalayan sedimentary record of foreland basin sediments holds valuable information on the past weathering regime. Provenance and diagenesis have great influence on the sedimentary record, nevertheless by taking variations in provenance, diagenesis and grain size into account, weathering signals can be extracted from the geochemistry of the sedimentary record.

Heavy-mineral assemblages and petrography document repeated provenance changes, with deposits of local tributaries episodically interbedded with trunk-river deposits chiefly derived from the LHS and HHCS similar to the modern Kameng and Brahmaputra. Diagenetic dissolution of less stable minerals is most extensive in the lower part of the section. The residual assemblage does not necessarily represent the original assemblage, but the influence of diagenesis on major element composition appear minimal.

There is an overall increase in weathering from Lower Siwaliks to Mid/Upper Siwaliks. Clay mineral assemblages and major elements independently indicate a regime of enhanced weathering starting at ~8 Ma. Another change at ~3.5 Ma is probably linked to more Siwalik recycling or wetter climate. Changes in K/Al and K/Si* and the high smectite abundance since 8 Ma, do not entirely correlate with the changes in provenance; we therefore interpret them as an enhanced weathering signal, caused by more seasonal and overall drier climate. As the exhumation and accumulation rates stay more or less constant over the last 13 Ma, we suggest that the change in weathering environment thus originates from changes in climate. Changes in weathering are subtle, but they exist. Their impact on vegetation and other environmental parameters remains to be discussed and investigated with different methods, such as e.g. pollen analysis.

The Siwalik sedimentary record bears important proximal information on the paleo-climate. Compared to the marine record, foreland-basin sediments constitute a more proximal source, therefore the signal cannot be biased by transport far into the ocean. Multiproxy analyses are crucial for such studies. Clay mineralogy in combination with major element analysis can give new insight in to past weathering regimes, even though quantification of weathering rates remains challenging.

3.7 Supplementary Information

3.7.1 Heavy mineral and petrography: report

Heavy-mineral and sandstone petrography analyses were performed at the Department of Earth and Environmental Sciences at Università di Milano-Bicocca.

3.7.1.1 Method: Sand/stone petrography

A split aliquot of 16 Neogene sandstone and 1 modern sand samples were either impregnated with araldite or cut directly into standard thin sections, stained with alizarine red to distinguish dolomite and calcite, and analysed by counting 400 points under the petrographic microscope (Gazzi-Dickinson method; Ingersoll et al. (1984)). Sand and sandstones are classified according to their main components (Q = quartz; F = feldspars; L = lithic fragments), considered only, where is QFL higher than 10%. They are listed in order of abundance (e.g., in a feldspatho-quartzose sand Q > F > 10%QFL > L); an adjective reflecting the most common rock-fragment type may be added (e.g., metamorphiclastic).

Full quantitative information was collected on coarse-grained rock fragments, and metamorphic types were classified according to the protolith composition and metamorphic rank. Average rank of rock fragments in each sample is expressed by the Metamorphic Indices MI and MI*, which vary from 0 (in detritus shed by exclusively sedimentary and volcanic cover rocks) or from 100 (in very-low-rank detritus shed by exclusively very low-grade metamorphic rocks) to 500 (in very-high-rank detritus shed by exclusively high-grade basement rocks), respectively (Garzanti and Vezzoli, 2003). Very low- to low-rank metamorphic lithics, where the protolith can still be inferred, are subdivided into metasedimentary (Lms) and metavolcanic (Lmv) categories. Medium- to high-rank metamorphic lithics are subdivided into felsic (metapelite, metapsammite and metafelsite; Lmf) and mafic (metabasite; Lmb) categories.

3.7.1.2 Method: Heavy minerals

Although bulk-sample analyses represent the only correct option to accurately estimate percentages of detrital minerals, the presence of detrital grains with great differences in grain-size in relatively poorly-sorted alluvial sediments makes mounting and identification difficult (Mange and Maurer, 1992). Practical reasons thus may exist to set lower and upper size limits to the analysed fraction, which should be large enough to include most of the detrital population, in order to obtain a faithful characterization of the heavy-mineral suite (Garzanti et al., 2009). In this study we selected a very wide ($\geq 5\ \phi$ size window for analysis (> 15 μm or 15-500 μm), and thus considered 85% of the bulk sediment, cutting only the extreme fine (12±7%) and coarse (3±3%) tails of the size distribution. The split aliquot of the chosen size-window was separated by dry sieving. Thereafter, the dense fraction was separated by centrifuging in sodium polytungstate (density ~2900 kg/m^3) and recovered by partial freezing with liquid nitrogen. From each sample, 200 to 280 transparent detrital minerals were analysed in grain mounts by point counting under the petrographic microscope, the technique that allows us to obtain true volume percentages of each mineralogical species (Galehouse, 1971).

The ZTR index (sum of zircon, tourmaline and rutile over total transparent heavy minerals; (Hubert, 1962)) defines the “mineralogical stability” of the detrital assemblage. The “Hornblende Colour Index” HCI and “Metasedimentary Minerals Index” MMI (Andó et al., 2014) are used to estimate the average metamorphic grade of metaigneous and metasedimentary source rocks, respectively. They vary from 0, in detritus from greenschist-facies to lowermost amphibolite-facies rocks yielding exclusively blue/green amphibole and chloritoid, to 100 in detritus from granulite-facies rocks yielding exclusively brown hornblende and sillimanite. The “Sillimanite Index”, defined as the ratio between prismatic sillimanite and total (prismatic + fibrolitic) sillimanite grains, varies from 0, in detritus from upper amphibolite-facies metasediments, to 100, in detritus from granulite-facies metasediments. Heavy-mineral concentration was calculated as the volume percentage of total (HMC) and transparent (tHMC) heavy minerals (Garzanti and Andó, 2007). Heavy-mineral suites are defined as “extremely poor” (tHMC < 0.1), “very poor” (0.1 ≤ tHMC < 0.5), “poor” (0.5 ≤ tHMC < 1), “moderately poor” (1 ≤ tHMC < 2), “moderately rich” (2 ≤ tHMC < 5) or “rich” (5 ≤ tHMC < 10). Detrital components are listed in order of abundance throughout this report.

3.7.1.3 Results

Detrital modes (petrographic composition and heavy mineral assemblages) are described in stratigraphic order (oldest to youngest). Samples with similar detrital modes are grouped.

KM-13-5-c (13Ma): The sample KM-13-5-c is a virtually pure quartzarenite with few muscovite flakes and very low-rank metasedimentary rock fragments. The extremely poor heavy-mineral assemblage (tHMC 0.02) is zircon-dominated, with subordinate tourmaline, rutile, few epidote grains and rare apatite, titanite and monazite (ZTR 91). Detrital modes are most different from the modern Kameng sand and document recycling of quartzose sedimentary to very low-rank metasedimentary rocks.

Lower Siwaliks to lower Middle Siwaliks (12.3 to 8 Ma): The overlying succession (KM13-26, KM13-8, KM13-11, KM13-23 and KM13-1) includes feldspatho-quartzose and litho-feldspatho-quartzose metamorphiclastic sandstones with subequal plagioclase and K-feldspar (orthoclase, perthite, cross-hatched microcline; P/F 51±7), quartz-mica, schist, gneiss, metasandstone, phyllite, slate, granitoid, and dolostone rock fragments (MI* 289±21; MI 283±25). Micas are common, with biotite predominating over muscovite, which suggests contribution from amphibolite-facies schists of the HHCS. Very poor heavy-mineral assemblages (tHMC 0.3±0.2) are garnet-dominated with tourmaline, zircon, apatite, rutile and minor epidote (ZTR 36±10). Similarity with modern Kameng sand is moderate. Strong diagenetic overprint on the heavy-mineral assemblage makes precise provenance assessments difficult.

KM-13-2 (8.3 Ma): KM13-2 at the base of the section is a feldspatho-quartzose sandstone with K-feldspar prevailing over plagioclase (P/F 20), a few metasedimentary rock fragments (metasandstone, quartz-mica), and common biotite predominating over muscovite (MI* 192, MI 192). The poor heavy mineral assemblage (tHMC 0.5) includes mainly garnet with subordinate zircon, tourmaline, epidote, staurolite, rutile, and minor apatite, titanite, kyanite and andalusite (ZTR 42). Similarity with modern Kameng sand is moderate.

Middle Siwaliks (8.3 to 4 Ma): The overlying succession (KM13-30, KM13-4, KM13-29, KM13-17 and KM13-18) includes litho-feldspatho-quartzose metamorphiclastic sandstones, with plagioclase prevailing over K-feldspar (orthoclase, cross-hatched microcline, perthite; P/F 60±4), quartz-mica, schist, gneiss, metasandstone, phyllite, slate, granitoid, volcanic to metavolcanic (felsite, metarhyolite, metadacite, chloritoschist) and rare sedimentary (sandstone, chert, dolostone) rock fragments (MI* 265±38; MI 229±40). Micas are common, with biotite predominating over muscovite. Heavy-mineral assemblages range from moderately poor to rich (tHMC 3.8±3.5) and include mainly amphiboles (mostly blue-green to green hornblende; HCI 7±4), garnet, epidote, minor zircon, titanite, tourmaline, kyanite, apatite, chloritoid, staurolite, rutile, and locally sillimanite (ZTR 5±4). Detrital modes are most similar to modern Kameng sand.

KM13-28 (3.2 Ma): KM13-28 is a feldspatho-quartzose metamorphiclastic sandstone with K-feldspar (orthoclase, cross-hatched microcline, perthite) predominating over plagioclase (P/F 18), a few metamorphic (gneiss, schist, quartz-mica, metasandstone) and rare chert rock fragments (MI* 358; MI 358). Micas are very common, with biotite predominating over muscovite. The poor heavy mineral assemblage (tHMC 0.5) includes mainly amphiboles (mostly blue-green to green hornblende; HCI 14), epidote, garnet, tourmaline, kyanite, mostly fibrous sillimanite (Sillimanite Index 5), staurolite, zircon, minor rutile, titanite, chloritoid, and rare andalusite (ZTR 15). KM13-28c has a peculiar signature, with very low P/F ratio and low heavy-mineral concentration contrasting with the highest MI indices of all samples.

KM13-19 (2 Ma): KM13-19 is a quartzarenite with a few low-rank metamorphic rock fragments (schists, paragneisses), biotite, K-feldspar and minor plagioclase and arenaceous rock fragments (MI* 229; MI 200). The very poor heavy-mineral assemblage (tHMC 0.1) is dominated by zircon, tourmaline and rutile, with minor garnet, amphibole, epidote and titanite (ZTR 88). Detrital modes are very different from the modern Kameng sand.

KM13-20 (0.8 Ma): KM13-20 is a litho-feldspatho-quartzose metamorphiclastic sandstone with K-feldspar (orthoclase, cross-hatched microcline, perthite) prevailing over plagioclase (P/F 38), quartz-mica, metasandstone, slate, gneiss, schist, phyllite, granitoid and sedimentary (sandstone, shale) rock fragments (MI* 231; MI 203). Biotite predominates over muscovite. The moderately poor heavy mineral assemblage (tHMC 1.4) includes mainly garnet, amphiboles (mostly blue-green to green hornblende; HCI 10), epidote, tourmaline, kyanite, mainly fibrous sillimanite (Sillimanite Index 25), zircon, and minor staurolite, titanite, apatite, rutile and chloritoid (ZTR 9). Detrital modes are similar to modern Kameng sand, but the Q/F ratio is higher and the P/F ratio and heavy-mineral concentration lower.

Modern Kameng sand: Modern Kameng sand is litho-feldspatho-quartzose metamorphiclastic with subequal plagioclase and K-feldspar (orthoclase, cross-hatched microcline, perthite; P/F 50±0), quartz-mica, gneiss, schist, metasandstone, granitoid and rare sedimentary (shale, sandstone, dolostone) and volcanic rock fragments (MI* 273±20; MI 224±27). Micas are common, with biotite predominating over muscovite. Moderately rich heavy-mineral assemblages (tHMC 3.3±0.6) include abundant amphiboles (mostly blue-green to green-brown hornblende; HCI 17±4), garnet, subordinate epidote, and minor fibrous and prismatic sillimanite (Sillimanite Index 40), tourmaline, zircon, diopsidic clinopyroxene, titanite, kyanite, rutile, staurolite and apatite (ZTR 5±1). Provenance is largely from metamorphic Greater Himalayan units, with significant contribution from the Lesser Himalaya as revealed by relatively low metamorphic indices and abundance of microcline, and some recycling of Siwaliks molasse units accreted at the front of the orogen (Garzanti et al., 2004).

3.7.2 n-alkane analysis on the Kameng river section

3.7.2.1 Introduction

n-alkanes are biomarkers derived from leaf waxes of terrestrial plants and are the most widely used plant biomarkers (Bush and McInerney, 2013; Chibnall et al., 1934). n-alkanes are especially stable (at lower temperatures) and long-lived molecules, that can survive in the fossil record (Eglinton et al., 1991). Different long chain-length (number of carbon atoms) indicate different biological sources, whereas short-chained n-alkanes indicate thermal heating of the organic matter, with chain breakdown. Leaf waxes record the isotopic imprint of meteoric water (Sachse et al., 2012). Hydrogen isotopes of long-chained n-alkanes could therefore be a powerful tool to reconstruct paleo-hydrology (Sachse et al., 2006, 2012), whereas carbon isotopes could be used as an indicator of vegetation (Freeman and Colarusso, 2001). Carbon isotopes of n-alkanes have been investigated in Siwalik sediment in Nepal (Freeman and Colarusso, 2001). Here, we aim to measure carbon and hydrogen isotopes in n-alkanes in the Kameng section in order to reconstruct paleohydrology in the eastern Himalaya.

3.7.2.2 Method

With the aim to analyze hydrogen and carbon isotopes on n-alkanes, organic matter was extracted from approximately 100g of sample. Samples with different organic matter content and grainsize were chosen to investigate potential variations in the amount of n-alkanes within different samples. Dry samples were ground with an agate mortar. A total of two times ~50 g of powder per sample was used for the total lipid extraction (TLE). In order to avoid clumping of the sample during extraction, the powder was mixed with diatomaceous earth or combusted quartz sand. The TLE was extracted with a Dionex ASE 550 Accelerated Solvent Extractor. For the extraction 9:1 Dichlormethane (DCM): Methanol (MeOH) solvent was used. After extraction, the TLE was evaporated by using a Turbovap with dry N2 and then transferred into Gas chromatography (GC) vials. While extracting the TLE, the Dionex ASE 550 had various problems showing errors. Samples were reloaded several times in order to extract as much lipids as possible.

The TLE of eleven samples was analyzed on the Agilent Technologies GC-MSD/FID 7890A Gas Chromatography-Mass Selective Detector system. In order to analyze fatty acids on the GC-MS the TLE was derivatized, therefore 50μl of BSTFA (N,O-Bis(trimethylsilyl)trifluoroacetamide) was added to each sample, the samples were heated for 60 minutes at 75°C in closed GC vials. 20.5μg of Androstane for the first six and 20.7μg of Androstanol for the other five samples was added as an internal standard. The first six samples were analyzed for 37 min, whereas the other five were measured for over a 67 min timespan. All samples were compared to a standard homology series of n-alkanes from C12 to C40.

The n-alkane fraction of 27 samples was analyzed. The TLE was dried down by using dry N2 gas. Afterwards it was separated into two fractions, the hydrocarbon fraction and the fatty acid fraction, by using silica gel columns. Columns were cleaned by rinsing with first acetone, DCM and hexane and afterwards dried for 3-4 hours at 50°C. Before adding the sample, columns were rinsed with hexane.

The alkane fraction was separated by rinsing the sample through the column with approximately 7 ml of hexane. The fatty acids fraction was separated by rinsing the remaining sample with 9:1 DCM: MeOH. Afterwards samples were dried down in the Turbovap.

Between 4.1μg and 10.25μg of Androstane as a standard was added after column separation, depending on the amount of total lipids in the sample. Samples were transferred into inserts as low amounts of alkanes are expected in old sediments.

The unpolar fraction, containing n-alkanes, was quantified with an Agilent GC MSD (Agilent 5975C MSD, Agilent 7890A GC with Agilent J&W HP-5ms column, 30 m x 0.25 mm x 0.25 μm film) equipped with an additional Flame Ionization Detector. Knowing the amount of standard and sample, a quantitative analysis was performed by analyzing the intensity of the peaks. By running a standard homology series of n-alkanes from C12 to C40, different compounds with different chain lengths were determined. All analyses were conducted at the laboratory of the Institut für Erd- und Umweltwissenschaften at the University of Potsdam. The Carbon Preference Index (CPI) and Average Chain Length (ACL) were calculated as follows (Bush and McInerney, 2013).

CPI= (∑odd(C21-33)+∑odd(c23-25))/(2∑even(c22-34))

ACL= (∑(Cn×n))/(∑(Cn))

In sediments CPI is used as an indicator of thermal maturity of the rocks and as a source indicator. ACL indicates different biological source of n-alkanes (Eglinton and Hamilton, 1967).

3.7.2.3 Results

Overall the samples contained very little alkanes, and especially long chained alkanes were rare. CPI values vary from 0.603 to 5.77. Only 8 samples have a CPI over 1, which means an even over odd carbon number preference (Figure 3.10). Considering n-alkanes with C21-C33, the ACL varies from 25 to 29.69. ACL (C21-C33) is 26.34 (Figure 3.11). CPI and ACL only show a slight correlation, of higher CPI with higher ACL. The total content of alkanes is mostly below 1μg/g, the highest content is 2.7μg/g. Only 3 samples have a reasonable amount of long-chained (C27-C31) n-alkanes and CPI>1. CPI < 1 indicates chain breakdown, where long-chained n-alkanes break down to short-chained. This is can happen due to thermal overprinting, when the sample has resided in the oil window (60-100°C). Hydrogen and carbon isotopes were not measured, due to the too low amount of n-alkanes and CPI values < 1 (thermal overprinting), which destroys the isotopic signal.

3.7.2.4 Discussion

CPI values below one indicate thermal overprint, where long-chained alkanes (C27-C31), which are produced by plants in leaf waxes, break down to short chains (C18-C25) (Kolattukudy, 1976). Only the youngest four samples in the Kameng river section, including a modern river sediment, show values

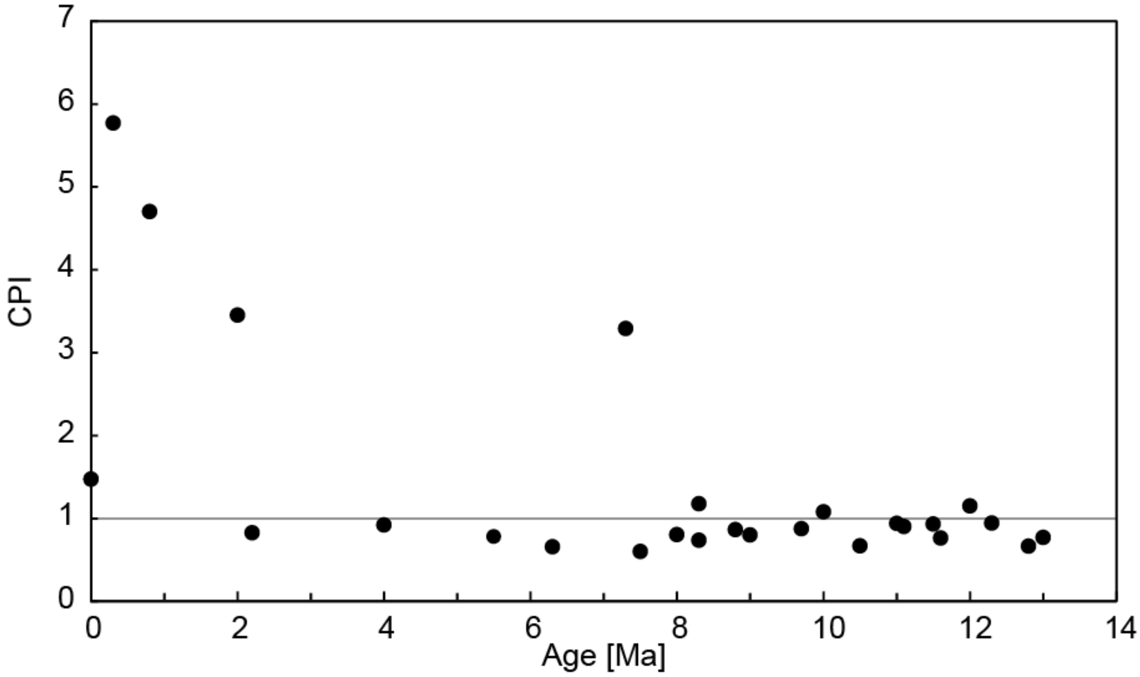

Figure 3.10: Carbon Preference Index (CPI). CPI > 1 shows an odd over even numbered chain length preference; indicating original leaf waxes.

above one. Older samples show all values below or very close to one, with one exception (KM13-3, CPI = 3.29). Thermal overprinting is confirmed by partially reset apatite fission track ages in samples older than 8 Ma at a stratigraphic depth of 4000m (Chirouze et al., 2013). CPI can be used as a temperature indicator for diagenesis, with CPI<1 indicating temperature of the oil window (60-120°C). Isotopic analyses would have been only possible on samples with a CPI>1, these samples do not contain enough n-alkanes to be analyzed for hydrogen or carbon isotopes. Therefore we decided not to proceed with analyzing hydrogen isotopes. Samples might contain more fatty acids, but as they are also affected by thermal overprinting, they are also dismissed for further analyses. Carbon isotopes are less sensitive to thermal overprinting and could be measured. Freeman and Colarusso (2001) measuredδ^{13}C in n-alkanes in Siwalik sediments in Nepal to reconstruct paleo-vegetation and found a shift towards more positive values, as it has been documented in studies on bulk organic carbon (Quade and Cerling, 1995; Sanyal et al., 2004; Vögeli et al., subb, amongst others).

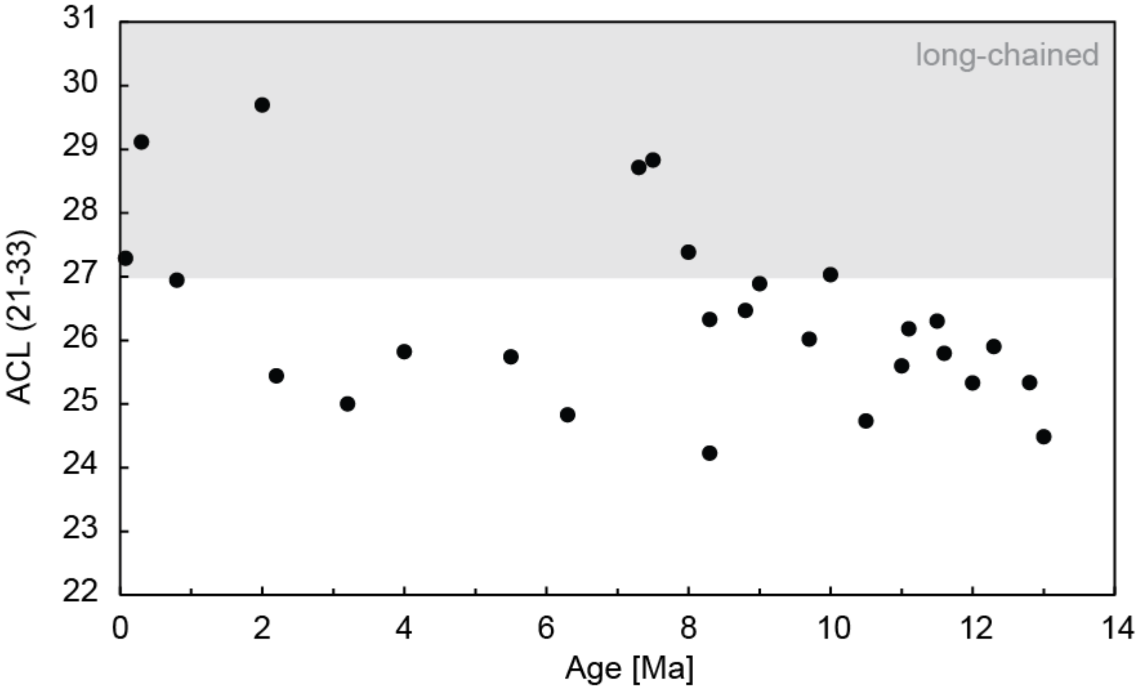

Figure 3.11: Average chain length (ACL) C21-C33, indicated in grey are long-chained n-alkanes, which are directly produced by plants in leaf waxes; in white are short-chained alkanes produced by thermal cracking.

3.8 Appendices

Appendix 3.1: Table of heavy minerals and petrography

Table 3.1: Heavy minerals and petrography

Sample	Age [Ma]	Q	KF	P	Lv	Lc	Lp	Lch	Lms	Lmv	Lmf	Lmb	Lu	ms	bt	HM	total
Kameng sand	0	51	12	11	0.32	0.63	1.3	0	11	1.3	3.8	0	0	1.9	4.4	0.63	100
Kameng sand	0	55	12	12	0.82	0.27	2.2	0	1.6	0	4.4	0	0	2.3	6.7	2.5	100
KM13-20-c	0.8	69	8.2	4.9	0	0	1.4	0	5.7	0.54	4.9	0	0	1.5	3.7	0.27	100
KM13-19-c	2	96	1.1	0.28	0	0	0	0	0.55	0	0.55	0	0	0	1.7	0	100
KM13-28-c	3.2	68	11	2.4	0	0	0	0.27	0.82	0	1.9	0	0	3.7	11	0.54	100
KM13-18	4	57	11	12	0.54	0	1.4	0	4.3	0.81	2.8	0.14	0	1.9	4.3	3.3	100
KM13-17	5.5	57	8.3	14	0	0	0.28	0.55	2.2	0.83	4.7	0	0	0.69	4	7.7	100
KM13-29	6.3	66	6.7	9.8	0.55	0	0.55	0.55	2.8	3	2.2	0	0	1.1	3.6	3.3	100
KM13-4	6.8	60	6.4	12	0.51	0.26	0.51	0	1.5	1	4.7	0.13	0	3.7	7.5	2	100
KM13-30-c	7.5	71	4.8	7	0.8	0	1.9	0.27	2.4	0.53	4	0.27	0	0.8	1.9	4.3	100
KM13-2	8.3	80	7.8	1.9	0	0	0	0	1.4	0.28	0.83	0	0	0.55	5	2.2	100
KM13-1	8.6	70	5.3	7.8	0	1.5	0.25	0	3	0	4	0	0	1.1	5.7	1.5	100
KM13-23-c	9.7	72	7.6	7.6	0.26	0	0.26	0	0.78	0.52	5.2	0	0	2.1	3.1	0.26	100
KM13-11-c	10.5	72	5.6	4.3	0	2.3	0.51	0	1.3	1.8	4.6	0	0	1.8	5.6	0.51	100
KM13-8	12	75	6.5	5.3	0	0	0	0	0.5	0.25	4.5	0	0	1.5	6	0.75	100
KM13-26-c	12.3	73	6.2	8	0	0	0	0	0.77	0.26	3.1	0	0	3.6	3.9	1.3	100
KM13-5-c	13	99	0	0	0	0	0	0	0.27	0	0	0	0	0.54	0	0	100

Table 3.1: Heavy minerals and petrography (cont.)

Sample	Age [Ma]	MI*	MI	Qp/Q	P/F	Q/F	bt/ms	Q	F	L	Lm	Lv	Ls
Kameng sand	0	260	240	22	49	2.2	2.3	55	25	20	54	5.1	41
Kameng sand	0	290	200	16	50	2.3	2.9	62	27	10	56	8.8	35
KM13-20-c	0.8	230	200	16	38	5.3	2.5	73	14	13	64	2.2	34
KM13-19-c	2	230	200	12	20	70	n.d.	97	1.4	1.1	n.d.	n.d.	n.d.
KM13-28-c	3.2	360	360	9.6	18	5	3.1	80	16	3.5	n.d.	n.d.	n.d.
KM13-18	4	250	210	22	54	2.5	2.3	63	25	11	55	9.5	35
KM13-17	5.5	280	270	12	63	2.6	5.8	65	25	9.8	73	4.8	23
KM13-29	6.3	210	180	26	59	4	3.3	72	18	11	53	21	26
KM13-4	6.8	300	270	20	65	3.3	2	69	21	10	71	12	18
KM13-30-c	7.5	280	210	13	59	6	2.3	76	13	11	57	11	33
KM13-2	8.3	190	190	7.4	20	8.3	9	87	11	2.7	n.d.	n.d.	n.d.
KM13-1	8.6	290	280	42	60	5.3	5	76	14	9.6	63	0	37
KM13-23-c	9.7	310	300	36	50	4.8	1.5	77	16	7.5	83	7.4	9.3
KM13-11-c	10.5	260	240	29	44	7.3	3.1	78	11	11	59	8.5	33
KM13-8	12	290	290	36	45	6.3	4	81	13	5.8	93	2.4	4.8
KM13-26-c	12.3	310	310	32	56	5.2	1.1	80	15	4.5	n.d.	n.d.	n.d.
KM13-5-c	13	n.d.	0	24	n.d.	n.d.	0	100	0	0.27	n.d.	n.d.	n.d.

Table 3.1: Heavy minerals and petrography (cont.)

Sample Sample	Age] [Ma]	HM %	HM% . transp.	zircon zircon	tourmaline tourmaline	rutile rutile	Ti Oxides	titanite	apatite	epidote	garnet
Kameng sand	0	4.4	3.7	1.4	3.8	0.47	0	0.94	0	7	36
Kameng sand	0	6	2.9	1.5	1.5	1.5	0	1.5	0.98	12	21
KM13-20-c	0.8	3.2	1.4	3.3	4.8	0.96	0	0.96	0.96	9.1	42
KM13-19-c	2	0.43	0.14	44	29	16	1	0.5	0	2	5
KM13-28-c	3.2	2.3	0.49	5.4	7.9	1.8	0	1.4	0	17	14
KM13-18	4	4.3	1.6	1.4	2.3	0	0	1.4	0.46	26	40
KM13-17	5.5	11	8.5	0.42	0.85	0	0	1.3	1.3	14	32
KM13-29	6.3	2.6	1.1	5.4	1.5	1.5	0	3.4	3	37	24
KM13-4	6.8	3.7	1.2	4.9	3.4	0.49	0	2.5	2.9	29	20
KM13-30-c	7.5	7.4	6.4	0	0.49	0.49	0	0.98	0	20	33
KM13-2	8.3	1.2	0.49	19	19	4.6	0.46	0.93	1.4	9.7	39
KM13-1	8.6	2.2	0.52	6.4	15	2	0.98	0.49	6.4	0.49	68
KM13-23-c	9.7	2	0.084	16	26	6.4	0	0	2.9	0.98	48
KM13-11-c	10.5	2.2	0.5	20	12	3.4	0.99	0.49	6.4	0	57
KM13-8	12	1	0.23	15	24	5.8	0	0.48	9.1	0	45
KM13-26-c	12.3	1.2	0.37	6.7	22	6.2	0.48	0	3.8	0.48	60
KM13-5-c	13	0.049	0.018	61	17	12	5.7	0.47	0.94	1.9	0

Table 3.1: Heavy minerals and petrography (cont.)

Sample	Age [Ma]	chloritoid	staurolite	kyanite	sillimanite	amphibole	clinopyroxene	other tHM	Total	ZTR	HCI
Kameng sand	0	0	0.94	0.47	0.47	46	1.9	0	100	5.6	13
Kameng sand	0	0	0.49	1.5	4.9	53	0.98	0	100	4.4	20
KM13-20-c	0.8	0.48	0.96	3.8	3.8	29	0	0	100	9.1	10
KM13-19-c	2	0	0	0	0	3.5	0	0	100	88	n.d.
KM13-28-c	3.2	0.72	5.8	7.6	7.2	31	0	0.36	100	15	14
KM13-18	4	0.91	0	1.4	0	26	0	0	100	3.7	3.8
KM13-17	5.5	0	0.42	1.7	0	48	0	0	100	1.3	10
KM13-29	6.3	2	0.49	3	0	19	0	0	100	8.4	2.4
KM13-4	6.8	2.9	1.5	1.5	0	31	0	0	100	8.8	4.5
KM13-30-c	7.5	0	1.5	0.49	0.98	42	0	0	100	0.98	12
KM13-2	8.3	0	5.6	0.93	0	0	0	0.46	100	42	n.d.
KM13-1	8.6	0	0	0	0	0	0	0	100	24	n.d.
KM13-23-c	9.7	0	0	0	0	0	0	0	100	49	n.d.
KM13-11-c	10.5	0	0	0	0	0	0	0	100	35	n.d.
KM13-8	12	0	0	0	0	0	0	0	100	45	n.d.
KM13-26-c	12.3	0	0	0	0	0	0	0	100	35	n.d.
KM13-5-c	13	0	0	0	0	0	0.47	100	91	n.d.	

Table 3.1: Heavy minerals and petrography (cont.)

Sample	Age [Ma]	MMI	Sil.I.	trans-parent [%]	opaque [%]	Fe oxides [%]	Ti oxides [%]	turbid [%]	rock fragments [%]	soils & n.n. [%]	chlorite [%]	biotite [%]	carbonates [%]	light minerals [%]	Total [%]
Kameng sand	0	44	n.d.	85	6.4	0	0	0	0	8.8	0	0	0	0	100
Kameng sand	0	79	40	49	0.77	0.39	0.39	0	2.7	3.5	3.9	40	0	0	100
KM13-20-c	0.8	62	25	44	1.5	0	0.26	0	2.3	7.5	8.2	36	0	0	100
KM13-19-c	2	n.d.	n.d.	34	1.3	0.67	6.1	0	2.9	18	20	18	0	0	100
KM13-28-c	3.2	51	5	22	1.4	0	0	0	0.97	2.9	3.9	69	0	0	100
KM13-18	4	40	n.d.	37	1.7	0	0	0	0.69	8.6	4.8	44	2.4	0	100
KM13-17	5.5	60	n.d.	77	0.97	0	0.32	0	1.9	7.1	3.6	9.1	0	0.32	100
KM13-29	6.3	39	n.d.	41	0.87	0	0	0	0.44	6.1	1.3	45	3.9	0.44	100
KM13-4	6.8	25	n.d.	34	1.4	0.69	0.69	0.69	0	2.4	3.8	56	0.34	0	100
KM13-30-c	7.5	53	n.d.	87	2.6	0	0.43	0	0	3.4	0	6.8	0	0	100
KM13-2	8.3	38	n.d.	40	3.2	0	0.35	0	0.7	11	7.7	37	0	0.35	100
KM13-1	8.6	n.d.	n.d.	23	1.6	0	0	0	1.6	0	2.7	70	0	1.1	100
KM13-23-c	9.7	n.d.	n.d.	4.2	0	0	0	0	0	0	2.6	93	0	0.52	100
KM13-11-c	10.5	n.d.	n.d.	23	1.5	0	2	0	0	0.99	7.4	65	0	0	100
KM13-8	12	n.d.	n.d.	22	0	0	2.4	0	0	2.4	5.3	67	0	0	100
KM13-26-c	12.3	n.d.	n.d.	30	0.98	0	0.49	0	0	5.4	9.3	54	0	0	100
KM13-5-c	13	n.d.	n.d.	37	2.7	0	57	0	0.45	0.91	1.4	0	0	0	100

Bulk-petrography and heavy-mineral data: Q= quartz; F= feldspars (KF= K-feldspar; P= plagioclase); L= aphanitic lithic grains (Lv= volcanic and subvolcanic; Lc= carbonate; Lp= shale/siltstone; Lch= chert; Lms= low-rank metasedimentary; Lmv= low-rank metavolcanic; Lmf= medium-rank and high-rank felsic metamorphic; Lmb= medium-rank and high-rank metabasite; Lu= ultramafic); ms= muscovite; bt= biotite; HM= heavy minerals. MI* and MI= Metamorphic Indices (Garzanti and Vezzoli, 2003). HM%= weight percent of the heavy-mineral fraction; ZTR= (zircon + tourmaline + rutile) / total transparent heavy minerals (Hubert, 1962); HCI= Hornblende Color Index, MMI= Metasedimentary Minerals Index and Sillimanite Index after Garzanti and Andò (2007) and Andò et al. (2014); tHM= transparent heavy minerals.

Appendix 3.2: Table of major elements

Table 3.2: Major Element concentrations

Sample	Grain-size	Age [Ma]	Lith. Unit	SiO_2	TiO_2	Al_2O_3	Fe_2O_3 t	MnO	MgO	CaO	Na_2O	K_2O	P_2O_5	LOI	H_2O^+	K/Al [mol:mol]	K/Si* [norm.]	H_2O^+/Si* [norm.]
Kameng Down c	c	0	modern	79.14	0.4	9.97	3.04	0.05	0.88	0.9	1.36	2.49	0.07	2.05		0.27	0.056	
Kameng Down f	f	0	modern	79.97	0.46	8.41	3.16	0.07	0.9	1	1.35	2.34	0.11	1.73	1.21	0.3	0.06	0.2259
Holocene Terrasse	c	0.01		74.74	0.6	12.46	3.81	0.04	0.78	0.1	0.49	2.42	0.03	5.17	3.52	0.21	0.045	0.3592
KM13-22	f	0.3	US	71.23	0.51	15.54	3.39	0.04	0.98	n.d.	1.31	2.58	0.02	5.72		0.18	0.041	
KM13-21-carbon	c	0.5	US	77.86	0.43	8.4	2.85	0.04	0.87	0.28	0.58	1.82	0.02	6.66		0.23	0.046	
KM13-20-c	c	0.8	US	81.4	0.34	9.37	2.42	0.04	0.66	n.d.	0.98	2.62	0.07	2.23	1.5	0.3	0.062	0.237
KM13-20-f	f	0.8	US	63.74	0.73	14.94	6.13	0.09	1.99	0.44	0.85	3.45	n.d.	6.88	3.71	0.25	0.057	0.2973
KM13-19-c	c	2	US	88.99	0.32	6.12	1.77	0.01	0.4	n.d.	0.22	1.3	0.02	2.7		0.23	0.037	
KM13-19-c-nan	c	2	US	87.31	0.36	6.4	1.83	0.01	0.4	0.05	0.09	1.52	n.d.	2.51		0.26	0.044	
KM13-19-f	f	2	US	67.1	0.69	16.65	4.3	0.03	1.04	0.08	0.31	2.65	0.04	7.71		0.17	0.04	
KM13-19-f-nan	f	2	US	65.15	0.74	17.21	4.45	0.03	1.03	0.17	0.21	3.16	0.04	7.71		0.2	0.046	
KM13-27	c	2.2	US	81.13	0.33	9.68	2.62	0.05	0.71	0.01	0.94	2.32	0.1	2.19		0.26	0.052	
KM13-28-c	c	3.2	MS	80.78	0.35	8.71	2.52	0.02	0.66	n.d.	0.66	2.38	0.02	2.94	2.04	0.3	0.059	0.3361
KM13-28-c-nan	c	3.2	MS	79.9	0.36	9.89	2.65	0.03	0.7	0.26	0.73	2.75	n.d.	2.71		0.3	0.062	
KM13-28-f	f	3.2	MS	71.78	0.66	12.91	4.89	0.04	1.11	n.d.	0.38	2.6	0.03	5.23	3.77	0.22	0.048	0.3664
KM13-28-f-nan	f	3.2	MS	70.75	0.69	13.72	5.2	0.04	1.17	0.21	0.36	2.99	n.d.	5.01		0.24	0.052	
KM13-18 bis	c	4	MS	60.93	0.34	8.96	3.66	1.05	0.96	10.96	1.43	1.86	0.1	9.56	1.43	0.22	0.047	0.215
KAM6	c	5.4	MS	79.81	0.27	9.85	1.96	0.02	0.59	1.03	1.66	2.12	0.05	1.78		0.23	0.047	
KM13-17 bis	c	5.5	MS	79.12	0.56	10.51	3.62	0.1	1.11	2.02	1.78	1.83	0.09	1.59	1.22	0.19	0.038	0.1692
KAM15	c	5.6	MS	78.33	0.32	10.01	2.64	0.04	0.87	1.28	1.73	1.99	0.05	2.23		0.22	0.044	
KM13-29	c	6.3	MS	65.68	0.32	8.29	2.34	0.82	0.82	11.06	1.15	1.67	n.d.	9.63		0.22	0.044	
KM13-4	c	6.8	MS	73.86	0.52	11.23	4.6	0.09	1.5	1.05	1.35	2.36	0.25	3.88		0.23	0.048	
KM13-4-nan	c	6.8	MS	73.23	0.53	11.04	4.87	0.09	1.54	1.34	1.33	2.47	0.26	3.51		0.24	0.051	
KM13-4-nodule	f	6.8	MS	69.66	0.66	15.67	4.11	0.04	1.04	0.25	0.23	2.69	0.03	6.56		0.19	0.042	
KM13-3	f	7.3	MS	63.91	0.73	17.99	4.86	0.04	1.29	0.22	0.35	3.1	0.04	7.05		0.19	0.044	
KM13-30-c	c	7.5	MS	84.84	0.3	8.17	2.42	0.06	0.61	0.93	1.08	1.72	n.d.	1.76	1.23	0.23	0.042	0.2441
KM13-30-f	f	7.5	MS	62.35	0.74	19.42	4.86	0.04	1.32	n.d.	0.29	3.15	0.04	9.59	5.41	0.18	0.042	0.323
KM13-30-nodule	f	7.5	MS	68.61	0.68	15.67	4.38	0.06	1.05	0.27	0.32	2.67	0.03	7.49		0.18	0.042	
KM13-16-c	c	8	MS	67.33	0.76	15.41	6.28	0.06	1.74	n.d.	0.93	3.56	0.05	3.62		0.25	0.057	
KM13-16-c-DUP	c	8	MS	68.14	0.74	14.47	6.25	0.06	1.75	n.d.	0.84	3.39	0.06	3.62		0.25	0.057	
KM13-16-f-bis	f	8	MS	61.17	0.84	20.54	5.15	0.04	1.46	n.d.	0.38	3.65	0.03	6.74		0.19	0.046	
KM13-15-c	c	8.3	MS	88.92	0.29	4.89	1.7	0.03	0.34	n.d.	0.29	1.08	0.03	2.01	1.44	0.24	0.033	0.5116
KM13-15-f	f	8.3	MS	72.12	0.62	14.22	4.65	0.04	1.02	n.d.	0.5	2.73	0.02	3.43	3.68	0.21	0.046	0.3193
KM13-2	c	8.3	MS	83.64	0.4	7.94	1.8	0.02	0.51	n.d.	0.29	2.05	0.03	3.32		0.28	0.054	
KM13-1	c	8.6	MS	80.69	0.35	8.57	4.31	0.07	1.37	0.37	0.95	2.14	0.07	2.41		0.27	0.053	
KM13-14-f	f	8.8	MS	69.66	0.66	13.73	4.91	0.05	1.66	0.25	0.73	2.9	0.04	4.39		0.23	0.051	
KM13-13-c	c	9	MS	79	0.5	9.3	3.33	0.09	0.9	0.34	0.95	1.99	0.1	2.63		0.23	0.046	
KM13-13-c-nan	c	9	MS	78.78	0.55	9.97	3.58	0.09	0.93	0.43	1.02	2.22	0.11	2.83		0.24	0.049	
KM13-13-f	f	9	MS	64.19	0.72	19.06	5.3	0.06	1.75	n.d.	0.86	3.64	0.04	5.63		0.21	0.049	
KM13-13-f-nan	f	9	MS	63.48	0.71	17.63	5.5	0.06	1.73	0.31	0.82	3.87	0.04	5.54		0.24	0.055	
KM13-23-c	c	9.7	MS	80.73	0.32	8.91	3.96	0.05	0.91	0.17	0.87	2.16	n.d.	2.48	2.01	0.26	0.052	0.323
KM13-23-c-DUP	c	9.7	MS	80.86	0.32	8.95	3.97	0.05	0.91	0.16	0.91	2.11	0.08	2.48	0	0.26	0.051	
KM13-23-f	f	9.7	MS	73.9	0.55	10.98	4.2	0.06	1.56	0.32	0.9	2.54	0.08	3.52	2.45	0.25	0.053	0.2937
KM13-12-c	c	10	MS	82.89	0.25	8.52	2.75	0.04	0.76	0.18	1.11	2	0.06	2.51		0.25	0.049	
KM13-12-f bis	f	10	MS	55.16	0.78	21.93	7.26	0.07	2.44	n.d.	0.45	4.69	0.07	7.01		0.23	0.055	

Table 3.2: Major Element concentrations (cont.)

Sample	Grain-size	Age [Ma]	Lith. Unit	SiO_2	TiO_2	Al_2O_3	Fe_2O_3 t	MnO	MgO	CaO	Na_2O	K_2O	P_2O_5	LOI	H_2O^+	K/Al [mol:mol]	K/Si* [norm.]	H_2O^+/Si* [norm.]
KM13-11-c	c	10.5	LS	79.52	0.45	9.18	3.16	0.07	1.24	0.69	1	2.22	0.08	3.32		0.26	0.053	
KM13-11-c-DUP	c	10.5	LS	79.37	0.46	9.27	3.16	0.07	1.24	0.68	1.01	2.22	0.08	3.32		0.26	0.052	
KM13-11-f	f	10.5	LS	76.88	0.45	9.17	3.66	0.08	1.34	0.89	0.89	2.13	0.08	3.37		0.25	0.051	
KM13-10-c	c	11	LS	77.17	0.57	9.23	4.19	0.05	1.08	n.d.	0.82	2.21	0.03	3.81	2.59	0.26	0.052	0.3834
KM13-10-f	f	11	LS	57.16	0.72	19.85	6.96	0.06	3.03	0.66	0.73	4.58	0.11	6.44	4.56	0.25	0.059	0.2584
KM13-25	f	11.1	LS	54.56	0.72	15.56	5.69	0.16	3.58	5.86	0.72	3.5	0.1	10.34		0.24	0.056	
KM13-9	c	11.1	LS	66.93	0.48	9.83	3.43	0.06	2.32	5.52	0.94	2.18	0.09	7.66		0.24	0.051	
KM13-7-c	c	11.6	LS	73.55	0.3	7.48	2.24	0.14	1.17	5.86	0.87	1.69	0.07	5.63		0.24	0.047	
KM13-7-f	f	11.6	LS	68.72	0.78	15.74	4.98	0.04	1.91	n.d.	0.78	3.53	0.02	4.49		0.24	0.055	
KM13-8	c	12	LS	81.83	0.45	8.4	3.36	0.04	0.86	n.d.	1.01	1.98	0.08	2.41		0.26	0.05	
KM13-26-c	c	12.3	LS	83.2	0.39	7.33	2.49	0.04	0.57	n.d.	0.77	1.71	0.08	1.98		0.25	0.046	
KM13-26-f	f	12.3	LS	66.43	0.75	15.42	7.34	0.22	1.39	n.d.	0.79	3.13	0.2	5.08		0.22	0.05	
KM13-6-c-bis	c	12.8	LS	82.64	0.41	8.25	2.84	0.06	0.8	n.d.	0.96	1.99	n.d.	1.97	1.43	0.26	0.05	0.2687
KM13-6-c-nan	c	12.8	LS	82.31	0.46	8.13	3.05	0.06	0.81	0.47	0.94	2.13	0.1	1.92		0.28	0.055	
KM13-6-f	f	12.8	LS	66.33	0.65	14.6	5.91	0.06	1.6	0.07	0.79	3.17	0.05	4.05	3.88	0.23	0.053	0.3219
KM13-6-f-nan	f	12.8	LS	66.13	0.71	16.07	6.21	0.06	1.65	0.17	0.71	3.78	0.06	4.08		0.25	0.058	
KM13-6-nodule	f	12.8	LS	66.37	0.69	13.62	4.68	0.04	1.41	0.06	0.64	3.12	0.02	5.2		0.25	0.055	
KM13-5-c	c	13	LS	87.1	0.27	9.74	0.12	n.d.	n.d.	n.d.	0.08	0.14	0.02	4		0.02	-0.002	
KM13-5-f	f	13	LS	68.52	1.11	22.42	0.34	n.d.	0.02	n.d.	0.14	0.39	0.09	8.53		0.02	0.008	

nan: measured in Nancy

Table 3.3: International Standards and Average Accuracy of the Analysis

Standards [measured]	SiO_2	TiO_2	Al_2O_3	Fe_2O_3 t	MnO	MgO	CaO	Na_2O	K_2O	P_2O_5
JSd1	66.41	0.65	14.76	4.95	0.1	1.8	2.93	2.62	2.15	0.12
JSd2	61.35	0.6	12.5	11.46	0.12	2.75	3.72	2.38	1.12	0.11
BCR-2	54.05	2.27	13.5	13.82	0.2	3.6	7.32	3.07	1.78	0.35
RGM	74.69	0.27	13.59	1.84	0.04	0.27	0.98	4.01	4.12	0.04
BEN	38.62	2.63	9.83	12.65	0.2	13.17	13.75	3.13	1.41	1.06
Devation from international Std. [%]	SiO_2	TiO_2	Al_2O_3	Fe_2O_3 t	MnO	MgO	CaO	Na_2O	K_2O	P_2O_5
JSd1	0.28	-1.87	-0.42	2.24	-5.36	0.62	3.51	4.01	1.27	-2.25
JSd2	-0.9	1.94	-1.62	2.1	-1.43	-0.81	-1.56	2.4	3.08	3.26
BCR-2	0.1	-0.3	0.03	-0.13	-0.57	-0.35	-2.78	2.89	0.7	0.59
RGM	-1.66	-1.36	0.98	1.24	1.02	1.34	17.72	1.4	4.47	13.74
BEN	-1.08	-0.72	2.41	1.47	0.78	-0.14	0.84	1.75	-1.1	-1.23
Average accuracy per element [%]	0.8	1.24	1.09	1.43	1.83	0.65	5.28	2.49	2.13	4.21
Average accuracy [%]	2.12									

Table 3.4: Normalization for K/Si and H_2O^+/Si

Grainsize Normalization Kameng section

coarse endmember Al/Si	coarse endmember K/Si	coarse endmember H_2O^+/Si	average Al/Si
0.0	0.0082	-0.0491	0.22
K/Si linear regression y=0.1903x+0.0082			
H_2O^+/Si linear regressiony=1.4615x-0.0491			

linear regression from average fine-grained and average coarse-grained

Appendix 3.3: XRD diffractogram of clay mineralogy

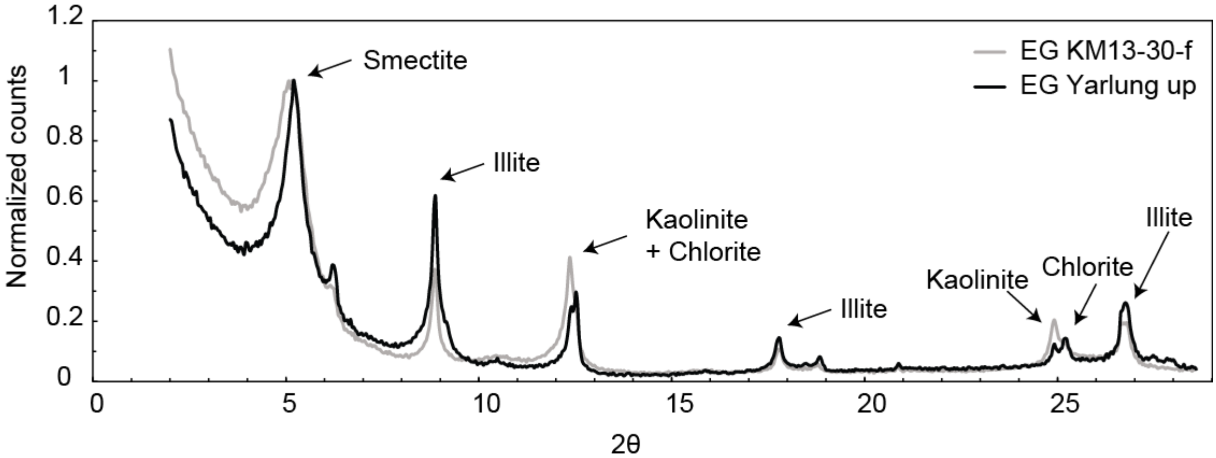

Figure 3.12: X-ray diffractogramm of the KM13-30-f sample (7.5 Ma) and the modern Yarlung up sample, showing slightly different smectites.

Chapter 4

Weathering in the Himalayas, an East-West comparison: Indications from major elements and clay mineralogy

in preparation to be submitted to Palaleogeography, Palaeoclimatology, Palaeoecology

Abtract

It is important to study past weathering regimes to better understand the influence of climate on weathering, erosion and runoff. The Himalayan foreland basin contains a record of tectonics and paleoclimate since Miocene times in the pre-Siwalik and Siwalik Groups. Spanning the entire mountain range, the Siwalik Group allows studies to directly compare the western and eastern Himalaya within similar sedimentary settings. In this study, we use major elements and clay mineralogy to reconstruct weathering regime since Miocene times. We studied previously dated pre-Siwalik and Siwalik sections in the western (Joginder Nagar, Jawalamukhi and Haripur Kolar sections) and eastern (Kameng section) Himalaya in order to constrain variations in weathering regimes along strike in the Himalaya. The compilation of the three sections in the west makes one of the longest continuous sedimentary records in the Himalaya, spanning over 20 Ma. K/Al ratio is used as a weathering proxy, showing a trend toward stronger weathering over time in the west and the east, but with sediments in the western Himalaya generally more weathered, than in the east. Clay minerals and major elements indicate lateral variations in weathering. More weathering in the west is linked to a more seasonal climate, where sediments weather during the dry season, whereas in the east faster erosion and more runoff inhibit extensive weathering.

4.1 Introduction

The Himalayan mountain belt, together with the Tibetan plateau, exerts a strong influence on regional climate, and acts as an orographic barrier for the Asian monsoon (Boos and Kuang, 2010). The monsoonal climate has a major influence on erosion and relief pattern (Thiede et al., 2004; Bookhagen and Burbank, 2006; Clift et al., 2008), which influence chemical weathering and weathering fluxes (West et al., 2005). Chemical weathering and weathering fluxes to the ocean are a response to climate, tectonics and erosion (Galy and France-Lanord, 1999). Chemical weathering plays an important role in the global CO_2 drawdown. Lateral variations in erosion and exhumation rates have been investigated (Thiede and Ehlers, 2013; van der Beek et al., 2016), but studies on spatial and temporal variations of the weathering regime and intensities are rare. Spatial variations in tectonics, erosion pattern and weathering can have implications on the past climate and the evolution of the mountain belt. Past weathering rates and regimes are rarely studied, but are crucial to unravel interactions between tectonics, erosion, climate and weathering.

Today's monsoonal climate has an important impact on the precipitation pattern in the Himalayan region. Monsoonal winds take up moisture in the Arabian Sea and the Bay of Bengal and transport it towards the Himalayan mountain front. This results in strong precipitation during the northern hemisphere summer months. The precipitation pattern varies along strike, with generally more precipitation in the east than in the west. During the winter months, precipitation is focused on the syntaxes, the western and eastern termination of the mountain belt, but the amount of precipitation remains higher in the east (Bookhagen and Burbank, 2010). Runoff of the Himalayan rivers and sediment transport to the sea is linked to precipitation, and has, therefore, an impact on the storage of sediment in the floodplain (Andermann et al., 2012a,b). Lupker et al. (2012) showed that sediments are significantly weathered in the floodplain. Sediments in the floodplain are more weathered than sediments collected from Himalayan rivers at the mountain front (Lupker et al., 2012).

The Himalayan foreland basin sediments and marine sediments of the Indus and Bengal fans hold a record of climate since Miocene times and have been used to reconstruct paleo-vegetation and monsoon evolution (Quade et al., 1989; France-Lanord and Derry, 1994; Freeman and Colarusso, 2001; Clift et al., 2010). Latest studies on the onset of the monsoon, date it back to Eocene (Licht et al., 2014), even though the evolution of the monsoon and its impact on precipitation patterns remains to be discussed. A change of vegetation has been documented at ~7 Ma, which was interpreted as a drying of the climate and the climate becoming more seasonal (Dettman et al., 2001). Paleo-precipitation and past weathering regimes are poorly studied (Derry and France-Lanord, 1996).

The Himalayan foreland basin sediments crop out along the entire mountain front, allowing west-east comparisons, within similar sedimentary settings. Here we present results of newly sampled pre-Siwalik and Siwalik sections in north western India (Figure 1), the compilation of the sections makes for the longest continuous sedimentary record in the Himalayan foreland basin. We use clay mineralogy and whole-rock geochemistry to reconstruct the weathering signal and compare Siwalik section in the western Himalaya with the Kameng river section (Vögeli et al. (suba), chapter 4) in the eastern part of the Himalayan foreland basin. Lateral differences in δ^{13}C of organic matter of bulk sediments, were interpreted as differences in the evolution of the vegetation from west to east (Vögeli et al. (subb), chapter 2). This study allows us to better understand the relationship between changes in vegetation/climate and the weathering regime and to directly compare the evolution of the weathering regime in the west and the east, with the same proxies.

4.2 Geological Setting

The evolution of the Himalaya is mainly driven by the early Cenozoic collision of the Indian and Eurasian continents (Hu et al., 2016), which resulted in major crustal shortening and thickening (Hodges, 2000; Yin and Harrison, 2000). A north-dipping fault system separates the Himalaya south of the suture zone into four major lithotectonic units (Figure 1), which are (from north to south) the Tethyan Sedimentary Series (TSS), the Higher Himalayan Crystalline Series (HHCS), the Lesser Himalayan Series (LHS) and the Sub-Himalayas (SH). The faults are from north to south, the South Tibetan Detachment System (STDS), which separates the TSS from the HHCS, the Main Central Thrust (MCT) lies between the HHCS and the LHS, the Main Boundary Thrust (MBT), which separates the LHS and the SH and the Main Frontal Thrust (MFT), which thrusts the SH over the Ganga/Brahmaputra plain (DeCelles et al., 2001; Le Fort, 1986; Yin and Harrison, 2000). The TSS is a Palaeozoic-Eocene sedimentary succession that was deposited on the Indian passive margin (Gaetani and Garzanti, 1991). The HHCS comprises high-grade metamorphic rocks and granites, whereas the LHS is composed of low-grade metasedimentary rocks (Hodges, 2000). The LHS has been subdivided into the Inner Lesser Himalaya (iLH) and the Outer Lesser Himalaya (oLH), based on different ϵNd isotopic signatures (Ahmad et al., 2000). The iLH has a more negative ϵNd, whereas the oLH has ϵNd similar to the HHCS and represents the low metamorphic cover of the HHCS. The Sub-Himalaya, the outer most unit, consists of the deformed Mio-Pliocene foreland basin sediments of the Siwalik Group, and crops out along the Himalaya from Pakistan all the way to north-eastern India (DeCelles et al. (1998b); Ojha et al. (2009), Figure 4.1).

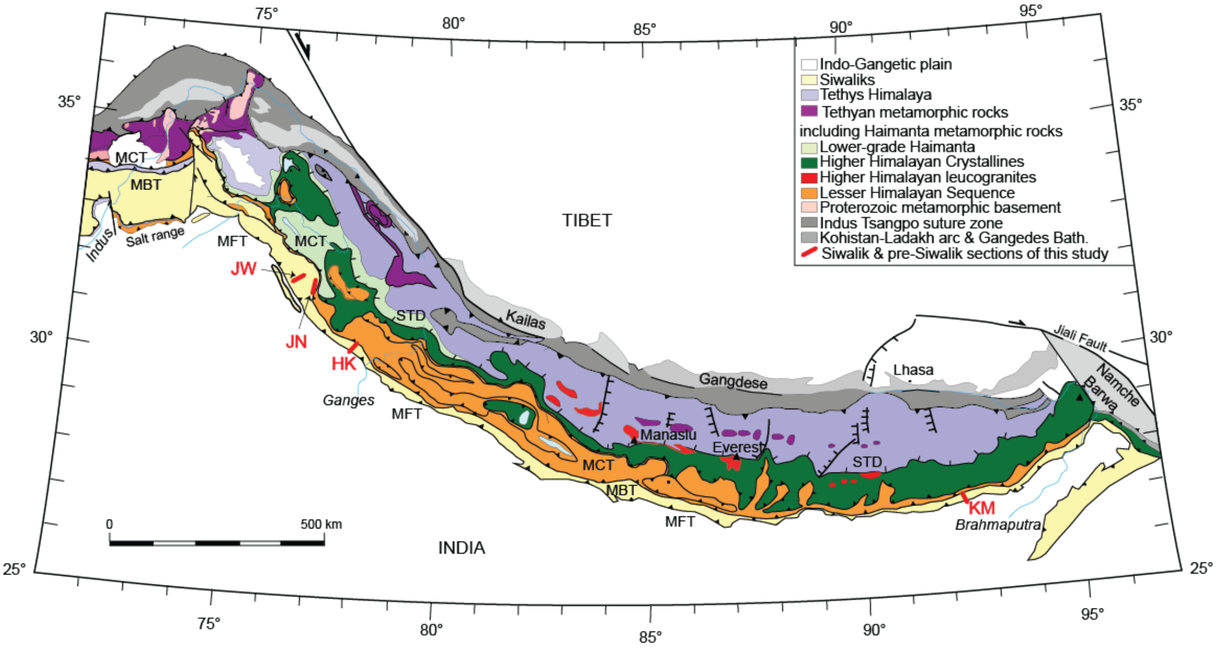

Figure 4.1: Geological map of the Himalaya modified after Guillot et al. (2008). Sampled Siwalik sections are indicated in red. JN: Joginder Nagar; JW: Jawalamukhi; HK: Haripur Kolar; KM: Kameng.

The Cenozoic foreland basin sedimentary rocks (pre-Siwaliks) are termed the Dharamsala Group and represent the Late Oligocene/ Early Miocene infill of the Himalayan foreland basin (DeCelles et al., 1998b). They consist of continental fluvial, lacustrine or deltaic sediments (Raiverman and Seshavataram, 1983). They contain fine-to medium grained sandstones, siltstone and overbank mudstones with soil carbonate nodules (White et al., 2001). The Siwalik Group is divided into the Lower, Middle and Upper Siwalik sub-groups, which are sometimes locally named differently. The Lower Siwaliks (LS) consist of mudstones with some development of paleosols, alternating with fine- to coarse-grained sandstones. The abundance of paleosols varies laterally along strike and decrease towards the east. LS were deposited by high-sinuosity streams. The Middle Siwaliks (MS) are characterized by massively bedded sandstones. Sandstones are medium- to coarse-grained and often rich in mica. The MS are associated with a depositional environment of large braided rivers. The Upper Siwalik (US) consist of beds of conglomerates alternating with sandstone beds deposited by a gravelly braided river (Nakayama and Ulak, 1999). Mudstones and paleosols are less frequent. An overall coarsening upward is observed in the entire Siwalik Group and boundaries between the sub-groups are gradual.

The three sampled sections of this study in north-western India contain pre-Siwalik (Joginder Nagar) and Siwalik (Joginder Nagar (JN), Jawalamukhi (JW) and Haripur Kolar (HK)) sediments. They were previously dated by magnetostratigraphy (Meigs et al., 1995; Sangode et al., 1996; White et al., 2001) and provide a composite age record that ranges from 20 to 1 Ma (Figure 4.2). The Joginder Nagar section ranges from ~20 to 12 Ma and contains rocks of the Lower and Upper Dharamsala and Lower Siwalik subgroups, with boundaries for the Lower/Upper Dharamsala at 16.5 Ma and Upper Dharamsala/LS at 12.5 Ma (White et al., 2001). In the Jawalamukhi section, all three Siwalik sub-groups (LS, MS and US) are present, with boundaries set at 10.9 Ma between LS and MS and at 6.8 Ma for the MS/US boundary (Meigs et al., 1995). The Haripur Kolar section contains MS and US with the boundary at 5.23 Ma (Sangode et al., 1996). Soil carbonate nodules are present in Siwalik sediments in northwestern India, Pakistan (Quade et al., 1989; Sanyal et al., 2010) and in western and central Nepal (Quade et al., 1995; DeCelles et al., 1998b). They have never been reported more eastwards and are lacking in the Kameng (Vögeli et al. (suba), chapter 3) and Remi river (Govin et al., 2015) sections in Arunachal Pradesh, northeastern India. The setting of the eastern Himalayan Siwalik section (Kameng section) can be found in chapter 3 (Vögeli et al., suba).

4.3 Sampling and Methods

4.3.1 Sampling strategy

In order to maximize the age constraint, we sampled according to the magnetostratigraphic sampling points of White et al. (2001) for the JN, Meigs et al. (1995) for the JW and Sangode et al. (1996) for the HK section, using field notes and maps of previous publications. 2-3 samples per Myr were collected to obtain a continuous age record. Samples were collected in pairs of adjacent fine- (mud/siltstones) and coarse-grained (sandstones) sediment beds of the same age; fine-grained samples were sampled in paleosols, where present. Additionally, where present, soil carbonate nodules were collected, which were analyzed for stable isotopes (Vögeli et al. (subb), chapter 2). Modern river sand and mud was collected in proximity to the sections.

4.3.2 Methods

4.3.2.1 Clay mineralogy

The $<2\mu$m fraction of clay minerals was extracted from selected samples from the JN, JW and HK sections. To remove carbonate and organic matter, the samples were treated with 1M acetic acid and dissolved $Na_4P_2O_7$, respectively. Samples were cleaned with MilliQ water after each removal. The $<2\mu$m fraction was separated by centrifuging the samples (diluted in MilliQ), for eight minutes at 700 rpm and pumping off the top 7 cm of the suspended fraction. This procedure was repeated until a volume of two liters was reached (Moore and Reynolds, 1997). Oriented aggregates were made on glass slides.

X-ray diffractograms were carried out on air-dried and ethylene glycosylated samples on a Bruker D8 Advance X-Ray Diffractometer at ISTerre, University of Grenoble-Alpes.

Clay mineral assemblages were obtained by a semi-quantitative peak analysis of the XRD patterns. Based on their peak heights, clay minerals were added up to 100% (Capet et al., 1990), obtaining a percentage of different clay minerals with a relative error of ~5% (Holtzappel, 1985). Illite crystallinity, also known as the Kübler Index (KI), was obtained by measuring the full width at half maximum of the illite 10 Å peak on an X-ray diffractogram. The KI determines three zones of very low grade metamorphism: diagenesis, anchizone and epizone (Kübler and Jaboyedoff, 2000). Additionally, clay mineral assemblages can be used as an indicator for weathering regimes. Smectite forms as a secondary clay mineral in soils and is enhanced in seasonal and warmer climates (Hillier, 1995; Huyghe et al., 2005, 2011). Kaolinite is formed in warmer and rain intensive climate (Righi and Meunier, 1995; Setti et al., 2014). With increasing weathering intensity, smectite and kaolinite should become more abundant, and they can thus be used as an indicator for weathering (Setti et al., 2014). Source rocks can potentially influence clay mineralogy (Chamley, 1989; Garzanti et al., 2014), and provenance has therefore to be taken into account when interpreting weathering.

4.4 Results

Here we present clay mineral assemblages and major element data of the Joginder Nagar, Jawalamukhi and Haripur Kolar sections in northwest India. These are compared with similar data of the eastern Himalaya (Kameng river section), which were described in chapter 3 (Vögeli et al., suba).

4.4.1 Clay mineralogy

Clay minerals in the $<2\mu$m fraction of clayey beds in the three western sections consist mainly of illite, chlorite, smectite and kaolinite; the relative proportions of which vary with time. In the JN and the lower part of the JW sections, from 20 to ~10.5 Ma, clays are dominated by illite (illite+chlorite/$\sum$clays > 0.6), which is followed by a period when smectite and kaolinite are dominant (illite+chlorite/$\sum$clays < 0.5). Especially the samples between ~8 and 5 Ma have high smectite (> 50 %) content. From 4 to 1 Ma, illite concentrations increase again, but smectite remains more abundant than in the lower part of the section. The modern Beas river sample is dominated by illite, with an illite content of 65 % (Figures 4.2,4.3).

Illite crystallinity (KI) is fairly constant over the whole time span (Figure 4.3). Values vary from 0.12 to 0.23 Δ °2Θ with illite crystallinity similar to muscovites from the Higher Himalayan Crystalline Series (Huyghe et al., 2005). These values are representative for the epizone of low-grade metamorphism.

4.4.2 Major elements

Pairs of coarse- and fine-grained samples were analyzed. Major elements compositions reflect the difference in grain size, with coarse-grained samples containing more SiO_2, whereas finer sediments

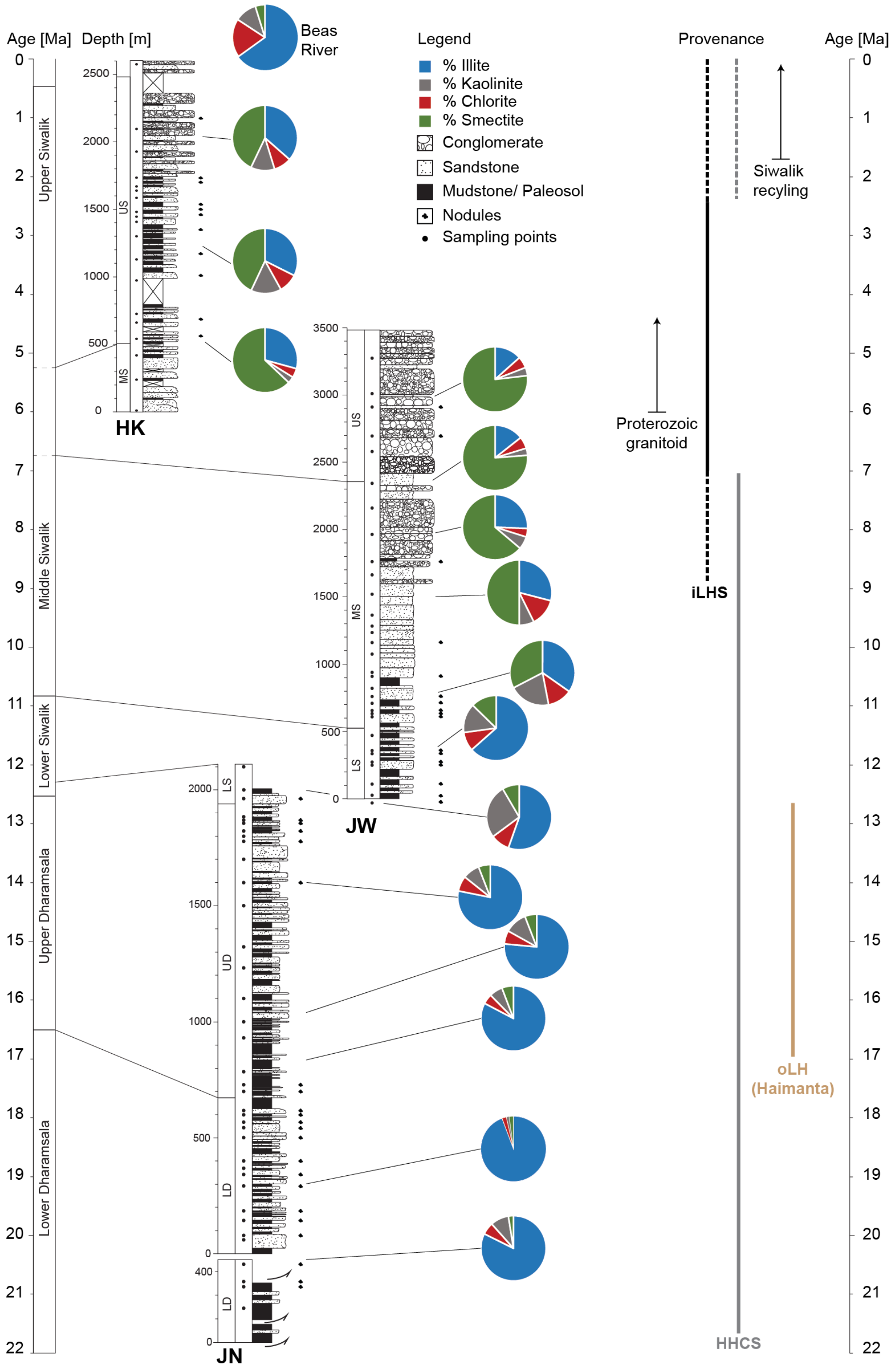

Figure 4.2: Stratigraphy, sampling points, clay mineral assemblages and inferred provenance of the Joginder Nagar, Jawalamukhi and Haripur Kolar sections. Stratigraphy and age-dating after Meigs et al. (1995); Sangode et al. (1996); White et al. (2001). Provenance from White et al. (2001, 2002), Najman et al. (2009) and Suresh et al. (2004).

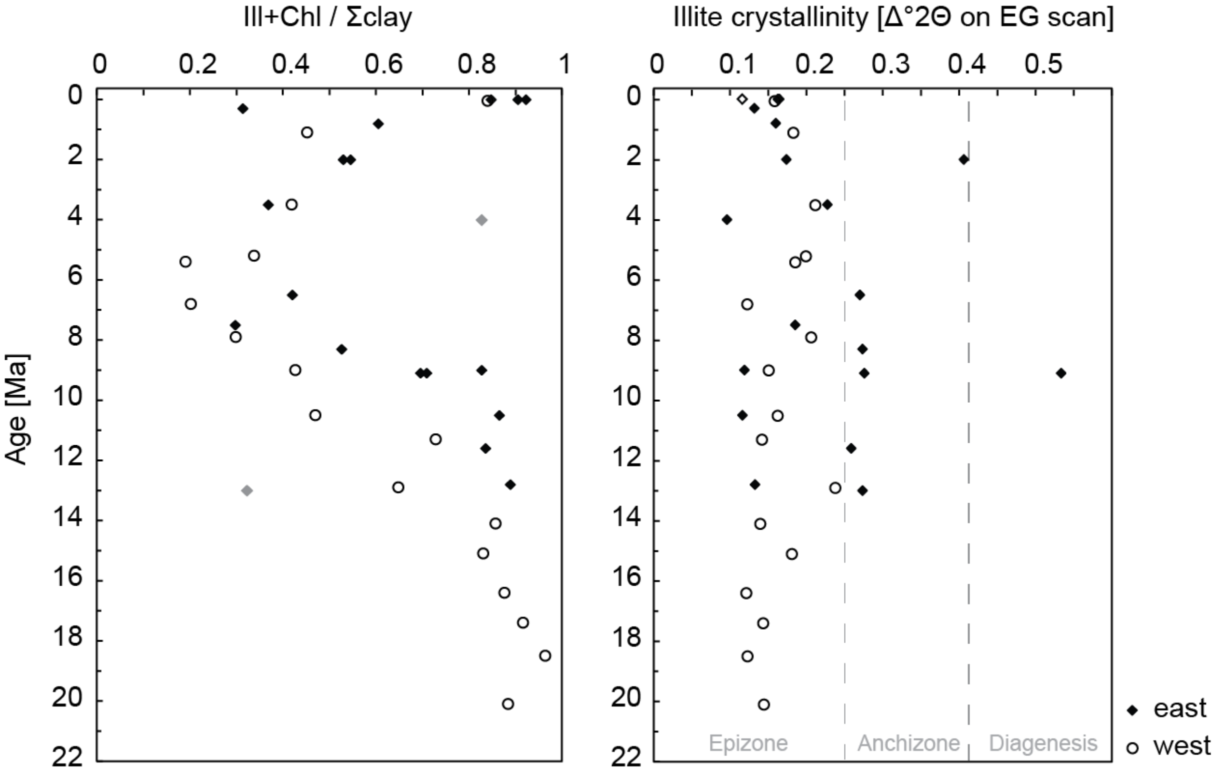

Figure 4.3: Comparison of western (empty circles) and eastern (black diamonds) clay mineral assemblages and illite crystallinity. Samples represented in grey diamonds show anomalous clay assemblages, due to very low clay concentration (4 Ma) and proximity to a local thrust (13 Ma) of Vögeli et al. (suba).

have higher K_2O and Al_2O_3 concentrations. The ratio of the immobile elements Al_2O_3/ SiO_2 reflects the grain size of the sample (Lupker et al., 2012). Plots of the concentrations of SiO_2 vs K_2O and Al_2O_3 show a separation of fine- and coarse-grained sediments (Figure 4.4). Ratios of mobile to immobile elements, such as K/Al are used to quantitatively track weathering intensity over time (Figure 4.5). K/Al ratios in the western sections are relatively constant at ~0.2 over the last 20 Ma, with an excursion to higher values of ~0.4, between ~7 and 5 Ma. The concentration of calcium is very variable and generally higher in the western sections, with an average of 3.7 wt % oxide compared to 0.7 wt % oxide in the east. Concentration of calcium does not correlate with K/Al (Figure 4.6). Complete major element results are provided in the appendix 4.1.

4.5 Discussion

Lateral variation in the climatic evolution of the Himalaya is reflected in the difference in the evolution of vegetation, as inferred from the record of stable carbon isotopes, with C4 plants appearing in the western Himalaya around 7 Ma, but not in the east. The vegetation in the eastern part of the orogen is characterized by C3 plants since Miocene times ((Vögeli et al., subb), chapter 2). The appearance of

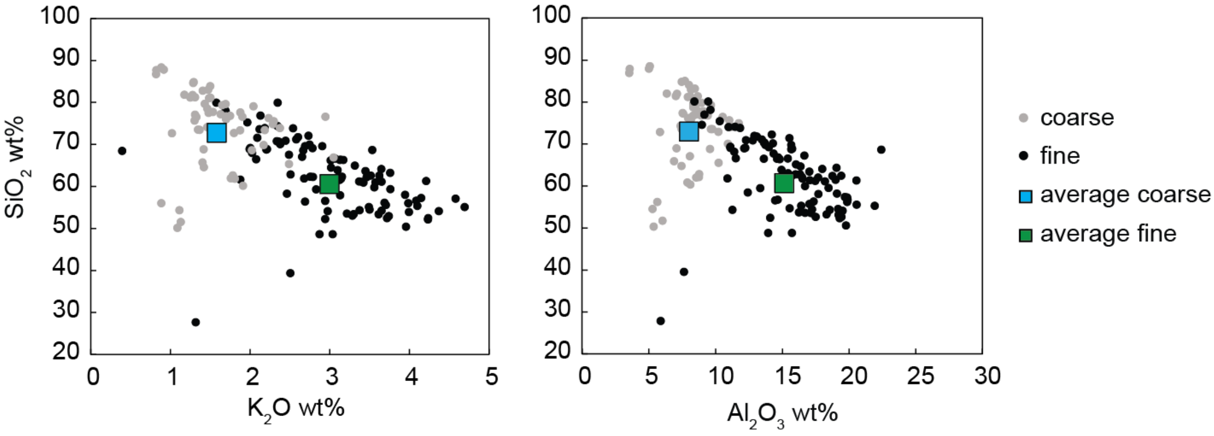

Figure 4.4: Correlation between SiO_2 and K_2O and Al_2O_3; fine-grained sediments (in black) show depletion in SiO_2. Mineralogy and major element concentrations vary from fine- to coarse-grained sediment. Compilation of all samples of the western sections (JN, JW, HK).

C4 plants at 7 Ma is interpreted as the onset of an overall drier and more seasonal climate, especially in the west (Quade et al., 1989; Quade and Cerling, 1995; Dettman et al., 2001). In contrast, climate in the east has remained too humid to develop C4 vegetation. By using other proxies such as clay minerals and major elements, influences of this difference in climate, on weathering rates and regimes are investigated, depending also on the sensibility of the different proxies. In the following, we first discuss and exclude potential provenance and diagenetic influence on weathering signals in the western sections and then compare the west and the east.

Lateral variation in the climatic evolution of the Himalaya is reflected in the difference in the evolution of vegetation, as inferred from the record of stable carbon isotopes, with C4 plants appearing in the western Himalaya around 7 Ma, but not in the east. The vegetation in the eastern part of the orogen is characterized by C3 plants since Miocene times ((Vögeli et al., suba), chapter 2). The appearance of C4 plants at 7 Ma is interpreted as the onset of an overall drier and more seasonal climate, especially in the west (Quade et al., 1989; Quade and Cerling, 1995; Dettman et al., 2001). In contrast, climate in the east has remained too humid to develop C4 vegetation. By using other proxies such as clay minerals and major elements, influences of this difference in climate, on weathering rates and regimes are investigated, depending also on the sensibility of the different proxies. In the following, we first discuss and exclude potential provenance and diagenetic influence on weathering signals in the western sections and then compare the west and the east.

4.5.1 Provenance and diagenesis in the western sections

Provenance of sediments from the Joginder Nagar section have been determined with whole rock Sm-Nd, Rb-Sr, Ar-Ar in white mica (White et al., 2002) and detrital monazite U-Pb isotopic studies (White et al., 2001). Najman et al. (2009) analyzed Ar-Ar ages on white micas, sandstone petrography and Sr-Nd

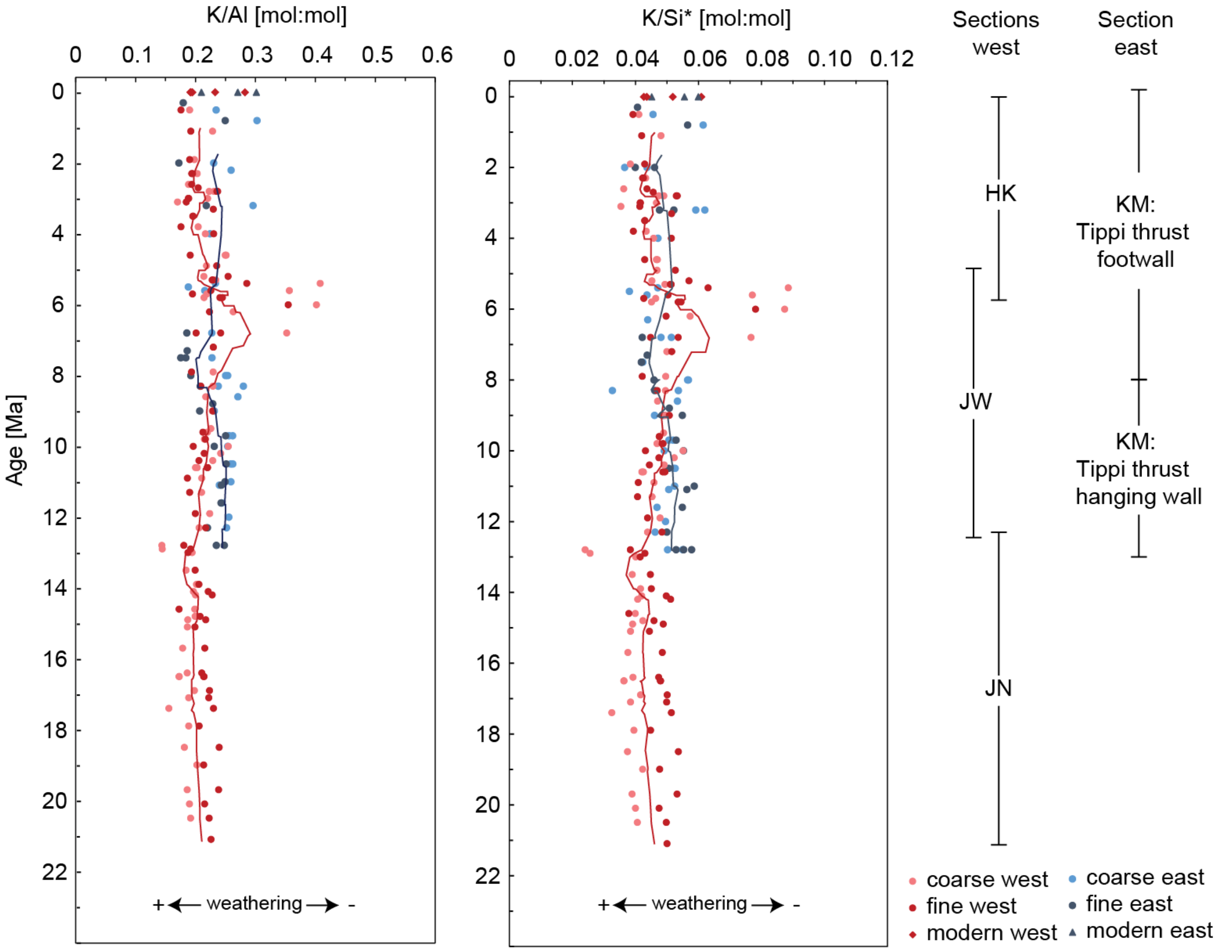

Figure 4.5: Ratios of K/Al and K/Si* (normalized). Red dots represent the western Himalaya and blue dots the eastern Himalaya Kameng river section). Lighter red and blue dots are coarse-grained samples. Samples in the west show generally a higher degree of weathering except between 7 -5 Ma, where they are exceptionally little weathered in the west. Red and blue lines are eight point moving averages, showing general trends of weathering over time. Western sections are indicated; JN: Joginder Nagar; JW: Jawalamukhi; HK: Haripur Kolar.

isotopic compositions in the Jawalamukhi section to reconstruct changes in provenance. The Lower Dharamsala (~20-17 Ma) sediments are mainly sourced from the HHCS (Figure 4.2). At the boundary from the Lower to Upper Dharamsala the provenance changes from high-grade metamorphic rocks to low-grade metamorphic and sedimentary rocks of the outer Lesser Himalaya (Haimanta) (White et al., 2002). Inner Lesser Himalayan material is present in the Siwalik sediments from at least ~9 Ma. In the Jawalamukhi section, HHCS material cuts out completely at 7 Ma (Najman et al., 2009) and the inner Lesser Himalaya becomes the dominating source of the Siwalik sediments. From 6 Ma on, detritus from Proterozoic granitoids of the iLH is present. Isotopic provenance studies in the Haripur Kolar section are lacking. Basic provenance analysis was made based on clay minerals and stratigraphy and indicate

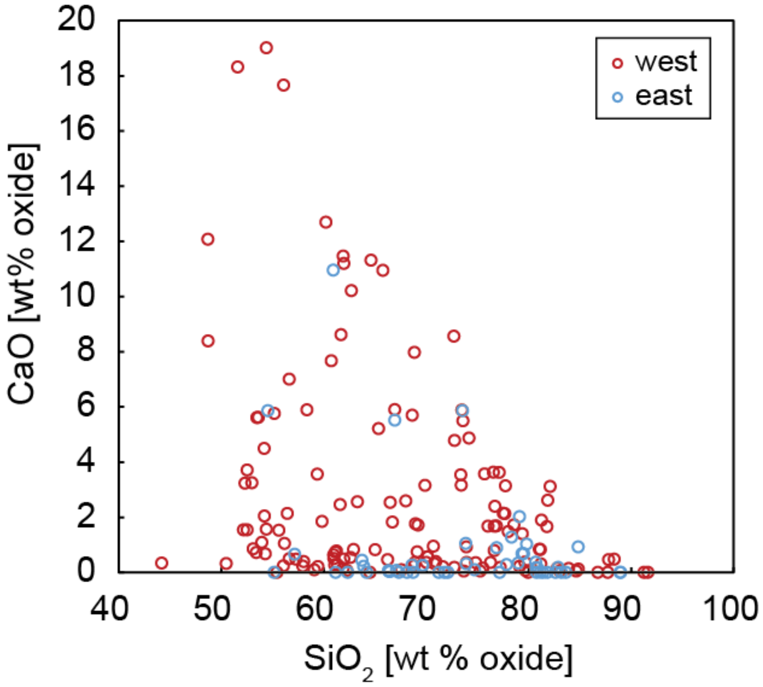

Figure 4.6: CaO vs.SiO$_2$, calcium comcentration does not correlate with SiO$_2$ concentration. Red circles show western pre-Siwalik and Siwalik; blue circles are sediments of the Kameng river section. Calcium concentration is elevated in the western Siwaliks.

a source of HHCS and LHS (Suresh et al., 2004). The peak activity of the Main Frontal Thrust is at 1.77 Ma, thereafter sub-Himalayan sedimentary rocks were deposited (recycling of Siwaliks) (Kumar et al., 2003). Major changes in provenance (Figure 4.2) thus occurred at ~17 Ma (oLH coming in), at 9 Ma (iLHS starts coming in) at 7 Ma (HHCS cuts out).

Illite crystallinity (Kübler Index) can be used to distinguish different low-grade metamorphic zones. In other Siwalik sections, illite crystallinity varies systematically with depth. In the Karnali section in western Nepal, illite crystallinity starts to increase from a depth of ~2100 m (Huyghe et al., 2005). Illitisation of smectite begins at a temperature of 70-95°C (Dunoyer De Segonzac, 1970). It is important to approximately know to what temperatures sedimentary rocks could have been heated up, in order to see potential influence on other proxies. Additionally to illite crystallinity, reset apatite fission track (AFT) ages can be used to constrain a burial temperature. Reset AFT ages are a clear indicator that sedimentary rocks were heated above 60-120°C, the AFT partial annealing zone (Tagami and O'Sullivan, 2005). AFT analyses are lacking for the JN, JW and HK sections, but estimated burial depths for apatite annealing are ~4000m in the Kameng (Chirouze et al., 2013) and ~3000 m in central/western Nepal (Surai, Tinau, Karnali) (van der Beek et al., 2006), respectively. In contrast, in the western sections (this study), the illite crystallinity is relatively constant and lies in the epizone field, suggesting that the illite is mostly detrital, similar to the Kameng section (Figure 4.3). The illite crystallinity therefore reflects the source area metamorphism. None of the western samples fall into the diagenesis field, which should

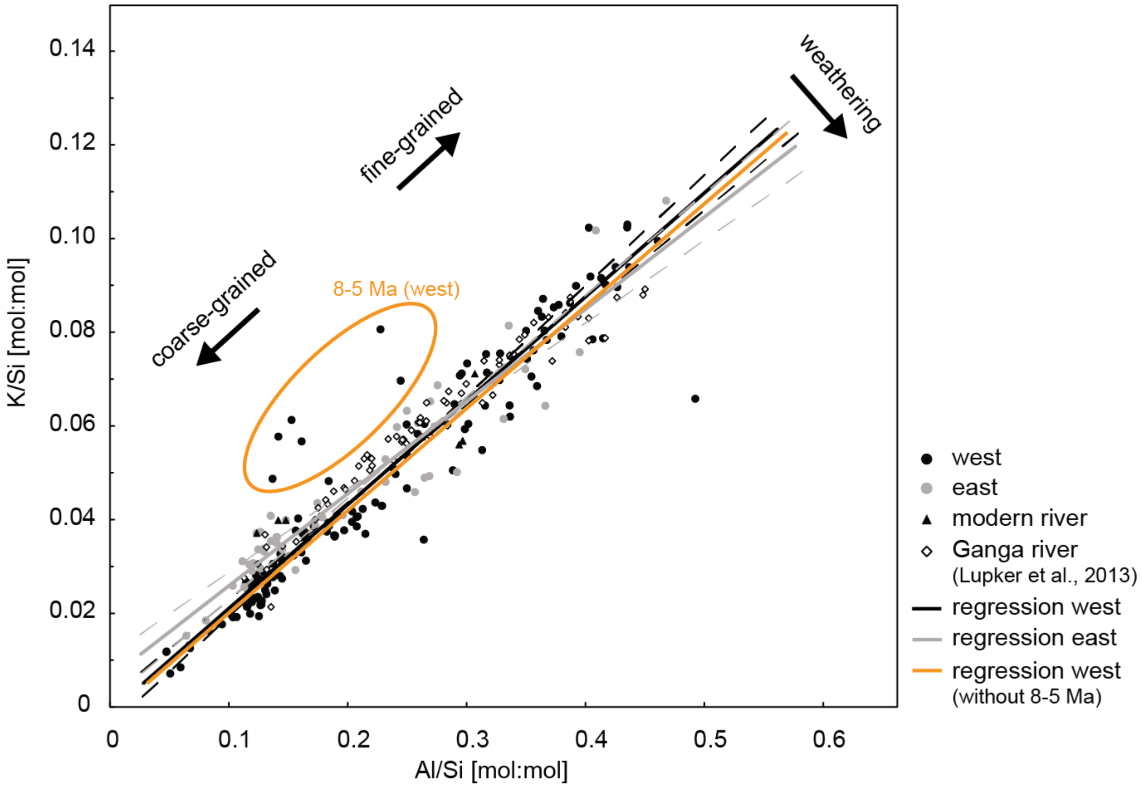

Figure 4.7: Evolution of the K/Si of fine- and coarse-grained sediments of the western (black) and eastern (grey) Siwaliks. Dashed lines represent the 0.95 confidence level of the linear regressions of the west and east (method after Lupker et al. (2013)). Anomalous values between 8 and 5 Ma are encircled in orange, orange regression line show the variation of the regression line without anomalous point (in orange circle).

be the case if illitisation of smectite had occurred (Lanson et al., 1995; Huyghe et al., 2005). There is no sign of illitisation of smectite throughout the western sections, suggesting that the influence of diagenesis is likely to be minor, or at least not affecting the clay minerals in the western section. Clay mineralogy begins to change at ~11 Ma, when smectite becomes more abundant and remains abundant until ~1 Ma(Figure 4.2). Clay mineralogy does not appear correlated with changes in provenance and diagenesis is unlikely to bias the clay signal, therefore variations of clay mineralogy can be ascribed to changes in weathering intensity and regime.

K/Al ratios in the west remain relatively constant over time, except between ~7 and 5 Ma, where K/Al values are anomalously high (Figure 4.5). Several samples between 7 and 5 Ma have K/Al ratios of ~0.4. High K/Al ratios indicate the presence of "fresh", less weathered material. The samples were collected in the upper part of the Jawalamukhi section (Middle Siwalik), where conglomerate is frequent (Figure 4.2). Conglomerates represent a depositional environment closer to the mountain front, where sediments are less weathered compared to that in the floodplain. Additionally the proximity to the mountain front could be related to increased landslide activity exposing and depositing more less-weathered, “fresh” material with higher K/Al between ~7 and 5 Ma. Sedimentary rocks of the lower most part of the Haripur Kolar, where conglomerate is less abundant, are more weathered. Provenance changes between 7 and 6 Ma, when material sourced from Proterozoic granitoids are brought in and HHCS is cut out, could potentially influence K/Al ratios because these granitoid sources are expected to have elevated potassium concentration. However, potassium concentration in these samples does not show exceptionally high values. The decrease in K/Al between ~7 and 5 Ma is therefore more likely to be related to the depositional environment becoming locally more proximal and an additional change in provenance, than to a change of climate. K/Al ratios do not show a correlation with burial depth; diagenesis is therefore likely to be of negligible influence on K/Al ratios.

4.5.2 West-east comparison of weathering regimes

The three pre-Siwalik and Siwalik sections in the western Himalaya form the longest composite continuous sedimentary record in the Himalayan foreland basin, which allows us to reconstruct weathering history since the Early Miocene. Weathering intensity in the western Himalayas is fairly constant from ~21 to ~13 Ma, after which it slightly decreases until 7 Ma, as inferred from K/Al and K/Si* ratios (Figure 4.5). The period between 7 and 5 Ma is characterized by exceptionally low weathering, reflected in a high K/Al. From 5 to 1 Ma weathering is relatively constant at a K/Al value of ~0.20, similar to the period from 21 to 13 Ma, with some variation around 3 Ma (Figure 4.5). In the eastern Kameng section K/Al indicates increase in weathering with time, the Upper Siwaliks are more weathered than the Lower Siwaliks. As the Kameng river section only spans over 13 Ma, a direct comparison can only be made from mid-Miocene to Pleistocene. Sediments of the Dharamsala Group in the west (older than 13 Ma, and absent in the east), are generally more weathered than the Lower Siwaliks in the east. Generally sediment in the east show a higher K/Al ratio, hence are less weathered, than sediments in the western sections. The period between ~7 and 5 Ma is exceptional with sediment in the west being less weathered, showing anomalous values of K/Al up to 0.4.

By plotting K/Si against Al/Si (Figure 4.7), a secondary signal of weathering can be extracted from the steepness of regression lines (Lupker et al., 2013). We calculated the 95% confidence interval for each linear regression, to show the uncertainty of the regression line. Confidence levels of regression do not show a clear separation, even though eastern sediments seem to be slightly more weathered, which contradicts trends of K/Al and seems to be due to the period of very low weathering in the west between 7 and 5 Ma (Figure 4.7, orange circle). By taking out the anomalously low weathered points between 7 and 5 Ma, we would expect the regression line of the eastern sediments to change its steepness, but the regression line of the eastern sediments stays less steep (more weathered). In any case, by plotting K/Si versus Al/Si, primary control of grain-size is observed. Coarse-grained sediments of the western sections are more weathered than coarse-grained sediments in the Kameng, this slight difference influences the steepness of the regression line. In order to directly compare weathering in the west and east plotting K/Al versus age is more suitable (Figure 4.5).

Other weathering proxies, such as the Chemical Index of Alteration (CIA) (Nesbitt and Young,

1984) are more difficult to use, due to the variations of carbonate content in the sediments and changes in source. Calcium concentrations vary laterally, with higher Ca concentration in the west resulting in the abundance of soil carbonate nodules in the western section (Figure 4.6). In the Kameng section, as well as in the Remi section even further east (Govin et al., 2015), soil carbonate nodules are not abundant. They have never been reported more eastwards than eastern Nepal. As the climate is and probably has been more humid in the past in the east (Bookhagen and Burbank, 2006; Vögeli et al., subb), it is likely that calcium was dissolved and the formation of soil carbonate nodules was inhibited. δ^{13}Corg show important variations from west to east along the Himalayan front at ~7/8 Ma (Vögeli et al. (subb), chapter 2), which are not reflected in the clay mineralogy. Clay mineralogy within the different Siwalik sections is quite similar, with clay mineral assemblages starting to be more smectite rich somewhere between 11 and 7 Ma, varying laterally, and being characterized by a high illite content in the stratigraphically lower series (Dharamsala and LS). This is also observed in the distal part of the Bengal Fan (France-Lanord et al., 1993). In the Kameng river section, the smectite rich period starts at 8 Ma until 3 Ma, where kaolinite becomes more abundant. On the other hand, smectite starts to be more abundant at ~11 Ma in the west and stays the dominant clay mineral up to 1 Ma. Kaolinite is less abundant in the west than in the east. The modern clay mineral assemblages of the Beas river in the west is dominated by illite, similar to other Himalayan rivers (Kameng and Subansiri rivers) and the Brahmaputra in the east (Vögeli et al. (suba), chapter 3). In contrast the Ganges carries more smectite (Huyghe et al., 2011). Smectites can be formed under enhanced weathering and seasonal conditions. In the east the smectite rich period also coincides with a change in source (Vögeli et al. (suba), chapter 3). Sources in the west and the east are different, but smectites seem to be similar (Figure 4.8); we therefore suggest, that the abundance of smectite is likely to be controlled by climate rather than by provenance. The higher abundance of smectite can be interpreted to reflect a change towards a more seasonal climate (Huyghe et al., 2005). More smectite in the west between 8 and 5 Ma could therefore be an indicator of more seasonal climate, which is supported by the appearance of C4 plants during this time (Quade and Cerling, 1995; Vögeli et al., subb). C4 plants are known to be more resistant to water stress, hence seasonal climate (Ehleringer, 1988). Clay minerals and carbon stable isotopes, hence vegetation, therefore both reflect mostly seasonality of the climate. The clay mineralogy suggests strengthening of weathering with the abundance of smectite at ~8 Ma. Major elements, in contrast, suggest less weathering in the period between ~7 to 5 Ma. In the Kameng section an overall increase of weathering is observed, with a major change towards stronger weathering at 8 Ma (Figure 4.5) (Vögeli et al. (suba), chapter 3).

Generally, Siwalik sediments in the eastern Himalayas are less weathered than in the west. Climate in the east is overall more humid. Modern precipitation is higher and less seasonal in the eastern part of the Himalaya (Bookhagen and Burbank, 2006), and acts as a driver for more runoff and erosion. Lupker et al. (2012) showed that sediments are predominantly weathered in the floodplain, rapid transport through the floodplain therefore inhibits extensive weathering. K/Al ratios show that sedimentary rocks of the Kameng section have been less weathered than in the west, indicating that the eastern Himalayan region was more humid, since mid-Miocene and sediments were being less stored in the floodplain. The Indian

Summer Monsoon is the main driver for the precipitation pattern along the Himalayan front. Latest studies on the onset of the Indian Summer Monsoon suggest that the monsoon was evolved in Eocene times (Licht et al., 2014). We can therefore assume that monsoonal winds was transporting moisture from the Bay of Bengal to the Himalaya since Eocene, in what strength remains to be discussed. Marine records of the Bengal and the Indus fan have been used to reconstruct paleoclimate in the Himalayan region (France-Lanord et al., 1993; Clift and Gaedicke, 2002; Clift et al., 2008, amongst others). Figure 4.9 shows sedimentary rocks of western and eastern Siwaliks together with sediments of the Ganga river (Lupker et al., 2013) and the Indus (~16-1 Ma) (Clift et al., 2008) and the Bengal fan (~32-1 Ma) (France-Lanord et al., 2015). Indus fan sediment ranging from early/mid Miocene are slightly stronger weathered, than the proximal Siwalik record and the sediments of the Bay of Bengal. This supports our finding of stronger weathering in the west since Miocene time, where sediments in the west are generally more weathered than in the east.

4.6 Conclusions

The Himalayan foreland basin is a good laboratory to study lateral variations in the evolution of the climate and weathering regime, as they crop out along the entire mountain front. The lack of longer records in the east limits the direct comparison to mid-Miocene and later times, whereas in the western part the compilation of the three sections (JN, JW, HK) allows the reconstruction of climate and weathering as far back as the early Miocene. By looking at clay mineralogy and major element compositions, and taking provenance and diagenesis into account, important information on past weathering and climatic regimes can be gained.

Smectite content increases from 11 Ma in the west and 8 Ma in the east, respectively. Illite crystallinity does not increase down section, suggesting that illitisation of smectite did not occur. The influence of diagenesis can therefore be considered negligible and the change in clay mineralogy can be ascribed to change towards a more seasonal climate. Generally, less smectite and more kaolinite in the east could indicate less seasonality in the east. K/Al is generally higher in the east, indicating less intense weathering. During the period between ~7 and 5 Ma, sediments in the west are less weathered, which appear linked to a proximal depositional environment, rather than a major change in climate. Weaker weathering in the eastern part of the orogen is interpreted as a result of wetter climate and more erosion and runoff, hence the residence time of the sediments in the floodplain is shorter, which results in weaker weathering. In both, the west and the east a slight trend towards stronger weathering can be observed, indicating the evolution of a more seasonal climate over time.

Reconstruction of past climate and weathering regimes remains a challenging task. Monsoonal climate and evolution is still not fully understood, especially its influence on seasonality linked with overall humidity needs to be further investigated. Paleo-vegetation, clay mineralogy and major elements can be used as indicators for seasonality, but more paleo-seasonality studies are crucial to understand the evolution of the monsoon.

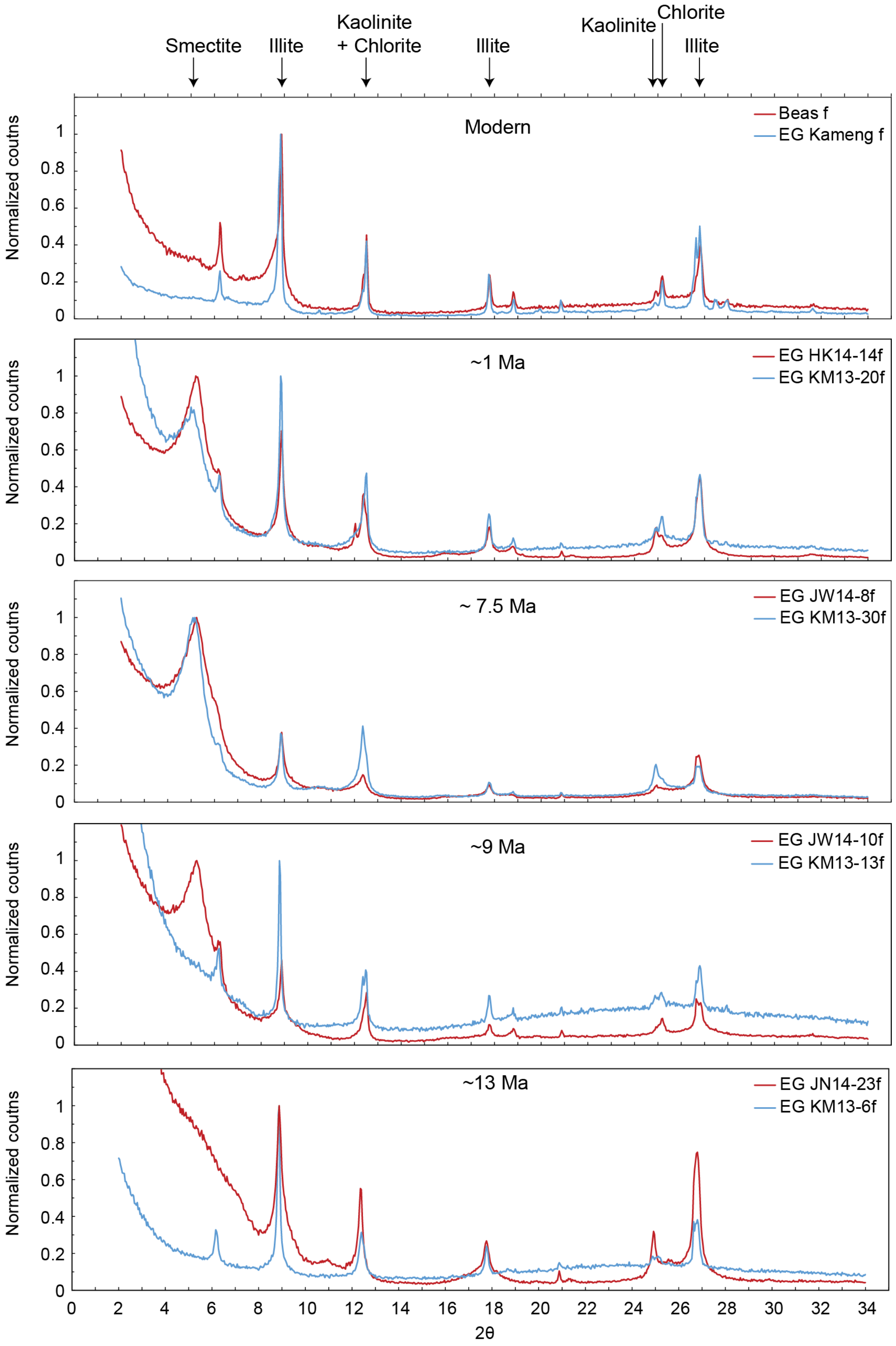

Figure 4.8: XRD diffractogramms of clays of similar age from west (red line) and east (blue line), showing variations in the evolution of the clay mineralogy between west and east; smectites are similar in the west and the east.

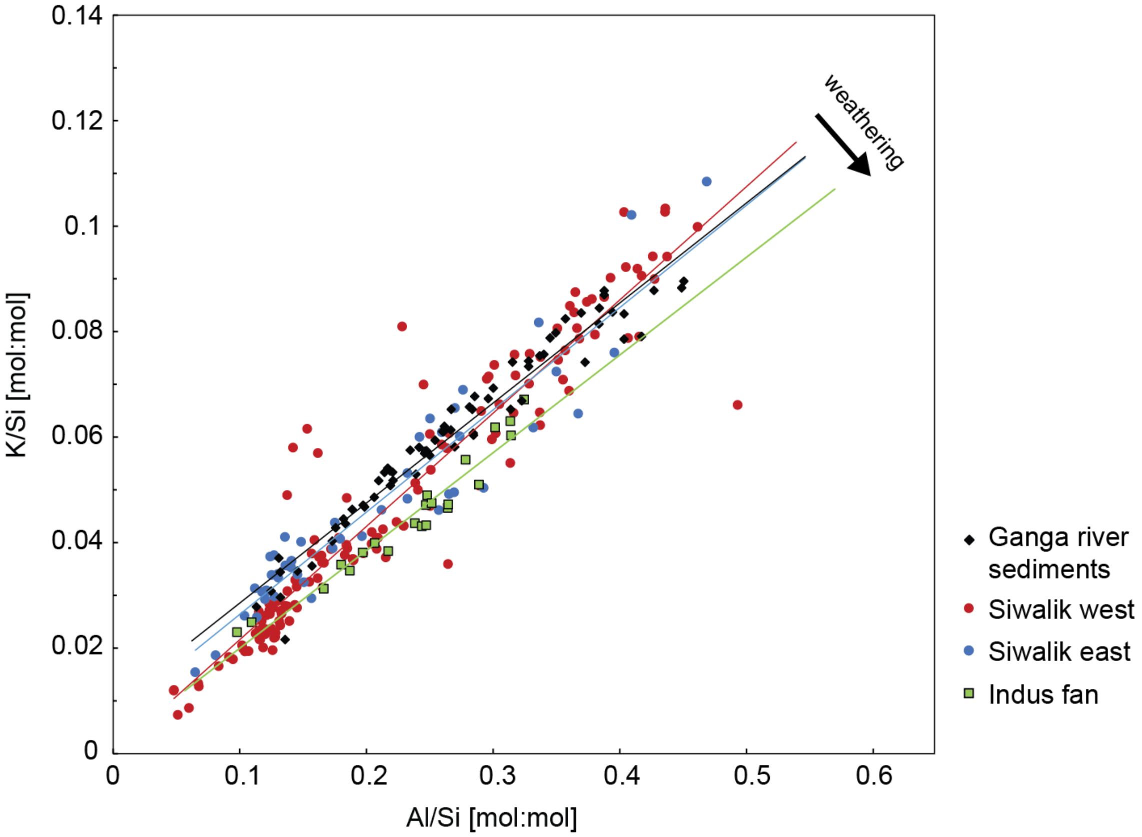

Figure 4.9: Comparison of western and eastern Siwalik sediments with marine sediments of the Indus Fan (Clift et al., 2008) and the modern river sediments of the Ganga river (Lupker et al., 2013).

Appendices

Appendix 4.1

Table 4.1: Major Element concentration

Sample	Grain-size	Age [Ma]	Lith. Unit	SiO_2	TiO_2	Al_2O_3	Fe_2O_3 t	MnO	MgO	CaO	Na_2O	K_2O	P_2O_5	LOI	H_2O^+	K/Al [mol:mol]	K/Si* [norm.]	H_2O^+/Si* [norm.]
Kameng Down c	c	0	modern	79.14	0.4	9.97	3.04	0.05	0.88	0.9	1.36	2.49	0.07	2.05		0.27	0.056	
Kameng Down f	f	0	modern	79.97	0.46	8.41	3.16	0.07	0.9	1	1.35	2.34	0.11	1.73	1.21	0.3	0.06	0.2259
Holo. Terrasse	c	0.01		74.74	0.6	12.46	3.81	0.04	0.78	0.1	0.49	2.42	0.03	5.17	3.52	0.21	0.045	0.3592
KM13-22	f	0.3	US	71.23	0.51	15.54	3.39	0.04	0.98	n.d.	1.31	2.58	0.02	5.72		0.18	0.041	
KM13-21-carbon	c	0.5	US	77.86	0.43	8.4	2.85	0.04	0.87	0.28	0.58	1.82	0.02	6.66		0.23	0.046	
KM13-20-c	c	0.8	US	81.4	0.34	9.37	2.42	0.04	0.66	n.d.	0.98	2.62	0.07	2.23	1.5	0.3	0.062	0.237
KM13-20-f	f	0.8	US	63.74	0.73	14.94	6.13	0.09	1.99	0.44	0.85	3.45	n.d.	6.88	3.71	0.25	0.057	0.2973
KM13-19-c	c	2	US	88.99	0.32	6.12	1.77	0.01	0.4	n.d.	0.22	1.3	0.02	2.7		0.23	0.037	
KM13-19-c-nan	c	2	US	87.31	0.36	6.4	1.83	0.01	0.4	0.05	0.09	1.52	n.d.	2.51		0.26	0.044	
KM13-19-f	f	2	US	67.1	0.69	16.65	4.3	0.03	1.04	0.08	0.31	2.65	0.04	7.71		0.17	0.04	
KM13-19-f-nan	f	2	US	65.15	0.74	17.21	4.45	0.03	1.03	0.17	0.21	3.16	0.04	7.71		0.2	0.046	
KM13-27	c	2.2	US	81.13	0.33	9.68	2.62	0.05	0.71	0.01	0.94	2.32	0.1	2.19		0.26	0.052	
KM13-28-c	c	3.2	MS	80.78	0.35	8.71	2.52	0.02	0.66	n.d.	0.66	2.38	0.02	2.94	2.04	0.3	0.059	0.3361
KM13-28-c-nan	c	3.2	MS	79.9	0.36	9.89	2.65	0.03	0.7	0.26	0.73	2.75	n.d.	2.71		0.3	0.062	
KM13-28-f	f	3.2	MS	71.78	0.66	12.91	4.89	0.04	1.11	n.d.	0.38	2.6	0.03	5.23	3.77	0.22	0.048	0.3664
KM13-28-f-nan	f	3.2	MS	70.75	0.69	13.72	5.2	0.04	1.17	0.21	0.36	2.99	n.d.	5.01		0.24	0.052	
KM13-18 bis	c	4	MS	60.93	0.34	8.96	3.66	1.05	0.96	10.96	1.43	1.86	0.1	9.56	1.43	0.22	0.047	0.215
KAM6	c	5.4	MS	79.81	0.27	9.85	1.96	0.02	0.59	1.03	1.66	2.12	0.05	1.78		0.23	0.047	
KM13-17 bis	c	5.5	MS	79.12	0.56	10.51	3.62	0.1	1.11	2.02	1.78	1.83	0.09	1.59	1.22	0.19	0.038	0.1692
KAM15	c	5.6	MS	78.33	0.32	10.01	2.64	0.04	0.87	1.28	1.73	1.99	0.05	2.23		0.22	0.044	
KM13-29	c	6.3	MS	65.68	0.32	8.29	2.34	0.82	0.82	11.06	1.15	1.67	n.d.	9.63		0.22	0.044	
KM13-4	c	6.8	MS	73.86	0.52	11.23	4.6	0.09	1.5	1.05	1.35	2.36	0.25	3.88		0.23	0.048	
KM13-4-nan	c	6.8	MS	73.23	0.53	11.04	4.87	0.09	1.54	1.34	1.33	2.47	0.26	3.51		0.24	0.051	
KM13-4-nodule	f	6.8	MS	69.66	0.66	15.67	4.11	0.04	1.04	0.25	0.23	2.69	0.03	6.56		0.19	0.042	
KM13-3	f	7.3	MS	63.91	0.73	17.99	4.86	0.04	1.29	0.22	0.35	3.1	0.04	7.05		0.19	0.044	
KM13-30-c	c	7.5	MS	84.84	0.3	8.17	2.42	0.06	0.61	0.93	1.08	1.72	n.d.	1.76	1.23	0.23	0.042	0.2441
KM13-30-f	f	7.5	MS	62.35	0.74	19.42	4.86	0.04	1.32	n.d.	0.29	3.15	0.04	9.59	5.41	0.18	0.042	0.323
KM13-30-nodule	f	7.5	MS	68.61	0.68	15.67	4.38	0.06	1.05	0.27	0.32	2.67	0.03	7.49		0.18	0.042	
KM13-16-c	c	8	MS	67.33	0.76	15.41	6.28	0.06	1.74	n.d.	0.93	3.56	0.05	3.62		0.25	0.057	
KM13-16-c-dup	c	8	MS	68.14	0.74	14.47	6.25	0.06	1.75	n.d.	0.84	3.39	0.06	3.62		0.25	0.057	
KM13-16-f-bis	f	8	MS	61.17	0.84	20.54	5.15	0.04	1.46	n.d.	0.38	3.65	0.03	6.74		0.19	0.046	
KM13-15-c	c	8.3	MS	88.92	0.29	4.89	1.7	0.03	0.34	n.d.	0.29	1.08	0.03	2.01	1.44	0.24	0.033	0.5116
KM13-15-f	f	8.3	MS	72.12	0.62	14.22	4.65	0.04	1.02	n.d.	0.5	2.73	0.02	3.43	3.68	0.21	0.046	0.3193
KM13-2	c	8.3	MS	83.64	0.4	7.94	1.8	0.02	0.51	n.d.	0.29	2.05	0.03	3.32		0.28	0.054	

Table 4.1: Major Element concentration (cont.)

Sample	Grain-size	Age [Ma]	Lith. Unit	SiO_2	TiO_2	Al_2O_3	Fe_2O_3 t	MnO	MgO	CaO	Na_2O	K_2O	P_2O_5	LOI	H_2O^+	K/Al [mol:mol]	K/Si* [norm.]	H_2O^+/Si* [norm.]
KM13-1	c	8.6	MS	80.69	0.35	8.57	4.31	0.07	1.37	0.37	0.95	2.14	0.07	2.41		0.27	0.053	
KM13-14-f	f	8.8	MS	69.66	0.66	13.73	4.91	0.05	1.66	0.25	0.73	2.9	0.04	4.39		0.23	0.051	
KM13-13-c	c	9	MS	79	0.5	9.3	3.33	0.09	0.9	0.34	0.95	1.99	0.1	2.63		0.23	0.046	
KM13-13-c-nan	c	9	MS	78.78	0.55	9.97	3.58	0.09	0.93	0.43	1.02	2.22	0.11	2.83		0.24	0.049	
KM13-13-f	f	9	MS	64.19	0.72	19.06	5.3	0.06	1.75	n.d.	0.86	3.64	0.04	5.63		0.21	0.049	
KM13-13-f-nan	f	9	MS	63.48	0.71	17.63	5.5	0.06	1.73	0.31	0.82	3.87	0.04	5.54		0.24	0.055	
KM13-23-c	c	9.7	MS	80.73	0.32	8.91	3.96	0.05	0.91	0.17	0.87	2.16	n.d.	2.48	2.01	0.26	0.052	0.323
KM13-23-c-dup	c	9.7	MS	80.86	0.32	8.95	3.97	0.05	0.91	0.16	0.91	2.11	0.08	2.48		0.26	0.051	
KM13-23-f	f	9.7	MS	73.9	0.55	10.98	4.2	0.06	1.56	0.32	0.9	2.54	0.08	3.52	2.45	0.25	0.053	0.294
KM13-12-c	c	10	MS	82.89	0.25	8.52	2.75	0.04	0.76	0.18	1.11	2	0.06	2.51		0.25	0.049	
KM13-12-f bis	f	10	MS	55.16	0.78	21.93	7.26	0.07	2.44	n.d.	0.45	4.69	0.07	7.01		0.23	0.055	
KM13-11-c	c	10.5	LS	79.52	0.45	9.18	3.16	0.07	1.24	0.69	1	2.22	0.08	3.32		0.26	0.053	
KM13-11-c-dup	c	10.5	LS	79.37	0.46	9.27	3.16	0.07	1.24	0.68	1.01	2.22	0.08	3.32		0.26	0.052	
KM13-11-f	f	10.5	LS	76.88	0.45	9.17	3.66	0.08	1.34	0.89	0.89	2.13	0.08	3.37		0.25	0.051	
KM13-10-c	c	11	LS	77.17	0.57	9.23	4.19	0.05	1.08	n.d.	0.82	2.21	0.03	3.81	2.59	0.26	0.052	0.383
KM13-10-f	f	11	LS	57.16	0.72	19.85	6.96	0.06	3.03	0.66	0.73	4.58	0.11	6.44	4.56	0.25	0.059	0.258
KM13-25	f	11.1	LS	54.56	0.72	15.56	5.69	0.16	3.58	5.86	0.72	3.5	0.1	10.34		0.24	0.056	
KM13-9	c	11.1	LS	66.93	0.48	9.83	3.43	0.06	2.32	5.52	0.94	2.18	0.09	7.66		0.24	0.051	
KM13-7-c	c	11.6	LS	73.55	0.3	7.48	2.24	0.14	1.17	5.86	0.87	1.69	0.07	5.63		0.24	0.047	
KM13-7-f	f	11.6	LS	68.72	0.78	15.74	4.98	0.04	1.91	n.d.	0.78	3.53	0.02	4.49		0.24	0.055	
KM13-8	c	12	LS	81.83	0.45	8.4	3.36	0.04	0.86	n.d.	1.01	1.98	0.08	2.41		0.26	0.05	
KM13-26-c	c	12.3	LS	83.2	0.39	7.33	2.49	0.04	0.57	n.d.	0.77	1.71	0.08	1.98		0.25	0.046	
KM13-26-f	f	12.3	LS	66.43	0.75	15.42	7.34	0.22	1.39	n.d.	0.79	3.13	0.2	5.08		0.22	0.05	
KM13-6-c-bis	c	12.8	LS	82.64	0.41	8.25	2.84	0.06	0.8	n.d.	0.96	1.99	n.d.	1.97	1.43	0.26	0.05	0.269
KM13-6-c-nan	c	12.8	LS	82.31	0.46	8.13	3.05	0.06	0.81	0.47	0.94	2.13	0.1	1.92		0.28	0.055	
KM13-6-f	f	12.8	LS	66.33	0.65	14.6	5.91	0.06	1.6	0.07	0.79	3.17	0.05	4.05	3.88	0.23	0.053	0.322
KM13-6-f-nan	f	12.8	LS	66.13	0.71	16.07	6.21	0.06	1.65	0.17	0.71	3.78	0.06	4.08		0.25	0.058	
KM13-6-nodule	f	12.8	LS	66.37	0.69	13.62	4.68	0.04	1.41	0.06	0.64	3.12	0.02	5.2		0.25	0.055	
KM13-5-c	c	13	LS	87.1	0.27	9.74	0.12	n.d.	n.d.	n.d.	0.08	0.14	0.02	4		0.02	-0.002	
KM13-5-f	f	13	LS	68.52	1.11	22.42	0.34	n.d.	0.02	n.d.	0.14	0.39	0.09	8.53		0.02	0.008	

Table 4.1: Major Element concentration (cont.)

Sample	Grain-size	Age [Ma]	Lith. Unit	SiO_2	TiO_2	Al_2O_3	Fe_2O_3 t	MnO	MgO	CaO	Na_2O	K_2O	P_2O_5	LOI	H_2O^+	K/Al [mol:mol]	K/Si* [norm.]	H_2O^+/Si^* [norm.]
HK14-19-c	c	0.5	US	72.75	0.66	10.21	5.49	0.1	1.43	0.19	0.27	1.8	0.12	5.66	3.47	0.19	0.041	0.442
HK14-19-f	f	0.5	US	62.91	0.84	15.43	6.42	0.1	1.89	0.83	0.72	2.51	0.2	7.59	4.47	0.18	0.039	0.344
HK14-14-c	c	1.1	US	54.4	0.25	5.28	1.88	0.07	0.75	19.01	0.55	1.11	0.07	16.09		0.23	0.048	
HK14-14-f	f	1.1	US	68.02	0.63	11.4	4.5	0.07	1.62	2.59	0.5	2.02	0.09	7.51		0.19	0.042	
HK14-15-c	c	1.9	US	87.81	0.27	5.01	2.22	0.03	0.72	0.46	0.28	0.92	0.04	2.52	1.43	0.2	0.038	0.494
HK14-15-f	f	1.9	US	54.4	0.86	19.17	7.1	0.07	2.42	1.57	0.23	3.37	0.13	10	5.58	0.19	0.043	0.332
HK14-16-c	c	2.3	US	51.6	0.37	6.03	2.51	0.85	0.84	18.32	0.36	1.13	0.08	17.29		0.2	0.043	
HK14-16-f	f	2.3	US	68.96	0.64	11.11	4.53	0.05	1.61	1.76	0.45	1.99	0.12	7.61		0.19	0.042	
HK14-16-f-bis	f	2.3	US	69.21	0.64	11.1	4.55	0.05	1.63	1.72	0.45	2	0.11	7.61		0.2	0.042	
HK14-17-c	c	2.6	US	88.37	0.32	5.08	2.04	0.03	0.58	0.48	0.44	0.88	0.04	2.37		0.19	0.036	
HK14-17-f	f	2.6	US	53.11	0.71	18.32	6.55	0.06	2.3	0.86	0.34	3.28	0.09	14.7		0.19	0.044	
HK14-18-f	f	2.7	US	61.6	0.72	16.52	5.88	0.07	2.13	2.46	0.88	3.12	0.09	7.7		0.2	0.045	
HK14-13-c	c	2.8	US	76.86	0.31	8.49	2.29	0.05	1.22	1.68	1.12	1.75	0.09	4.38	1.65	0.22	0.047	0.283
HK14-13-c-dup	c	2.8	US	76.04	0.32	7.95	2.28	0.05	1.19	1.67	1.04	1.7	0.1	4.38		0.23	0.049	
HK14-13-f	f	2.8	US	52.18	0.75	19.3	7.16	0.08	3.35	1.54	0.53	4.23	0.08	9.75	5.43	0.24	0.053	0.318
HK14-13-f-bis	f	2.8	US	52.54	0.75	19.43	7.23	0.08	3.38	1.54	0.53	4.23	0.08	9.75		0.24	0.053	
HK14-10-c	c	3	US	65.78	0.3	6.89	2.32	0.17	0.83	10.95	1.13	1.4	0.08	9.15		0.22	0.046	
HK14-10-f	f	3	US	70.11	0.65	13.63	5.09	0.06	1.4	0.56	0.48	2.38	0.04	5.66		0.19	0.041	
HK14-10-f-dup	f	3	US	70.16	0.63	13.66	5.09	0.06	1.39	0.56	0.49	2.38	0.04	5.66		0.19	0.041	
HK14-9-c	c	3.1	US	56.09	0.56	5.64	3.1	0.25	0.53	17.66	0.72	0.89	0.58	14.15		0.17	0.035	
HK14-9-f	f	3.1	US	61.09	0.75	17.47	3.94	0.04	1.5	0.27	0.33	2.98	0.03	10.47		0.18	0.041	
HK14-8-f	f	3.3	US	56.16	0.76	17.34	7.2	0.09	3.54	1.05	0.77	3.68	0.11	9.26		0.23	0.051	
HK14-7-f	f	3.5	US	68.92	0.67	12.22	5.05	0.05	1.4	0.36	0.5	2.21	0.04	8.81		0.2	0.043	
HK14-7-f-bis	f	3.5	US	68.84	0.66	12.15	5.03	0.05	1.41	0.24	0.5	2.2	0.04	8.81		0.2	0.043	
HK14-6-c	c	3.8	US	79.64	0.54	8.96	2.78	0.05	1.1	0.37	1	1.69	0.12	4.04	1.88	0.2	0.043	0.301
HK14-6-f	f	3.8	US	61.96	0.74	16.49	6.4	0.07	1.58	0.49	0.53	2.68	0.08	9.27	4.85	0.18	0.039	0.346
HK14-5-c	c	4	US	68.86	0.38	7.08	2.39	0.37	1.08	7.97	0.69	1.42	0.08	9.69		0.22	0.046	
HK14-5-f	f	4	US	59.84	0.65	16.7	6.17	0.06	2.33	1.85	0.84	3.56	0.1	7.71		0.23	0.051	
HK14-4-c	c	4.6	US	87.73	0.26	3.57	2.82	0.02	0.56	n.d.	0.26	0.82	n.d.	2.08		0.25	0.046	
HK14-4-c-bis	c	4.6	US	86.76	0.26	3.54	2.82	0.02	0.57	n.d.	0.26	0.82	n.d.	2.08		0.25	0.047	
HK14-4-f	f	4.6	US	57.96	0.76	17.7	7.22	0.07	1.92	0.23	0.32	3.13	n.d.	11.03		0.19	0.043	
HK14-3-c	c	4.9	US	76.65	0.41	9.42	3.19	0.1	1.31	0.79	1.05	1.9	n.d.	4.06	2.15	0.22	0.047	0.314
HK14-3-f	f	4.9	US	55.62	0.73	17.02	6.35	0.09	3.08	1.53	0.75	3.7	0.1	8.91	4.39	0.24	0.052	0.296
HK14-2-c	c	5.2	US	79.38	0.36	8.34	3.11	0.06	1.16	1.41	1.17	1.65	0.08	2.64		0.21	0.045	
HK14-2-f	f	5.2	US	54.21	0.73	18.55	6.72	0.07	3.24	2.05	0.92	4.36	0.11	9.46		0.25	0.057	
HK14-11-c	c	5.3	US	77.24	0.37	7.54	5.79	0.45	1.06	0.19	0.82	1.63	0.06	4.17		0.23	0.049	
HK14-11-f	f	5.3	US	54.29	0.69	17.22	7.77	0.08	3.39	0.67	0.72	3.65	0.09	10.87		0.23	0.051	
HK14-11-f-bis	f	5.3	US	53.42	0.69	17.13	7.74	0.08	3.38	0.72	0.72	3.61	0.09	10.87		0.23	0.051	
Hk14-12-c	c	5.7	MS	50.2	0.39	5.37	2.66	0.15	0.96	21.8	0.54	1.09	0.08	17.61		0.22	0.046	
HK14-12-f	f	5.7	MS	66.49	0.69	11.51	4.47	0.07	1.94	2.54	0.72	2.07	0.24	9.38		0.19	0.043	
HK14-1-c	c	5.8	MS	74.18	0.38	7.39	3.12	0.1	1.01	4.87	0.7	1.46	0.14	6.23	1.67	0.21	0.045	0.334
HK14-1-f	f	5.8	MS	61.14	0.72	15.3	7.71	0.08	2.8	0.74	0.67	3.41	0.15	6.21	4.27	0.24	0.053	0.33
HK14-1-f2	f	5.8	MS	62.63	0.7	15.99	6.86	0.06	2.82	0.54	0.56	3.62	0.12	7.09		0.24	0.054	
HK14-1-f-bis	f	5.8	MS	60.98	0.72	15.34	7.72	0.08	2.81	0.63	0.66	3.42	0.15	6.21		0.24	0.053	

Table 4.1: Major Element concentration (cont.)

Sample	Grain-size	Age [Ma]	Lith. Unit	SiO_2	TiO_2	Al_2O_3	Fe_2O_3 t	MnO	MgO	CaO	Na_2O	K_2O	P_2O_5	LOI	H_2O^+	K/Al [mol:mol]	K/Si* [norm.]	H_2O^+/Si* [norm.]
JW14-1-m	c	5	US	44.18	1.55	18.48	15.39	0.26	1.13	0.34	0.84	2.29	0.16	15.54		0.13	0.031	
JW14-1-f	f	5	US	59.07	1.01	13.26	9.03	0.06	0.5	0.1	0.08	1.66	0.09	15.91		0.14	0.03	
JW14-2-c bis	c	5.4	US	66.95	0.33	8.07	2.44	0.05	3.16	5.9	0.81	3.04	0.1	9.32	1.45	0.41	0.088	0.256
JW14-2-f	f	5.4	US	54.18	0.61	11.27	4.88	0.11	4.44	4.49	0.26	2.97	0.14	16.74	3.43	0.29	0.063	0.371
JW14-3-c	c	5.6	US	76.64	0.46	8.93	2.61	0.04	1.55	1.68	0.34	2.94	0.09	4.84		0.36	0.077	
JW14-3-f	f	5.6	US	52.31	0.66	14.1	6.22	0.13	3.96	3.23	0.11	2.94	0.14	15.42		0.23	0.05	
JW14-4-c	c	6	US	60.73	0.3	7.89	1.93	0.05	4.68	7.67	0.09	2.93	0.09	14.72		0.4	0.087	
JW14-4-f	f	6	US	39.43	0.33	7.63	2.09	0.07	8.47	15.25	0.07	2.5	0.09	25.32		0.35	0.078	
JW14-5-c	c	6.2	US	65.37	0.38	10.23	3.11	0.04	3.11	5.21	0.13	2.48	0.08	10.44		0.26	0.057	
JW14-5-f	f	6.2	US	65.02	0.62	16.03	4.93	0.04	2.22	0.82	0.1	3.31	0.09	6.86		0.22	0.05	
JW14-6-cs	c	6.8	US	4.46	0.03	0.61	0.12	0.32	0.51	48.01	0.05	0.2	0.01	41.6		0.35	0.076	
JW14-6b-f	f	6.8	US	27.75	0.25	5.89	2.14	0.25	1.35	32.41	0.18	1.32	0.04	28.57		0.24	0.053	
JW14-6-f	f	6.8	US	56.46	0.67	14.47	5.8	0.04	2.96	2.14	0.23	2.69	0.17	14.34		0.2	0.045	
JW14-7-c	c	7.2	MS	73.95	0.55	11.18	3.68	0.04	1.45	0.37	1	2.37	0.09	4.45	2.67	0.23	0.05	0.31
JW14-7-f	f	7.2	MS	52.52	0.61	17.5	7.19	0.08	3.29	3.71	0.13	3.71	0.12	12.77	4.84	0.23	0.051	0.316
JW14-8-c	c	7.9	MS	76.3	0.44	10.53	3.47	0.03	1.28	0.36	0.64	2.23	0.1	4.61		0.23	0.049	
JW14-8-f	f	7.9	MS	73.67	0.61	11.85	4.79	0.09	1.45	0.05	0.27	2.12	0.05	5.68		0.19	0.042	
JW14-22-c	c	8.3	MS	61.91	0.45	8.55	3.46	0.25	1.08	11.46	0.83	1.81	0.08	11.18		0.23	0.049	
JW14-22-f-bis	f	8.3	MS	48.72	0.58	15.72	6.92	0.09	2.21	8.39	0.16	3.03	0.02	14.02		0.21	0.047	
JW14-9-c	c	8.6	MS	61.97	0.41	8.75	3.11	0.2	0.91	11.2	0.76	1.76	0.08	11.21		0.22	0.047	
JW14-10-c	c	9	MS	68.65	0.39	9.59	2.94	0.06	2	5.7	0.77	2.02	0.09	8.38	2.11	0.23	0.049	0.293
JW14-10-f	f	9	MS	59.37	0.65	13.36	5.63	0.07	2.59	3.56	0.26	2.83	0.16	10.32	4.1	0.23	0.051	0.37
JW14-11-c	c	9.5	MS	75.53	0.43	11.02	4.1	0.06	1.11	0.16	0.98	2.3	0.08	3.36		0.23	0.049	
JW14-12-c	c	9.6	MS	62.7	0.38	8.78	2.83	0.11	1.91	10.21	0.79	1.78	0.08	11.1		0.22	0.047	
JW14-12-f	f	9.6	MS	61	0.68	18.19	6.97	0.03	2.21	0.5	0.15	3.57	0.02	6.78		0.21	0.047	
JW14-13-c	c	9.8	MS	69.89	0.45	10.92	4.19	0.07	1.83	3.16	1.03	2.17	0.1	6.19		0.22	0.047	
JW14-13-f	f	9.8	MS	50.49	0.6	19.77	7.43	0.06	2.99	0.32	0.5	3.95	0.11	13.23		0.22	0.049	
JW14-14-c	c	10	MS	60.22	0.25	8.12	1.83	0.21	0.96	12.69	0.84	1.91	0.21	12.28	1.72	0.25	0.055	0.286
JW14-14-f	f	10	MS	70.93	0.57	13.47	4.62	0.06	1.89	0.39	0.61	2.44	0.09	5.92	3.56	0.2	0.043	0.327
JW14-15-c	c	10.2	MS	73.43	0.34	9.76	2.55	0.03	1.71	3.16	1.08	2.18	0.09	5.59		0.24	0.052	
JW14-15-f	f	10.2	MS	58.35	0.59	12.42	4.71	0.12	3.83	5.89	0.57	2.46	0.14	10.75		0.21	0.047	
JW14-16-c	c	10.4	MS	79.11	0.4	9.66	2.82	0.02	1.04	0.22	0.85	2.04	0.06	3.46		0.23	0.049	
JW14-16-f	f	10.4	MS	75.28	0.67	10.32	4.39	0.05	1.18	0.05	0.57	1.96	0.04	4.57		0.21	0.044	
JW14-17-c	c	10.6	MS	81.17	0.46	8.12	2.91	0.1	0.86	0.83	0.73	1.5	0.09	3.38		0.2	0.042	
JW14-17-c-dup	c	10.6	MS	81.04	0.45	7.92	2.9	0.1	0.85	0.84	0.73	1.48	0.08	3.38		0.2	0.042	
JW14-17-f1	f	10.6	MS	59.43	0.69	18.46	6.2	0.05	2.55	0.21	0.67	3.76	0.11	7.16		0.22	0.049	
JW14-17-f2	f	10.6	MS	66.25	0.69	14.81	5.51	0.05	1.82	0.47	0.49	3.01	0.17	6.15		0.22	0.049	
JW14-18-c	c	10.9	MS	74.84	0.5	11.74	3.91	0.03	1.14	0.36	1.21	2.28	0.09	3.66	2.52	0.21	0.046	0.278
JW14-18-f	f	10.9	MS	61.7	0.54	10.89	4.61	0.38	1.45	8.62	0.92	1.88	0.19	10.21	2.65	0.19	0.041	0.305
JW14-19-c	c	11.3	LS	73.39	0.45	9.65	3.59	0.07	0.9	3.54	0.91	1.87	0.1	5.15		0.21	0.045	
JW14-19-f	f	11.3	LS	78.01	0.59	9.62	4.08	0.07	1.17	1.48	0.67	1.69	0.09	4.48		0.19	0.041	
JW14-20-c	c	11.9	LS	77.68	0.35	9.07	2.81	0.04	0.8	2.13	0.98	1.88	0	4.23		0.22	0.048	
JW14-20-f bis	f	11.9	LS	70.7	0.66	12.78	4.87	0.07	1.57	0.95	1.04	2.36	0.07	4.9		0.2	0.044	
JW14-21-c	c	12.3	LS	64.61	0.4	7.46	2.63	0.08	0.79	11.31	1.08	1.42	0.08	10.71	1.7	0.21	0.044	0.32
JW14-21-f	f	12.3	LS	56.63	0.64	14.65	6.63	0.19	1.85	7.01	0.84	2.94	0.13	10	3.58	0.22	0.048	0.286

Table 4.1: Major Element concentration (cont.)

Sample	Grain-size	Age [Ma]	Lith. Unit	SiO_2	TiO_2	Al_2O_3	Fe_2O_3 t	MnO	MgO	CaO	Na_2O	K_2O	P_2O_5	LOI	H_2O^+	K/Al [mol:mol]	K/Si* [norm.]	H_2O^+/Si* [norm.]
JN14-24-c	c	12.8	LS	91.28	0.4	3.96	1.92	0.02	0.26	n.d.	0.09	0.53	0.03	1.84		0.14	0.024	
JN14-24-f	f	12.8	LS	79.96	0.67	9.44	3.57	0.06	0.73	n.d.	0.38	1.58	0.04	5.29		0.18	0.038	
JN14-23-c	c	12.9	LS	91.64	0.31	4.66	1.58	0.02	0.34	n.d.	0.16	0.62	0.01	2.06	1.44	0.14	0.026	0.547
JN14-23-f	f	12.9	LS	61.89	0.7	17.69	6.11	0	1.35	0.15	0.23	3.14	0.03	9.68	5.1	0.19	0.043	0.336
JN14-22-c	c	13	UD	81.79	0.38	7.11	2.58	0.03	0.93	1.66	0.56	1.28	0.06	3.31		0.19	0.04	
JN14-22-f	f	13	UD	67.59	0.67	14.35	5.25	0.05	1.29	0.1	0.51	2.49	0.08	7.91		0.19	0.041	
JN14-21-c	c	13.5	UD	77.53	0.56	8.69	3.38	0.05	1.08	2.15	0.71	1.48	0.08	4.45	2.18	0.18	0.039	0.352
JN14-21-f	f	13.5	UD	62.25	0.75	18.76	6.35	0.06	1.92	0.08	0.52	3.46	0.04	6.62	4.99	0.2	0.045	0.306
JN14-20-c	c	13.9	UD	81.25	0.42	7.02	2.67	0.04	1.07	1.89	0.45	1.31	0.06	5.6		0.2	0.041	
JN14-20-f	f	13.9	UD	70.8	0.64	12.27	5.2	0.15	1.33	0.33	0.22	2.33	n.d.	6.82		0.21	0.045	
JN14-19-c	c	14.1	UD	76.72	0.55	9.34	3.37	0.04	1.24	2.39	0.78	1.7	0.07	4.47		0.2	0.042	
JN14-19-f	f	14.1	UD	53.97	0.68	19.51	7.96	0.12	2.17	1.09	0.13	3.99	0.15	10.56		0.22	0.05	
JN14-18-c	c	14.2	UD	81.87	0.34	6.36	2.49	0.05	0.76	2.62	0.51	1.17	0.06	3.65		0.2	0.041	
JN14-18-f	f	14.2	UD	57.29	0.67	19.68	6.84	n.d.	1.86	0.48	0.15	4.14	n.d.	9.06		0.23	0.051	
JN14-17-c	c	14.6	UD	82.11	0.33	5.81	1.92	0.04	0.7	3.11	0.46	1.07	0.05	4.03	1.36	0.2	0.04	0.391
JN14-17-f	f	14.6	UD	71.64	0.67	13.09	3.87	n.d.	1.49	0.21	0.79	2.09	n.d.	6.51	3.45	0.17	0.038	0.328
JN14-16-c	c	14.8	UD	72.77	0.47	8.21	3.09	0.07	1.2	4.78	0.91	1.51	0.08	7.21		0.2	0.042	
JN14-16-f	f	14.8	UD	70	0.68	14.3	5.39	n.d.	1.6	0.36	0.7	2.74	0.07	5.61		0.21	0.046	
JN14-15-c	c	14.9	UD	77.14	0.41	7.56	2.77	0.04	1.2	3.63	0.68	1.31	0.07	4.31		0.19	0.039	
JN14-15-f	f	14.9	UD	56.07	0.73	19.85	8.13	0.13	2.35	0.24	0.22	3.98	0.09	8.86		0.22	0.049	
JN14-14-c	c	15.1	UD	84.66	0.4	7.47	2.38	0.01	0.6	0.05	0.29	1.29	n.d.	2.74		0.19	0.038	
JN14-14-f	f	15.1	UD	64.5	0.73	16.37	5.69	n.d.	1.2	n.d.	0.29	3.01	n.d.	8.51		0.2	0.044	
JN14-13-c	c	15.7	UD	79.68	0.45	8.67	3.12	0.04	0.77	0.08	0.39	1.43	0.07	3.3	2.38	0.18	0.037	0.384
JN14-13-f	f	15.7	UD	55.42	0.68	20.57	7.24	n.d.	2.05	n.d.	0.17	4.09	0.08	10.11	5.48	0.22	0.048	0.3
JN14-12-c	c	16.4	UD	73.59	0.46	7.82	2.91	0.06	1.11	5.49	0.68	1.35	0.09	6.74		0.19	0.039	
JN14-12-f	f	16.4	UD	52.99	0.71	19.22	8.21	0.08	2.23	3.25	0.35	3.74	0.13	10.17		0.21	0.047	
JN14-11-c	c	16.5	UD	75.7	0.36	8.16	2.89	0.04	0.98	3.57	0.75	1.3	0.07	5.44		0.17	0.036	
JN14-11-c-dup	c	16.5	UD	76.57	0.37	8.32	2.94	0.04	1	3.63	0.75	1.33	0.08	5.44		0.17	0.036	
JN14-11-f	f	16.5	UD	53.48	0.72	16.7	7.25	0.06	1.98	5.61	0.46	3.3	0.13	10.95		0.21	0.048	
JN14-11-f dup	f	16.5	UD	53.61	0.74	16.24	7.24	0.06	1.99	5.62	0.45	3.21	0.13	10.95		0.21	0.048	
JN14-10-c	c	16.9	LD	73.49	0.43	7.46	2.93	0.05	1.14	5.88	0.74	1.37	0.09	7	1.7	0.2	0.041	0.334
JN14-10-f	f	16.9	LD	58.06	0.66	19.1	7.62	0.07	2.29	0.39	0.54	3.94	0.13	6.83	4.84	0.22	0.05	0.288
JN14-9-c	c	17.1	LD	72.71	0.34	5.84	2.23	n.d.	0.91	8.56	0.56	1.02	0.07	8.97		0.19	0.038	
JN14-9-f	f	17.1	LD	56.64	0.68	19.89	6.88	0.05	2.06	0.5	0.44	4.08	0.12	8.93		0.22	0.05	
JN14-8-c	c	17.4	LD	81.19	0.47	8.67	3.01	n.d.	0.95	0.31	1.11	1.25	0.11	2.91		0.16	0.032	
JN14-8-f	f	17.4	LD	55.17	0.62	16.42	6.17	0.11	2.13	5.76	0.75	3.49	0.21	10.16		0.23	0.051	
JN14-7-c	c	17.9	LD	83.06	0.34	8.46	2.64	n.d.	0.7	n.d.	0.76	1.47	0.04	2.67		0.19	0.039	
JN14-7-f	f	17.9	LD	73.94	0.52	11.47	4.69	0.08	1.27	0.92	0.51	2.18	0.06	4.93		0.21	0.045	

Table 4.1: Major Element concentration (cont.)

Sample	Grain-size	Age [Ma]	Lith. Unit	SiO_2	TiO_2	Al_2O_3	Fe_2O_3 t	MnO	MgO	CaO	Na_2O	K_2O	P_2O_5	LOI	H_2O^+	K/Al [mol:mol]	K/Si* [norm.]	H_2O^+/Si* [norm.]
JN14-6-c	c	18.5	LD	84.87	0.33	7.71	2.47	n.d.	0.64	0.12	0.79	1.29	0.05	2.46	1.62	0.18	0.037	0.325
JN14-6-f	f	18.5	LD	61.34	0.63	18.99	5.94	n.d.	1.84	0.28	0.49	4.21	0.05	6.18	4.32	0.24	0.053	0.257
JN14-5-c	c	19	LD	83.91	0.34	8.02	2.65	n.d.	0.85	0.15	0.79	1.5	0	2.44		0.2	0.042	
JN14-5-f	f	19	LD	61.25	0.78	17.06	6.8	0.07	2.33	0.78	1.04	3.37	0.14	6.12		0.21	0.048	
JN14-3-c	c	19.7	LD	82.8	0.33	8.16	2.71	n.d.	0.75	0.15	0.96	1.41	0.07	2.58	1.73	0.19	0.039	0.317
JN14-3-f	f	19.7	LD	63.3	0.59	17.02	4.79	0.11	1.81	2.56	0.92	3.75	0.15	6.64	3.47	0.24	0.053	0.234
JN14-2-c	c	20.1	LD	78.56	0.44	8.33	3.07	0.07	0.99	1.72	0.86	1.46	0.1	3.51		0.19	0.04	
JN14-2-f	f	20.1	LD	69.13	0.53	13.99	5.45	0.1	1.95	0.75	1.04	2.78	0.15	4.35		0.22	0.047	
JN14-1-c	c	20.5	LD	77.75	0.49	8.65	2.82	0.07	0.94	3.14	0.96	1.53	0.08	4.35	1.75	0.19	0.04	0.292
JN14-1-f	f	20.5	LD	48.69	0.52	13.94	5.57	0.18	2.05	12.07	0.8	2.87	0.11	13.4	3.19	0.22	0.05	0.262
JN14-2-f2	f	21.1	LD	66.7	0.6	14.68	5.74	0.07	1.84	1.82	0.67	3.06	0.06	5.57		0.23	0.05	
Beas-f	f	0	modern	62.62	0.7	16.33	6.14	0.09	2.72	1.24	1.73	3.51	0.16	4.99	2.99	0.23	0.052	0.209
Somb-f	f	0	modern	62.3	0.65	15.72	5.73	0.09	2.05	2.17	0.58	2.79	0.08	8.24		0.19	0.043	
Somb-f-DUP	f	0	modern	62.35	0.67	15.56	5.72	0.09	2.05	2.16	0.58	2.75	0.08	8.24		0.19	0.043	
Jner Khad-f	f	0	modern	74.42	0.63	8.97	5.23	0.08	1.53	1.77	0.79	2.34	0.08	5.52		0.28	0.061	

nan: measured in Nancy

Table 4.2: International Standards and Average Accuracy of the Analysis

Standards [measured]	SiO_2	TiO_2	Al_2O_3	Fe_2O_3 t	MnO	MgO	CaO	Na_2O	K_2O	P_2O_5
JSd1	66.57	0.65	14.64	4.92	0.09	1.78	2.98	2.67	2.1	0.12
JSd2	60.68	0.59	12.44	11.4	0.12	2.73	3.65	2.38	1.12	0.1
BCR-2	54.15	2.26	13.59	13.88	0.2	3.61	7.21	3.1	1.79	0.32
BEN	38.38	2.64	9.91	12.77	0.2	13.25	13.79	3.22	1.46	1.06

Devation from international Std. [%]	SiO_2	TiO_2	Al_2O_3	Fe_2O_3 t	MnO	MgO	CaO	Na_2O	K_2O	P_2O_5
JSd1	0.04	-1.22	0.4	2.77	-3.27	1.83	1.58	2.28	3.63	1.19
JSd2	0.19	4.08	-1.1	2.61	0.35	-0.03	0.37	2.62	2.27	6.51
BCR-2	-0.09	0.07	-0.65	-0.6	0.15	-0.54	-1.3	1.85	-0.19	9.48
BEN	-0.47	-0.96	1.57	0.55	0.66	-0.76	0.6	-1.1	-5.12	-1.28
Average accuracy per element [%]	0.2	1.58	0.93	1.63	1.11	0.79	0.96	1.96	2.8	4.61
Average accuracy [%]	1.66									

Table 4.3: Normalization for K/Si and H_2O^+/Si

Grainsize Normalization Kameng section

coarse endmember Al/Si	coarse endmember K/Si	coarse endmember H_2O^+/Si	average Al/Si
0.0	0.0082	-0.0491	0.22
K/Si linear regression y=0.1903x+0.0082			
H_2O^+/Si linear regressiony=1.4615x-0.0491			

linear regression from average fine-grained and average coarse-grained

Grainsize Normalization Western section

coarse endmember Al/Si	coarse endmember K/Si	coarse endmember H_2O^+/Si	average Al/Si
0.0	0.0023	-0.0617	0.22
K/Si linear regression y=0.0205x+0.0023			
H_2O^+/Si linear regression y=1.6975x-0.0603			

linear regression from average fine-grained and average coarse-grained

Appendix 4.2

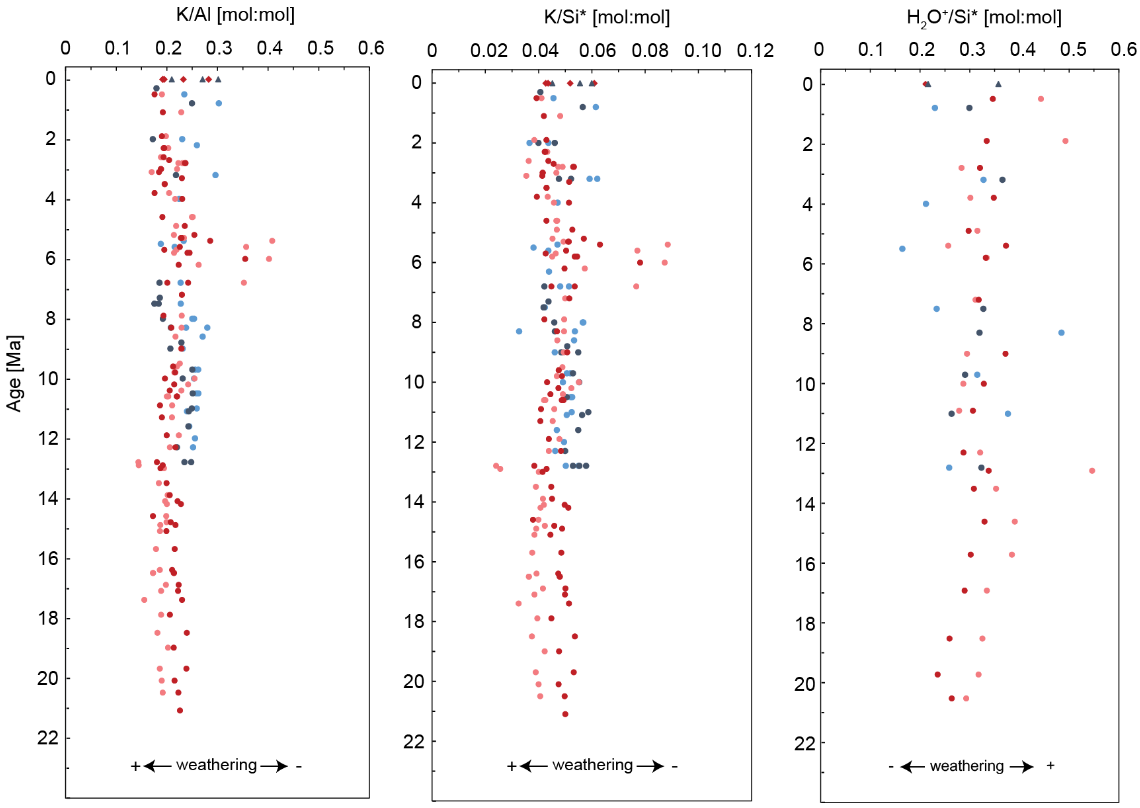

Figure 4.10: H_2O^+/Si^* vs age

Appendix 4.3

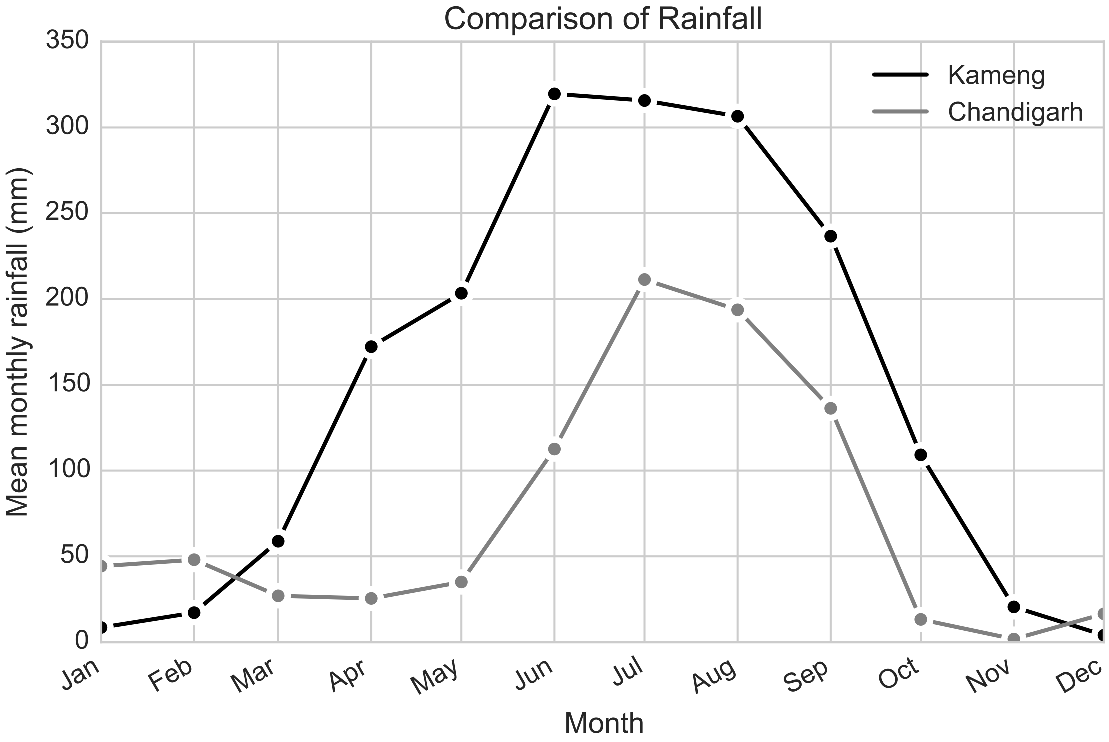

Figure 4.11: Western and eastern annual rainfall distribution, from (TRMM) Multi-satellite Precipitation Analysis (TMPA) - 3B42 V7, averaged over each month. Showing a clear difference between the more humid east and the drier west.

Chapter 5

Lithium isotope record of the Siwalik Group- a new approach to studying paleo-weathering regimes

Abtract

Chemical weathering of continental rocks plays an important role in the carbon cycle. Physical erosion and runoff, together with temperature, are limiting factors for chemical weathering (West et al., 2005). The Himalayan range has a major influence on global and regional climate; the orogen is a key laboratory to study the link between tectonics, erosion and climate and its implication for chemical weathering and the global carbon cycle. The sedimentary foreland basin of the Himalaya contains a proximal record of tectonics and paleoclimate since Miocene times, within the so called pre-Siwalik and Siwalik Group. Several sedimentary sections within the foreland basin have previously been dated and studied with respect to determining hinterland exhumation rates, provenance and paleoclimatology (Quade et al., 1995; DeCelles et al., 1998b; Huyghe et al., 2005; van der Beek et al., 2006, amongst others). Paleo weathering rates and intensities remain hard to reconstruct and are still not completely understood. In recent years, lithium isotopic compositions of river waters and associated sediments have been used to infer chemical weathering as these are promising tracers of silicate weathering (Kisakürek et al., 2005; Dellinger et al., 2014, 2015). Here, we present results of lithium isotopic composition, applied for the first time on Miocene pre-Siwalik and Siwalik sediments. We sampled sections located both in the western and eastern Himalaya. We used the newly developed method of Bohlin et al. (prep) to measure δ^7Li on bulk sediments.

δ^7Li values on bulk sediment in the western Himalaya increase from -8 ‰ to -4 ‰, the modern Beas river has a value of -12 ‰. In the eastern Himalaya values are relatively constant at a value of ~-7 ‰. Our preliminary interpretation suggests a shift towards more congruent weathering in the west and constant, more incongruent weathering in the east.

5.1 Introduction

Chemical weathering of continental rocks has a long-term influence on the carbon cycle and the Earth's climate (Berner et al., 1983; Walker et al., 1981). Together with organic carbon burial, the intensity of silicate weathering plays a central role in atmospheric CO_2 drawdown. Physical erosion and runoff, together with temperature, are limiting factors for chemical weathering e.g. (West et al., 2005), which make understanding interactions between erosion and climate crucial. It is critical to understand how changes in climate influence chemical weathering in order to determine the long-term behavior of the carbon cycle. Atmospheric CO_2 has an influence on global temperature, which in turn influences climate and possibly weathering (e.g. Berner, 2004), thereby generating a powerful negative feedback loop. By understanding past variations of the carbon cycle, present and future variations can better be predicted.

Determining past weathering rates, as a function of climate or tectonic activity, remains challenging. Therefore, unraveling couplings of climate, erosion and tectonics in the Himalaya, one of the largest mountain belts on earth, is crucial to reconstruct the evolution of the mountain belt and the climate on a global scale. Osmium and strontium isotopes have been most widely used to investigate chemical weathering on a global scale. Strontium isotopes have been used to track chemical weathering (Raymo and Ruddiman, 1992; Derry and France-Lanord, 1996), but varying isotopic composition in the source area render interpretations ambiguous (Bickle et al., 2001; Oliver et al., 2003). While strontium isotopic composition is highly reflective of the bedrock and osmium isotopes are to a large extent indicating the exposure of black shales (Ravizza and Esser, 1993), lithium isotopes are fractionated mainly during weathering (Kisakürek et al., 2005). In recent years, lithium isotopic compositions of river waters and associated sediments have been used as a proxy for chemical weathering intensity (Huh et al., 2001; Kisakürek et al., 2005; Dellinger et al., 2014, 2015). Lithium is the lightest alkali element and has two stable isotopes,^{6}Li and ^{7}Li (7.52 % ^{6}Li and 92.48 % ^{7}Li). It has several advantages as a tracer for weathering: 1) its two isotopes have a large relative mass difference; 2) lithium is not critical in biological or atmospheric cycles like other tracers such as oxygen, carbon or calcium isotopes; 3) it is relatively uniformly distributed in the Earth's crust (Pistiner and Henderson, 2003). Lithium is highly enriched in silicates and largely depleted in carbonate, which makes it an excellent proxy for silicate weathering (Vigier et al., 2008). Silicate rocks have a narrow range of δ^7Li (continental crust with an average of ~0‰ and an average basalt with ~2-5‰ (Teng et al., 2004). δ^7Li values of the Earth's surface environment in turn span ~35 ‰ (Huh et al., 1998; Pistiner and Henderson, 2003; Kisakürek et al., 2005). Modern seawater has a δ^7Li value of ~ +31‰ (Chan and Edmond, 1988). δ^7Li of modern river waters range from ~+6 ‰ to +42 ‰, with an average of +23 ‰ (Burton and Vigier, 2011). Changes in δ^7Li in the Earth's surface environment can therefore bear important information on chemical weathering.

Weathering systems can be congruent or incongruent, depending on the limiting factor of the system, being transport- or weathering-limited, respectively (e.g. Misra and Froelich, 2012; West et al., 2005). When weathering is congruent, all weathering products are dissolved and the degree of weathering is limited only by the supply of material (transport-limited), this results in thicker soils (Huh et al., 2001; West et al., 2005). In case of congruent weathering, river water δ^7Li values are similar to rock values (Pogge von Strandmann et al., 2010, 2013). (Pogge von Strandmann et al., 2010; Pogge von Strandmann et al., 2013). On the other hand, when weathering is incongruent, the regime is weathering limited, with formation of secondary minerals and rather thin soils (West et al., 2005). In this case the δ^7Li of river water is different from the host rock as ^{6}Li is preferentially taken up by clays (Kisakürek et al., 2005; Pogge von Strandmann et al., 2010). There is a positive correlation of δ^7Li of suspended river sediments and δ^7Li bed sediments, where suspended sediments, which contain the clay fraction have slightly lower δ^7Li (Kisakürek et al., 2005). Kisakürek et al. (2005) suggest that weathering intensity can be constrained from differences between δ^7Li of suspended load and the δ^7Li of dissolved load. Li-isotopic compositions of waters are largely overlapping in rivers draining carbonate and silicate lithology (Kisakürek et al., 2005). Solid weathering products can therefore be used as a tracer of chemical weathering (Burton and Vigier, 2011).

Lithium isotopes have been used to unravel the coupling between climate and weathering on a global scale, by using seawater Li isotopes (Misra and Froelich, 2012). The long-term marine record shows a stepwise +9 ‰ increase in δ^7Li of seawater since the early Cenozoic with a significant shift during the Middle-Late Miocene (Misra and Froelich, 2012). This is interpreted as being the result of major tectonic events such as the uplift of the Himalayas and Cenozoic cooling, which shifted weathering regimes from transport-limited to weathering-limited, hence δ^7Li in the dissolved load became more positive, due to more depleted lithium being carried in clays (Misra and Froelich, 2012; Wanner et al., 2014). Others argue that the variation of δ^7Li in seawater is due to storage of Li in secondary phases on the continents during Paleocene and Eocene, so that the role of erosion and uplift is still uncertain (Vigier and Goddéris, 2015). δ^7Li of river waters and sediments and Holocene clays in fluvial terraces have been used to reconstruct weathering rates in the Himalayan region on shorter timescales (Dosseto et al., 2015). Holocene records of weathering in the Himalaya show a decrease in weathering, and increasing δ^7Li from 25 ka on and suggest that weathering is inhibited due to an increase in runoff and physical erosion with temperature only playing a secondary role (Dosseto et al., 2015).

The Himalayan foreland basin sediments provide a proximal record of erosion, climate and weathering since Miocene times. They span the entire mountain front, allowing a comparison between the western and the eastern part of the orogeny. Here we present for the first time results of δ^7Li in bulk sediments of proximal sedimentary records in the western and eastern Himalaya, in order to reconstruct the weathering history since Miocene times in the Himalaya.

5.2 Sampling and methods

5.2.1 Sampling

Samples were collected from sedimentary sections in the Himalayan foreland basin, in both the so-called pre-Siwalik (Dharamsala Formation) and Siwalik Group. In the western part of the Himalaya samples of the Joginder Nagar, Jawalamukhi and Haripur Kolar sections were collected. In the eastern part, we sampled along the Kameng river section (Figure 5.1). All sections have previously been dated by magnetostratigraphy (Meigs et al., 1995; Sangode et al., 1996; White et al., 2001; Chirouze et al., 2012). To have a continuous age record, 2-3 samples per Ma were collected, according to the magnetostratigraphic sampling points. Stratigraphic profiles of the sections are described in chapter 1.

5.2.2 Method

A total of 31 selected fine-grained samples from the Joginder Nagar, Jawalamukhi, Haripur Kolar and the Kameng sections were prepared for analyses of lithium concentration and lithium isotopes. Two Modern river mud samples of the Kameng and Beas Rivers were also treated.

The complete description of the method can be found in Bohlin et al. (prep). δ^7Li and Li concentration were analyzed on 21 bulk samples from the western Himalaya and 12 from the eastern Himalaya, respectively. All samples were grinded and ignited in a furnace at 950°C for 8 hours to eliminate organic matter. Ca 30 mg of each sample was treated with a 1:4 mixture of H_2O_2:HNO_3 and left at 70°C overnight, in order to dissolve remaining organic matter. The residue was then dissolved in 4ml of a mixture of HNO_3, HCl and HF, all concentrated and at a ratio of 1:1:1. After dissolution, the samples were dried down and taken up in 1 ml 6N HCl for storage. All acids used in the procedure (and all

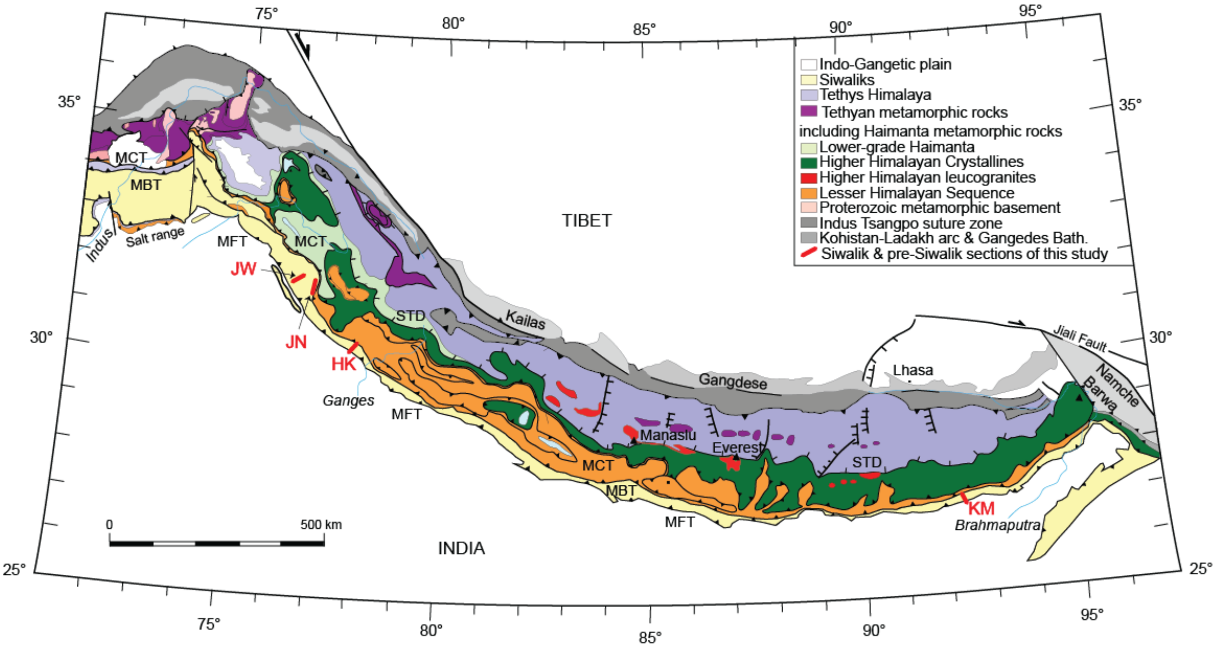

Figure 5.1: Geological map of the Himalaya modified after Guillot et al. (2008). Sampled Siwalik sections are indicated in red. JN: Joginder Nagar; JW: Jawalamukhi; HK: Haripur Kolar; KM: Kameng.

following procedures) were doubly distilled. Li concentration was measured by ICP-MS (ElementXR) at the University of Cambridge against an inhouse standard with an external reproducibility of better than 5%.

A quantitative separation of Li from matrix elements is crucial for accurate and precise isotopic measurements. The method of Bohlin et al. (prep) uses a single column passing to effectively separate Li from Na, Al and Ti, which all have significantly higher concentrations than Li in the sediments. Aliquots were collected right before and after the Li cut to ensure a 100% yield, which is essential as the Li isotopes fractionate heavily in the columns. The columns were typically loaded with 5-10 ng Li, which is fully eluted in a 10 mL cut. Each column batch included a standard (international reference material; BHVO2) to ensure reproducibility. When eluted, the cut was evaporated to dryness and refluxed in concentrated HNO_3 overnight to eliminate organics that might have come off the columns. The sample was then dried down again before being taken up in 2% HNO_3, ready to be analyzed for isotopic composition by MC-ICP-MS (Neptune PLUS) at the University of Cambrdige, United Kingdom.

5.3 Results

In this study we measured δ^7Li on bulk sediment without removing exchangeable surface lithium. Observed changes in δ^7Li therefore have to be interpreted with care and compared to other proxies, such as clay mineralogy and major elements, in order to be sure that variations reflect changes in weathering

Sample	Age [Ma]	Lithological Unit	Section	Li [ppm]	Average Li [ppm]	Average 2stdev	δ^7Li [‰]	2stdev	Average δ^7Li [‰]	Average 2stdev
JN14-23-f	12.9	LS	JN	50.51			-6.68	0.13		
JN14-21-f	13.5	Upper Dharamsala	JN	53.52			-6.43	1.2		
JN14-17-f	14.6	Upper Dharamsala	JN	39.53			-5.87	0.16		
JN14-13-f	15.7	Upper Dharamsala	JN	52.01			-8.38	0.17		
JN14-10-f	16.9	Lower Dharamsala	JN	50.92			-6.77	0.11		
JN14-6-f	18.5	Lower Dharamsala	JN	54.08			-8.18	0.14		
JN14-3-f	19.7	Lower Dharamsala	JN	40.03	JN		-7.82	0.19	JN	
JN14-1-f	20.5	Lower Dharamsala	JN	28.08	48.66	12.4	-6.55	0.74	-7.16	1.92
JW14-2-f	5.4	US	JW	49.48			-6.67	0.49		
JW14-4-f	6	US	JW	35.04			-9.09	0.4		
JW14-7-f	7.2	MS	JW	50.23			-5.27	0.2		
JW14-10-f	9	MS	JW	32.24						
JW14-14-f	10	MS	JW	43.82			-7.01	0.36		
JW14-18-f	10.9	MS	JW	33.42	JW		-6.41	0.25	JW	
JW14-21-f	12.3	LS	JW	32.92	38.15	16.94	-4.89	0.36	-6.56	2.72
HK14-15-f	1.9	US	HK	47.51			-5.15	0.22		
HK14-13-f	2.8	US	HK	61.9			-4.63	0.37		
HK14-6-f	3.8	US	HK	65.58						
HK14-3-f	4.9	US	HK	58.84	HK		-4.97	0.26	HK	
HK14-1-f	5.8	MS	HK	47.48	48.93	24.74	-6.27	0.16	-5.26	1.42
Holocene Terrasse	0.01	US	KM	29.28						
KM-13-20-f	0.8	US	KM	50.37			-6.69	0.34		
KM-13-28-f	3.2	MS	KM	28.35			-7.4	0.21		
KM-13-18 bis	4	MS	KM	22.35						
KM-13-17 bis	5.5	MS	KM	17.22			-6.83	0.29		
KM-13-4	6.8	MS	KM	26.6			-7.62	0.4		
KM-13-30-f	7.5	MS	KM	47.5			-6.94	0.95		
KM-13-15-f	8.3	MS	KM	31.37			-7.7	0.19		
KM-13-23-f	9.7	MS	KM	28.21			-7	0.31		
KM-13-10-f	11	LS	KM	39.09	KM		-6.24	0.35	KM	
KM-13-6-f	12.8	LS	KM	39.55	32.72	10.28	-7.65	0.34	-7.12	1.01
Kameng down f	0	modern		21.57			-7.37	0.15		
Beas-f	0	modern		120.96			-12.12	0.41		

Table 5.1: Lithium concentration and lithium isotopic composition

and cannot be attributed to changes in provenance or post-depositional alterations.

Lithium concentration and δ^7Li are reported in Table 5.1 and Figure 5.2. Lithium concentrations vary from ca. 20 to 70 ppm, except the modern Beas river sample, which contains 120 ppm Li. The average Li concentration of the Kameng Siwaliks is 33±10.3 ppm, in the west the average is slightly higher with 46±10.2 ppm. Modern Kameng river mud has a relatively low Li concentration of 21 ppm, especially compared to the modern Beas river mud in the west. The modern Beas river mud has an unusually high Li concentration and likewise and unusually low δ^7Li (Figure 5.2).

δ^7Li of the bulk sediments varies from – 4.63 ‰ to -9.09 ‰, with again the modern Beas river deviating with a value of -12.12 ‰. Average values of the sections are -7.09±0.96 ‰ for Joginder Nagar, -6.56±1.36 ‰ for Jawalamukhi, -5.26±0.71 ‰ for Haripur Kolar and -7.12±0.50 ‰ for Kameng, respectively. Values throughout the Kameng section are relatively constant, whereas in the west the values increase by ~4 ‰ between 20 and 1 Ma. In the west the general trend towards more positive values is interrupted by a negative outlier at 6 Ma of -9.09 ‰ (Figure 5.2). Lithium concentrations do not correlate with δ^7Li (Figure 5.3).

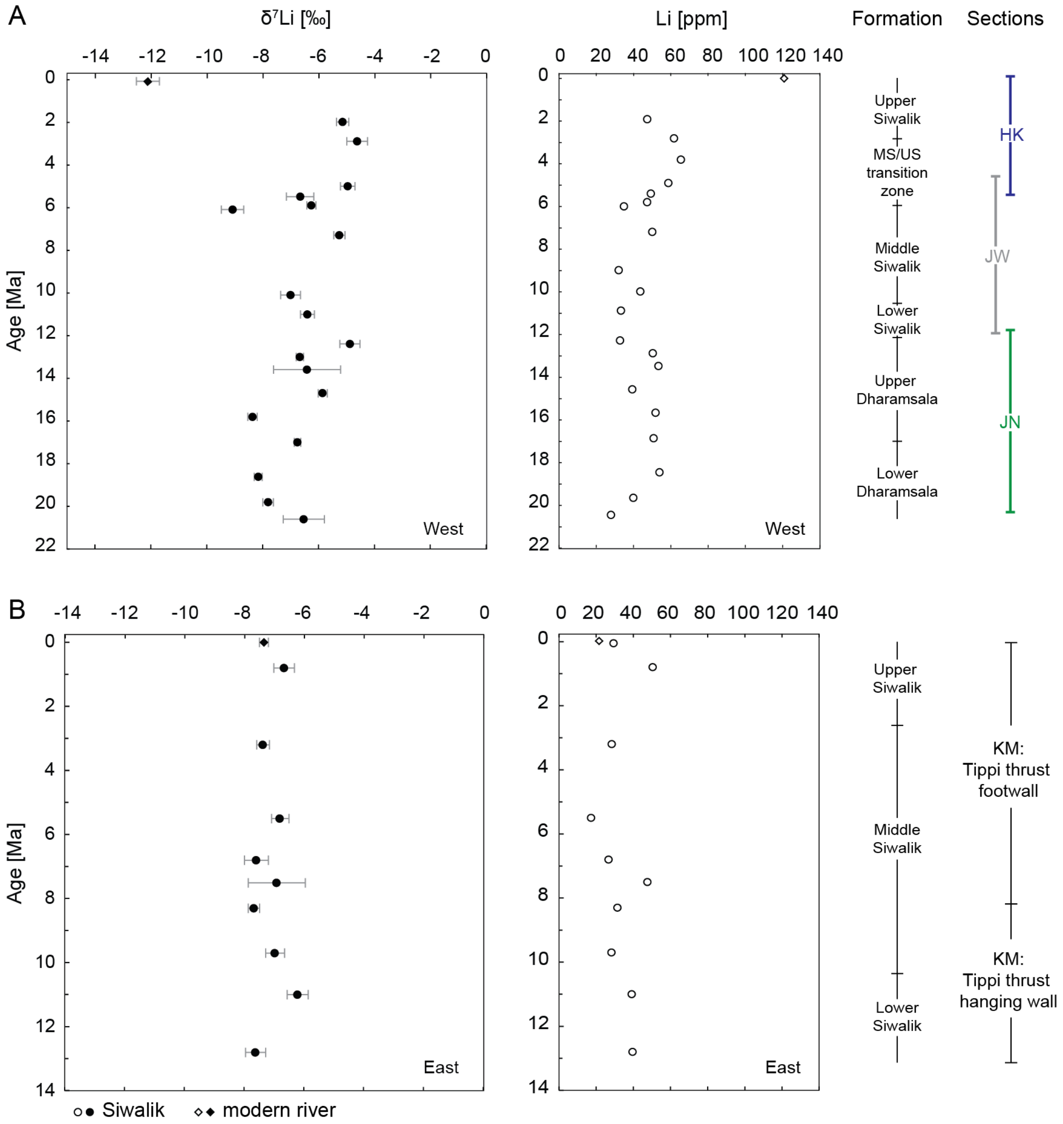

Figure 5.2: A: Lithium concentration and isotopic composition of the western Siwalik sections Joginder Nagar(JN), Jawalamukhi (JW) and Haripur Kolar (HK); B: Lithium concentration and isotopic composition of the eastern Siwalik Kameng (KM) section.

5.4 Discussion

Lithium isotopic compositions of river waters, suspended and bedload in Himalayan rivers have been used to constrain modern chemical weathering intensities (Kisakürek et al., 2005; Dellinger et al., 2014). Fractionation of lithium between bedrock and river waters is controlled by weathering, hence secondary clay formation (Millot et al., 2010; Pogge von Strandmann et al., 2013, amongst others). Dosseto et al. (2015) used δ^7Li of clays and bulk sediments in Holocene alluvial Himalayan sediments to reconstruct silicate weathering in the Holocene. Clay is expected to follow the trend of δ^7Li values with silicate

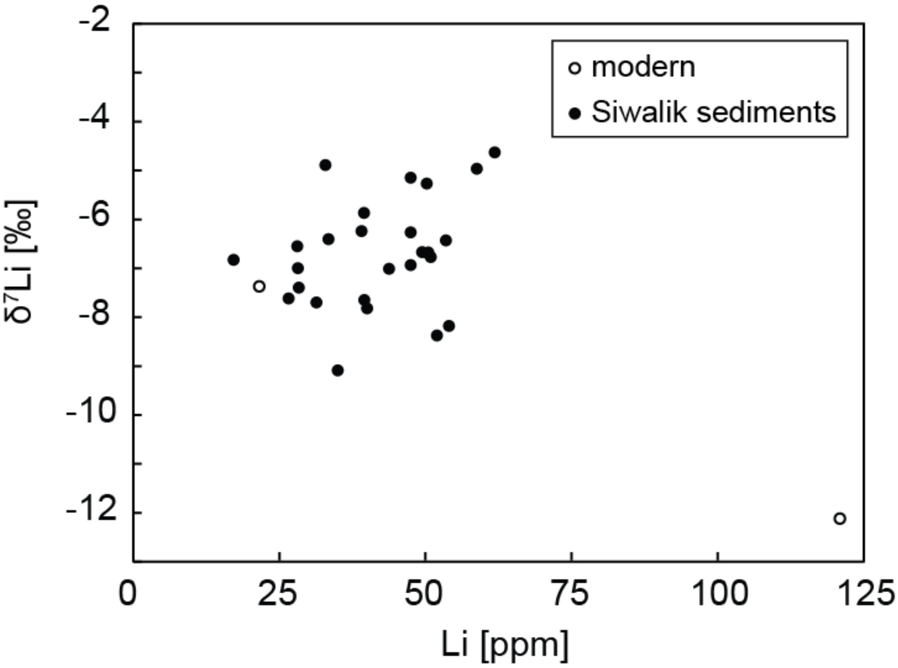

Figure 5.3: Relationship between δ^7Li [‰] and Li concentration [ppm].

weathering (Figure5.2), with a constant fractionation factor between water and clay ($\delta^7\text{Li}_{clay-water}$). Li isotopic composition of water is more positive when weathering is more incongruent and in a weathering-limited system, where formation of clay occurs. In a purely transport-limited system δ^7Li in water is similar to that of the parent rock and clays are absent (Figure 5.4). Ranges of Li isotopic composition are broader in the clay fraction compared to bulk sediments. Dosseto et al. (2015) argued that observed changes are linked to changes in chemical weathering rate and not due to changes in source area or post-depositional overprint.

δ^7Li of bulk sediments could be biased by post-depositional fluids circulating within the sediments, affecting mainly the "exchangeable" lithium on the mineral surface. Vigier et al. (2008) showed with experimental work that lithium can be incorporated into clay octahedral sites quickly and remains there, independent of the duration of the experiment. Post-depositional fluids would therefore only affect "exchangeable" lithium. Exchangeable lithium was not removed from the bulk sediments; to definitely exclude post-depositional influence, measurements will have to be redone. However, if the δ^7Li of bulk sediments h been influenced by post-depositional fluids or diagenesis, there should be a correlation between δ^7Li and sample depth (Figures 5.2), which is not observed. Illite crystallinity of clay assemblages from the same sedimentary rocks do not show major diagenetic influence (Vögeli et al., suba,p). Qiu et al. (2009) investigated Paleozoic rocks from southern England and found that low-grade metamorphism does not affect the lithium isotopic composition. Therefore, we assume here that diagenesis does not bias the δ^7Li signal.

The K/Al ratio can be used as a proxy of chemical weathering in sediments (Lupker et al., 2013).

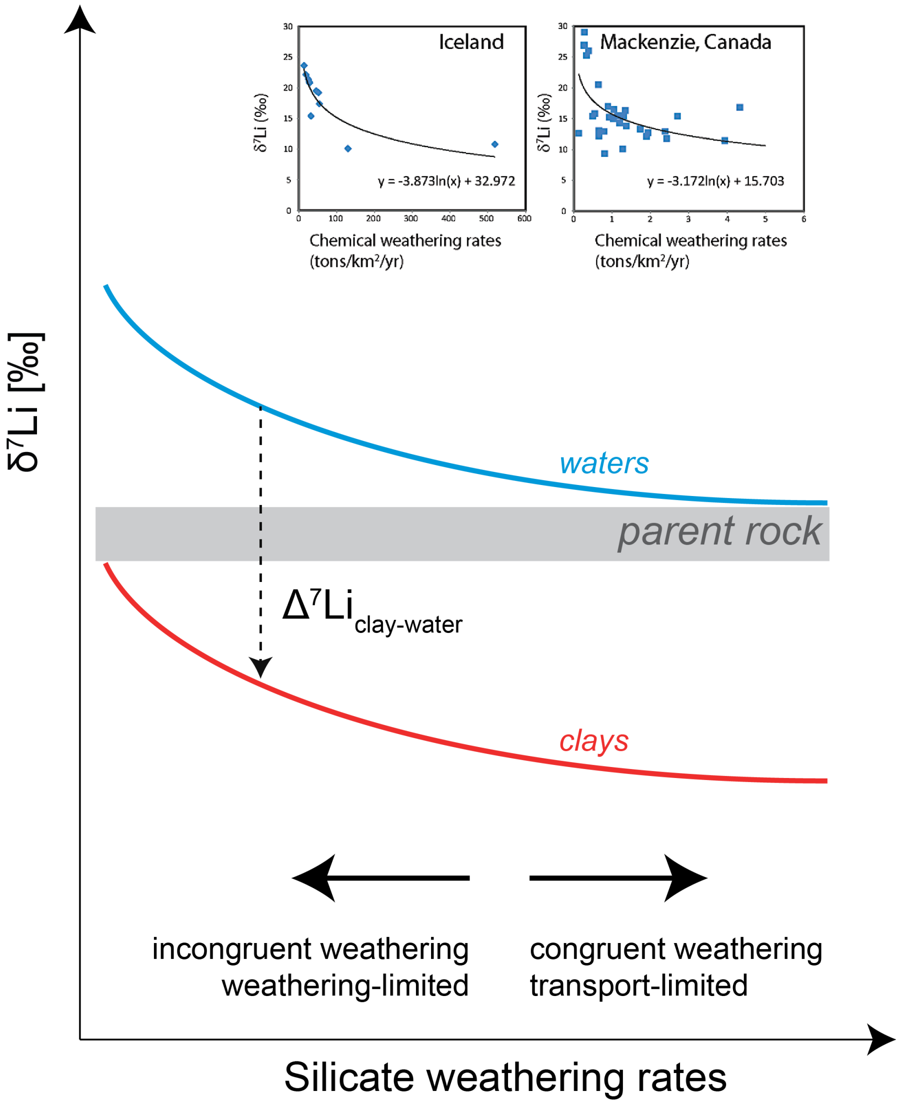

Figure 5.4: Relationship between δ^7Li of waters, clay and silicate weathering rate (modified from Dosseto et al. (2015)). Data from Millot et al. (2010) and Vigier et al. (2009). Clay is expected to follow the same trends as river water with silicate weathering rates.

Potassium is a mobile element and is therefore leached in more intensely weathered sediments. When sediment transport is rapid, sediments are likely to be less weathered, therefore if sediments are stored in the floodplain, they would become more weathered and hence have a lower K/Al ratio, due to longer residence time. δ^7Li of Siwalik sediment should reflect rates of chemical weathering in the source rocks, being secondarily influenced by formation of authigenic clays. However, no consistent correlation is observed between δ^7Li and K/Al (Figure 5.5); even though δ^7Li increases, the K/Al ratio slightly decreases over time. A decreasing K/Al ratio is interpreted as indicating an increase in chemical weathering (Lupker et al., 2013; Vögeli et al., suba). Lupker et al. (2013) showed an increase

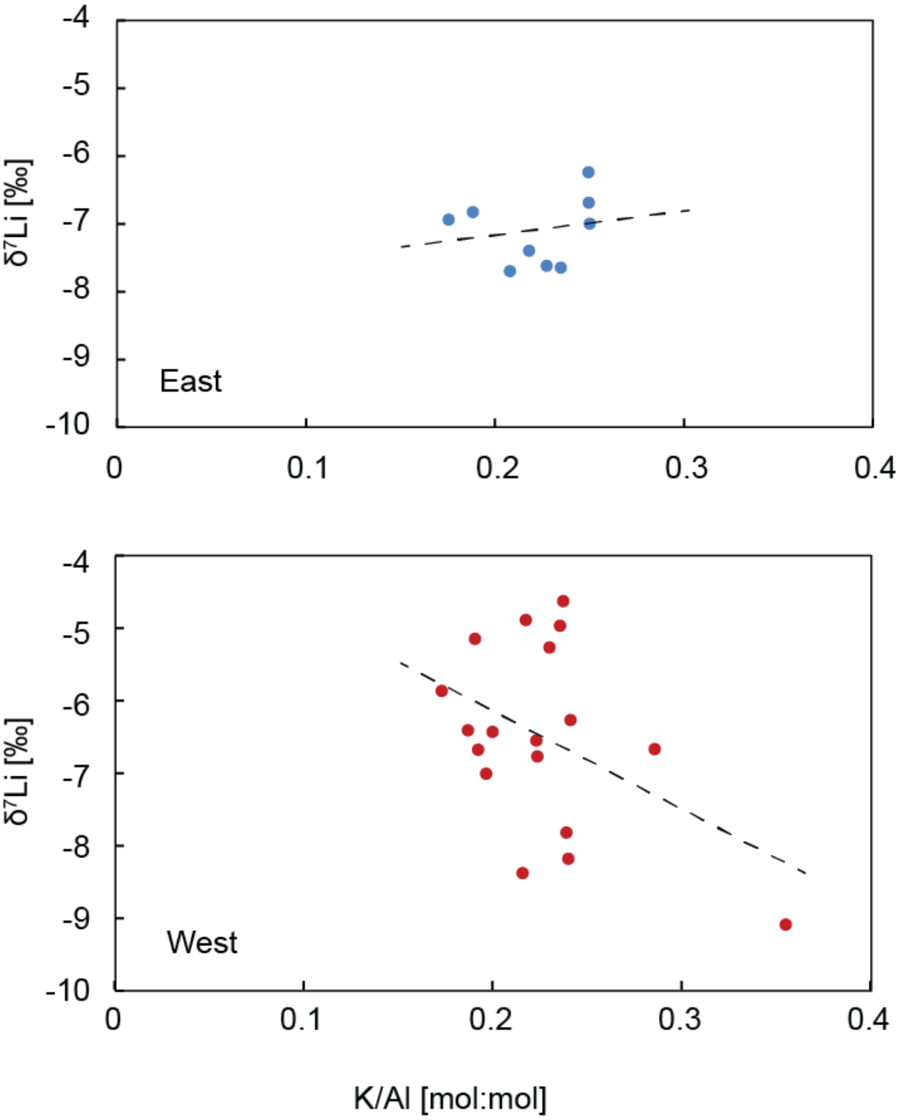

Figure 5.5: K/Al and δ^7Li do not show any correlation.

in weathering with time over the Holocene, which is inconsistent with the findings of Dosseto et al. (2015), who interpreted the increase in δ^7Li as a decrease in chemical weathering over Holocene time. Likewise, our data (Vögeli et al., prep) shows an decrease in the K/Al ratio, thus an increase in weathering intensity over the last 20 Ma. The δ^7Li of the same sediments, in contrast, shows an increase over time, which would imply a decrease in chemical weathering intensity. There is a clear inconsistency between these two weathering proxies, which could indicate that either δ^7Li in the Siwaliks is more sensitive to chemical weathering and the formation of secondary clays than the K/Al ratio, or that the two proxies do not record the same processes.

The Li-isotopic composition in the sedimentary record is controlled by the relative amount of secondary clays to unweathered minerals. Clays preferentially incorporate the light isotope ^{6}Li in their structure (Burton and Vigier, 2011; Dosseto et al., 2015), hence have a more negative δ^7Li. With more secondary clay minerals, δ^7Li values decrease. In bulk sediment the overall clay content is therefore likely to be a primary factor controlling δ^7Li. A possible explanation of very low δ^7Li values is a high clay content in the specific sample. Relative quantities of secondary smectite increase in the Siwalik sections after ~9 Ma (Vögeli et al., suba,p). δ^7Li values do not show a clear correlation with smectite occurrence over time (Figure 5.6), but as clay content was only determined semi-quantitatively, the quantitative clay concentration is not known. The modern Beas river and the sample JW14-4-f of the Jawalamukhi section show very low δ^7Li values, thus one possible explanation would be that the concentration of secondary clays in these samples is higher than in the others.

The modern Beas sample, river mud taken in proximity of the Joginder Nagar section, is characterized by a very low δ^7Li of -12.12‰ and an elevated lithium concentration of ~120 ppm. Kisakürek et al. (2005) measured δ^7Li and Li concentrations in Himalayan rivers (Ganga tributaries in Nepal) waters and sediments (suspended and bedload) and showed that δ^7Li is dependent on fractionation during silicate weathering. Suspended load has slightly lower δ^7Li than bedload (Kisakürek et al., 2005). They found δ^7Li values of suspended load ranging from -3.9 ‰ to +3.0 ‰, the value of the Beas river is therefore outstanding. Anthropogenic influence on lithium fractionation, e.g. due to fertilizer would render δ^7Li much more positive, sometimes with shifts of ~400‰ (Qi et al., 1997; Tomascak et al., 2016), we can therefore exclude influence of fertilizer in the Beas river sample. Kisakürek et al. (2005) found that samples with low δ^7Li and high Li concentration have a hydrothermal input, which could be an explanation for the low δ^7Li values in the Beas river, as secondary clays, smectite and kaolinite, which would render the δ^7Li negative, are rare. Hydrothermal activity can occur in proximity to the main Himalayan thrusts, such as the MBT. Occurrence of hydrothermal activity in proximity of the sampling location would need to be further investigated.

Influences of soil formation and development on lithium isotopic composition have been investigated by some authors (Kisakürek et al., 2004; Rudnick et al., 2004, amongst others). Paleosols are developed in the Siwalik Group, with some temporal and lateral variations. It is therefore important to know if soil formation could control the δ^7Li compositions that we measure. So far studies on lithium isotopic composition were conducted on soils that form on bedrock, mostly basalts (Huh et al., 2004; Rudnick et al., 2004; Pogge von Strandmann et al., 2012, amongst others), and a general correlation between the degree of weathering and a depletion in δ^7Li, with δ^7Li from -9 to -16 ‰, was found (Rudnick et al., 2004). Studies on soils formed in floodplains, hence from sediments, are currently lacking. Huh et al. (2004) and Kisakürek et al. (2004) found that the most important control on Li isotopic composition during soil formation is the formation of secondary minerals, which would render δ^7Li more negative, and input of aerosols derived from seawater, which would render the signal more positive. Seawater-derived aerosols could influence the Siwalik paleosols. This influence can be considered as relatively constant over time. If anything, influence would be strongest in the east, due to the greater proximity seawater, but δ^7Li in the east are stable and more negative. Formation of authigenic clays most likely plays an important role in controlling δ^7Li of sedimentary rocks. Samples analyzed in this study for δ^7Li do not only derive from paleosols, but are also mudstones from fine layers and poorly developed

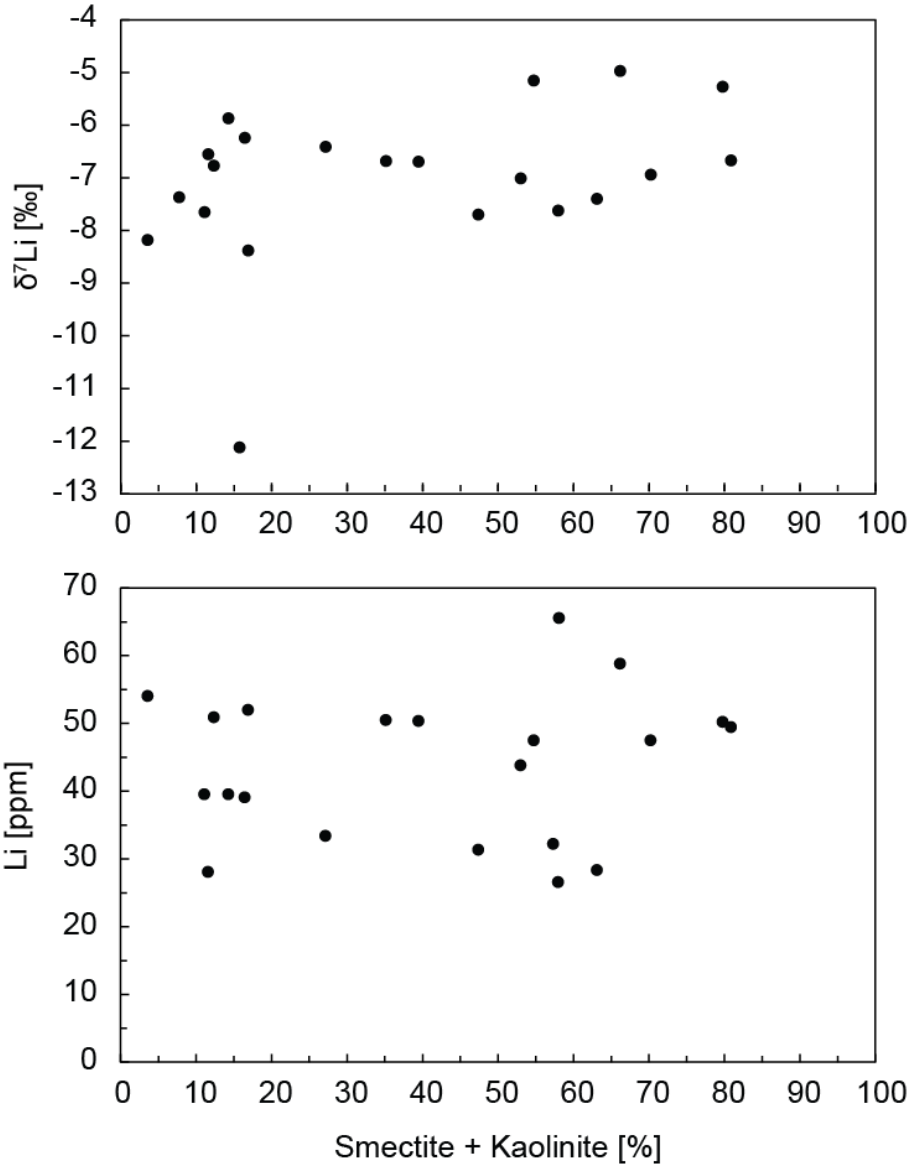

Figure 5.6: No clear correlation between δ^7Li [‰], Li concentration [ppm] and Smectite + Kaolinite [%].

paleosols. The formation of authigenic clay though, is not restricted to paleosols, but can also occur in poorly developed paleosols or mudstones. Paleosols in the west are better developed, than in the east, and development does not vary much within the different sections, we can therefore assume that degrees of paleosol development are comparable at least within the western section.

A slight variation of grainsize of the sediments could also influence the δ^7Li signal. Studies of bedload and suspended load of river sediments have shown that δ^7Li bedload is ~2 ‰ more positive than δ^7Li of suspended load (Kisakürek et al., 2005; Millot et al., 2010). Dellinger et al. (2014) showed a strong correlation between δ^7Li and Al/Si, used as a grainsize proxy with higher Al/Si, hence fine-

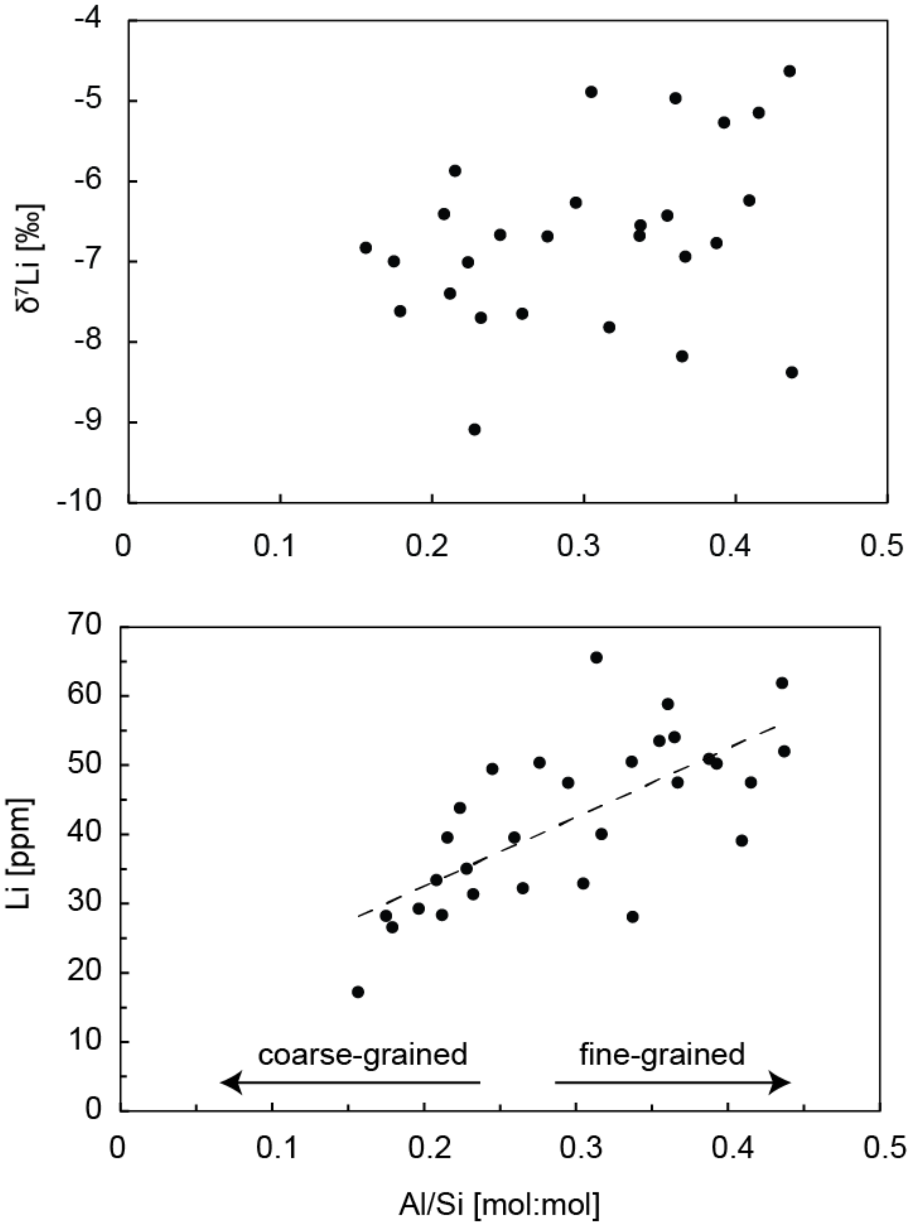

Figure 5.7: Top: No clear correlation between δ^7Li [‰] and Al/Si [mol:mol]. Bottom: Al/Si [mol:mol] showing a positive correlation with lithium concentration [ppm]; finer sediments with higher Al/Si have generally higher Li concentration. Assemblage of samples of the west and the east.

grained sediments, having lower δ^7Li. In this study we analyzed fine-grained sediment, on the higher end of the Al/Si ratio scale. Therefore, δ^7Li and Al/Si do not show a clear correlation (Figure 5.7). Grainsize can bias the δ^7Li signal, but as analyses were mainly conducted on similarly fine-grained sediments (mud- and siltstones) such a control of grainsize on the δ^7Li signal can be neglected.

Kisakürek et al. (2005) showed that source lithology does not strongly influence δ^7Li values in waters, but that it is mainly controlled by fractionation during weathering. Lithium is mainly derived from silicates, and even in carbonate dominated catchments, Li comes from dissolution of fine-grained silicates in the carbonate matrix. In the western sections, major provenance changes are observed at 17 Ma, where the source changed from High Himalayan Crystalline series to rocks sourced in the Higher Himalayan cover of lower metamorphic grade and between 9 and 6 Ma, when Lesser Himalayan rock became more prominent (Najman et al., 2009). Between 7 and 6 Ma, the Lesser Himalaya became the dominant source and Higher Himalayan rocks are completely cut out in the JW section(Najman et al., 2009). δ^7Li shows a negative peak in the sample JW14-4-f, at 6 Ma (Figure 5.2), if it would be linked to a change in provenance, we would expect the signal to stay negative, as the Lesser Himalaya remains the main source after 6 Ma. In the east, a change in source is observed between 7 and 3 Ma, when sediments were deposited by the paleo-Brahmaputra and carry a signal of the Gangdese batholith (Chirouze et al., 2013). Changes in δ^7Li in the studied Siwalik sections do not correlate with changes in provenance. δ^7Li seems therefore not to be controlled by changes in source material, which confirms the findings of Kisakürek et al. (2005). Siwalik sediments show a coarsening upward trend, interpreted as a gradual transition from distal to proximal facies. Less fine-grained, generally more weathered, sediments are present in the Middle and upper Siwaliks, compared to the Lower Siwaliks, which could influence the δ^7Li signal, but as only fine-grained samples were analyzed and the shift in δ^7Li is not constant in the west and east, the depositional environment is unlikely to influence δ^7Li.

Dosseto et al. (2015) found consistent δ^7Li variations in bulk sediments and in the clay fraction, but clay fraction shows a broader range of δ^7Li values. In the Siwalik sections in the west, we observe a variation of +4 ‰ since Miocene times. Since influences of diagenesis, post-depositional weathering and provenance appear minor, variations are likely to be controlled by changes in silicate weathering. There is a difference between the western and eastern sections. Values in the west show a clear variation with time and are generally more positive than in the east. Values from 13 Ma to ~9 Ma are similar in the west and the east (~-7 ‰), whereas after ~9 Ma values become less negative in the west, but stay at ~-7‰ in the east. Lateral variations are observed in several proxies, such as stable carbon isotope or major elements; Vögeli et al. (suba) showed that the evolution of vegetation varies laterally, likely due to differences in climate and seasonality, with the east being wetter and less seasonal due to the proximity to the moisture source of the Bay of Bengal. Dosseto et al. (2015) interpreted the increase in δ^7Li of the clay fraction of Holocene fluvial terraces as a decrease in weathering rates. Weathering rates are difficult to reconstruct with the lack of actual fluxes, but different weathering regimes can be evaluated. The generally more negative signal in the east could be interpreted as reflecting more congruent weathering in the east. The variations in the west could therefore be interpreted as a change towards a more weathering-limited system and more incongruent weathering. Misra and Froelich (2012) also reported an increase of δ^7Li since the Mid-Miocene climatic optimum, this is consistent with our data of the western Himalaya and was interpreted by these authors as silicate weathering becoming less efficient and the system becoming more weathering-limited. Climate cooling and mountain uplift potentially make removal of atmospheric CO_2 more efficient, but more erosion would switch the system to more weathering-limited with more formation of clay (incongruent weathering), and increase of δ^7Li in river water. The increase in δ^7Li over time can therefore be interpreted as the system becoming more weathering-limited, suggesting CO_2 drawdown being less efficient over time.

5.5 Preliminary conclusions and perspectives

Lithium isotopic composition of sedimentary rocks can be influenced by many factors, such as clay formation, clay content relative to unweathered bulk minerals, “exchangeable” surface lithium, river water composition during the time of clay formation and others. It is important to take these into account in order to interpret if changes and trends are reflecting variations in weathering rates. If we assume that the main control on Li isotopic fractionation is weathering, evolution of weathering rates since Miocene times can be inferred from these data.

In the western part of the Himalaya an increase of +4 ‰ in δ^7Li is observed on bulk sediments over the last 20 Myr. An increase in δ^7Li can be linked to an increase in clay formation, hence weathering becoming more incongruent. This implies that the system becomes more weathering-limited over time in the west, and silicate weathering becoming less efficient. Constant values in the east suggest no change in the weathering system and weathering being more congruent and transport-limited than in the west. However, this interpretation is not consistent with the lower K/Al ratios observed in the west, which indicate more intense weathering, nor with stable carbon-isotope data that indicate a dryer and more seasonal climate. Both these proxies suggest that due to longer residence times in the floodplain, sediments would be more weathered and the system transport- rather than weathering-limited in the west. Changes in lithium isotopic composition are likely to reflect something different than the K/Al ratio, as this inconsistency is also observed in the interpretation of Holocene weathering trends (Dosseto et al., 2015; Lupker et al., 2013). More δ^7Li studies are needed to understand the origin of this discrepancy. In order to better define possible trends and to rule out influences such as clay concentration and formation, it is necessary to measure δ^7Li directly on the clay fraction of the sediments or, if that is not possible, to at least remove the exchangeable surface lithium to avoid influences of diagenesis, since fluids circulating in the sediment might have altered the original isotopic signature of the sediment. Evaluating the total clay concentration would allow to have a better understanding of the influence of secondary clay formation on the lithium isotopic composition.

Conclusions and perspectives

Conclusions

In my thesis I was able to apply different methods (stable carbon isotopes, major-element geochemistry, clay mineralogy, lithium isotopes) on pre-Siwalik and Siwalik sediments in order to gain a better understanding of the past weathering regimes and intensities, lateral variations in the monsoon climate, and the evolution of vegetation along strike in the Himalaya. I was able to test new methods, such as stable isotopes on n-alkanes to constrain past precipitation and climate, which turned out to be not applicable in the Siwalik sections of this study. Other newly developed methods such as lithium isotopic composition are more promising, and could be an excellent tool to reconstruct paleo-weathering rates. I have been able to extend the data set in the Himalaya further to the east and provide a more complete insight to the weathering regime and climatic evolution in the eastern Himalaya. I have showed that using a multi-proxy approach to reconstruct weathering regimes is crucial and that changes in provenance and diagenesis have to be taken into account when interpreting past weathering regimes. I have studied three pre-Siwalik and Siwalik sections in the western Himalaya and one Siwalik section in the eastern Himalaya to reach the following main conclusions regarding the evolution of vegetation, weathering, and monsoon climate:

- The lack of carbonate nodules in Siwalik sediments east of Nepal is a first indicator for lateral environmental differences in the Himalaya. Stable carbon and oxygen isotopes were analyzed in carbonate nodules of the Joginder Nagar, Jawalamukhi and Haripur Kolar sections in the western Himalaya. $\delta^{13}C_{soilcarb.}$ values show a clear shift towards more positive values at ~7 Ma, similar to the results of earlier studies in the western and central Himalaya. In order to directly compare west and east, we analyzed stable carbon isotopes on organic matter, which show a clear difference between the west and the east. In the west, $\delta^{13}C_{org}$ values shift towards more positive values at 7 Ma, consistent with the results on carbonate nodules, whereas they remain constant over the last 13 Ma in the east.$\delta^{13}C$ of organic matter reflects the evolution of the vegetation, with the development of C4 plants in the west and an environment that remains favorable for C3 plants in the east. Such variations in vegetation imply differences in climate, which became more seasonal and overall drier in the west at ~7 Ma. The eastern Himalaya is much more proximal to the main moisture source for precipitation (the Bay of Bengal); therefore, even though climate may have varied, it remained less seasonal and more humid, inhibiting C4 plants to evolve.

- Given the suggestion of overall drying of the climate at ~7 Ma, I analyzed sediments of the eastern Kameng section in more detail, in order to resolve the possible influence of climate on the sedimentary record and to reconstruct weathering regimes in the eastern Himalaya since the Miocene. I show that provenance and diagenesis have no impact on the K/Al ratio and it can therefore be used to track weathering intensities in pre-Quaternary sediments. The major-element composition (K/Al, K/Si*, H2O+/Si* ratios) and clay mineralogy indicate that weathering intensity increases over time, with a remarkable change towards more intense weathering at ~8 Ma, which is reflected by a decrease in the K/Al ratio and the dominance of smectite in the clay-mineral assemblage after ~8 Ma.

- I compared weathering regimes in the western and eastern Himalaya using the K/Al ratio and clay mineralogy, to show that weathering is overall more intense in the west, reflected by lower K/Al ratios. A period of very low weathering between 7 and 5 Ma in the west is suggested to be linked to deposition closer to the mountain front. Less intense weathering in the east, in a more humid climate, implies that stronger runoff and erosion limit weathering intensity. The more seasonal climate in the west allows sediment to become more weathered, possibly because it is stored for longer periods in the floodplain.

- Lithium isotopes constitute a new tool to reconstruct weathering intensities and especially to quantify silicate weathering, which has a major impact on the global carbon cycle,. We applied lithium-isotopic analyses for the first time on pre-Siwalik and Siwalik sediments to unravel weathering intensities and regimes since Miocene times. The initial results show increasing δ^7Li values with time in the western sections and constant, more negative values in the east. Increasing δ^7Li values in the west indicate that weathering has become more incongruent and weathering-limited since the Early Miocene, whereas weathering has remained more incongruent in the east. Our analyses on bulk sediment show evidence of changes in silicate weathering rates and regimes; however, a more precise interpretation will require more analyses on clay minerals and/or in bulk sediments after removing exchangeable lithium.

These results show the existence of lateral differences in weathering, climate and vegetation in the Himalaya that have persisted on timescales of 10^7 years. I suggest that climate became more seasonal and overall drier since the mid-Miocene, especially in the west. In the eastern Himalaya, the amplitude of these changes is smaller and insufficient to influence vegetation patterns. Due to its proximity to the main moisture source, the eastern Himalaya is generally more humid and less seasonal than the west; I show that this difference has been in place since at least the mid-Miocene.

Perspectives

The Himalayan foreland-basin sediments have been widely used to unravel provenance, tectonics and climate history, but their potential as a record of weathering intensity and regime has not yet been fully exploited. New Siwalik sections are currently being dated, in particular in the eastern half of the orogeny (Bhutan, Arunachal Pradesh), and could be used to better constrain lateral variations in climate using traditional methods such as major-element geochemistry, stable isotopes and clay mineralogy. The expected climate shift in the eastern Himalaya following the uplift of the Shillong plateau (Najman et al., 2016) could provide an excellent opportunity for continued research on the links between tectonics, climate and erosion. In order to better define and understand the evolution of (monsoonal) climate, more studies on paleo-precipitation, paleo-temperature and paleo-humidity are needed. Previously dated Siwalik sections provide a good opportunity to study climate since Miocene times by less conventional methods, such as the pollen record or stable isotopes of biomarkers, which would allow paleo-vegetation and paleo-environments to be distinguished more precisely. Foreland-basin sediments do not only record the past climate, but also provenance and diagenesis. I have showed that it is possible to extract climate signals from these records while taking provenance changes into account. Nevertheless, it is important to further investigate the diagenetic influence on the pre-Siwalik and Siwalik sediments and to constrain changes in provenance as precisely as possible. The attempt to use stable isotopes on biomarkers in Siwalik sediments proved unsuccessful due to diagenetic overprinting. However, analyzing the stable oxygen and hydrogen isotopic composition of clays would allow more precise reconstruction of the origin and the formation temperature of clay minerals (Rosenau and Tabor, 2013).

Clumped isotopes on soil-carbonate nodules could possibly be used to reconstruct paleo-temperatures (Quade et al., 2013). Temperature is both controlled by and has an impact on the global carbon cycle; reconstructions of paleo-temperatures are therefore crucial to interpret changes in silicate weathering. Preliminary results on the lithium-isotopic composition of Siwalik sediments presented in this thesis show that they potentially track changes in weathering rate and regime in these older, more complex settings. To exclude potential controls on Li-isotopic composition by the relative amounts of clay, it is crucial to measure lithium-isotopic composition directly on the clay fraction. If the same change is observed in the clay fraction and the bulk sediments, lithium isotopes could be a powerful tool to reconstruct weathering regimes and intensities in the past, by using both continental and marine sedimentary records globally.

In order to reconstruct the Asian monsoon climate and to compare different studies with each other, the term “monsoon” should be more clearly defined with regard to physical parameters that describe “climate” (seasonality, aridity, rainfall patterns and amounts, wind speeds and directions), to create a common understanding of how monsoonal winds actually influence climate, and how this is recorded by sediments. The currently widely adopted practice of interpreting sedimentary records in terms of “monsoon intensity” is too imprecise, leading to confusion of what is actually recorded. For instance, an “increase in monsoon intensity” generally translates into increased seasonality, but this does not tell us whether precipitation increased during the wet season or decreased during the dry season.

In my thesis, I have focused on lateral variations in the evolution of vegetation and weathering regimes, and have showed that clay mineralogy together with major-element compositions are useful tools to constrain paleo-weathering regimes. In order to further constrain weathering regimes in other tectonic settings, similar studies could be applied in sedimentary basins such as the Tarim Basin or Qaidam Basin on the Tibetan Plateau, or even more globally in foreland-basin sediments. Such extended studies could reveal regional- or global-scale trends in weathering intensities and regimes, which would provide significant new insight into the history of the global carbon cycle and atmospheric CO_2.

Bibliography

Ahmad, T., Harris, N., Bickle, M., Chapman, H., Bunbury, J., and Prince, C. (2000). Isotopic constraints on the structural relationships between the lesser himalayan series and the high himalayan crystalline series, garhwal himalaya. *GSA Bulletin*, 112(3):467–477.

Aitchison, J. C., Ali, J. R., and Davis, A. M. (2007). When and where did india and asia collide? *Journal of Geophysical Research: Solid Earth*, 112(B5).

Allen, M. and Armstrong, H. (2012). Reconciling the intertropical convergence zone, himalayan/tibetan tectonics, and the onset of the asian monsoon system. *Journal of Asian Earth Sciences*, 44(C):36–47.

An, W., Hu, X., Garzanti, E., BouDagher-Fadel, M. K., Wang, J., and Sun, G. (2014). Xigaze forearc basin revisited (south tibet): Provenance changes and origin of the xigaze ophiolite. *Geological Society of America Bulletin*, 126(11-12):1595–1613.

Andermann, C., Bonnet, S., Crave, A., Davy, P., Longuevergne, L., and Gloaguen, R. (2012a). Sediment transfer and the hydrological cycle of himalayan rivers in nepal. *Comptes Rendus Geoscience*, 344(11-12):627–635.

Andermann, C., Crave, A., Gloaguen, R., Davy, P., and Bonnet, S. (2012b). Connecting source and transport: Suspended sediments in the nepal himalayas. *Earth and Planetary Science Letters*, 351–352:158 – 170.

Andó, S., Morton, A., and Garzanti, E. (2014). Metamorphic grade of source rocks revealed by chemical fingerprints of detrital amphibole and garnet. in: Scott, r.a., smyth. h.r., morton, a.c., richardson, n. (eds.), sediment provenance studies in hydrocarbon exploration and production. *Geological Society London, Special Publication*, 386:351–371.

Beerling, D. J. and Royer, D. L. (2011). Convergent cenozoic co_2 history. *Nature Geosci*, 4(7):418–420. 10.1038/ngeo1186.

Benn, D. I. and Owen, L. A. (1998). The role of the indian summer monsoon and the mid-latitude westerlies in himalayan glaciation: review and speculative discussion. *Journal of the Geological Society, London*, 155:353–363.

Berner, R., Lasaga, A., and Garrels, R. (1983). The carbonate-silicate geochemical cycle and its effect on atmospheric carbon dioxide over the past 100 million years. *American Journal of Science*, 283:641–683.

Berner, R. A. (2004). The phanerozoic carbon cycle: Co_2 and o_2. *Oxford University Press, Oxford*, page 150p.

Bickle, M. J., Harris, N. B. W., Bunbury, J. M., Chapman, H. J., Fairchild, I. J., and Ahmad, T. (2001). Controls on the ^{87}sr/^{86}sr ratio of carbonates in the garhwal himalaya, headwaters of the ganges. *The Journal of Geology*, 109(6):737–753.

Bohlin, M., Misra, S., and Bickle, M. (in prep). Single column separation of li and mg from natural samples.

Bookhagen, B. and Burbank, D. W. (2006). Topography, relief, and trmm-derived rainfall variations along the himalaya. *Geophysical Research Letters*, 33(8):L08405.

Bookhagen, B. and Burbank, D. W. (2010). Toward a complete himalayan hydrological budget: Spatiotemporal distribution of snowmelt and rainfall and their impact on river discharge. *Journal of Geophysical Research: Earth Surface*, 115(F03019).

Bookhagen, B., Thiede, R. C., and Strecker, M. R. (2005). Late quaternary intensified monsoon phases control landscape evolution in the northwest himalaya. *Geology*, 33(2):149–152.

Boos, W. R. and Kuang, Z. (2010). Dominant control of the south asian monsoon by orographic insulation versus plateau heating. *Nature*, 463(7278):218–222. 10.1038/nature08707.

Bouchez, J., Gaillardet, J., Lupker, M., Louvat, P., France-Lanord, C., Maurice, L., Armijos, E., and Moquet, J.-S. (2012). Floodplains of large rivers: Weathering reactors or simple silos? *Chemical Geology*, 332-333:166–184.

Burgess, P. W., Yin, A., Dubey, C. S., Shen, Z.-K., and Kelty, T. K. (2012). Holocene shortening across the main frontal thrust zone in the eastern himalaya. *Earth and Planetary Science Letters*, 357-358:152–167.

Burton, K. W. and Vigier, N. (2011). Lithium isotopes as tracers in marine and terrestrial environments. *IN: Baskaran, M., Handbook of Environmental Isotope Geochemistry: Vol I, Springer Verlag Berlin*, pages 41–59.

Bush, R. T. and McInerney, F. A. (2013). Leaf wax n-alkane distributions in and across modern plants: Implications for paleoecology and chemotaxonomy. *Geochimica et Cosmochimica Acta*, 117(0):161–179.

Capet, X., Chamley, H., Beck, C., and Holtzappel, T. (1990). Clay mineralogy of odp sites 671 and 672, barbados ridge accretionary complex and atlantic abyssal plain: palaeoenvironmental and diagenetic implications. *In: Proceedings of the Ocean Drilling Program, Scientifc Results, Vol. 110 (Ed. by A.Mascle, J.C. Moore E. Taulor, et al.). Ocean Drilling Program, College Station,TX.*, pages 85–96.

Cerling, T. E. (1984). The stable isotopic composition of modern soil carbonate and its relationship to climate. *Earth and Planetary Science Letters*, 71(2):229–240.

Cerling, T. E., Harris, J. M., MacFadden, B. J., Leakey, M. G., Quade, J., Eisenmann, V., and Ehleringer, J. R. (1997). Global vegetation change through the miocene/pliocene boundary. *Nature*, 389(6647):153–158. 10.1038/38229.

Cerling, T. E., Quade, J., Wang, Y., and Bowman, J. R. (1989). Carbon isotopes in soils and palaeosols as ecology and palaeoecology indicators. *Nature*, 341(6238):138–139. 10.1038/341138a0.

Chamley, H. (1989). Clay sedimentology. *Springer Verlag, Berlin*, page 623.

Chan, L.-H. and Edmond, J. M. (1988). Variation of lithium isotope composition in the marine environment: A preliminary report. *Geochimica et Cosmochimica Acta*, 52(6):1711–1717.

Chauvel, C., Bureau, S., and Poggi, C. l. (2011). Comprehensive chemical and isotopic analyses of basalt and sediment reference materials. *Geostandards and Geoanalytical Research*, 35(1):125–143.

Chibnall, A. C., Piper, S. H., Pollard, A., Williams, E. F., and Sahai, P. N. (1934). The constitution of the primary alcohols, fatty acids and paraffins present in plant and insect waxes. *Biochemical Journal*, 28(6):2189–2208.

Chirouze, F., Dupont-Nivet, G., Huyghe, P., van der Beek, P., Chakraborti, T., Bernet, M., and Erens, V. (2012). Magnetostratigraphy of the neogene siwalik group in the far eastern himalaya: Kameng section, arunachal pradesh, india. *Journal of Asian Earth Sciences*, 44:117–135. Chirouze, Francois Dupont-Nivet, Guillaume Huyghe, Pascale van der Beek, Peter Chakraborti, Tapan Bernet, Matthias Erens, Veronique Si.

Chirouze, F., Huyghe, P., van der Beek, P., Chauvel, C., Chakraborty, T., Dupont-Nivet, G., and Bernet, M. (2013). Tectonics, exhumation, and drainage evolution of the eastern himalaya since 13 ma from detrital geochemistry and thermochronology, kameng river section, arunachal pradesh. *Geological Society of America Bulletin*, 125(3-4):523–538.

Cina, S. E., Yin, A., Grove, M., Dubey, C. S., Shukla, D. P., Lovera, O. M., Kelty, T. K., Gehrels, G. E., and Foster, D. A. (2009). Gangdese arc detritus within the eastern himalayan neogene foreland basin: Implications for the neogene evolution of the yalu-brahmaputra river system. *Earth and Planetary Science Letters*, 285(1-2):150–162.

Clift, P. and Gaedicke, C. (2002). Accelerated mass flux to the arabian sea during the middle to late miocene. *Geology*, 30(3):207–210.

Clift, P. D., Hodges, K. V., Heslop, D., Hannigan, R., Van Long, H., and Calves, G. (2008). Correlation of himalayan exhumation rates and asian monsoon intensity. *Nature Geosci*, 1(12):875–880. 10.1038/ngeo351.

Clift, P. D., Tada, R., and Zheng, H. (2010). Monsoon evolution and tectonics-climate linkage in asia: an introduction. *Geological Society, London, Special Publications*, 342(1):1–4.

Clift, P. D., Wan, S., and Blusztajn, J. (2014). Reconstructing chemical weathering, physical erosion and monsoon intensity since 25 ma in the northern south china sea: A review of competing proxies. *Earth-Science Reviews*, 130(0):86–102.

Dansgaard, W. (1961). The isotopic composition of natural waters. *Medd. om Gronland*, 165(2):1–120.

DeCelles, P. G., Gehrels, G. E., Quade, J., and Ojha, T. P. (1998a). Eocene-early miocene foreland basin development and the history of himalayan thrusting, western and central nepal. *Tectonics*, 17(5):741–765.

DeCelles, P. G., Gehrels, G. E., Quade, J., Ojha, T. P., Kapp, P. A., and Upreti, B. N. (1998b). Neogene foreland basin deposits, erosional unroofing, and the kinematic history of the himalayan fold-thrust belt, western nepal. *Geological Society of America Bulletin*, 110(1):2–21.

DeCelles, P. G., Robinson, D. M., Quade, J., Ojha, T. P., Garzione, C. N., Copeland, P., and Upreti, B. N. (2001). Stratigraphy, structure, and tectonic evolution of the himalayan fold-thrust belt in western nepal. *Tectonics*, 20(4):487–509.

Dellinger, M., Gaillardet, J., Bouchez, J., Calmels, D., Galy, V., Hilton, R. G., Louvat, P., and France-Lanord, C. (2014). Lithium isotopes in large rivers reveal the cannibalistic nature of modern continental weathering and erosion. *Earth and Planetary Science Letters*, 401:359–372.

Dellinger, M., Gaillardet, J., Bouchez, J., Calmels, D., Louvat, P., Dosseto, A., Gorge, C., Alanoca, L., and Maurice, L. (2015). Riverine li isotope fractionation in the amazon river basin controlled by the weathering regimes. *Geochimica et Cosmochimica Acta*, 164:71–93.

Derry, L. A. and France-Lanord, C. (1996). Neogene himalayan weathering history and river 87sr/86sr: impact on the marine sr record. *Earth and Planetary Science Letters*, 142(1-2):59–74.

Dettman, D. L., Kohn, M. J., Quade, J., Ryerson, F., Ojha, T. P., and Hamidullah, S. (2001). Seasonal stable isotope evidence for a strong asian monsoon throughout the past 10.7 m.y. *Geology*, 29(1):31–34.

Dobremez, J. e. a. (1978). Carte écologique du népal 1/250000. *University of Grenoble, Grenoble*.

Donelick, R. A., O'Sullivan, P. B., and Ketcham, R. A. (2005). Apatite fission-track analysis. *Reviews in Mineralogy and Geochemistry*, 58(1):49–94.

Dosseto, A., Vigier, N., Joannes-Boyau, R., Moffat, I., Singh, T., and Srivastava, P. (2015). Rapid response of silicate weathering rates to climate change in the himalaya. *Geochemical Perspectives Letters*, 1:10–19.

Dunoyer De Segonzac, G. (1970). The transformation of clay minerals during diagenesis and low-grade metamorphism: A review. *Sedimentology*, 15(3-4):281–346.

Eglinton, G. and Hamilton, R. J. (1967). Leaf epicuticular waxes. *Science*, 156:1322–1335.

Eglinton, G., Logan, G. A., Ambler, R. P., Boon, J. J., and Perizonius, W. R. K. (1991). Molecular preservation. *Philosophical Transactions of the Royal Society B: Biological Sciences*, 333(1268):315–328.

Ehleringer, J. R. (1988). Carbon isotope ratios and physiological processes in aridland plants. in ehleringer, j.r., nagy, k.a. (eds.), stable isotope in ecological research. *Springer, New York*, pages 41–54.

Fischer, K. (1935). Neues verfahren zur analytischen bestimmung des wassergehaltes von flüssigkeiten und festen körpern. *Angewandte Chemie*, 48(26):394–396.

France-Lanord, C. and Derry, L. A. (1994). δ^{13}c of organic carbon in the bengal fan: Source evolution and transport of c3 and c4 plant carbon to marine sediments. *Geochimica et Cosmochimica Acta*, 58(21):4809–4814.

France-Lanord, C., Derry, L. A., and Michard, A. (1993). Evolution of the himalaya since miocene time: isotopic and sedimentological evidence from the bengal fan. *Geological Society, London, Special Publications*, 74(1):603–621.

France-Lanord, C., Spiess, V., Klaus, A., and the Expedition 354 Scientists (2015). Bengal fan: Neogene and late paleogene record of himalayan orogeny and climate: a transect across the middle bengal fan. *International Ocean Discovery Program Preliminary Report, 354*.

Freeman, K. H. and Colarusso, L. A. (2001). Molecular and isotopic records of c4 grassland expansion in the late miocene. *Geochimica et Cosmochimica Acta*, 65(9):1439–1454.

Gaetani, M. and Garzanti, E. (1991). Multicyclic history of the northern india continental margin (northwestern himalaya). *American Association of Petroleum Geologists Bulletin*, 75:1427–1446.

Galehouse, J. (1971). Point counting. *In: Carver, R.E. (Ed.), Procedures in sedimentary petrology. Wiley, New York*, pages 385–407.

Galy, A. and France-Lanord, C. (1999). Weathering processes in the ganges-brahmaputra basin and the riverine alkalinity budget. *Chemical Geology*, 159(1-4):31–60.

Galy, A., France-Lanord, C., and Derry, L. A. (1996). The late oligocene-early miocene himalayan belt constraints deduced from isotopic compositions of early miocene turbidites in the bengal fan. *Tectonophysics*, 260(1-3):109–118.

Galy, V., Beyssac, O., France-Lanord, C., and Eglinton, T. (2008a). Recycling of graphite during himalayan erosion: A geological stabilization of carbon in the crust. *Science*, 322:943–945.

Galy, V., Eglinton, T., France-Lanord, C., and Sylva, S. (2011). The provenance of vegetation and environmental signatures encoded in vascular plant biomarkers carried by the ganges brahmaputra rivers. *Earth and Planetary Science Letters*, 304(1-2):1–12.

Galy, V., France-Lanord, C., and Lartiges, B. (2008b). Loading and fate of particulate organic carbon from the himalaya to the ganga-brahmaputra delta. *Geochimica et Cosmochimica Acta*, 72(7):1767–1787.

Galy, V., France-Lanord, C., Peucker-Ehrenbrink, B., and Huyghe, P. (2010). Sr-nd-os evidence for a stable erosion regime in the himalaya during the past 12 myr. *Earth and Planetary Science Letters*, 290(3-4):474–480.

Gansser, A. (1964). The geology of the himalaya. *Wiley Interscience, New York*, page 289 pp.

Garzanti, E. and Andó, S. (2007). Heavy-mineral concentration in modern sands: implications for provenance interpretation. *In: Mange, M.A., Wright, D.T. (Eds.), Heavy Minerals in Use. Elsevier, Amsterdam, Developments in Sedimentology Series*, 58:517–545.

Garzanti, E., Andó, S., and Vezzoli, G. (2009). Grain-size dependence of sediment composition and environmental bias in provenance studies. *Earth and Planetary Science Letters*, 277:422–432.

Garzanti, E., Baud, A., and Mascle, G. (1987). Sedimentary record of the northward flight of india and its collision with eurasia (ladakh himalaya, india). *Geodinamica Acta*, 1:297–312.

Garzanti, E., Padoan, M., Setti, M., López-Galindo, A., and Villa, I. M. (2014). Provenance versus weathering control on the composition of tropical river mud (southern africa). *Chemical Geology*, 366:61–74.

Garzanti, E. and Vezzoli, G. (2003). A classification of metamorphic grains in sands based on their composition and grade. *Journal of Sedimentary Research*, 73(5):830–837.

Garzanti, E., Vezzoli, G., Andó, S., France-Lanord, C., Singh, S. K., and Foster, G. (2004). Sand petrology and focused erosion in collision orogens: the brahmaputra case. *Earth and Planetary Science Letters*, 220(1-2):157–174.

Ghosh, P., Padia, J. T., and Mohindra, R. (2004). Stable isotopic studies of palaeosol sediment from upper siwalik of himachal himalaya: evidence for high monsoonal intensity during late miocene? *Palaeogeography, Palaeoclimatology, Palaeoecology*, 206(1-2):103–114.

Govin, G., Najman, Y., van der Beek, P., Huyghe, P., Millar, I., Bernet, M., Dupont-Nivet, G., Wijbrans, J., Gemignani, L., and V geli, N. (2015). Constraining the timing of exhumation of the eastern himalayan syntaxis, from a study of the palaeo-brahmaputra deposits, siwalik group, arunachal pradesh, india. *EGU Abstract*.

Guillot, S., Mahéo, G., de Sigoyer, J., Hattori, K. H., and Pêcher, A. (2008). Tethyan and indian subduction viewed from the himalayan high- to ultrahigh-pressure metamorphic rocks. *Tectonophysics*, 451(1-4):225–241.

Guo, Z. T., Sun, B., Zhang, Z. S., Peng, S. Z., Xiao, G. Q., Ge, J. Y., Hao, Q. Z., Qiao, Y. S., Liang, M. Y., Liu, J. F., Yin, Q. Z., and Wei, J. J. (2008). A major reorganization of asian climate by the early miocene. *Climate of the Past*, 4(3):153–174.

Hillier, S. (1995). Erosion, sedimentation and sedimentary origin of clays. *In: Velde, B., ed., Origin and Mineralogy of Clays: Clays and the Environment, Springer Verlag, Berlin*, pages 162–219.

Hirschmiller, J., Grujic, D., Bookhagen, B., Coutand, I., Huyghe, P., Mugnier, J.-L., and Ojha, T. (2014). What controls the growth of the himalayan foreland fold-and-thrust belt? *Geology*, 42(3):247–250.

Hodges, K. V. (2000). Tectonics of the himalaya and southern tibet from two perspectives. *Geological Society of America Bulletin*, 112(3):324–350.

Holtzappel, T. (1985). Les minéraux argileux, préparation, analyse diffractométrique et détermination. *Soc. Géol.Nord.*, 12:1–36.

Hu, X., Wang, J., BouDagher-Fadel, M., Garzanti, E., and An, W. (2016). New insights into the timing of the india-asia collision from the paleogene quxia and jialazi formations of the xigaze forearc basin, south tibet. *Gondwana Research*, 32:76–92.

Hubert, J. (1962). A zircon-tourmaline-rutile maturity index and the interdependence of the composition of heavy minerals assemblages with the gross composition and texture of sandstones. *Journal of Sedimentary Petrology*, 32:440–450.

Huh, Y., Chan, L.-H., and Chadwick, O. A. (2004). Behavior of lithium and its isotopes during weathering of hawaiian basalt. *Geochemistry, Geophysics, Geosystems*, 5(9):Q09002.

Huh, Y., Chan, L.-H., and Edmond, J. M. (2001). Lithium isotopes as a probe of weathering processes: Orinoco river. *Earth and Planetary Science Letters*, 194(1-2):189–199.

Huh, Y., Chan, L.-H., Zhang, L., and Edmond, J. M. (1998). Lithium and its isotopes in major world rivers: implications for weathering and the oceanic budget. *Geochimica et Cosmochimica Acta*, 62(12):2039–2051.

Huyghe, P., Guilbaud, R., Bernet, M., Galy, A., and Gajurel, A. P. (2011). Significance of the clay mineral distribution in fluvial sediments of the neogene to recent himalayan foreland basin (west-central nepal). *Basin Research*, 23(3):332–345.

Huyghe, P., Mugnier, J.-L., Gajurel, A., and Delcaillau, B. (2005). Tectonic and climatic control of the changes in sedimentary record of the karnali river section (siwaliks of western nepal). *The Island Arc*, 14:311–327.

Hébert, R., Bezard, R., Guilmette, C., Dostal, J., Wang, C. S., and Liu, Z. F. (2012). The indus-yarlung zangbo ophiolites from nanga parbat to namche barwa syntaxes, southern tibet: First synthesis of petrology, geochemistry, and geochronology with incidences on geodynamic reconstructions of neo-tethys. *Gondwana Research*, 22(2):377–397.

Iaffaldano, G., Husson, L., and Bunge, H.-P. (2011). Monsoon speeds up indian plate motion. *Earth and Planetary Science Letters*, 304(3-4):503–510.

Ingersoll, R., Bullard, T., Ford, R., Grimm, J., Pickle, J., and Sares, S. (1984). The effect of grain size on detrital modes: a test of the gazzi-dickinson point-counting method. *Journal of Sedimentary Petrology*, 54:103–116.

Karunakaran, C. and Rao, R. (1976). Status of exploration of hydrocarbon in the himalayan region-contributions to stratigraphy and structure. *Geological Society of India Miscellaneous Publication*, 41:66 p.

Kisakürek, B., James, R. H., and Harris, N. B. W. (2005). Li and δ^7li in himalayan rivers: Proxies for silicate weathering? *Earth and Planetary Science Letters*, 237(3-4):387–401.

Kisakürek, B., Widdowson, M., and James, R. H. (2004). Behaviour of li isotopes during continental weathering: the bidar laterite profile, india. *Chemical Geology*, 212(1-2):27–44.

Kolattukudy, P. E. (1976). *Chemistry and biochemistry of natural waxes*. Elsevier Scientific Pub. Co., Amsterdam; New York.

Kotlia, B. S., Singh, A. K., Joshi, L. M., and Dhaila, B. S. (2015). Precipitation variability in the indian central himalaya during last ca. 4,000 years inferred from a speleothem record: Impact of indian summer monsoon (ism) and westerlies. *Quaternary International*, 371:244–253.

Kroon, D., Steens, T., and Troelstra, S. (1991). Onset of monsoonal related upwelling in the western arabian sea as revealed by planktonic foraminifers. *Proceedings of the Ocean Drilling Programm, Scientific Results*, 117:257–263.

Kumar, G. (1997). Geology of arunachal pradesh. *Bangalore, Geological Society of India, Special Publication*.

Kumar, R., Ghosh, S. K., Mazari, R. K., and Sangode, S. J. (2003). Tectonic impact on the fluvial deposits of plio-pleistocene himalayan foreland basin, india. *Sedimentary Geology*, 158(3-4):209–234.

Kump, L., Brantley, S., and Arthur, M. (2000). Chemical weathering, atmospheric co$_2$, and climate. *Annual Review of Earth and Planetary Sciences*, 28(1):611–667.

Kübler, B. and Goy-Eggenberger, D. (2001). La cristallinité de l'illite revisitée: Un bilan des connaissances acquises ces trente dernières années. *Clay Minerals*, 36:143–157.

Kübler, B. and Jaboyedoff, M. (2000). Illite crystallinity. *Comptes Rendus de l'Académie des Sciences - Series IIA - Earth and Planetary Science*, 331(2):75–89.

Lanson, B., Beaufort, D., Berger, G., Petit, S., and Lacharpagne, J. (1995). Evolution de la structure cristallographique des minéraux argileux dans le réservoir grèseux rotliegend des pays-bas. *Bulletin des Centres de Recherche Elf Aquitaine Production*, 19:243–265.

Le Fort, P. (1986). Metamorphism and magmatism during the himalayan collision. *Geological Society, London, Special Publications*, 19(1):159–172.

Licht, A., van Cappelle, M., Abels, H. A., Ladant, J. B., Trabucho-Alexandre, J., France-Lanord, C., Donnadieu, Y., Vandenberghe, J., Rigaudier, T., Lecuyer, C., Terry Jr, D., Adriaens, R., Boura, A., Guo, Z., Soe, A. N., Quade, J., Dupont-Nivet, G., and Jaeger, J. J. (2014). Asian monsoons in a late eocene greenhouse world. *Nature*, 513(7519):501–506.

Lupker, M., France-Lanord, C., Galy, V., Lavé, J., Gaillardet, J., Gajurel, A. P., Guilmette, C., Rahman, M., Singh, S. K., and Sinha, R. (2012). Predominant floodplain over mountain weathering of himalayan sediments (ganga basin). *Geochimica et Cosmochimica Acta*, 84(0):410–432.

Lupker, M., France-Lanord, C., Galy, V., Lavé, J., and Kudrass, H. (2013). Increasing chemical weathering in the himalayan system since the last glacial maximum. *Earth and Planetary Science Letters*, 365(0):243–252.

Mange, M. and Maurer, H. (1992). Heavy minerals in colour. *Chapman and Hall, London*, page 147 pp.

Meigs, A. J., Burbank, D. W., and Beck, R. A. (1995). Middle-late miocene (>10 ma) formation of the main boundary thrust in the western himalaya. *Geology*, 23(5):423–426.

Millot, R., Vigier, N., and Gaillardet, J. (2010). Behaviour of lithium and its isotopes during weathering in the mackenzie basin, canada. *Geochimica et Cosmochimica Acta*, 74(14):3897–3912.

Misra, S. and Froelich, P. N. (2012). Lithium isotope history of cenozoic seawater: Changes in silicate weathering and reverse weatheirng. *Science*, 335:818–823.

Molnar, P. (2005). Mio-pliocene growth of the tibetan plateau and evolution of east asian climate. *Palaeontologia Electronica*, 8(1):1–23.

Molnar, P., Boos, W. R., and Battisti, D. S. (2010). Orographic controls on climate and paleoclimate of asia: Thermal and mechanical roles for the tibetan plateau. *Annual Review of Earth Planetary Sciences*, 38:77–102.

Molnar, P., England, P., and Martinod, J. (1993). Mantle dynamics, uplift of the tibetan plateau, and the indian monsoon. *Reviews of Geophysics*, 31(4):357–396.

Moore, D. M. and Reynolds, R. C. (1997). *X-Ray diffraction and the identification and analysis of clay minerals*. Oxford University Press.

Najman, Y., Appel, E., Boudagher-Fadel, M., Bown, P., Carter, A., Garzanti, E., Godin, L., Han, J., Liebke, U., Oliver, G., Parrish, R., and Vezzoli, G. (2010). Timing of india-asia collision: Geological, biostratigraphic, and palaeomagnetic constraints. *Journal of Geophysical Research: Solid Earth*, 115(B12):n/a–n/a.

Najman, Y., Bickle, M., Garzanti, E., Pringle, M., Barfod, D., Brozovic, N., Burbank, D., and Ando, S. (2009). Reconstructing the exhumation history of the lesser himalaya, nw india, from a multitechnique provenance study of the foreland basin siwalik group. *Tectonics*, 28(5):TC5018.

Najman, Y., Bracciali, L., Parrish, R. R., Chisty, E., and Copley, A. (2016). Evolving strain partitioning in the eastern himalaya: The growth of the shillong plateau. *Earth and Planetary Science Letters*, 433:1–9.

Nakayama, K. and Ulak, P. D. (1999). Evolution of fluvial style in the siwalik group in the foothills of the nepal himalaya. *Sedimentary Geology*, 125(3-4):205–224.

Nesbitt, H. W. and Young, G. M. (1984). Prediction of some weathering trends of plutonic and volcanic rocks based on thermodynamic and kinetic considerations. *Geochimica et Cosmochimica Acta*, 48(7):1523–1534.

Ojha, T. P., Butler, R. F., DeCelles, P. G., and Quade, J. (2009). Magnetic polarity stratigraphy of the neogene foreland basin deposits of nepal. *Basin Research*, 21(1):61–90.

Oliver, L., Harris, N., Bickle, M., Chapman, H., Dise, N., and Horstwood, M. (2003). Silicate weathering rates decoupled from the 87sr/86sr ratio of the dissolved load during himalayan erosion. *Chemical Geology*, 201(1-2):119–139.

Pagani, M., Zachos, J. C., Freeman, K. H., Tipple, B., and Bohaty, S. (2005). Marked decline in atmospheric carbon dioxide concentrations during the paleogene. *Science*, 309:600.

Pistiner, J. S. and Henderson, G. M. (2003). Lithium-isotope fractionation during continental weathering processes. *Earth and Planetary Science Letters*, 214(1-2):327–339.

Pogge von Strandmann, P. A. E., Burton, K. W., James, R. H., van Calsteren, P., and Gislason, S. R. (2010). Assessing the role of climate on uranium and lithium isotope behaviour in rivers draining a basaltic terrain. *Chemical Geology*, 270(1-4):227–239.

Pogge von Strandmann, P. A. E., Jenkyns, H. C., and Woodfine, R. G. (2013). Lithium isotope evidence for enhanced weathering during oceanic anoxic event 2. *Nature Geosci*, 6(8):668–672.

Pogge von Strandmann, P. A. E., Opfergelt, S., Lai, Y.-J., Sigfusson, B., Gislason, S. R., and Burton, K. W. (2012). Lithium, magnesium and silicon isotope behaviour accompanying weathering in a basaltic soil and pore water profile in iceland. *Earth and Planetary Science Letters*, 339-340:11–23.

Pratt-Sitaula, B., Burbank, D. W., Heimsath, A., and Ojha, T. (2004). Landscape disequilibrium on 1000-10,000 year scales marsyandi river, nepal, central himalaya. *Geomorphology*, 58(1-4):223–241.

Qi, H., Coplen, T., Wang, Q., and Wang, Y. (1997). Unnatural isotopic composition of lithium reagents. *Anal. Chem.*, 69:4076–4078.

Qiu, L., Rudnick, R. L., McDonough, W. F., and Merriman, R. J. (2009). Li and δ^7li in mudrocks from the british caledonides: Metamorphism and source influences. *Geochimica et Cosmochimica Acta*, 73(24):7325–7340.

Quade, J., Cater, J., Ojha, T., Adam, J., and Harrison, T. (1995). Late miocene environmental change in nepal and the northern indian subcontinent: Stable isotopic evidence from paleosols. *Geological Society of America Bulletin*, 107(12):1381–1397.

Quade, J. and Cerling, T. E. (1995). Expansion of c4 grasses in the late miocene of northern pakistan: evidence from stable isotopes in paleosols. *Palaeogeography, Palaeoclimatology, Palaeoecology*, 115(1-4):91–116.

Quade, J., Cerling, T. E., and Bowman, J. R. (1989). Development of asian monsoon revealed by marked ecological shift during the latest miocene in northern pakistan. *Nature*, 342(6246):163–166. 10.1038/342163a0.

Quade, J., Eiler, J., Daëron, M., and Achyuthan, H. (2013). The clumped isotope geothermometer in soil and paleosol carbonate. *Geochimica et Cosmochimica Acta*, 105(0):92–107.

Raiverman, V. and Seshavataram, B. (1983). On mode deposition of subathu and dharamsala sediments in the himlayan foothills in punjab and himachal pradesh. *Wadia Commemorative Volume*, pages 556–571.

Ravizza, G. and Esser, B. K. (1993). Third international symposium on the geochemistry of the earth surface a possible link between the seawater osmium isotope record and weathering of ancient sedimentary organic matter. *Chemical Geology*, 107(3):255–258.

Raymo, M. E. and Ruddiman, W. F. (1992). Tectonic forcing of late cenozoic climate. *Nature*, 359(6391):117–122. 10.1038/359117a0.

Righi, D. and Meunier, A. (1995). Origin of clays by rock weathering and soil formation. *In: Velde, B., ed., Origin and Mineralogy of Clays: Clays and the Environment, Springer Verlag, Berlin*, pages 43–161.

Robinson, D., DeCelles, P., Garzione, C., Pearson, O., Harrison, T., and Catlos, E. (2003). Kinematic model for the main central thrust in nepal. *Geology*, 31(4):359–362.

Rosenau, N. A. and Tabor, N. J. (2013). Oxygen and hydrogen isotope compositions of paleosol phyllosilicates: Differential burial histories and determination of middle late pennsylvanian low-latitude terrestrial paleotemperatures. *Palaeogeography, Palaeoclimatology, Palaeoecology*, 392(0):382–397.

Rudnick, R. L., Tomascak, P. B., Njo, H. B., and Gardner, L. R. (2004). Extreme lithium isotopic fractionation during continental weathering revealed in saprolites from south carolina. *Chemical Geology*, 212(1-2):45–57.

Sachse, D., Billault, I., Bowen, G. J., Chikaraishi, Y., Dawson, T. E., Feakins, S. J., Freeman, K. H., Magill, C. R., McInerney, F. A., van der Meer, M. T., Polissar, P., Robins, R. J., Sachs, J. P., Schmidt, H.-L., Sessions, A. L., White, J. W., West, J. B., and Kahmen, A. (2012). Molecular paleohydrology: Interpreting the hydrogen-isotopic composition of lipid biomarkers from photosynthesizing organisms. *Annual Review of Earth and Planetary Sciences*, 40(1):221–249.

Sachse, D., Radke, J., and Gleixner, G. (2006). δd values of individual n-alkanes from terrestrial plants along a climatic gradient - implications for the sedimentary biomarker record. *Organic Geochemistry*, 37(4):469–483.

Sangode, S. J., Kumar, R., and Ghosh, S. K. (1996). Magnetic polarity stratigraphy of the siwalik sequence of haripur area (h.p.), nw himalaya. *Journal Geological Society India*, 47(June 1996):683–704.

Sanyal, P., Bhattacharya, S. K., Kumar, R., Ghosh, S. K., and Sangode, S. J. (2004). Mio pliocene monsoonal record from himalayan foreland basin (indian siwalik) and its relation to vegetational change. *Palaeogeography, Palaeoclimatology, Palaeoecology*, 205(1 2):23–41.

Sanyal, P., Sarkar, A., Bhattacharya, S. K., Kumar, R., Ghosh, S. K., and Agrawal, S. (2010). Intensification of monsoon, microclimate and asynchronous c4 appearance: Isotopic evidence from the indian siwalik sediments. *Palaeogeography, Palaeoclimatology, Palaeoecology*, 296(1-2):165–173.

Sanyal, P. and Sinha, R. (2010). Evolution of the indian summer monsoon: synthesis of continental records. *Geological Society, London, Special Publications*, 342:153–183.

Searle, M. P., Windley, B. F., Coward, M. P., Cooper, D., Rex, A. J., Rex, D., Tingdong, L., Xuchang, X., Jan, M. Q., Thakur, V. C., and Kumar, S. (1987). The closing of tethys and the tectonics of the himalaya. *Geological Society of America Bulletin*, 98(6):678–701.

Setti, M., Lopez-Galindo, A., Padoan, M., and Garzanti, E. (2014). Clay mineralogy in southern africa river muds. *Clay Minerals*, 49:717–733.

Singh, B. P., Lee, Y. I., Pawar, J. S., and Charak, R. S. (2007). Biogenic features in calcretes developed on mudstone: Examples from paleogene sequences of the himalaya, india. *Sedimentary Geology*, 201(1-2):149–156.

Singh, S. K. and France-Lanord, C. (2002). Tracing the distribution of erosion in the brahmaputra watershed from isotopic compositions of stream sediments. *Earth and Planetary Science Letters*, 202(3-4):645–662.

Strecker, M., Alonso, R., Bookhagen, B., Carrapa, B., Hilley, G., Sobel, E., and Trauth, M. (2007). Tectonics and climate of the southern central andes. *Annual Review of Earth and Planetary Sciences*, 35(1):747–787.

Suresh, N., Ghosh, S. K., Kumar, R., and Sangode, S. J. (2004). Clay-mineral distribution patterns in late neogene fluvial sediments of the subathu sub-basin, central sector of himalayan foreland basin: implications for provenance and climate. *Sedimentary Geology*, 163(3-4):265–278.

Tagami, T. and O'Sullivan, P. (2005). Fundamentals of fission-track thermoschronology. *Reviews in Mineralogy and Geochemistry*, 58:19–47.

Teng, F. Z., McDonough, W. F., Rudnick, R. L., Dalpé, C., Tomascak, P. B., Chappell, B. W., and Gao, S. (2004). Lithium isotopic composition and concentration of the upper continental crust. *Geochimica et Cosmochimica Acta*, 68(20):4167–4178.

Thiede, R. C., Bookhagen, B., Arrowsmith, J. R., Sobel, E. R., and Strecker, M. R. (2004). Climatic control on rapid exhumation along the southern himalayan front. *Earth and Planetary Science Letters*, 222(3-4):791–806.

Thiede, R. C. and Ehlers, T. A. (2013). Large spatial and temporal variations in himalayan denudation. *Earth and Planetary Science Letters*, 371-372:278–293.

Thomas, J. V., Parkash, B., and Mohindra, R. (2002). Lithofacies and palaeosol analysis of the middle and upper siwalik groups (plio-pleistocene), haripur-kolar section, himachal pradesh, india. *Sedimentary Geology*, 150(3-4):343–366.

Tomascak, P. B., Magna, T., and Dohmen, R. (2016). The surficial realm: Low temperature geochemistry of lithium. *In: Advances in Lithium Isotope Geochemistry, Springer International Publishing*, pages 157–189.

van der Beek, P., Litty, C., Baudin, M., Mercier, J., Robert, X., and Hardwick, E. (2016). Contrasting tectonically driven exhumation and incision patterns, western versus central nepal himalaya. *Geology*.

van der Beek, P., Robert, X., Mugnier, J.-L., Bernet, M., Huyghe, P., and Labrin, E. (2006). Late miocene - recent exhumation of the central himalaya and recycling in the foreland basin assessed by apatite fission-track thermochronology of siwalik sediments, nepal. *Basin Research*, 18(4):413–434.

Vigier, N., Decarreau, A., Millot, R., Carignan, J., Petit, S., and France-Lanord, C. (2008). Quantifying li isotope fractionation during smectite formation and implications for the li cycle. *Geochimica et Cosmochimica Acta*, 72(3):780–792.

Vigier, N., Gislason, S. R., Burton, K. W., Millot, R., and Mokadem, F. (2009). The relationship between riverine lithium isotope composition and silicate weathering rates in iceland. *Earth and Planetary Science Letters*, 287(3-4):434–441.

Vigier, N. and Goddéris, Y. (2015). A new approach for modeling cenozoic oceanic lithium isotope paleo-variations: the key role of climate. *Climate of the Past*, 11:635–645.

Vögeli, N., Huyghe, P., Van der Beek, P., Najman, Y., Garzanti, E., and Chauvel, C. (sub.a). Weathering regime in the eastern himalaya since the mid-miocene: Indications from detrital geochemistry and clay mineralogy of the kameng river section, arunachal pradesh, india. *Basin Research*.

Vögeli, N., Najman, Y., van der Beek, P., Huyghe, P., and Wynn, P. (2015). Climatic variation along strike in the himalayas since mid-miocene. *AGU Abstract*.

Vögeli, N., Najman, Y., Van der Beek, P., Huyghe, P., Wynn, P., and Govin, G. (sub.b). Lateral climatic variation in the himalaya since the miocene: a west-east comparison. *Geology*.

Vögeli, N., Van der Beek, P., Huyghe, P., and Najman, Y. (in prep). Weathering, climate and seasonality in the himalayas, an east- west comparison: Indications from major elements and clay mineralogy.

Walker, J. C. G., Hays, P. B., and Kasting, J. F. (1981). A negative feedback mechanism for the long-term stabilization of earth's surface temperature. *Journal of Geophysical Research: Oceans*, 86(C10):9776–9782.

Wanner, C., Sonnenthal, E. L., and Liu, X.-M. (2014). Seawater ?7li: A direct proxy for global co2 consumption by continental silicate weathering? *Chemical Geology*, 381:154–167.

Wen, D.-R., Liu, D., Chung, S.-L., Chu, M.-F., Ji, J., Zhang, Q., Song, B., Lee, T.-Y., Yeh, M.-W., and Lo, C.-H. (2008). Zircon shrimp u-pb ages of the gangdese batholith and implications for neotethyan subduction in southern tibet. *Chemical Geology*, 252(3-4):191–201.

West, A. J., Galy, A., and Bickle, M. (2005). Tectonic and climatic controls on silicate weathering. *Earth and Planetary Science Letters*, 235(1-2):211–228.

Whipple, K. X. (2009). The influence of climate on the tectonic evolution of mountain belts. *Nature Geoscience*, 2(2).

White, N. M., Parrish, R. R., Bickle, M. J., Najman, Y. M. R., Burbank, D., and Maithani, A. (2001). Metamorphism and exhumation of the nw himalaya constrained by u-th-pb analyses of detrital monazite grains from early foreland basin sediments. *Journal of the Geological Society*, 158(4):625–635.

White, N. M., Pringle, M., Garzanti, E., Bickle, M., Najman, Y., Chapman, H., and Friend, P. (2002). Constraints on the exhumation and erosion of the high himalayan slab, nw india, from foreland basin deposits. *Earth and Planetary Science Letters*, 195(1-2):29–44.

Willett, S. (1999). Orogeny and orography: The effects of erosion on the structure of mountain belts. *Journal of Geophysical Research: Earth Surface*, 104(B12):28957–28981.

Wobus, C. W., Hodges, K. V., and Whipple, K. X. (2003). Has focused denudation sustained active thrusting at the himalayan topographic front? *Geology*, 31(10):861–864.

Yin, A. (2006). Cenozoic tectonic evolution of the himalayan orogen as constrained by along-strike variation of structural geometry, exhumation history, and foreland sedimentation. *Earth-Science Reviews*, 76(1-2):1–131.

Yin, A. and Harrison, T. M. (2000). Geologic evolution of the himalayan-tibetan orogen. *Annual Review of Earth Planetary Sciences*, 28(1):211. Yin, An Harrison, T. Mark; Source Info: 2000, Vol. 28 Issue 1, p211; Subject Term: OROGENY; Subject Term: HIMALAYA Mountains; Subject Term: TIBET, Plateau of; Subject Term: ASIA; Subject Term: CHINA; Number of Pages: 73p; Document Type: Article.

Appendix A

Sampling points

A.1 Kameng

Table A.1: Sample coordinates, type and corresponding age of the Kameng section

Sampling point	Latitude	Longitude	Age [Ma]	Stratigraphic unit	Sample type
KM-13-1	27.07635	92.59032	8.6	MS	c
KM-13-2	27.01457	92.64555	8.3	MS	c
KM-13-3	27.01756	92.63719	7.3	MS	f
KM-13-4	27.01831	92.63689	6.8	MS	c
KM-13-5	27.04039	92.6027	13	LS	c, f
KM-13-6	27.04193	92.6016	12.8	LS	c, f
KM-13-7	27.04796	92.595	11.6	LS	c, f
KM-13-8	27.04968	92.59694	12	LS	c
KM-13-9	27.05243	92.59606	11.1	LS	c
KM-13-10	27.05601	92.59451	11	LS	c, f
KM-13-11	27.0603	92.59332	10.5	LS	c, f
KM-13-12	27.06508	92.59296	10	MS	c, f
KM-13-13	27.07064	92.59106	9	MS	c, f
KM-13-14	27.07384	92.59095	8.8	MS	f
KM-13-15	27.07664	92.58941	8.3	MS	c, f
KM-13-16	27.08288	92.58792	8	MS	c, f
KM-13-17	27.02503	92.631	5.5	MS	c
KM-13-18	27.02714	92.62373	4	MS	c
KM-13-19	27.02773	92.61025	2	MS	c, f
KM-13-20	27.03583	92.60939	0.8	US	c, f
KM-13-21	27.037	92.60768	0.5	US	c (org. mat.)
KM-13-22	27.03744	92.60702	0.3	US	f
KM-13-23	27.06862	92.59293	9.7	MS	c, f
KM-13-24	27.05757	92.59494	10.6	LS	f (org. mat.)
KM-13-25	27.05343	92.59627	11.5	LS	f
KM-13-26	27.0473	92.60042	12.3	LS	c, f
KM-13-27	27.03262	92.61753	2.2	US	c
KM-13-28	27.03198	92.62179	3.2	MS	c, f
KM-13-29	27.02077	92.6359	6.3	MS	c
KM-13-30	27.01873	92.63692	7.5	MS	c, f, fossil leave
Holocene Terrace	26.93378	92.83468	0.01		f

c: coarse, f: fine

A.2 Joginder Nagar

Table A.2: Sample coordinates, type and corresponding age of the Joginder Nagar section

Sampling point	Latitude	Longitude	Age [Ma]	Stratigraphic unit	Sample type
JN14-1	31.832519	76.783903	20.5	Lower Dharamsala	c,f
JN14-2	31.844329	76.783191	20.3	Lower Dharamsala	c,f , nod
JN14-3	31.844175	76.785683	19.7	Lower Dharamsala	c,f
JN14-4	31.848471	76.788411	18.3	Lower Dharamsala	f, nod
JN14-5	31.850269	76.782111	19	Lower Dharamsala	c,f , nod
JN14-6	31.850489	76.783844	18.5	Lower Dharamsala	c,f , nod
JN14-7	31.850984	76.786948	17.9	Lower Dharamsala	c, f
JN14-8	31.853343	76.788734	17.4	Lower Dharamsala	c,f , nod
JN14-9	31.854516	76.790818	17.1	Lower Dharamsala	c,f , nod
JN14-10	31.862037	76.781569	16.9	Lower Dharamsala	c,f , nod
JN14-11	31.869033	76.779044	16.5	Upper Dharamsala	c,f , nod
JN14-12	31.87137	76.780192	16.4	Upper Dharamsala	c, f
JN14-13	31.872613	76.781879	15.7	Upper Dharamsala	c, f
JN14-14	31.872876	76.784146	15.1	Upper Dharamsala	c, f
JN14-15	31.872321	76.78606	14.9	Upper Dharamsala	c, f
JN14-16	31.874686	76.78732	14.8	Upper Dharamsala	c, f
JN14-17	31.881877	76.782861	14.6	Upper Dharamsala	c, f
JN14-18	31.884321	76.784738	14.2	Upper Dharamsala	c, f
JN14-19	31.884812	76.787677	14.1	Upper Dharamsala	c,f , nod
JN14-20	31.891199	76.785031	13.9	Upper Dharamsala	c, f
JN14-21	31.894146	76.786538	13.5	Upper Dharamsala	c, f
JN14-22	31.902505	76.787398	13	Upper Dharamsala	c, f
JN14-23	31.904705	76.791124	12.9	LS	c, f
JN14-24	31.913499	76.790466	12.8	LS	c, f
JN14-25	31.842158	76.781531	20.2	Lower Dharamsala	f, nod
JN14-26	31.842611	76.783061	20.3	Lower Dharamsala	f, nod
JN14-27	31.845608	76.786672	19.3	Lower Dharamsala	f, nod
JN14-28	31.84966	76.782814	18.9	Lower Dharamsala	f, nod
JN14-29	31.850646	76.787683	17.8	Lower Dharamsala	f, nod
JN14-30	31.855632	76.791255	17	Lower Dharamsala	f, nod
JN14-31	31.858415	76.792138	16.95	Lower Dharamsala	f, nod
JN14-32	31.86697	76.778729	16.6	Upper Dharamsala	f, nod
JN14-33	31.894298	76.785955	13.6	Upper Dharamsala	f, nod
JN14-34	31.894503	76.787434	13.4	Upper Dharamsala	f, nod
JN14-35	31.89595	76.78894	13.3	Upper Dharamsala	f, nod
JN14-36	31.900566	76.788625	13.2	Upper Dharamsala	f, nod
JN14-37	31.904901	76.789995	12.95	LS	f, nod

c: coarse, f: fine, nod: nodule

A.3 Jawalamukhi

Table A.3: Sample coordinates, type and corresponding age of the Jawalamukhi section

Sampling point	Latitude	Longitude	Age [Ma]	Stratigraphic unit	Sample type
JW14-1	31.972751	76.444391	5	US	c, f
JW14-2	31.955242	76.44086	5.4	US	c, f
JW14-3	31.956282	76.433288	5.6	US	c, f, nod
JW14-4	31.945351	76.418196	6	US	c, f, nod
JW14-5	31.944845	76.413217	6.2	US	c, f
JW14-6	31.943809	76.405015	6.8	MS	c, f, carbonate
JW14-7	31.930847	76.399151	7.2	MS	c, f
JW14-8	31.924717	76.394695	7.9	MS	c, f
JW14-9	31.917328	76.387299	8.6	MS	c
JW14-10	31.914415	76.377819	9	MS	c, f
JW14-11	31.913041	76.370347	9.5	MS	c
JW14-12	31.910544	76.368468	9.6	MS	c, f
JW14-13	31.903253	76.370404	9.8	MS	c, f
JW14-14	31.900522	76.367963	10	MS	c, f
JW14-15	31.896142	76.358342	10.2	MS	c, f
JW14-16	31.890341	76.331851	10.4	MS	c, f
JW14-17	31.882859	76.327415	10.6	MS	c, f, nod
JW14-18	31.89122	76.319381	10.9	MS	c, f
JW14-19	31.892302	76.311248	11.3	LS	c, f, nod
JW14-20	31.895187	76.308222	11.9	LS	c, f, nod
JW14-21	31.895522	76.304351	12.3	LS	c, f, nod
JW14-22	31.91991	76.391853	8.3	MS	c, f, nod
JW14-23	31.902769	76.370004	9.75	MS	f, nod
JW14-24	31.8879	76.342199	10.3	MS	f, nod
JW14-25	31.883671	76.33209	10.5	MS	f, nod
JW14-26	31.883034	76.327745	10.55	MS	f, nod
JW14-27	31.886201	76.325564	10.7	LS	f, nod
JW14-28	31.886867	76.32561	10.8	LS	f, nod
JW14-29	31.887467	76.313624	11.2	LS	f, nod
JW14-30	31.893709	76.308119	11.8	LS	f, nod
JW14-31	31.896271	76.305745	12.1	LS	f, nod
JW14-32	31.895093	76.299226	12.5	LS	f, nod

c: coarse, f: fine, nod: nodule

A.4 Haripur Kolar

Table A.4: Sample coordinates, type and corresponding age of the Haripur Kolar section

Sampling point	Latitude	Longitude	Age [Ma]	Stratigraphic unit	Sample type
HK14-1	30.440827	77.388473	5.8	MS	c, f
HK14-2	30.454227	77.378693	5.2	US	c, f, nod
HK14-3	30.45651	77.391293	4.9	US	c, f, nod
HK14-4	30.458289	77.398214	4.6	US	c, f
HK14-5	30.463234	77.404342	4	US	c, f, nod
HK14-6	30.46468	77.406275	3.8	US	c, f, nod
HK14-7	30.467512	77.406858	3.5	US	f, nod
HK14-8	30.468376	77.407078	3.3	US	f, nod
HK14-9	30.468968	77.408174	3.1	US	c, f, nod
HK14-10	30.472932	77.408848	3	US	c, f, nod
HK14-11	30.450384	77.384183	5.3	US	c, f
HK14-12	30.447568	77.385491	5.7	MS	c, f
HK14-13	30.473022	77.415367	2.8	US	c, f
HK14-14	30.480278	77.427128	1.1	US	c, f, nod
HK14-15	30.479464	77.425421	1.9	US	c, f
HK14-16	30.475985	77.42282	2.3	US	c, f
HK14-17	30.474333	77.419519	2.6	US	c, f, nod
HK14-18	30.473521	77.417782	2.7	US	f, nod
HK14-19	30.49312	77.419857	0.5	US	c, f

c: coarse, f: fine, nod: nodule

A.5 Modern Rivers

Table A.5: Sample coordinates, type of modern river samples

Sample Name	Latitude	Longitude	Age [Ma]	Sample type
Kam-down	26.93378	92.83468	modern	water, mud, sand
Dikrang	27.14587	93.74529	modern	water, mud, sand
Subansiri	27.51177	94.25575	modern	water, mud, sand
Siang	28.10266	95.29497	modern	water, mud, sand
Yarlung down	29.264383	91.469583	modern	mud
Yarlung up	29.333833	90.704517	modern	mud
Beas River	31.830909	76.789381	modern	water, mud sand
Sutlej River	31.413033	76.871794	modern	water, mud sand
Somb River	30.437373	77.384317	modern	water, mud sand
Yamuna River	30.434058	77.629143	modern	water, mud sand
Jner Khad	31.955242	76.44086	modern	mud, sand
Siw-Riv-1	27.02077	92.6359	modern	water, mud sand
Siw-Riv-2	26.97562	93.60062	modern	water, mud sand
Siw-Riv-3	27.51348	94.25149	modern	water, mud sand
Siw-Riv-4	28.00866	95.23151	modern	water, mud sand

Appendix B

Water Analysis of Eastern Himalayan Rivers

Table B.1: Results of water analysis of eastern Himalayan Rivers

Sample Name	Ba μg/L	Be μg/L	Bi μg/L	Cd μg/L	Ce ng/L	Co μg/L	Cr μg/L	Cs μg/L	Cu μg/L	Dy ng/L	Er ng/L	Eu ng/L	Ga μg/L	Gd ng/L	Ho ng/L	In μg/L
Manas	8.0493	< L.D.	< L.D.	< L.D.	< L.D.	< L.D.	0.3255	1.1722	0.9463	< L.D.	< L.D.	< L.D.	0.0117	< L.D.	< L.D.	< L.D.
Dikrang	1.6576	< L.D.	< L.D.	< L.D.	< L.D.	< L.D.	0.1044	0.0131	0.2317	4.7255	3.4669	< L.D.	0.0064	3.662	< L.D.	< L.D.
Kameng up	6.8826	< L.D.	< L.D.	< L.D.	< L.D.	< L.D.	0.1172	0.08	0.383	< L.D.	< L.D.	< L.D.	< L.D.	< L.D.	< L.D.	< L.D.
Kameng down	6.8839	< L.D.	< L.D.	< L.D.	< L.D.	< L.D.	0.1259	0.0637	0.2036	< L.D.	< L.D.	< L.D.	0.0035	< L.D.	< L.D.	< L.D.
Subansiri	10.6785	< L.D.	< L.D.	< L.D.	< L.D.	< L.D.	0.2242	0.1866	0.0886	< L.D.	< L.D.	< L.D.	0.007	< L.D.	< L.D.	< L.D.
Siw-Riv-1	4.7287	< L.D.	< L.D.	< L.D.	< L.D.	< L.D.	0.2955	0.0241	0.1819	< L.D.	< L.D.	< L.D.	0.0064	< L.D.	< L.D.	< L.D.
Siw-Riv-2	3.5078	< L.D.	< L.D.	< L.D.	< L.D.	< L.D.	0.5085	0.021	0.2044	< L.D.	< L.D.	< L.D.	0.0396	< L.D.	< L.D.	< L.D.
Siw-Riv-3	3.6833	< L.D.	< L.D.	< L.D.	< L.D.	< L.D.	0.3331	0.0258	0.0592	< L.D.	< L.D.	< L.D.	0.0209	< L.D.	< L.D.	< L.D.
Siw-Riv-4	8.3999	< L.D.	< L.D.	< L.D.	< L.D.	< L.D.	0.3287	0.0115	< L.D.	< L.D.	< L.D.	< L.D.	0.0058	< L.D.	< L.D.	< L.D.
Siang	11.3497	< L.D.	< L.D.	< L.D.	< L.D.	< L.D.	0.4138	1.2065	0.2373	< L.D.	< L.D.	< L.D.	0.007	< L.D.	< L.D.	< L.D.

Sample Name	La ng/L	Lu ng/L	Nd ng/L	Ni μg/L	Pb μg/L	Pr ng/L	Rb μg/L	Sm ng/L	Sr μg/L	Tb ng/L	Th μg/L	Tm ng/L	U μg/L	V μg/L	Y μg/L	Yb ng/L
Manas	< L.D.	< L.D.	< L.D.	< L.D.	< L.D.	< L.D.	2.936	< L.D.	77.3966	< L.D.	< L.D.	< L.D.	2.694	0.2725	0.0046	< L.D.
Dikrang	10.9519	< L.D.	11.7166	< L.D.	< L.D.	2.7857	2.1272	< L.D.	20.5818	< L.D.	< L.D.	< L.D.	0.0649	0.3939	0.0309	3.4278
Kameng up	< L.D.	< L.D.	< L.D.	< L.D.	< L.D.	< L.D.	2.8108	< L.D.	36.7069	< L.D.	< L.D.	< L.D.	0.3276	0.2275	0.0053	< L.D.
Kameng down	< L.D.	< L.D.	< L.D.	< L.D.	< L.D.	< L.D.	2.4705	< L.D.	37.1763	< L.D.	< L.D.	< L.D.	0.4122	0.2628	0.0042	< L.D.
Subansiri	< L.D.	< L.D.	< L.D.	< L.D.	< L.D.	< L.D.	2.4865	< L.D.	65.3767	< L.D.	< L.D.	< L.D.	0.2442	0.2447	0.0048	< L.D.
Siw-Riv-1	< L.D.	< L.D.	< L.D.	< L.D.	< L.D.	< L.D.	3.0203	< L.D.	92.4931	< L.D.	< L.D.	< L.D.	0.0934	0.3467	0.0028	< L.D.
Siw-Riv-2	< L.D.	< L.D.	< L.D.	< L.D.	< L.D.	< L.D.	2.1112	< L.D.	106.4889	< L.D.	< L.D.	< L.D.	0.5337	1.3077	0.0077	< L.D.
Siw-Riv-3	< L.D.	< L.D.	< L.D.	< L.D.	< L.D.	< L.D.	2.2207	< L.D.	155.0884	< L.D.	< L.D.	< L.D.	0.0942	0.3778	0.0048	< L.D.
Siw-Riv-4	< L.D.	< L.D.	< L.D.	< L.D.	< L.D.	< L.D.	0.7043	< L.D.	42.6561	< L.D.	< L.D.	< L.D.	0.0067	0.8944	< L.D.	< L.D.
Siang	< L.D.	< L.D.	< L.D.	< L.D.	< L.D.	< L.D.	3.5309	< L.D.	133.9609	< L.D.	< L.D.	< L.D.	1.6107	0.3664	0.0075	< L.D.

Sample Name	Zn μg/L	Al μg/L	Mn μg/L	Si mg/L	Fe mg/L	Mg mg/L	Ca mg/L	Na mg/L	K mg/L	Ti mg/L	P mg/L
Manas	6.7853	13.3046	< L.D.	3.936	< L.D.	3.663	18.56	3.223	1.228	< L.D.	< L.D.
Dikrang	< L.D.	11.8439	0.4117	6.67	< L.D.	0.812	4.33	3.486	1.062	< L.D.	< L.D.
Kameng up	4.7548	2.6816	< L.D.	4.755	< L.D.	1.458	7.761	2.596	1.046	< L.D.	< L.D.
Kameng down	1.2473	7.3596	< L.D.	4.766	< L.D.	1.504	8.117	2.609	0.979	< L.D.	< L.D.
Subansiri	< L.D.	6.9038	< L.D.	3.966	< L.D.	4.03	15.41	2.261	0.854	< L.D.	< L.D.
Siw-Riv-1	< L.D.	1.7203	1.9084	9.554	< L.D.	4.233	18.2	9.244	1.423	< L.D.	< L.D.
Siw-Riv-2	< L.D.	7.5338	< L.D.	11.77	< L.D.	8.548	30.15	13.14	3.065	< L.D.	< L.D.
Siw-Riv-3	< L.D.	7.8622	< L.D.	4.868	< L.D.	3.825	26.5	6.399	1.16	< L.D.	< L.D.
Siw-Riv-4	< L.D.	3.1077	< L.D.	4.508	< L.D.	3.026	8.43	1.803	0.607	< L.D.	< L.D.
Siang	< L.D.	14.3098	< L.D.	3.362	< L.D.	4.174	23.02	4.087	1.472	< L.D.	< L.D.